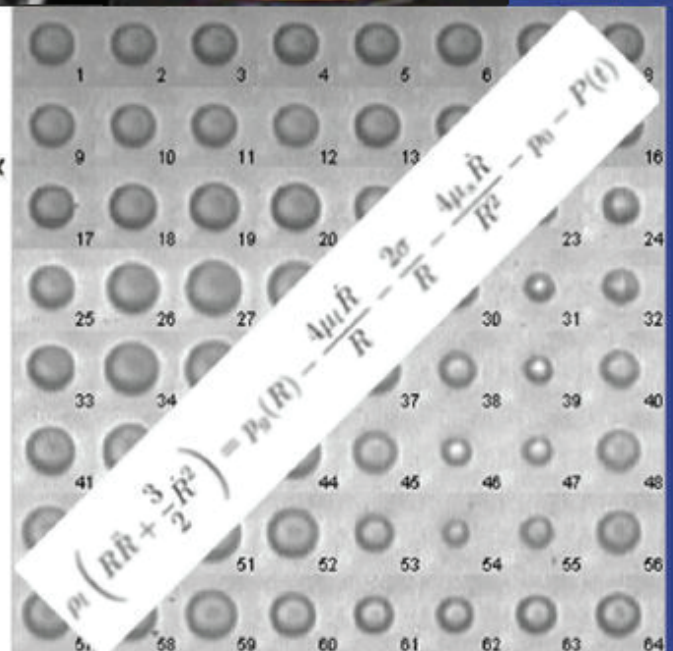
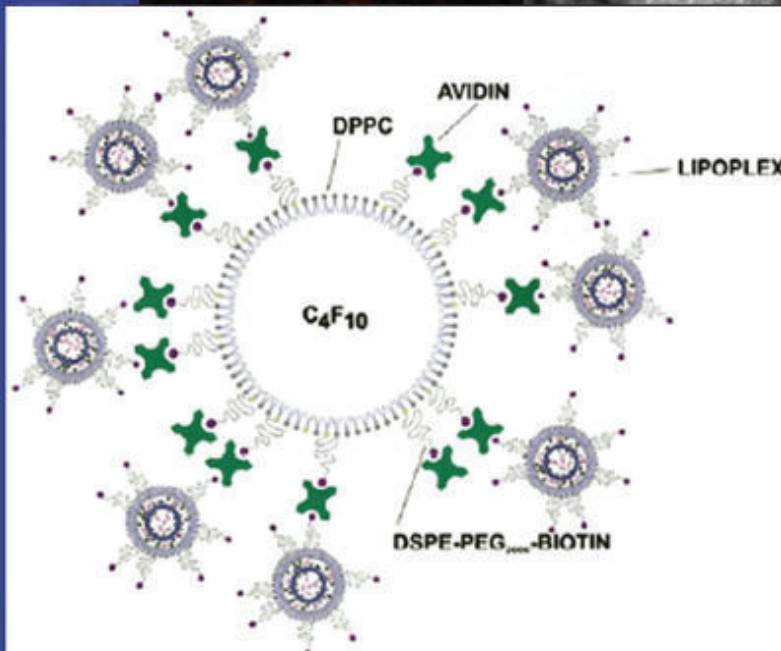
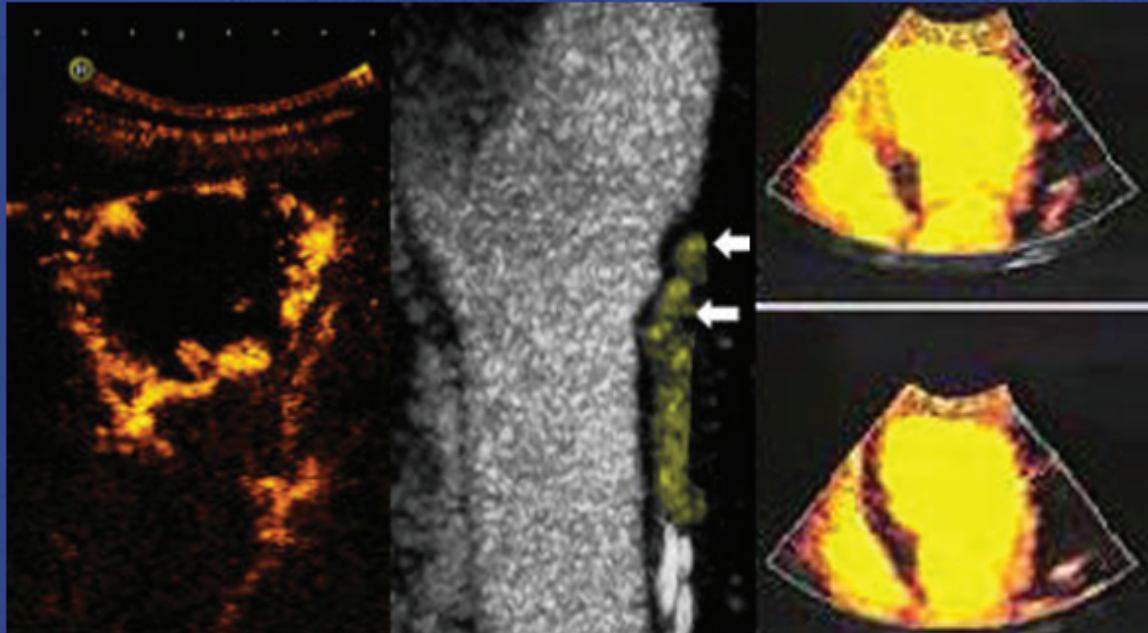


The 19th European Symposium on Ultrasound Contrast Imaging

- An ICUS Conference -



Abstract book

January, 23-24 2014, Rotterdam, The Netherlands

Organized by Nico de Jong, Arend Schinkel, Edward Leen

Erasmus MC Rotterdam - Imperial College London

19th EUROPEAN SYMPOSIUM ON ULTRASOUND CONTRAST IMAGING
23-24 JANUARY 2014, Rotterdam, The Netherlands

WEDNESDAY, 22 January 2014

18.00 – 20.00 Registration - Welcome Drinks

THURSDAY, 23 January 2014

Oral program

08.00 – 09.00	Registration	
09.00 – 09.05	Introduction and opening	<i>Nico de Jong & Arend Schinkel</i>
09.05 – 10.35	NEW IMAGING MODALITIES	<i>Chairpersons: Folkert ten Cate & Otto Kamp</i>
Paul Dayton	High frequency contrast enhanced ultrasound: Acoustic angiography	1
Thomas Fischer	Microbubbles for molecular ultrasound: Detection and therapy of prostate cancer	2
Jeff Powers	EPIQ: An ultrasound platform designed for microbubble contrast imaging in clinic and laboratory	3
Dan Adam	Improvement of imaging of contrast agents using coded excitation.....	6
Mark Abel	Dynamic contrast enhanced ultrasound (DCE-US) predicts progression free survival and overall survival for patients with liver metastases undergoing biological therapies.....	7
10.35 – 11.00	Intermission	
11.00 – 12.30	RADIOLOGY	<i>Chairpersons: Peter Burns & Eleanor Stride</i>
Eddie Leen	Irreversible Electroporation (IRE) Ablation integrated with chemotherapy for unresectable pancreatic carcinoma: Value of CEUS	9
Pavel Taimr	The additional use of contrast-enhanced ultrasonography for the distinction between focal nodular hyperplasia and hepatocellular adenoma	11
Fuminori Moriyasu	State of the art of contrast imaging in Japan	12
David Cosgrove	The status of CEUS in China	14
Xiang Zhou	Characterization of focal liver lesions by means of assessment of hepatic transit time with contrastenhanced US	16
12.30 – 14.00	LUNCH	
14.00 – 14.30	Dutch Heart Foundation lecture	<i>Chairperson: Nico de Jong</i>
Liza Villanueva	Drug and gene delivery with contrast.....	17
14.30 – 16.00	THERAPY	<i>Chairpersons: Arend Schinkel & Paul Dayton</i>
Steve Feinstein	Advances in therapeutic ultrasound: Gene delivery for CV applications.....	19
Ine Lentacker	New insights in sonoporation	23
James Choi	Exploiting flow in the design of ultrasonic pulse shapes and sequences for cavitation-mediated drug delivery	24
Ine de Cock	Ultrasound mediated delivery: Pore formation or enhanced endocytosis?	25
Lynda Juffermans	StemBells: A novel technique to direct stem cells to the infarcted heart using targeted microbubbles.....	28
16.00 – 16.30	Intermission	
16.30 – 18.00	HIGH FRAME RATE IMAGING	<i>Chairpersons: Mike Averkiou & Jeff Powers</i>
Peter Burns	Velocity-resolved contrast colour doppler using fast amplitude modulation	29
Stuart Foster	Adventures with gas vesicles for high frequency ultrasound contrast imaging	30
Olivier Couture	Ultrafast contrast imaging: From millisecond transient bubble dynamics to sub-wavelength resolution	32
Klazina Kooiman	Ultrafast lipid movement in the microbubble coating during oscillation – a fluorescence high-speed camera study	35
Matthew Bruce	Clinical feasibility of ultrafast imaging of microbubbles	39
18.30 – 22.30	SOCIAL EVENT (Incl. Dinner buffet)	

19th EUROPEAN SYMPOSIUM ON ULTRASOUND CONTRAST IMAGING
23-24 JANUARY 2014, Rotterdam, The Netherlands

FRIDAY, 24 January 2014

07.30 – 08.00 Registration

Poster sessions

07.30 – 09.00

MODERATED POSTER SESSION A: BIOLOGY *Moderator: Arend Schinkel*

A1)	Wey Chyi Teoh/ Christina Kalli	Does DCE-US measurement of flow parameters correlate with absolute flow measurement clinically?	44
A2)	Francois Yu	Release, uptake and cytotoxicity of doxorubicin loaded lipopolyplexes exposed to low intensity ultrasound	48
A3)	Jacques Terretaz	Gas-filled microbubbles used as an antigen delivery vehicle for vaccination.....	52
A4)	Siv Eggen	Improved delivery of nanomedicine in cancer tissue using ultrasound and a novel nanoparticle-microbubble platform	57
A5)	Yannick Bohren	Can ultrasound and microbubbles induce fibrinolysis in vitro without rTPA?	59
A6)	Aya Zeghimi	Experimental evidence of the cytoskeleton involvement during cell sonoporation.....	62
A7)	Sebastiaan Roos	ROMIUS: Reduction of Microvascular Injury Utilizing Sonolysis – Study design and rationale	67
A8)	Damianos Christofides	Improvement of accuracy of liver lesion DCEUS quantification using automatic respiratory gating	69

07.30 – 09.00

MODERATED POSTER SESSION B: TECHNOLOGY *Moderator: Nico de Jong*

B1)	Kirsten Christensen	Super-resolution localisation using single bubble acoustics and ultrasound.....	74
B2)	Tony Cheung/ Dorothy Gujral	Attenuation correction and image normalisation improve quantification of ultrasound contrast enhancement in carotid artery adventitia in cancer patients after radiation therapy	77
B3)	Paul Sheeran	Detecting the acoustic signatures of volatile phase-change perfluorocarbon agents	81
B4)	Satya Kotapalli	Unique fracturing mechanism of polymer shelled microbubbles: Acoustic characterization and optical observation	82
B5)	Jason Raymond	Impulse response of echogenic liposomes	86
B6)	Maria-Louisa Izamis	Basic bolus kinetics explored in an ex vivo liver machine perfusion model	90
B7)	Tom van Rooij	Influence of DSPC versus DPPC on acoustical responses of lipid-coated microbubbles	94
B8)	Tim Segers	Acoustic bubble sorting of ultrasound contrast agents.....	98

Wednesday–Friday

POSTER SESSION C: NEW DIRECTIONS I *Election by the audience*

C1)	Ying Luan	Stable nonlinear dynamics of free-floating lipid-coated microbubbles	101
C2)	Bart Lammertink	Temporal aspects of membrane permeability induced by cavitating microbubbles	104
C3)	Ilya Skachkov	Sonoporation dynamics at different acoustic pressures	107
C4)	Alexander Klibanov	In vivo acoustic imaging of large albumin stabilized microfluidic-produced microbubbles	110
C5)	Marc Derieppe	Recruitment of endocytosis in ultrasound-mediated drug delivery: A real-time study	112
C6)	Kentaro Otani	Development of integrin $\alpha\beta 3$ -targeted microbubbles based on clinically available ultrasound contrast agent.....	115
C7)	Malin Larsson	Endocardial border delineation capability of a multimodal polymer-shelled contrast agent	117
C8)	Christina Keravnou	A method for calculating acoustic pressure in the liver using linear measurements in water	119
C9)	Jean-Michel Escoffre	Influence of serum on gene delivery using microbubble-assisted ultrasound	124
C10)	Rick Kwekkeboom	Ultrasound and cationic microbubble induced local delivery of microRNA-based therapeutics both in vitro and in vivo	127
C11)	Katrien Vanderperren	The use of self-made microbubbles for contrast-enhanced ultrasound imaging in dogs: Potential for image-guided drug delivery <i>in vivo</i>	129

Wednesday–Friday

POSTER SESSION D: NEW DIRECTIONS II *Election by the audience*

D1)	Avinoam Bar-Zion	Denosing of contrast-enhanced ultrasound movies based on a multiplicative model	130
D2)	Daniele Peruzzini	Which harmonic gives the highest CTR and SNR?.....	132
D3)	Caroline Harfield	Theoretical and experimental observations of lipid shedding.....	135
D4)	Yann Desailly	Sono-activated ultrasound localization microscopy (SAULM): Basic principles, theoretical limits and simulations	137
D5)	Nabil Bouhouch	Contrast-enhanced angiogenesis imaging by mutual information analysis.....	139
D6)	Maarten Kuenen	Maximum-likelihood estimation for quantitative analysis in dynamic contrast-enhanced ultrasound	143
D7)	Paul Rademeyer	A high throughput device for measuring single microbubble response to ultrasound excitation	148
D8)	Keita Omiya	Numerical study on nonlinear oscillation and translation of an insonified microbubble.....	150
D9)	Maarten Kok	Pinched flow fractionation for ultrasound contrast agent enrichment.....	153
D10)	Charles Tremblay	Adapting amplitude modulation to plane-wave Doppler imaging	156
D11)	Sally Peyman	Microbubbles as stable drug-loadable structures toward targeted, triggered drug delivery	160
D12)	Oleksandr Shpak	Acoustic droplet vaporization is initiated by superharmonic focusing	162

19th EUROPEAN SYMPOSIUM ON ULTRASOUND CONTRAST IMAGING
23-24 JANUARY 2014, Rotterdam, The Netherlands

FRIDAY, 24 January 2014

Oral program

09.00 – 10.30	TECHNOLOGY <i>Chairpersons: Stuart Foster & Michel Versluis</i>	
Mangala Srinivas	Clinically-relevant, customizable agents for multimodal imaging	165
Nicolas Rognin	Ultrasound molecular imaging enhancement by Volumic Acoustic Radiation Force (VARF)	167
Jason Castle	Effects of molecule size and microbubble affinity on delivery	171
Tom Kokhuis	Intravital microscopy of localized stem cell delivery using microbubbles and acoustic radiation force	173
Yesna Yildiz	Correction of nonlinear propagation artefact in contrast enhanced ultrasound imaging	176
10.30 – 11.00	Intermission	
11.00 – 12.30	VASCULAR IMAGING <i>Chairpersons: Steve Feinstein & Edward Leen</i>	
Mike Averkiou	Evaluation of carotid plaque perfusion using DCEUS	179
Bernd Raffener	CEUS in rheumatology	182
Daniel Staub	Perivascular venous vascularization on contrast-enhanced ultrasound (CEUS) is correlated with inflammation in patients with acute deep vein thrombosis	184
Stijn van den Oord	Prevalence of subclinical atherosclerosis and intraplaque neovascularization in patients with familial hypercholesterolemia	187
Will Mauldin	Ultrasound-based measurement of molecular marker concentration in large blood vessels	189
12.30 – 14.00	LUNCH	
14.00 – 14.30	COEUR LECTURE <i>Chairperson: David Cosgrove</i>	
Folkert ten Cate	Perfusion imaging in the eighties: Has the goal been reached?	192
14.30 – 16.00	COMPETITION: MOLECULAR IMAGING <i>Chairpersons: Nico de Jong & Ine Lentacker</i>	
Joshua Owen	The influence of blood on targeted microbubbles	194
Jean-Marc Hyvelin	Ultrasound molecular imaging of transient acute myocardial ischemia with a new multi-selectins targeted ultrasound contrast agent: Correlation with the expression of selectins	197
Verya Daeichin	Ultrasound molecular imaging: Overcoming pitfalls in crucial steps	200
Alexander Klibanov	A simplified translatable targeted microbubble formulation: The use of helper molecules for high-efficiency attachment of peptide ligands to the microbubble shell	206
Shah Rukh Abbas	Peptide targeted microbubbles: Potential for targeted Imaging	210
Alexandre Helbert	Ultrasound molecular imaging of tumoral angiogenesis with BR55: Added values for the monitoring of focalised and systemic anti-tumoral therapies	211
16.00 – 16.10	DISCUSSION AND CONCLUSIONS <i>Nico de Jong & Arend Schinkel</i>	
16.10	ADJOURN AND ANNOUNCEMENT OF THE WINNERS OF THE COMPETITION AND POSTER PRIZES	

SPONSORS

FIRST ANNOUNCEMENT 2015

The Scientific Board: Arend Schinkel, Edward Leen, Nico de Jong, Mike Averkiou, Folkert ten Cate, Paolo Colonna, David Cosgrove, Eleanor Stride

High frequency contrast enhanced ultrasound: Acoustic angiography

Paul A. Dayton

The University of North Carolina at Chapel Hill, Chapel Hill, USA

Through the use of new dual-frequency ultrasound transducer technology, contrast enhanced ultrasound can be performed with unprecedented resolution and contrast-to-tissue ratio. This imaging technique enables the visualization of microvascular architecture without signal from background tissues, and can simultaneously provide anatomical information for registration. The resulting images are similar to x-ray angiography, and provide a new means to assess microvascular density and structure. Initial results indicate this new imaging modality can provide non-invasive insight into angiogenic processes involved in tumor growth and progression. This talk reviews the principles behind high-frequency contrast imaging, and illustrates application examples.

Microbubbles for molecular ultrasound: Detection and therapy of prostate cancer

Prof. Dr. med. Thomas Fischer

*Leiter Interdisziplinäres US-Zentrum, Institut für Radiologie im CC6,
Charitéplatz 1, 10117 Berlin*

Rationale and Objectives

To investigate whether rat prostate cancer can be detected by means of molecular ultrasound (US) using target-specific microbubbles versus a nonspecific contrast agent.

Materials and Methods

Twenty Copenhagen rats were randomly examined 75-104 days after orthotopic implantation of G-Dunning rat prostatic tumor cells was using a high-end US system and either 1.2 ml/kg of the nonspecific agent A or 0.1 ml/kg of the target-specific agent B containing VEGFR2 binding peptide. Contrast inflow (AUC analysis) was determined during the first 30s, and all microbubbles were destroyed in the scan plane by means of the flash technique 20 min after intravenous administration to investigate specific accumulation of individual bubbles in tumors. Differences between normal prostate tissue and tumor were analyzed using luminance images. Sonographically determined tumor localization and extent were compared with MRI and histology.

Results

The median tumor size in the 20 rats determined on US (2.3 mm) and MRI (2.4 mm) showed a very high correlation ($r=0.92$, $p=0.01$). Both agent A and agent B demonstrated higher vascularization of tumor periphery compared with normal prostate ($p<0.05$) based on contrast inflow and AUC analysis. 20 min after administration luminance for agent B in the tumor was significantly higher ($P=0.003$) compared to nonspecific agent A (11.8 to 0.1). In consensus reading the increase of signal intensity in the tumor compared to normal prostate tissue was significantly higher for agent B ($p=0.005$), whereas no significant difference was found for agent A ($p=0.180$).

Conclusions

The target-specific contrast agent was superior to the unspecific ultrasound contrast agent both with regard to early inflow analysis and specific accumulation in prostate cancer after 20 min.

Keywords: Contrast-enhanced ultrasound (CEUS), MRI, rat, prostate cancer

EPIQ: An ultrasound platform designed for microbubble contrast imaging in clinic and laboratory

Vijay Shamdasani, Patrick Rafter, Unmin Bae, Jeffry Powers and Towa Matsumura

Over the last decade, microbubble contrast agents have found widespread use in a variety of cardiology and radiology applications. Key image quality attributes that can aid the clinician in making confident diagnosis with contrast enhanced ultrasound (CEUS) include tissue cancellation, sensitivity, bubble resolution, image uniformity, agent lasting time and penetration. Although a lot is known about the behavior of contrast agents in acoustic fields, it is not clear if commercial ultrasound systems of today have harnessed this information to optimize CEUS image quality. In the third quarter of 2013, Philips released the EPIQ Premium ultrasound system that includes a fully featured CEUS package with significantly improved contrast imaging performance compared to its predecessors, the iU22 and iE33. In this abstract we describe the design philosophy and some of the key hardware capabilities that were added to EPIQ specifically for CEUS imaging.

To allow precise control of transmit waveforms so that different bubble sizes may be excited, EPIQ has an arbitrary apodized wave shaping capability. Since it is challenging for a high-voltage transmitter circuit to transmit high fidelity waveforms at the lower voltages employed for imaging of microbubbles, EPIQ has been designed with a low voltage gain stage allowing it to faithfully reproduce programmed waveforms at low mechanical indices. On receive, a wide-dynamic range amplifier and analog to digital converter (ADC) allows EPIQ to receive small non-linear acoustic signals from microbubbles without running into amplifier and ADC saturation issues from strong specular reflectors which cause bright nearfield artifacts.

nSight Imaging is a proprietary technology that uses massively parallel beamforming technology to retrospectively dynamically reconstruct transmit beams. The resulting increase in SNR is especially significant for late phase contrast imaging where only a fraction of the injected microbubbles remain in blood circulation. Workflow and usability studies were conducted to design CEUS touchscreen layouts for ease of clinical use.

In conclusion, we would like to share the CEUS imaging capabilities of EPIQ with the larger contrast research community at Rotterdam Contrast Ultrasound Symposium. We would also like to describe some of the engineering and data analysis tools that have aided in optimizing EPIQ for excellent CEUS imaging seen in the attached images, and invite inputs on unexplored applications of this imaging

platform.



Figure 1. CEUS Image of a transplanted kidney in a 17-year old patient at 15, 18 and 21s after injection. The clinician injected contrast microbubbles to verify that the entire kidney was viable and perfused, and the diagnosis was that the kidney was performing well.



Figure 2: CEUS Image of a 4-cm tumor in a 70-year old patient at 31s after injection (arterial phase). In this case, the arterial enhancement of the tumor and wash out in under 3 minutes (not shown here) confirmed the clinician's suspicion that this was a hepatocellular carcinoma.

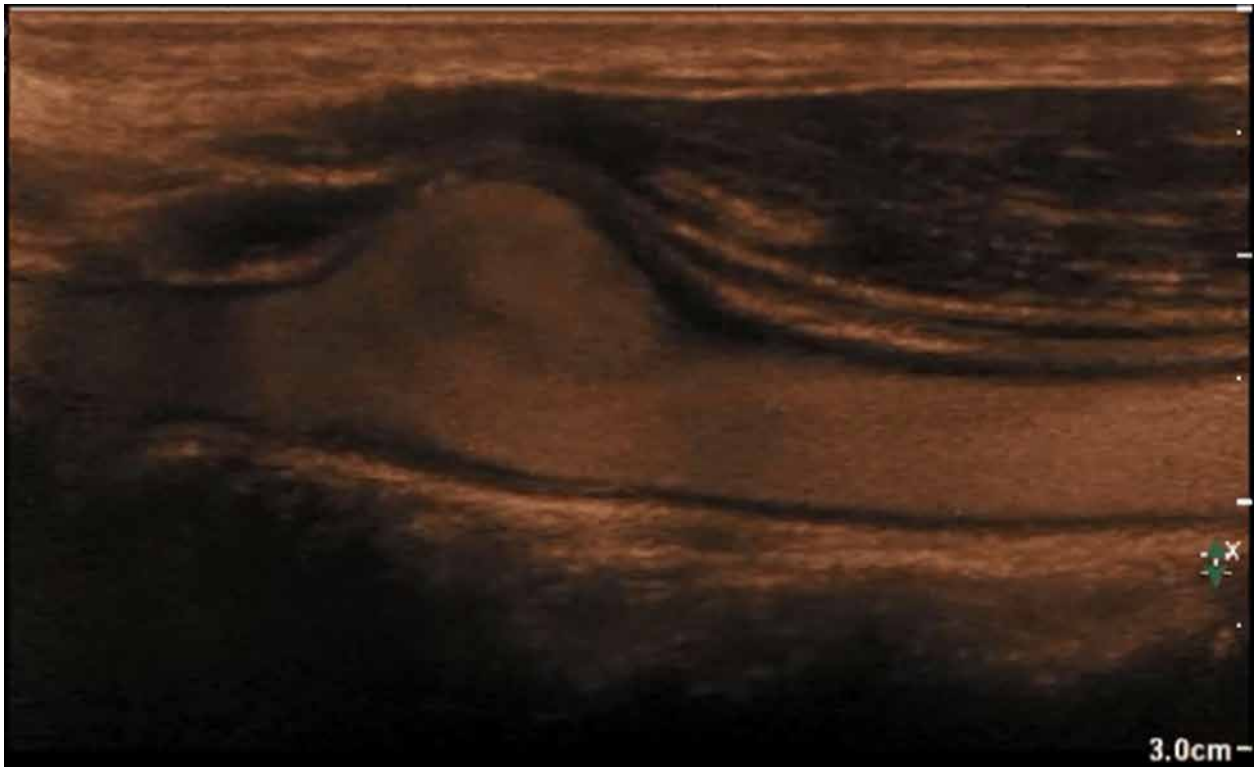


Figure 3: CEUS image of a carotid artery 25 seconds after injection of Sonovue. The artery is patent and intima-media complex is visible as a dark region between the bright adventitial layer and luminal contrast enhancement.

Improvement of imaging of contrast agents using coded excitation

Grigoriy Zurakhov, Zvi Friedman, Dan Adam

Department of Biomedical Engineering, Technion, Haifa 32000, Israel

Coded excitation (CE) is used in medical ultrasound in order to improve signal-to-noise-ratio (SNR) and penetration depth by overcoming the problem of peak transmit power limit while maintaining axial resolution. CE may be specifically beneficial when imaging ultrasound contrast agents (UCA), e.g. for measuring myocardial perfusion, while using specifically designed codes, at low mechanical index (MI). The goal of current study is to quantify the improvement obtained by CE use in comparison to Gaussian shaped pulse when UCA are insonated.

The study has been performed using the Field II simulation program in combination with the Bubblesim simulation program, where the latter enables modeling the behavior of a single or multiple microbubbles' (UCA) dynamics under various ultrasound pressure fields. The modeling scheme goes as follows: First, lateral and axial borders (at -6 dB) of resolution cell are calculated using an actual configuration of an ultrasound transducer (S3 probe, GE Healthcare, Inc.), and CE transmission. Second, N micro-bubbles with normally distributed radii are placed (at uniformly distributed random locations) within the resolution cell. In the next stage, each bubble is excited by the pressure field induced by one of several pulses, focused at the center of the resolution cell: An apodized long coded-excitation pulse ($\sim 10\mu S$) (Chirp), apodized sin wave of identical length, and a Gaussian shaped short pulse of equal magnitude Fourier spectrum to the Chirp. Finally, the bubbles' pressure responses received by aperture, are summed using appropriate delays. The location of the resolution cell (and the microbubbles within) was limited to be in the transmission plane, consequently out-of-plane effects are neglected and no elevation focusing is used.

Typical results demonstrate that for $N=100$ microbubbles, normally distributed $(\mu, \sigma) = (1.5, 0.3)\mu m$ and insonated at low MI (of 300 kPa peak-negative-pressure (PNP)), the Chirp pulses provide some enhancement of the echoes, at the main transmit frequencies as well as at the 2nd harmonic range of frequencies as shown at the table below.

	Average of 100 test-runs (for 100 microbubbles)	Standard deviation for 100 test-runs (for 100 microbubbles)
1 st Harmonic improvement	8.1 dB	0.8 dB
2 nd Harmonic improvement	7.2 dB	1.2 dB

Dynamic contrast enhanced ultrasound (DCE-US) predicts progression free survival and overall survival for patients with liver metastases undergoing biological therapies

M. Abel, C. Kalli, W.C. Teoh, W.S. Tian, H. Wasan & E. Leen

Experimental medicine division, Imperial College London, Hammersmith Hospital

Background

RECIST is well recognised to be limited in assessing liver cancer patients undergoing biological therapies, which are cytostatic rather than cytotoxic. There has been great interest in using DCE-US in monitoring/predicting response, as ultrasound microbubbles are pure intravascular tracers, ideal for measuring perfusion changes. As yet the effect of these agents on the global liver blood remains unknown.

Aim

To assess the value of using DCE-US in capturing perfusion changes both at tumour and global liver level.

Materials and methods

Thirty patients with liver metastases were studied using an iU22 ultrasound scanner (Philips, Bothwell, USA) with C5-1 transducer to carry out the DCE-US of the tumour, liver, the common hepatic artery and portal vein. All patients were fasted for at least 4 hours followed by DCE-US scans performed at baseline and at 2 weeks post treatment (Sorafenib, Sunitinib, Everolimus, Aflibercept, Axitinib).

The scans were analysed off-line using qLab software (Philips). Regions of interests (ROIs) were drawn around the perimetry of the tumour, hepatic artery, portal vein and the liver. The parameters from the Time Intensity Curves (TIC) were calculated for each ROI. Baseline TIC parameters were correlated with progression free survival (PFS) and overall survival (OS) of the patients. The PFS and OS of those classified as responders and non-responders were based on CT scans (Using RECIST 1.1) and based on 10%, 30% or 50% change in peak intensity and area under the curve of the liver and tumour.

Results

The baseline tumour-to-liver peak intensity ratio was significantly lower in responders vs non-responders (0.78 ± 0.46 vs 35.42 ± 11.17 ; $P=0.04$), as were the tumour wash in slope (WIS) ($P<0.02$) and its flow rate ($P<0.02$). At 2 weeks, responder had significantly higher rise time (RT) compared with non-responders.

Non-Responders based on a >30% increase in liver PI and AUC or >50% increase in liver (PI, AUC, WIS and FR) have significantly shorter PFS compared with responders. Non-Responders based on >50% reduction in tumour blood flow have significantly shorter OS (median 174 vs 252 days, $p=0.04$, 95% CI of ratio 0.65 to 12.17).

Discussion

The tumour and liver blood flow changes may be explained by the concept of “normalisation” of the tumour vasculature (Jain, R et al 2005). Normalisation is characterised by a reduction in “leakiness” of the tumour vessels, thereby restoring the tumoural interstitial pressure and a reduction in hypoxia. The reduction in the liver vascular volume/flow parameters may be due by the fact that these biological agents activity is not purely at tumoural level, but rather at a global systemic level.

Conclusion

DCE-US measurement of changes in liver blood flow parameters following anti-angiogenic therapies predicts PFS. The haemodynamic changes in the tumour and its microenvironment are adaptive and more complex than previously understood.

Irreversible electroporation (IRE) ablation integrated with chemotherapy for unresectable pancreatic carcinoma: value of CEUS

Professor Edward Leen

Chair of Radiology, Imperial College London, Hammersmith Hospital, London, UK

Background: Pancreatic Carcinoma

Pancreatic adenocarcinoma is the most lethal of the solid cancers and the fourth leading cause of cancer-related death with an increasing incidence in the Western world. The outcome is poor with an overall 5-year survival of less than 5%. Surgical resection (Whipple's) offers the potential for cure, but less than 10-15% will be suitable and the median survival is under 2 years in this group and the 5-year survival is poor, even with adjuvant chemotherapy at 11-21%; it is also associated with significant mortality (2-5%) and morbidity. In the majority who present with locally advanced or metastatic disease, the median survival ranges from 6-16 months. Considerable efforts have been made during the past decade to identify better systemic treatments; unfortunately, most trials have not shown a survival advantage for newer therapies. One of the major problems with systemic drugs is delivery, in that the tumours are often fibrotic, hypoxic and thus relatively avascular. Indeed, antiangiogenic approaches often led to deleterious survivals.

Local therapies

Radiation and chemoradiotherapy remain controversial. A recent phase III trial, The international LAP 07 study, determined whether chemoradiotherapy (CRT) affected overall survival in patients with inoperable locally advanced pancreatic cancer when tumors were controlled after 4 months of induction gemcitabine-based chemotherapy (CT). The CT (136 patients) and CRT (133 patients) arms had matched baseline characteristics. Median OS in the CT arm was 16.4 months compared with 15.2 months for the CRT group (hazard ratio [HR] 1.03, 95% CI [0.79, 1.34], $p = 0.8295$); The trial closed due to futility. No significant differences in PFS were observed: 11.8 months for CT compared with 12.5 months for CRT (HR 0.9, 95% CI [0.7, 1.1], $p = 0.2161$). This modern randomized trial is the largest and supports the results of the criticized ESPAC1 study, which also showed no benefit in the adjuvant setting. The hypoxic environment may thus be a severe impediment to radiation being effective.

(Hammel et al, 2013)

Ablative therapies

Radiofrequency ablation (RFA) combined with systemic chemotherapies have shown promising preliminary results as a novel approach for locally advanced pancreatic cancer management with median survival of 34 months compared with 25.6 months for those without RFA (Cantore et al, 2011). More recently RFA followed by neo-adjuvant chemotherapy showed an overall survival of 19 months with RFA related morbidity of 3.5% (Frigerio et al, 2013). As RFA is thermal-based, it is limited by heat-sink effect and associated with significant risk of injury to adjacent blood vessels, GI tract perforation and pancreatitis.

Irreversible Electroporation (IRE) ablation is a non-thermal based technique creating accurate volume of tissue ablation without the associated limitations of RFA. It is ideally suited for treating pancreatic carcinoma percutaneously or intra-operatively. Multiple overlapping IRE ablation zones can be planned to ablate large tumours of up to 5 cm, with sufficient ablation margin to minimise local recurrence. Its safety and efficacy in ablating unresectable pancreatic ca had been confirmed in previous studies maintaining the patency of adjacent vessels (Narayanan et al 2012). In a comparison of IRE patients to standard therapy, an improvement in local progression-free survival (14 vs. 6 months, $p = 0.01$), distant progression-free survival (15 vs. 9 months, $p = 0.02$), and overall survival (20 vs. 13 months) was shown in a recent study of 54 patients (Martin RC et al, 2012).

In a preliminary study of 25 patients with locally advanced and metastatic pancreatic carcinoma, the use of Contrast Enhanced US (CEUS) combined with CT scan will be discussed in the staging, guidance and assessment of response following IRE ablation of primary pancreatic carcinomas and its metastases.

The additional use of contrast-enhanced ultrasonography for the distinction between focal nodular hyperplasia and hepatocellular adenoma

*P. Taimr¹, M.E.E. Bröker², B. E.Hanssen¹, R. J. de Knegt¹, R. A. de Man¹,
J. N.M. IJzermans²*

¹Department of Gastroenterology and Hepatology

²Department of Surgery, Erasmus University Medical Center, Rotterdam, the Netherlands

Introduction

The diagnosis of hepatocellular adenoma has a great impact on the lives of young women due to the necessary surveillance or surgical resection. An adequate differentiation between benign liver masses is essential. At present MR Imaging is considered as the gold standard for definitive diagnosis. With the availability of contrast-enhanced ultrasound (CEUS), a novel technique to image liver tumors, we evaluated the clinical relevance of both imaging modalities and determined the value of CEUS, using SonoVue® (Bracco, Italy) in the diagnostic work-up of benign liver tumors compared to MRI.

Methods

Patients referred to our tertiary center between 1-5-07 and 1-5-13 because of a focal solid benign liver lesion and received a CEUS and a MRI were included. Consensus on the final diagnosis was reached after evaluation in a multidisciplinary tumor board committee

Results

Three hundred and four patients underwent a contrast-enhanced ultrasound to distinguish between hepatocellular adenoma and focal nodular hyperplasia. Patients were excluded if there was no lesion visible on CEUS, no MRI was performed or no final diagnosis was obtained (N=22). In 120/282 (43%) patients the final diagnosis was hepatocellular adenoma, in 162/282 (57%) focal nodular hyperplasia. Using contrast-enhanced ultrasonography the correct diagnosis was made in 254/282 patients. This results in a sensitivity of 86%, a specificity of 95% and accuracy 90,1% for the detection of hepatocellular adenoma with contrast-enhanced ultrasound.

Conclusion

Contrast-enhanced ultrasonography is suitable to make a fast differentiating between hepatocellular adenoma and focal nodular hyperplasia and should be combined with MRI to provide the accurate diagnosis and prevent biopsy.

State of the art of contrast imaging in Japan

Fuminori Moriyasu, M.D.

Department of Gastroenterology & Hepatology, Tokyo Medical University

Sonazoid has been launched in Japanese market in July, 2007. For these seven years more than 0.4 million injections were done to Japanese patients. There has been reported just 4 cases with nonfatal anaphylactoid reactions, which were recovered quickly and completely.

Application of Sonazoid which had been approved by Japanese FDA in 2007 was diagnosis of liver tumorous diseases, which means not only detection and characterization of the liver tumor but also efficacy evaluation of liver cancers after RFA (radio-frequency ablation) therapy. Detection of the space occupying lesions in the liver has been performed using “Kupffer cell imaging”, which is obtained more than ten minutes after intra-venous injection. Around 25% of injected Sonazoid microbubbles are accumulated in the liver being phagocytosed by Kupffer cells living in the endothelium of the sinusoidal space. Kupffer cell imaging lasts so long time as to be used for surveillance study of the whole liver and targeting and monitoring of RFA procedures for more than one hour.

Vascular contrast imaging is used for characterization of liver tumorous lesions. Maximum intensity projection (MIP) imaging is useful to visualize small sized blood vessels and bring diagnostic information about characteristic details of benign and malignant liver tumors. Parametric imaging such as arrival time imaging is also useful in clinical settings. Arrival time imaging is applied to evaluate hemodynamics of the tumor vessels.

Additional application of Sonazoid to breast tumor diagnosis has been approved by Japanese FDA in 2013. Differentiation between benign and malignant breast tumors using Sonazoid contrast ultrasound study superior to contrast MRI in the multi-center clinical trial performed by Daiichi-Sankyo pharmaceutical company.

Fusion imaging is referenced images between real time ultrasound imaging and previously obtained CT and MRI volume data, which are registered under magnetic field axes. Fusion imaging is also combination between real time ultrasound imaging and previously obtained 3D ultrasound volume data. Contrast ultrasound is used for fusion imaging. Not only vascular imaging, but also Kupffer cell imaging is used for this fusion imaging. Kupffer imaging inform us clearer border delineation of the tumor than fundamental imaging and vascular imaging.

Fusion imaging is used for simulation and navigation systems, which are used for guidance of local ablation therapies such as RFA, MWA (micro-wave ablation) and IRE (irreversible electroporation).

The applications of contrast ultrasound above-mentioned introduced in this talk.

The status of CEUS in China

David Cosgrove

Imperial and King's Colleges, London, UK

Ultrasonography in general is conducted in a special manner in mainland China: medical doctors take a speciality training in all uses of ultrasound, including therapeutic, and work in Departments of Ultrasound, where they have massive patient throughput and abundant helpers and nurses. Practitioners tend to perform a wide range of studies and it is not unusual for a Sonologist to move between diagnostic sessions in general body imaging, to an obstetric list, to an echocardiology session and on to an interventional session involving RF ablation of liver tumours. They may also perform HIFU. Though there is a recent tendency for Sonologists to narrow down their practices to focus on particular body parts, many are US Polymaths. Sonographers are rare, though starting to play a small role.

Contrast studies are usually performed in dedicated sessions, largely because patients bring their own agent with them (for which they pay) and so they need to change a prescription at the pharmacy.

Most patients pay for their own studies/treatments and insurance is restricted to the Military (a major and well-financed force in the country, with numerous high quality hospitals) and a few businesses employees. Thus 'private' medicine is the norm. The massive divide between the (relatively) wealthy eastern urban part of the country and the poor rural hinterland is a pervasive feature, which the government is trying to adjust.

SonoVue is the only contrast agent generally available in China though there are two interesting local products. A phospholipid microbubble containing perfluoropropane known as the Zifujixian agent (named for the city where it was developed) is licenced for the heart but is not widely used. The second is a soy-based liquid oral agent (Xinzhang) that is used to fill the stomach and improve access to the pancreas and the stomach wall; it can be used alone or in combination with SonoVue as a double contrast study, to improve the diagnosis and staging of gastric and pancreatic cancers.

Apart from its notable under-usage in echocardiology, CEUS with SonoVue is widely used in tertiary and academic centres and usage has increased steadily since its licencing in 2004. As in the west, its main use is for focal liver lesions in characterisation (especially for the all-too common HCC) and in monitoring interstitial ablation. It is also used for renal masses, gastric and pancreatic cancer and for characterising lymphadenopathy. The EFSUMB CEUS Guidelines are widely employed and have been translated into Chinese.

Much of the literature on CEUS (and other ultrasound research) is published in Chinese and so is not widely accessible, though there has been a notable surge in English language publications in recent years.

References

1. Xu HX, Lu MD, *The current status of contrast-enhanced ultrasound in China. J Med Ultrasonics (2010) 37:97-106*
2. Huang, P, S Li, WS Aronow, et al., *Double contrast-enhanced ultrasonography evaluation of preoperative Lauren classification of advanced gastric carcinoma. Archives of medical science : AMS, 2011. 7(2): p. 287-93*

Characterization of focal liver lesions by means of assessment of hepatic transit time with contrastenhanced US

Xiang Zhou, Ji-Bin Liu , Yan Luo, Feng Yan, Yulan Pen , Ling Lin, Hua Zhuang

Ultrasound Department, West China Hospital, P.R.China

Purpose

To assess whether hepatic transit times (HTTs), as measured with contrast material–enhanced ultrasonography (US), can help predict the nature of focal liver lesions.

Materials and Methods

The study was approved by the local institutional ethics committee, with written informed patient consent. A total of 402 patients were enrolled in the study. HTT, the time between the appearance of the microbubble contrast agent in the hepatic artery and its appearance in the hepatic vein, was measured in the contrast pulse sequencing mode after injection of a sulphur hexafluoride microbubble US contrast agent. Logistic regression was used to identify factors indicative of the malignant or nonmalignant status of focal liver lesions. Receiver operating characteristic (ROC) analysis was performed to determine the predictive value of the HTT.

Results

Observed HTTs for malignant focal liver lesions (mean, 6.2 seconds; range, 2–10 seconds) were significantly lower than those for nonmalignant lesions (mean, 9.5 seconds; range, 4–25 seconds; P , .001). ROC analysis revealed cutoff values of 7 seconds for HTT and 0.879 for area under the ROC curve. For HTTs of 7 seconds or shorter, hepatic malignancies were detected with a sensitivity of 79%, a specificity of 80%, a positive predictive value of 53%, and a negative predictive value of 93%. No malignant lesions had an HTT longer than 10 seconds.

Conclusion

HTT alone could be a good predictor for nonmalignancy of focal liver lesions.

Drug and gene delivery with contrast

*Andrew R. Carson, PhD; Charles F. McTiernan, PhD; Jianjun Wang, PhD;
Xucai Chen, PhD; Flordeliza S. Villanueva, MD*

*Center for Ultrasound Molecular Imaging and Therapeutics,
University of Pittsburgh Medical Center, Pittsburgh, PA*

Despite the rapid pace of development of RNA inhibition (RNAi) RNAi to treat disease, there are major barriers to clinical application, including siRNA instability in blood, rapid elimination, nonspecific accumulation in non-target tissue, poor penetration into target cells, and inefficient intracellular availability. One of the biggest impediments is the lack of an effective means to deliver siRNA to the cytoplasm of target cells in a fashion that retains siRNA activity, as the highly charged siRNA does not easily cross hydrophobic lipid cell membranes. Efforts to address these challenges include chemical modification of siRNA and the development of viral and non-viral carriers, which are associated with significant limitations. To address the obstacles to effective siRNA delivery, we and others have focused on the development of an siRNA delivery system that capitalizes on the unique bioeffects that ensue when microbubble carriers of siRNA are subjected to an ultrasound field. These bioeffects culminate in enhanced cell membrane permeability to macromolecules, including nucleic acids.

Microbubbles are microspheres containing a shell-encapsulated gas, used as intravascular ultrasound contrast agents in diagnostic echocardiography. Although microbubbles may vary in shell composition, all expand and contract (oscillate) when insonified by ultrasound at specific frequencies and acoustic pressures. Ultrasound-induced microbubble behaviors, ranging from stable to inertial cavitation and occurring in proximity to cell membranes, cause transient pores to form in cell membranes (sonoporation), endocytosis, and enhancement of endothelial permeability. These mechanisms may promote drug or nucleic acid uptake by the cell. Unlike other siRNA carriers which may rely on endocytosis for cell internalization, sonoporation, which is likely one major component of the ultrasound-microbubble delivery system, facilitates non-endosomal uptake of macromolecules.

We hypothesized that microbubbles and ultrasound targeted microbubble destruction (UTMD) could be used to enhance delivery of EGFR-directed siRNA (EGFR siRNA) and limit growth of squamous cell carcinoma tumors *in vivo*. Custom designed MBs were shown to efficiently bind high levels of siRNA (~7 μg per 10^9 microbubbles) and mediate protection from RNase. UTMD mediated delivery of microbubbles loaded with EGFR siRNA to murine squamous cell carcinoma cells (SCC-VII) *in vitro* slowed EGF-dependent cell replication in the subsequent 48 hrs, resulting in significantly fewer viable cells than following UTMD-mediated delivery of control siRNA ($3.3 \pm 0.4 \times 10^5$ vs. $8.3 \pm 2.4 \times 10^5$,

p<0.001). Serial UTMD mediated delivery of EGFR siRNA in vivo significantly and markedly increased the tumor doubling time in a murine model of squamous cell carcinoma (EGFR siRNA treated tumors 10 ± 6 days; control siRNA treated tumors 2 ± 0 days; no siRNA treated tumors 2 ± 0 days; p=0.002). UTMD of microbubbles loaded with EGFR siRNA also significantly decreased EGFR expression as assayed by immunofluorescent analysis (p=0.005) and RT PCR analysis (p=0.035) of tumor samples. These data indicate that custom designed microbubbles and UTMD can deliver gene-targeted siRNA to tumors and blunt tumor growth.

Advances in therapeutic ultrasound: Gene delivery for CV applications

*Steven B. Feinstein, MD, FACC, FESC,
Professor of Medicine/Cardiology*

Rush University Medical Center, Chicago, Illinois, USA

Translation of ultrasound-directed therapy

Site-specific, ultrasound-directed, drug/gene delivery systems provide unlimited potential to advance the field of personalized medicine and therapeutics. For nearly two decades investigators envisioned the uses of ultrasound directed therapies for the treatment of diseases including monogenic disease states. Today, there are a number of active pre-clinical programs poised to enter the clinics, thus bolstering the field of translational medicine.

Gene therapy

Gene Therapy (2013) Wired Carl Zimmer 08.13.2013. “Gene therapy emerges from disgrace to be the next big thing, again.”

Historically, the use of viral vectors held great promise for future therapeutic interventions. However, the unintended insertional nature of the viral-mediated process resulted in deleterious clinical events including deaths (1993). Recently, newer viral technologies revisited the applications using uses of Lenti-viruses. (Lentiviral hematopoietic stem cell gene therapy in patients with Wiskott-Aldrick Syndrome. Aituti a et al. Science 341 (2013)DOI:10.1126/science.1233151. Lentiviral hematopoietic stem cell gene therapy benefits metachromaticleukodystrophy. Science 341 (2013) DOI:10.1126/science. 1233158.

Ultrasound-directed, microbubble therapy

“...Conclusions: It is possible to combine ultrasound microbubbles, and chemotherapy in a clinical setting using commercially available clinical ultrasound scanners to increase the number of treatment cycles, prolonging the quality of life in patients with pancreatic adenocarcinoma compared to chemotherapy alone.” (Treatment of human pancreatic cancer using combined ultrasound, mcirobubbles, and gemcitabine: A clinical case study. Kotopoulos A et al., 2013; American Association of Physicists in Medicine [<http://dx.doi.org/10.1118/1.4808149>])

The premier CV therapeutic target = HDL cholesterol

Cardiovascular diseases remain the leading cause of death worldwide affecting men and women (Lloyd-Jones 2010). In the United States alone, 40 percent of all deaths are due to CVD, more than all forms of cancer combined (Lloyd-Jones 2007).

Historical perspective on HDL therapy

Previous epidemiologic data and clinical studies support the concept that increasing HDL cholesterol reduces a patient's risk of CVD. The inverse relationship between HDL serum levels and CV disease was demonstrated in the Framingham studies over 40 years ago (1970), *Am J Med* 1977; 62:707, *JAMA* 1986;256:2835. Based on a 15-year follow up from the Framingham cohort, individuals treated to increase serum HDL cholesterol resulted in longer lives (Asztalos 2010). And the extent of HDL's potential cardio-protective benefit may be such that for every 1% reduction in HDL cholesterol there was an increase of 2% to 3% in heart disease.

Based on historic clinical data provided from the FATS (Brown 1990), HATS (Brown 2001) and Coronary Drug Project (Canner 1986) in which combination therapies were used, the results were more promising regarding the clinical value of nicotinic acid when used to raise the serum HDL and reduce CV events and induce atherosclerosis regression.

In addition to the well-known health risks associated with elevated serum LDL (hyper-beta lipoproteinemia) and low serum HDL (hypo-alpha lipoproteinemia) are recognized as a CV risk factors for premature cardiovascular events.

Background

Fisher et al., *ATVB* 2012;32:2813-20 and Kontush A et al., *ATVB* 2013;33:2715-23 recently outlined the state of the art of HDL structure and function. The authors provided insight into future of HDL therapies highlighting the need for devising "functional" HDL moieties for the effective treatment of inflammatory-related diseases.

Accordingly, in high profile clinical studies the designated primary endpoint has been simply, the elevation of serum HDL. While this laudable goal has been ostensibly achieved, the clinical results were disappointing. (i.e., Roche's agent Dalcetrapib, Pfizer's agent Torcetrapib and Abbott's agent Niaspan). Specifically, Torcetrapib and Dalcetrapib (CETP inhibitors) dramatically increased serum HDL, however, in the Torcetrapib Phase III clinical trial, there was no evidence for coronary plaque regression by IVUS measurement and safety issues were identified. Correspondingly, the Dalcetrapib Phase III clinical trial was stopped due to lack of clinically efficacy, whereas, safety was not an issue

(Pharma& Healthcare, May 7, 2012, Roche Terminates Development of CETP Inhibitor Dalcetrapib). The increased death rates associated with the Torcetrapib treatment group may have been associated with elevated BP based on the effect on the rennin angiotensin-aldosterone axis. (Nissen 2007)

Similarly, the NIH-directed, Abbott -supported Aim High clinical trial was halted on May 26, 2011, due to ineffective outcomes (AIM-HIGH investigators 2011). There were initial safety concerns associated with the treatment group (Nicotinic acid supplement, Niaspan); however, in the final analysis increased cerebrovascular events were not statistically associated with the Nicotinic acid preparation, Niaspan. And the most recent clinical trial presented at the ACC meeting in San Francisco march 2013 Merck Thrive study also failed to improve CV outcomes.

The Lancet article (May 17, 2012) “Plasma HDL cholesterol and risk of myocardial infarction: a median randomisation study” (Voight 2012) supported the concept that simply raising HDL-cholesterol (HDL-c) is not cardioprotective. The authors noted that genetic polymorphisms associated with higher HDL-c levels due to decreased catabolism (example endothelial lipase or CETP deficiency) are not associated with reduced CV risks.

The mechanism of action of each drug may provide insight to the effectiveness of an elevated serum HDL and the related clinical results. It appears that the primary role of nicotinic acid and the CETP inhibitors may not be associated with the creation of de novo HDL but rather associated with delay in the downstream metabolism of the non-functional HDL. Therefore, the circulating levels of serum HDL may be misleading regarding clinical outcomes.

Newer concepts: Functional vs. non-functional HDL

The current therapeutic failures associated with HDL therapies may be attributed to the discordance between absolute serum HDL levels and “functional” HDL as evident in the recent clinical trial failures. Additionally, a report in *J Am Coll Cardiol* 2012;60(23):2372-79 and accompanying editorial *J Am Coll Cardiol* 2012;60(23):2380-3], highlighted the functional status of HDL as a critically important factor in outcome prediction. These recent articles focused on the high risk for CV death associated with patients with CRF on dialysis despite statin usage. The authors noted the functional status of HDL was impaired (as determined by reverse cholesterol pathway facilitation and inability to serve as a reservoir for oxidation products) despite “normal” serum HDL levels. The potent pleiotropic effects of HDL include anti-oxidant, anti-inflammatory, anti-tumor and anti-atherosclerosis clinical effects. However, these powerful effects are attenuated by acute and chronic stresses (acute MI, sepsis, DM, chronic inflammation, etc.).

Successful atherosclerosis regression: ApoA-I Milano infusion therapy

Individuals with genetically-elevated functional HDL Milano ApoA-1 were noted to have an extended lifespan; essentially free of premature CV deaths despite normal or lower levels of serum HDL.

The Esperion clinical trial showed the lipid content of the atheroma was dramatically and acutely reduced from the plaque within hours of infusion. Three human trials have similarly shown ApoA-1 infusions reduce atherma volumes (Shaw 2008, Nissen 2003 and Tardif 2007). Therefore a consensus is developing among lipid experts that increasing HDL-c by enhancing ApoA-1 production is the only method of affecting HDL-c levels.

HDL therapy: Site-specific, ultrasound-directed therapy

We report a novel mechanism for increasing serum HDL cholesterol via intravenously delivered human ApoA-I plasmid DNA accompanied by acoustic microspheres. Human ApoA-I plasmids co-administered with acoustic microspheres have been successfully accomplished in three pre-clinical species, mice, rats and rabbits. Once infused, an external ultrasound system confirmed the presence of contrast effect within the liver vasculature. Serial pulsed sequences of acoustic energy disrupted the microspheres in situ to delivery plasmids to targeted areas. Within hours following a single, treatment (50-70 seconds), human messenger RNA coding for ApoA-I was observed in the rat liver cells along with circulating human ApoA-I protein which ultimately resulted in de novo elevated serum HDL.

If successful, this method may be directly translated to the clinics for the acute treatment of coronary plaque vulnerability/instability.

New insights in sonoporation

Lentacker I., De Cock I., De Smedt S.C.

Laboratory for General Biochemistry and Physical Pharmacy, Ghent University, Ghent, Belgium

In this presentation we would like to give an overview of recent insights which have been published to explain the mechanisms behind ultrasound induced drug delivery [1-2]. In the past, ultrasound induced drug delivery has been attributed to direct pore formation as well as enhanced endocytosis [3-4]. When categorizing literature it becomes clear that mainly studies using low ultrasound intensities have mentioned endocytosis as the dominant mechanism while direct pore formation has been reported in studies applying higher ultrasound pressures. We will confirm this hypothesis with recent data from our group showing that both phenomenons are stimulated during sonoporation. Moreover, we demonstrate that the balance between endocytosis and pore formation can be shifted or influenced by using different acoustic pressures. As pressure increases microbubble implosions can lead to pore formation and acoustic radiation force can even lead to cellular entry of the microbubbles [5-6]. In contrary, lower pressures mainly lead to microbubble cavitation thereby gently “massaging” the cellular membrane. These different microbubble-cell interactions will be illustrated with real-time confocal movies and are a plausible explanation for the observed uptake mechanisms. Our results also show that drugs have to be present during sonoporation to stimulate direct uptake through cell membrane pores while endocytosis can occur within a larger time-frame. This illustrates that selecting proper acoustic conditions and the right time frame is mandatory to stimulate drug delivery through the preferred uptake route and hence fully explore ultrasound induced drug delivery.

References

1. *Lentacker I. et al. Ultrasound induced sonoporation: definitions and underlying mechanisms. Advanced drug delivery reviews 2014. DOI: 10.1016/j.addr.2013.11.008*
2. *Delalande et al. Sonoporation: Mechanistic insights and ongoing challenges for gene transfer. Gene 2013, 525, 191-199*
3. *Meijering et al. Ultrasound and Microbubble-Targeted Delivery of Macromolecules Is Regulated by induction of Endocytosis and Pore Formation. Circ.Res 2009., 104, 679-687*
4. *Lentacker I. et al. Ultrasound exposure of lipoplex loaded microbubbles facilitates direct cytoplasmic entry of the lipoplexes. Mol. Pharm. 2009, 6, 457-467*
5. *Fan et al. Spatiotemporally controlled single cell sonoporation. PNAS 2012, 109, 16486-91*
6. *Zhou et al. Controlled permeation of cell membrane by single bubble acoustic cavitation. J. Control. Release 2012, 157, 103-111*

Exploiting flow in the design of ultrasonic pulse shapes and sequences for cavitation-mediated drug delivery

James J. Choi, Antonios Pouliopoulos, Farah Shammout, Patrizia Lee, Simone Bonaccorsi

Department of Bioengineering, Imperial College London, London, United Kingdom

The use of ultrasound and microbubbles have been increasingly used to enhance drug delivery dose and distribution to target regions of the body. Two methods, which have sparked considerable interest is drug delivery across cell membranes (i.e., sonoporation) and across endothelial cells. Although considerable progress has been made in designing conventional ultrasound parameters to improve drug delivery characteristics, there has been limited incorporation of flow, which both poses a significant challenge, and, as we will explain here, provides an opportunity to improve delivery outcome. In addition, conventional parameters are limited to a simple ON-OFF pulse sequence, which does not fully exploit cavitation dynamics. Here, we incorporate the use of physiologically-relevant flow in our design of pulse shapes and sequences in order to better dictate the duration and distribution of a particular mode of cavitation across the target volume. We consider two in vitro setups modelling sonoporation and capillary permeability: (1) endothelial cells in a chamber mimicking arterial fluid velocities and (2) a 300 μm diameter tube mimicking arteriole and capillary fluid velocities. In both experimental setups, a focused ultrasound transducer (0.5 MHz) was applied to the target volume while acoustic emissions were passively captured using a co-axially aligned transducer (7.5 MHz). In the sonoporation experiments, a pulse sequence was designed using a peak-rarefactional pressure of 58 kPa, which enabled trans-membrane delivery rates of ~85% without exacerbating cellular damage. Meanwhile, a novel mobile cavitation excitation sequence based on bursting multiple pulse trains was previously shown to improve the delivery of drugs across endothelial cells. Here we provide a mechanistic explanation on how this was achieved. Collectively, we will have demonstrated how flow can be exploited in our pulse sequence designs to improve cavitation duration and distribution, and ultimately, drug delivery.

Ultrasound mediated delivery: Pore formation or enhanced endocytosis?

De Cock I., De Smedt S., Lentacker I.

Laboratory for General Biochemistry and Physical Pharmacy, Ghent University, Ghent, Belgium

Introduction

The formation of aspecific pores in the cell membrane is well-known to contribute to ultrasound mediated drug delivery. However, more recently, ultrasound enhanced endocytosis was also suggested to occur. Remarkably, papers reporting endocytosis applied relatively low acoustic pressures [1]. Therefore, our aim is to investigate if the uptake mechanism is dependent on the ultrasound settings used, e.g. acoustic pressure. In addition, it was observed that there are subpopulations in cells showing uptake after ultrasound treatment [2]. However, the reason for the existence of these subpopulations was never addressed. We hypothesize there might be a link with the mechanism of uptake.

Methods

2 MDa FITC-dextran, used as model drug, and microbubbles were added to BLM cells. Immediately afterwards, cells were exposed to ultrasound with increasing acoustic pressure. FITC-dextran uptake and cell viability, by calcein AM staining, was quantified by flow cytometry. Based on the levels of FITC-dextran uptake, cell populations were separated via Fluorescent Activated Cell Sorting (FACS). After sorting, the intracellular localization of FITC-dextran was analyzed by confocal microscopy.

Results

In the fluorescence intensity plots, 2 subpopulations can be distinguished in the cells having FITC-dextran uptake after ultrasound treatment, i.e. a low and a high fluorescence intensity population (Fig. 1). At 100 kPa, cells mainly belong to the low uptake subpopulation. When increasing the acoustic pressure, the fraction of cells having a high uptake increases. Moreover, after cell sorting, confocal images show that cells of the low intensity population had a dotted fluorescence pattern (Fig. 2). This indicates that FITC-dextran was located in endocytotic vesicles. In contrast, the high intensity population showed a diffuse pattern, suggesting uptake via pores.

Conclusion

Our data show that ultrasound delivery occurs both by enhanced endocytosis and by pore formation. However, by adjusting the acoustic pressure, one of both mechanisms can be favored.

References

1. Meijering et al. (2009). *Ultrasound and Microbubble-Targeted Delivery of Macromolecules Is Regulated by Induction of Endocytosis and Pore Formation. Circ.Res.*, 104, 679-687
2. Guzmán et al. (2001). *Ultrasound-mediated disruption of cell membranes. II. Heterogeneous effects on cells. J.Acoust.Soc.Am.*, 101, 597-606

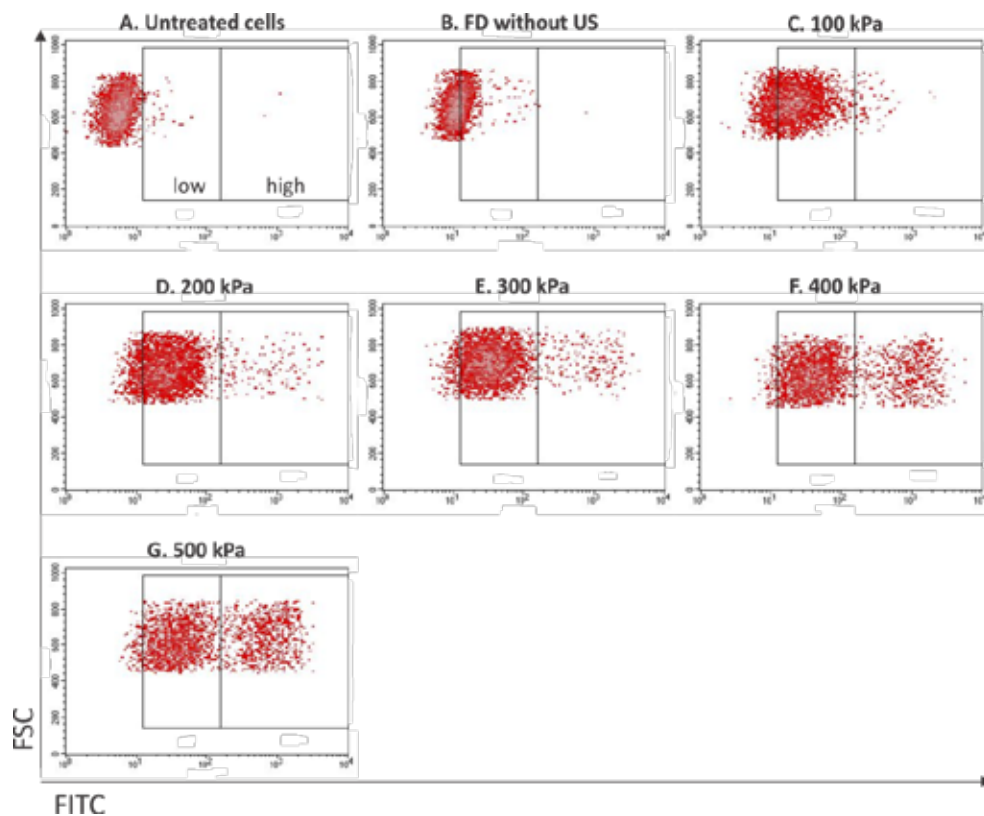


Figure 1: Flow cytometry plots (Forward scatter – FITC-fluorescence intensity). The low and high intensity subpopulations were gated as indicated. (A) Cells not treated with FITC-dextran and not exposed to ultrasound. (B) Cells incubated for 15 min with FITC-dextran and not exposed to ultrasound. (C)-(G) Cells incubated for 15 min with FITC-dextran and exposed to ultrasound with increasing acoustic pressure. Other ultrasound parameters include: center frequency of 1 MHz, pulse length of 2000 cycles, pulse repetition frequency of 125 Hz and exposure time of 5 sec.

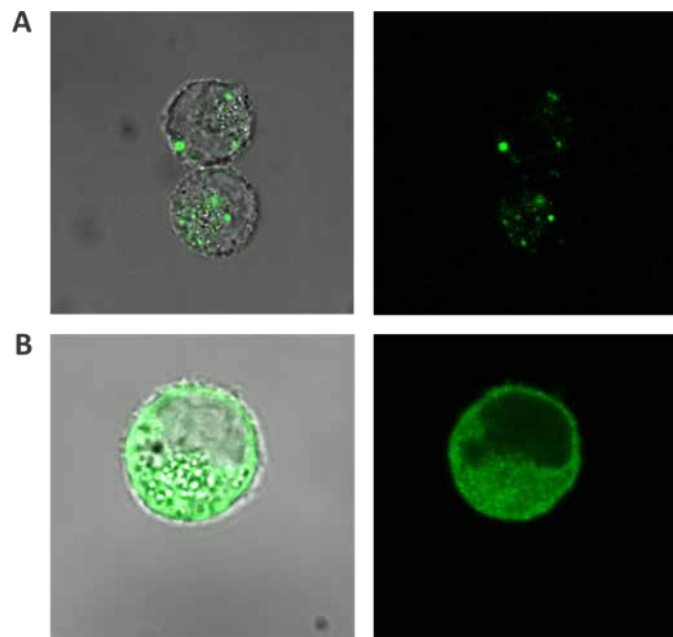


Figure 2: Confocal images. (A) Cells of the low intensity population with a dotted fluorescence pattern. (B) Cells of the high intensity population having a diffuse fluorescent signal over the whole cytoplasm.

StemBells: A novel technique to direct stem cells to the infarcted heart using targeted microbubbles

*B.A. Naaijens^{1,6,8}, P.A.J. Krijnen^{1,6}, T.J.A. Kokhuis^{7,8}, S.J.P. Bogaards^{3,6}, E. Meinster¹,
I. Bollen¹, O. Kamp^{4,6,8}, R.J.P. Musters^{2,6}, V.W.M. van Hinsbergh^{2,6}, M. Helder⁵,
N. de Jong^{7,8}, H.W.M. Niessen^{1,2,6}, A. van Dijk^{1,6} and L.J.M. Juffermans^{3,4,6,8}*

¹Depts. of Pathology, ²Cardiac Surgery, ³Physiology, ⁴Cardiology, ⁵Orthopedics, ⁶Institute for Cardiovascular Research, VU University Medical Center, Amsterdam, the Netherlands

⁷Dept. of Biomedical Engineering, Thorax Centre, Erasmus Medical Centre, Rotterdam, the Netherlands

⁸Interuniversity Cardiology Institute of the Netherlands, Utrecht, the Netherlands

Stem cell therapy is a promising tool to restore contractile function after myocardial infarction. Unfortunately, clinical trials show disappointing results with only minor improvements in cardiac function. The major problem of cellular therapy is lack of persistence of sufficient cells at the site of injury. We designed a novel technique to overcome this problem by directing stem cells to the infarcted area using targeted microbubbles (MB) and ultrasound (US). Adipose derived stem cells (ASC) were coupled to MB using an antibody against CD90. This stem cell-bubble complex was named StemBell. StemBells were targeted to the infarcted area via a second antibody: anti-CD54. US (1 MHz, 100 kPa, DC 10%) was applied to exert acoustic radiation force on the StemBells. *In vitro* we demonstrated that the formation of StemBells, as well as exposure to US had no negative effect on cell viability or attachment. In a flow system we showed that US was able to displace the StemBells from the center of flow to the side over a distance of tens to hundreds of microns. In a rat model for myocardial infarction and reperfusion, we demonstrated that 3h after intravenous injection of 1 million DAPI-labeled StemBells, significantly more cells (8-fold) were present specifically in the infarcted area ($p < 0.01$ vs 'ASC alone'), by performing fluorescence microscopy on heart cryosections. Furthermore, in a second long-term rat study, we showed that administration of StemBells significantly decreased the infarcted area at 5 weeks after injection (60% reduction, $p < 0.05$ vs control), by immunohistochemical staining of heart slices. Importantly, we found that the number of retrieved cells in the infarcted area had a strong significant correlation with improvement of the echocharacteristic value fractional shortening ($r = 0.75$, $p < 0.001$).

In conclusion, we successfully demonstrated proof-of-principle of a novel technique to increase the number of stem cells at the site of injury, which decreased infarct size. Importantly, we found that the more cells at the infarcted area resulted in a more improved heart function.

Velocity-resolved contrast colour doppler using fast amplitude modulation

Charles Tremblay-Darveau†, Ross Williams†, Matt Bruce, Peter N Burns†*

†Dept Medical Biophysics, University of Toronto

**Supersonic Imagine, Aix-en-Provence*

The most commonly used contrast imaging methods employ a short sequence of pulses that are modulated in phase, amplitude or both. The echoes are then combined to form a signal representing the power of the nonlinear component of the echo. A problem arises when tissue moves between pulses; this can be resolved by sending enough pulses to estimate the speed of motion of tissue and so create a highpass filter. At the same time, a method such as pulse inversion Doppler allows measurement of the effects of motion and the resolution of the Doppler shift of the nonlinear echoes, making a colour-resolved nonlinear Doppler image. However, in most scanners, the long ensemble lengths required for this mode lower the frame rate to an unacceptable level, so clinical contrast modes are often motion sensitive and show only Doppler power, with no velocity information. The impact of this shortcoming is evident both in radiological applications, where contrast imaging often fails to delineate vessels (frequently of diagnostic significance) in a perfused lesion, and in cardiology, where quantitative transthoracic imaging of coronary flow reserve is still not available.

Plane wave imaging offers image acquisition rate at the pulse repetition frequency, effectively increasing ultrasound imaging frame rate by up to two orders of magnitude. As well as fast imaging, this different form of acquisition can be used to achieve very long ensemble lengths for nonlinear modes such as pulse inversion Doppler (PID). We show how a 40 pulse PID sequence can be used to resolve bubble velocities in an in vivo setting, producing a new nonlinear colour Doppler mode with framerates of around 50Hz.

Further study shows that velocity measurement by a different segmentation of the Doppler spectrum can be made from a sequence of amplitude modulate pulses, which we call Amplitude Modulation Doppler (AMD). Careful observation of the AMD signal shows an unexpected gain over PID. While the superior signal to clutter ratio of AM over PI imaging has been noted in practice, this is often ascribed to engineering considerations, such as the increased bandwidth required for second harmonic imaging and the challenge of accurate phase modulation over the more straightforward array apodisation used in AM imaging. However, we show that there may be a specific behaviour of lipid coated bubbles that favours amplitude over pulse modulation schemes and we show the impact of this in AMD contrast imaging.

Adventures with gas vesicles for high frequency ultrasound contrast imaging

F. Stuart Foster¹, Melissa Yin¹, Emmanuel Cherin¹, Mikhail G. Shapiro²

¹Sunnybrook Research Institute and Dept. of Medical Biophysics, University of Toronto

²Department of Chemical Engineering, California Institute of Technology

The introduction of dedicated high frequency systems for preclinical ultrasound imaging has led to the development of specific microbubble agents (VisualSonics-MicroMarker, Targeson-Targestar) optimized for higher frequencies. The results achieved with these agents have been mixed: Whereas low frequency contrast studies routinely achieve >30 dB contrast to tissue ratios, high frequency agents are challenged to achieve 20dB and performance drops significantly above 30MHz. This situation has led investigators to pursue creative variations such as subharmonic imaging, self-demodulation imaging, and dual frequency imaging to improve performance. Additionally, several factors limit the range of applications of microbubbles in molecular imaging. Typical microbubble formulations are comprised of lipid-encapsulated gas, are 1.5-5 μm in diameter, and resonate effectively in the diagnostic frequency range of 3-10 MHz. The size of such microbubbles is limited to the micron or larger range by the partial pressure gradient between their gas interior and surrounding media. This physically unstable configuration can limit the in vivo lifetime of such agents. Also the size of microbubbles is such that they do not extravasate from the microcirculation or “leak” from the malformed angiogenic vasculature of tumors. They are therefore a mainly vascular contrast agent, whereas many important molecular imaging targets, including tumors, stem cells, infectious agents, neurodegeneration and inflammation reside outside the vasculature. Currently, although solid, liquid, hollow or phase-change contrast agents have been proposed as microbubble alternatives, none of these technologies have yet become widely adopted due to limitations in echogenicity, stability or synthesis. There is therefore a strong impetus to develop new ultrasound imaging agents with novel nanoscale structures.

To address this challenge, we have been developing and testing a new class of molecular imaging agents based on genetically encoded gas nanostructures derived from buoyant microorganisms such as *Halobacterium NRC-1* and *Anabaena flos-aquae* bacteria. These unique nanostructures, called gas vesicles (GVs), are 50-500 nm in size and interact with gas through a fundamentally different physical mechanism, endowing them with potential long-term stability despite their nanometer size. A brief introduction to the biophysical and biological properties of gas vesicles will be presented and preliminary in vitro and in vivo studies of their properties will be given. In particular, the results of our acute toxicity, dose response, disruption, and nonlinear properties studies will be discussed. One issue of importance to the use of GV as contrast agents is the requirement for in vivo stability. We are

investigating a number of approaches including Pegylation, surface charge modification, and the use of inherently disordered peptides (IDPs) to accomplish this. Results showing significantly increased GV lifetimes by means of pegylation will be demonstrated. Finally the potential future impact of a versatile, genetically tunable, nanoscale imaging agent based on GVs will be considered.

Ultrafast contrast imaging: From millisecond transient bubble dynamics to sub-wavelength resolution

Olivier Couture, Yann Desailly, Mathias Fink, Mickael Tanter

Institut Langevin (ESPCI, INSERM CNRS), Paris, France

In the last fifteen years, the development of shear-wave elastography has required the implementation of ultrafast (Frame rate > 1000 Hz) plane-wave imaging methods in a clinical scanner. In recent years, it was shown by our group that plane wave imaging could not only allow the quantitative assessment of tissue elasticity, but could also improve Doppler sensitivity and the detection of contrast agents.

In 2008, ultrafast contrast plane wave imaging was used to follow the dissolution of contrast agents in-vitro (fig 1). Microbubbles could be detected though their nonlinear echoes highlighted with plane-waves. But, also, their evolution in the first few milliseconds after the disruption pulse could be followed over an entire image. Ultrafast contrast imaging was then applied in-vivo to detect microbubbles targeted to tumor angiogenesis expression (fig 3). Plane-wave imaging was shown to reduce microbubble disruption, while increasing overall contrast (fig 2). Such an effect is due to the increase in intensity received by each pixel, despite lowered peak-negative pressure. Finally, ultrafast imaging could also be exploited to detect the generation of bubbles of perfluorocarbon during drug-delivery (fig 4).

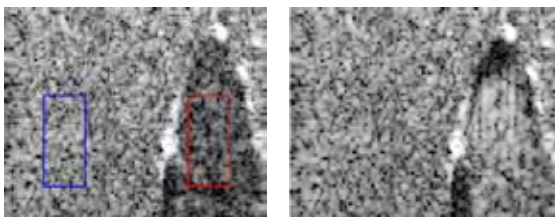


Fig 1: Microbubbles in a wall-less vessel phantom, before (left) and 4ms after a disruption pulses. [Couture et al., 2009]

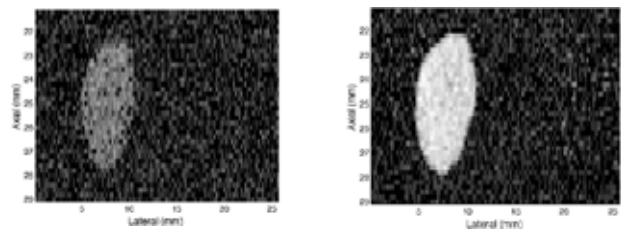


Fig 2: Microbubbles surrounded by a tissue phantom as observed by conventional focused CPS imaging (left) and plane-wave CPS imaging (right). The two pictures are taken at a fixed disruption ratio. [Couture et al., IEEE UFFC, 2012]

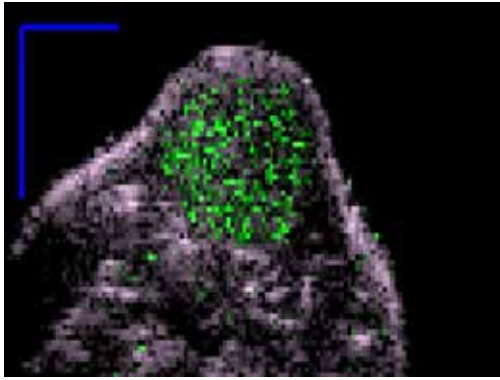


Fig 3: Plane-wave imaging of targeted contrast agents (green) in a subcutaneous tumor in a mouse. [Couture et al., *Molecular Imaging*, 2011]

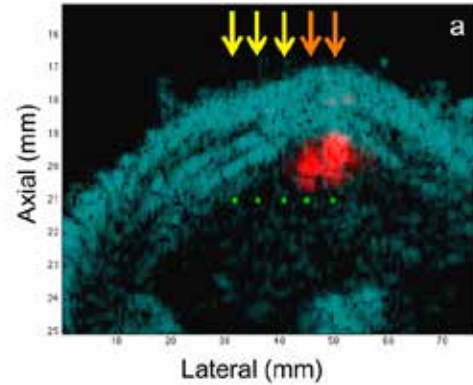


Fig 4: Plane-wave monitoring of the release of composite droplets in the liver of a rat. [Couture et al., *Medical Physics*, 2012]

In-vivo experiments have revealed that, under specific insonification conditions, microbubbles were not disrupting simultaneously over an entire image. In fact, under ultrafast imaging, contrast agents are destroyed in sequence and differential mapping yields punctual and isolated events originating from the microbubbles. For instance, during a millisecond of acquisition, many independent events can be observed on the differential plane-wave images of a tumor filled with targeted agents (fig 5). Since these events can be separated in time, their point-spread function do not superpose. Hence, the determination of the origin of the echo of disrupting microbubbles on ultrafast imaging is not diffraction-limited like conventional ultrasound imaging. However, to determine the exact position of the microbubbles, their echo have to be intercepted over a plane and not simply a line like the majority of clinical transducer. Consequently, “Sono-activated ultrasound superlocalisation” (SAULM) was implemented on a 2D array. In-vitro experiments where microbubbles were imaged within microfluidic channels demonstrated that channels could be resolve at $1/13$ of the wavelength. Two channels which were separated by $2/9$ of the wavelength could be distinguished, revealing that both the Rayleigh-criteria and the diffraction-limit could be surpassed (fig 6). With such subwavelength resolution, SAULM could lead to a complete reconstruction of the vascular tree down to the smallest capillaries at several centimeter depth.

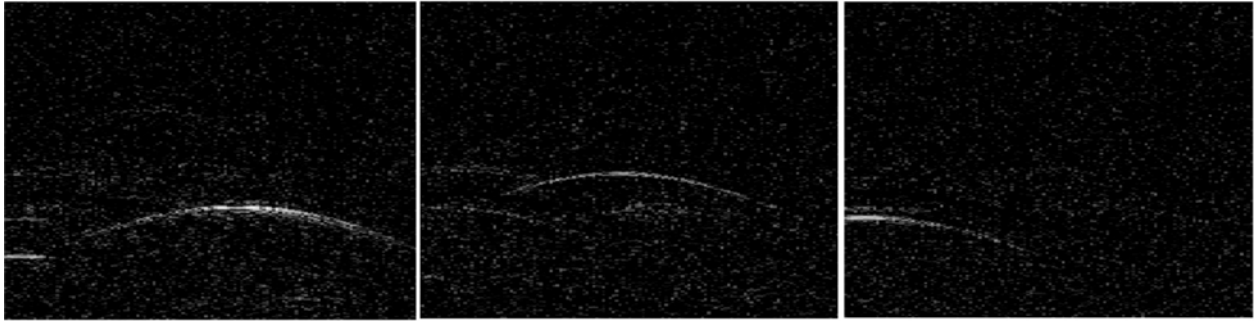


Fig 5. In-vivo observation of targeted contrast agents with differential ultrafast imaging. In the radio-frequency matrix, punctual events like bubbles are seen as parabolas. [Couture et al. 2011]

Ultrafast plane-wave imaging of microbubbles has shown improvement in contrast, disruption and time-resolution, along with surpassing the diffraction-limit. The implementation of these new modes on clinical scanners could drastically improve our sensitivity to blood-flow, blood volume, molecular targets and subwavelength structures.

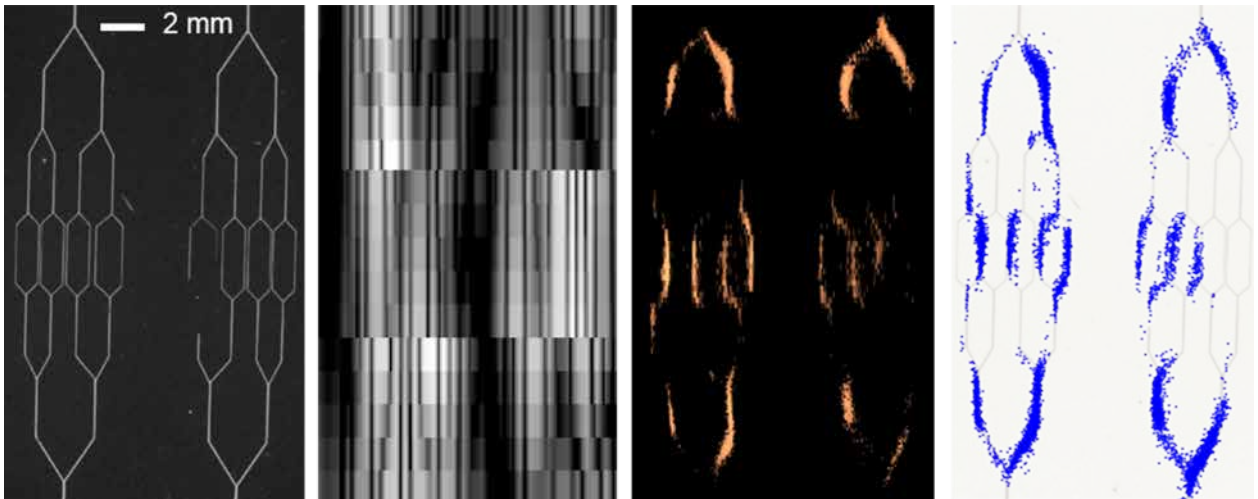


Fig 6: Sono-activated ultrasound superlocalisation in microfluidic channel, comparison between fluorescence microscopy, standard echography, SAULM and all the localized sources superimposed with optical image (from left to right). [Desailly et al., APL, 2013]

Ultra-fast lipid movement in the microbubble coating during oscillation – a fluorescence high-speed camera study

Klazina Kooiman^{1,2,3}, Flordeliza S. Villanueva¹, Bin Qin¹, Tom van Rooij³, Frits Mastik³, Alexander L. Klibanov⁴, Nico de Jong^{2,3}, Xucai Chen¹

¹*Center for Ultrasound Molecular Imaging and Therapeutics, University of Pittsburgh Medical Center, Pittsburgh, PA, USA*

²*Interuniversity Cardiology Institute of the Netherlands, Utrecht, the Netherlands*

³*Dept. of Biomedical Engineering, Thoraxcenter, Erasmus MC, Rotterdam, the Netherlands*

⁴*Dept. of Biomedical Engineering, School of Engineering and Applied Science, University of Virginia, Charlottesville, VA, USA*

Background

Ultrasound contrast agents consist of gas microbubbles (1-10 μm in diameter) dispersed in a suspension. To improve stability and corresponding circulation lifetime of the agent in the vascular system, adaptations have been made to the gas microbubbles. These include coating of the gas bubbles with for example a lipid, and using heavy molecular weight gasses as the gas core [1,2]. In an ultrasound field, microbubbles oscillate. It is this oscillation that provides enhanced signal for imaging [3,4] and induces bioeffects such as microbubble-mediated drug uptake [5]. Microbubble behavior has been widely studied, either by acoustic measurements or optical observations using high-speed cameras [6,7]. These studies have led to improved mathematical models of microbubble dynamics [1,6]. One of these models, the Marmottant model [8], also predicts specific behaviors of the lipid coating, such as buckling and rupture. However, these behaviors have never been experimentally demonstrated previously as optical high-speed imaging to resolve microbubble oscillations could only be performed in bright field, thereby visualizing the gas core, not the lipid coating.

This research aims to study the lipid movement in the microbubble coating during oscillation. Lipid-coated microbubbles were fluorescently labeled, and their oscillation in the ultrasound field was recorded with a fluorescence high-speed imaging camera at the University of Pittsburgh Medical Center, the UPMC Cam [9].

Methods

Two types of lipid-coated microbubbles were made. Microbubbles with a coating of DSPC and DSPE-PEG(2000)-PDP were made using the Vial Shaker method, after which

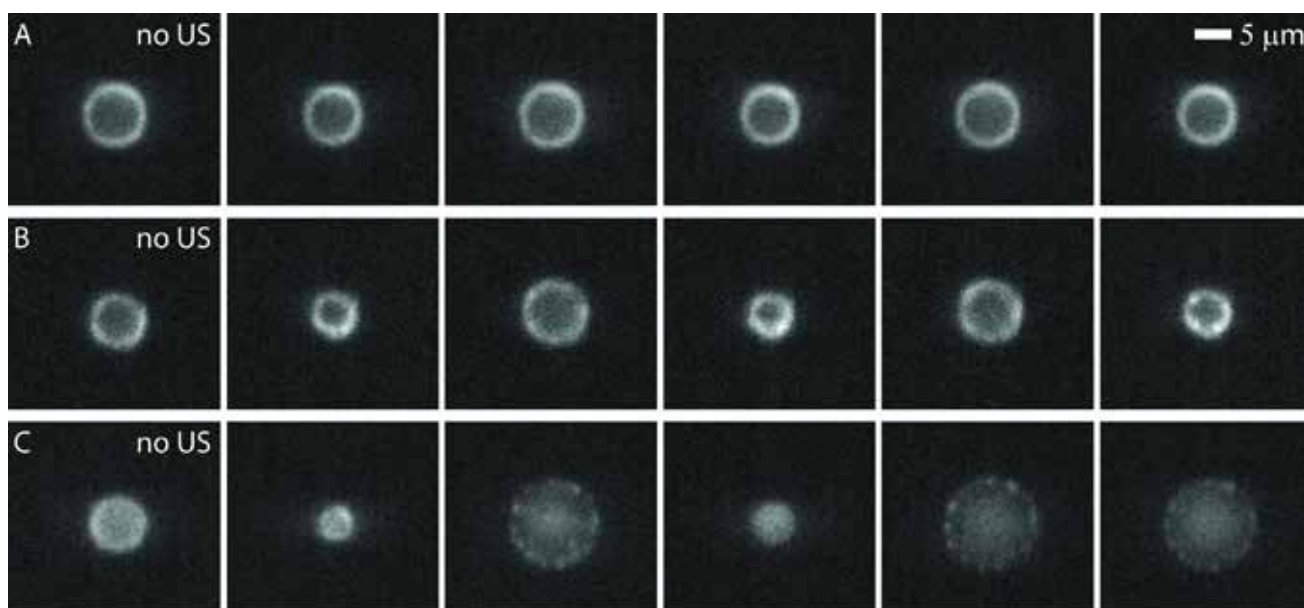
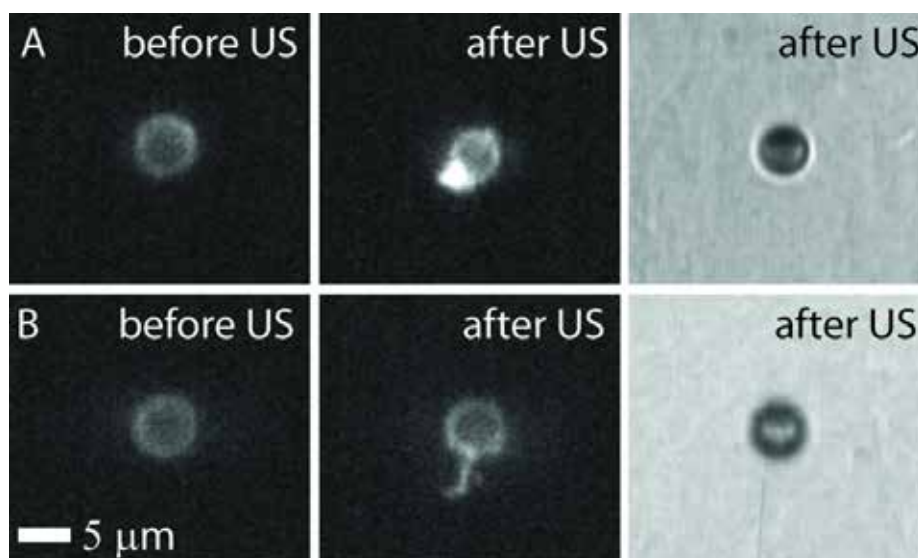


Fig. 1. Selected frames from fluorescence high-speed recordings (~ 5 Mfps) of insonified lipid-coated microbubbles. A) DSPC/DSPE-PEG(2000) microbubble insonified at 50 kPa (10 cycles) shows non-moving lipids; B) DSPC/DSPE-PEG(2000) microbubble insonified at 100 kPa (10 cycles) shows lipid movement in compression phase of oscillation; C) DSPC/PEG-40 stearate microbubble insonified at 300 kPa (10 cycles) shows rupture of the lipid coating in the expansion phase.



fluorescent Oregon Green 488-maleimide was conjugated to the microbubbles. Micro-bubbles with a coating of DSPC and PEG-40 stearate were made by sonication in the presence of the lipid dye DiO. During synchronized high-speed imaging, microbubbles were insonified at a frequency of 1 MHz with a 10 to 15-cycle sine wave. The peak negative acoustic pressure was varied between 50 and 300 kPa. Fluorescence (using a 488 nm laser) and bright field recordings were obtained at ~ 5 million frames per second with the UPMC Cam [9] to study acoustic behavior of these microbubbles.

Results

The fluorescence high-speed recordings revealed different lipid movements within the coating of microbubbles during insonification. Figure 1 shows several examples. In Fig 1A, a microbubble insonified at 50 kPa (10 cycles) is shown. The lipids did not appear to move on the microbubble surface during the oscillation. Another microbubble, similar in size, and insonified at 100 kPa (10 cycles), is shown in Fig 1B. This microbubble showed ultra-fast movement of the lipids on the microbubble surface during its oscillation, indicated by higher intensity fluorescence spots during the compression phase. These higher intensity spots became more pronounced at the end of the 10 acoustic cycles. From the few microbubbles we have analyzed so far, we observed a tendency of generation of second harmonics when higher intensity fluorescence spots appeared during the compression phase. When a microbubble was insonified at 300 kPa (10 cycles), see Fig 1C, a non-continuous lipid coating was observed in the expansion phase, suggesting a ruptured coating. The bubble diameter had shrunk by 13% during this oscillation, suggesting the ruptured coating correlated with deflation. We also observed microbubbles that formed a large high intensity spot (Fig 2A) or a tail (Fig 2B) during insonification that persisted after the ultrasound was turned off. This suggests buckling and/or folding of the lipids. These coating characteristics were not evident from the bright field images (see Fig 2, right panel).

Conclusion

This study reveals for the first time ultra-fast movement of lipids in the coating during insonification. Translocation, redistribution, and rupture of the lipids in the coating were observed. This suggests that lipids can move on the order of (sub)microns within one acoustic cycle, thereby reaching speeds on the order of 1 m/s. These observations can improve our understanding of microbubble behavior in an acoustic field and thereby aid in the optimization of imaging strategies as non-linear behavior may be influenced by the ultra-fast movement of the lipids. With this technique, the relationship between microbubble coating behavior and drug release can also be studied, leading to better designs of drug-loaded microbubbles and parameters for ultrasound-mediated therapies.

Acknowledgments

This research was financially supported by the Interuniversity Cardiology Institute of the Netherlands (fellowship to K.K.), the Center for Ultrasound Molecular Imaging and Therapeutics, University of Pittsburgh Medical Center, and the Center for Translational Molecular Medicine and the Dutch Heart Foundation (PARISk). The authors would like to thank Jianjun Wang and Regeant Pandey from the Center for Ultrasound Molecular Imaging and Therapeutics, University of Pittsburgh Medical Center, and Michiel Manten, Geert Springeling, Ying Luan, Tom Kokhuis, and Ilya Skachkov from the Dept. of Biomedical Engineering, Erasmus MC for technical assistance.

References

1. *Faez et al, IEEE Trans UFFC 2013; 60: p. 7*
2. *Hernot and Klibanov, Adv Drug Deliv Rev, 2008; 60: p. 1153*
3. *Leighton, The Acoustic Bubble, Academic Press, London, UK, 1994*
4. *Medwin, Ultrasonics 1977: p. 7*
5. *Kooiman et al, J Control Release 2011; 154: p. 35*
6. *Stride and Saffari, Prof Inst Mech Eng H 2003; 217:p. 429*
7. *Gelderblom et al, Rev Sci Instrum 2012: 83: p. 103706*
8. *Marmottant et al, J Acoust Soc Am 2005; 118: 3499*
9. *Chen et al, Rev Sci Instrum 2013; 84: p. 063701*

Clinical feasibility of ultrafast imaging of microbubbles

*Matthew Bruce¹, Kejian Wang², Thomas Frappart¹, Olivier Couture², Aline Criton²,
Jean-Michel Correas^{2,3}, Jeremy Bercoff¹, Mickael Tanter²*

¹*Supersonic Imagine, Aix en Provence, France*

²*Institut Langevin, ESPCI, CNRS (UMR 7587), INSERM (U979), Paris, France*

³*Necker University Hospital, Paris, France*

Introduction

The imaging of microbubbles with unfocussed ultrasound beams opens new opportunities for visualizing blood flow.[1-4] Unfocussed ultrasound beams enable the imaging of microbubbles hundreds of times faster (kHz) than conventional methods by enabling the reconstruction of an entire plane with a single transmit.[5] This approach in previous work has been referred to as ultrafast imaging or contrast plane-wave imaging[3,4] Traditional focused transmit/receive acquisitions used to image microbubbles have been limited to frame rates of 8 to 30Hz, due to the need of additional pulses to separate nonlinear from linear signals. This approach distributes ultrasound energy to microbubbles in temporally and spatially different manners than focused beams. The combination of ultrasound contrast pulsing sequences with unfocused ultrasound beams has been implemented on the *Aixplorer* diagnostic ultrasound system (Supersonic Imagine, France). Two approaches have been implemented. The first approach enables a single acquisition of a limited number of frames at ultrafast frame rates, enabling visualization of microbubble flow and behavior with millisecond temporal resolution. The second approach enables continuous real-time imaging of microbubbles with ultrafast synthetic acquisitions, where computational demands limit frame-rates. This work explores the initial practical experiences of in-vitro and in-vivo of ultrafast imaging of microbubbles.

Methods

Acquisitions from focussed and unfocussed transmits using microbubbles were acquired both *in-vitro* and *in-vivo* using an *Aixplorer* diagnostic ultrasound system (Supersonic Imagine, France). Both real-time acquisition and high frame rate single-shot acquisitions of synthetic plane imaging combined with contrast pulsing sequences were implemented on *Aixplorer*. The *in-vivo* and *in-vitro* data were acquired with the SL15-4 and SL10-2 linear probes. An ATS 523A flow phantom with a roller pump were used in the *in-vitro* acquisitions.[3] *In-vivo* data were acquired in renal transplant patients using the SL10-2 probe with an injection of 0.5mL of Sonovue.

Results

Figure 1 illustrates phantom images of single-shot ultrafast contrast acquisitions in the phantom with full image frame rates of roughly 1 kHz. Both Figure 1 acquisitions were performed with a single 0 degree angle. Single angle acquisitions realize the highest frame rates. However, as discussed in [2], the removal of the spatially constrained transmit beam leads to higher clutter levels, prohibiting use in applications with a lot of brighter structure like the breast. In these applications even given the low transmit acoustic levels combined with harmonic imaging, more angles will be required to enable visualization of microbubbles around brighter structure. Figure 2 illustrates real-time ultrafast contrast acquisitions in the phantom and human kidney using 11 angles, using both higher and lower frequency linear transducers. The resulting low frame rates are a result of the time of reconstruction.

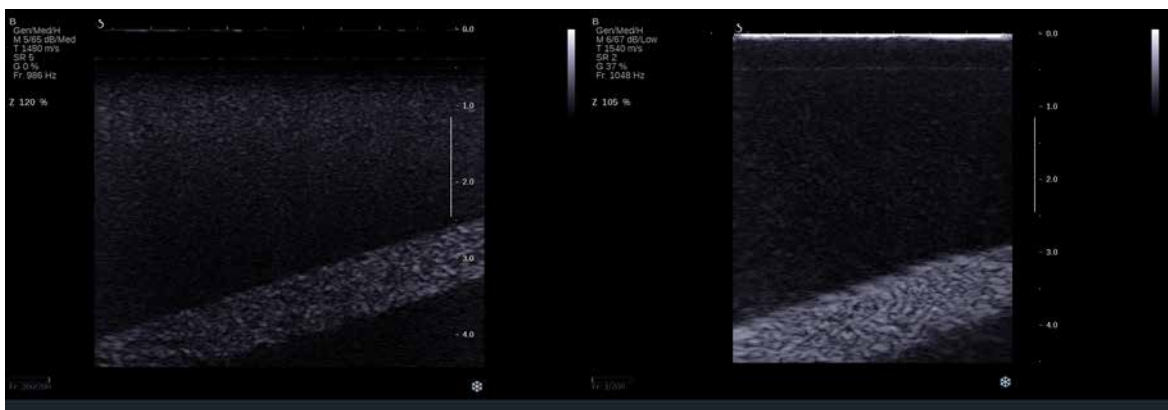


Figure 1: Single-shot acquisitions in flow phantom with SL15-4 and SL10-2 illustrating full image frame rates of roughly 1kHz.

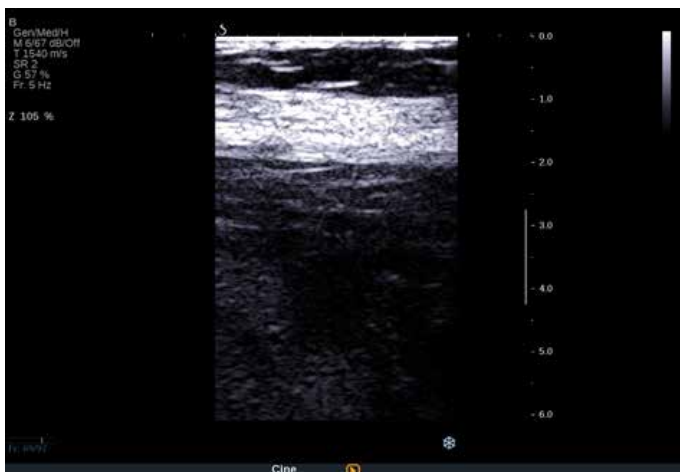


Figure 2: Real-time ultrafast acquisitions in the showing perfusion in the cortex of a transplanted kidney. The hypochoic region outlines an infarct.

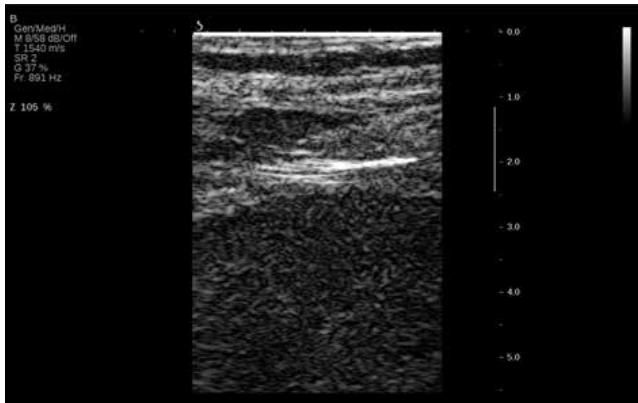


Figure 3: Single-shot ultrafast acquisitions in a normal region of the kidney and at the border of can infarct.

Figure 3 show a single-shot acquisition in a human kidney. Two different components of microbubble signal are observed in the single-shot acquisition. The first being a stationary signal of lower velocity microbubbles in the microcirculation. A second temporally nonstationary signal of higher velocity microbubbles composed of both a scintillating appearance and moving microbubbles traversing larger vessels within the imaging plane. Figure 4 shows an m-mode display of the mean across the left image of Figure 3. Figure 4 illustrates a constant signal demonstrating minimal microbubble disruption with kilohertz frame rates.

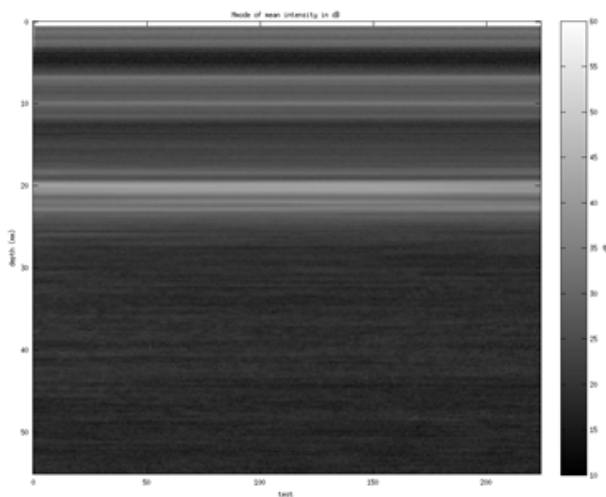


Figure 4: M-mode image of the mean across the image of the pulse-inverted unfocussed acquisitions illustrating consistent signal over the 200ms acquisition

Conclusions

The feasibility of imaging of microbubbles using unfocused beams has been demonstrated both in-vitro and in humans. Two different implementations consisting of a real-time and single-shot limited duration acquisition have been implemented on the *Aixplorer* diagnostic ultrasound imaging system. The benefits of imaging microbubbles with framerates from 100s to kilohertz frame-rates with synthetic plane wave imaging can now be further explored.

References

1. O. Couture, M. Fink, and M. Tanter, "Ultrasound contrast plane wave imaging," *IEEE Transactions on ultrasonics, ferroelectrics, and frequency control*, vol. 59, no. 12, pp. 2676–2683, 2012
2. C. Tremblay-Darveau et al. , *Ultrafast Doppler Imaging of Microbubbles, Proceedings IEEE-UFFC, 2012*
3. M. Bruce et al. , *Ultrafast Imaging of Microbubbles, The 18th European Symposium on Ultrasound Contrast Imagine 2013*
4. O. Couture, S. Bannouf, et al, "Ultrafast imaging of ultrasound contrast agents,," *Ultrasound Med Biol*, vol. 35 1908-1916, 2009
5. G. Montaldo et al. , *IEEE transactions on ultrasonics, ferroelectrics, and frequency control*, 56(3), 489–506, 2009



SOCIAL EVENT

Thursday JANUARY 23

**Oceanium, Blijdorp Zoo
Blijdorplan 8, Rotterdam
Dinner buffet: 7.30- 10.15pm**

Coaches will be leaving from Hilton at 6.30pm and will be back there around 10.30pm

Does DCE-US measurement of flow parameters correlate with absolute flow measurement clinically?

W.C. Teoh, C. Kalli, M. Abel, H. Wasan, M. Averkiou & E. Leen

*Experimental Medicine Division, Department of Medicine, Imperial College London,
Hammersmith Hospital*

Previous studies showing correlation of DCE-US flow parameters from time intensity curves with absolute flow rates had only been confirmed in flow models but never in humans. Human organ flow can be measured fairly accurately using duplex/color Doppler ultrasound of the feeding vessel area and velocity (Leen et al, 1995).

Aim

To assess the correlation between DCE-US flow parameters of hepatic artery, portal vein tumour and liver parenchyma with absolute flow from colour/spectral Doppler US (CSDU).

Materials and Methods

Fifty patients with proven liver malignancies were studied using an iU22 ultrasound scanner (Philips, Bothwell, USA) with C5-1 transducer to carry out the DCE-US of the liver, the common hepatic artery and main portal vein and colour/spectral Doppler US of the common hepatic artery and main portal vein. All patients were fasted for at least 4 hours prior to the US scans.

The DCE-US scans were analysed off-line using qLab software (Philips). Regions of interests (ROIs) were drawn around the perimetry of the hepatic artery, portal vein, the tumour and the liver. The parameters (Peak Intensity: PI, Wash-in slope: WIS, area under the curve: AUC, rise time: RT) from the Time Intensity Curves (TIC) were calculated for each ROI. Flow Rate (FR) from TIC is calculated as $WIS \times PI$.

Using CSDU, absolute flow of the common hepatic artery and main portal vein was measured as the product of the cross-sectional area of the vessel and its velocity. Total liver blood flow (TLBF) is calculated as the sum of the hepatic arterial and portal venous blood flow.

Correlations between the parameters were calculated using Spearman Rank and Pearson tests.

Results

Patients with liver malignancies instead of normal subjects were selected in this study to provide a wider range of flow values in the vessels. Of the 50 patients recruited, absolute flow parameters of the hepatic artery and portal vein from colour /spectral Doppler US are summarized in Table 1

Table 1: Range of absolute flow values in hepatic artery, portal vein and liver

	Velocity (cm/s) Mean+/-SE	Cross-sectional area (cm ² /s) Mean+/-SE	Flow Rate (cm ³ /s) Mean+/-SE
Hepatic Artery	22.97 ±1.427	0.1063 ±0.01543	2.737 ± 0.5375
Portal Vein	12.93 ±0.6397	0.7867 ±0.05116	9.998 ±0.8213
Total Liver Flow Rate	N/A	N/A	12.74 ± 0.7967

The correlation between the DCE-US flow parameters with absolute Vessel (Hepatic artery and portal vein grouped together) flow rate, vessel velocity and vessels area are summarized in Table 2, 3 & 4 respectively.

Table 2: Vessel Flow Rate vs vessel TIC parameters

	RT	PI	WIS	FR	AUC	MTT
Spearman	0.33	-0.15	-0.23	-0.19	-0.03	0.30
P Value	0.0009	0.1581	0.0253	0.0567	0.7799	0.0059

Table 3: Vessel Velocity vs vessel TIC parameters

	RT	PI	WIS	FR	AUC	MTT
Spearman	-0.53	0.28	0.39	0.34	0.17	0.48
P Value	< 0.0001	0.0057	< 0.0001	0.0006	0.1078	< 0.0001

Table 4: Vessel Area vs vessel TIC parameters

	RT	PI	WIS	FR	AUC	MTT
Spearman	0.45	-0.25	-0.35	-0.31	-0.12	0.38
P Value	< 0.0001	0.0150	0.0004	0.0021	0.2452	< 0.0001

There is some correlation between absolute vessel flow Rate with RT, WIS and MTT.

Strong correlation was observed between absolute vessel velocity with RT and MTT as well as between vessel area with RT.

DCE-US of liver parenchyma parameters correlation with hepatic arterial, portal and total liver blood flow are summarized in table 5, 6 and 7 respectively

Table 5: Hepatic arterial flow vs Liver TIC parameters

	RT	PI	WIS	FR	AUC	MTT
Pearson CC	-0.005	0.32	0.2640	0.2274	0.4148	-0.064
P Value	0.9741	0.0268	0.0698	0.1201	0.0034	0.6667

Table 6: Portal venous flow vs Liver TIC parameters

	RT	PI	WIS	FR	AUC	MTT
Pearson CC	-0.19	0.27	0.20	0.1753	0.30	-0.26
P Value	0.1910	0.0594	0.1601	0.2334	0.0448	0.0696

Table 7: Total Liver blood flow (TLBF) vs Liver TIC parameters

	RT	PI	WIS	FR	AUC	MTT
Pearson CC	-0.14	0.35	0.27	0.2349	0.4077	-0.22
P Value	0.3390	0.0147	0.0589	0.1080	0.0040	0.1308

DCE-US of Liver AUC and PI correlate with Hepatic Arterial flow, portal venous velocity and TLBF. DCE-US of Tumoral Tissue parameters correlation with hepatic arterial, and total liver blood flow are summarized in table 8 and 9 respectively.

Table 8: Hepatic arterial flow vs Tumour TIC parameters

	RT	PI	WIS	FR	AUC	MTT
Pearson CC	-0.14	0.33	0.5754	0.68	0.21	-0.07
P Value	0.3456	0.0217	< 0.0001	< 0.0001	0.1483	0.6118

Table 9: Total liver blood flow vs Tumour TIC parameters

	RT	PI	WIS	FR	AUC	MTT
Pearson CC	-0.26	0.24	0.45	0.51	0.1	-0.22
P Value	0.0739	0.1070	0.0015	0.0002	0.5013	0.1255

DCE-US measurement of WIS and FR of tumours correlated with hepatic arterial and total liver blood flow. There was no correlation between portal venous blood flow with any of the tumour TIC parameters. This is consistent with liver tumours being fed almost exclusively by hepatic arterial blood supply.

Conclusion

DCE-US time-based parameters (RT, WIS & MTT) measurement of organ feeding vessel may be used clinically to assess organ flow changes and DCE-US intensity based parameters (PI & AUC) measurement of tissue can be used to assess tissue flow changes.

Release, uptake and cytotoxicity of doxorubicin loaded lipopolyplexes exposed to low intensity ultrasound

Francois T.H. Yu, Xucai Chen, Jianjun Wang, Bin Qin, Regeant Panday and Flordeliza Villanueva

Center for Ultrasound Molecular Imaging and Therapeutics, University of Pittsburgh, Pittsburgh, PA, USA

Background

Doxorubicin (Dox) is a chemotherapeutic agent used in the treatment of various types of cancer, but its dosage and efficacy are limited by cardiotoxicity and myelosuppression. Encapsulating doxorubicin in liposomes (e.g. Doxil) has been successful at accumulating drug in the tumors and away from the heart, but has failed at improving patient outcome, possibly due to insufficient drug release from the liposomes [1]. Ultrasound (US) targeted microbubble (MB) oscillations have been shown to improve the cytotoxicity of liposomal doxorubicin (LDox) [2-4]. However, the ultrasound pulses that maximize drug release, drug uptake and therapeutic cytotoxicity remain to be elucidated. In this study, we compared the efficacy of different US pulses in inducing drug release, cellular drug uptake and growth inhibition in cell cultures using LDox conjugated to polymer MB.

Methods

LDox (DSPC:Chol:DSPE-Peg-Biotin, 65:30:5) were attached to nitrogen polymer encapsulated MB via biotin–streptavidin conjugation to form lipopolyplexes (DoxLPX). Squamous carcinoma cells (5×10^4 cells) were suspended with DoxLPX (300 MB/cell) carrying 2 μg of doxorubicin in 0.5 mL of RPMI 1640 (10% FBS). The suspension was agitated by a magnetic stirrer and placed in a degassed water bath maintained at 37°C for US exposure. A 1 MHz unfocussed transducer (A302S, Olympus, 0.5 inch) was used to deliver a variety of US pulses (Table 1) for 3 minutes. Drug release during exposure to the different pulses was assessed by fluorometry (Ex: 470 nm, Em: 595 nm) and compared to chemical release using 0.25% Triton-X100. Cell viability was assessed after US exposure using a trypan blue exclusion assay. Cells were then plated, washed with fresh media after 4h and incubated for 48h before assessing survival rate using an MTT assay. Drug uptake at 4h was assessed using flow cytometry. All experiments were repeated 3 times. Statistical comparisons were calculated using Student t-tests.

Pulse Name	Pressure (kPa)	# cycles	Duty cycle (%)	I _{SPTA} (W/cm ²)
H1500-5	1500	5	0.005%	0.0038
H1500-643	1500	643	0.64%	0.48
H1500-2k	1500	2000	2%	1.5
L170-50k	170	50000	50%	0.48
L300-50k	300	50000	50%	1.5

Table 1: Description of the 1 MHz pulses used in this study

Results

Release above 50% was obtained with DoxLPX when low pressure US (L170-50k and L300-50k) was used (Figure 1). The highest release was found for L170-50k, which reached ~70% after 5 min of exposure. DoxLPX without US maintained Dox encapsulated (< 10% leakage). High pressure ultrasound (H-prefix) and all ultrasound conditions tested without conjugating the liposomes to the MB resulted in less than 20% release (Figure 1B). Other pulse configurations with 50% duty cycle (different pulse lengths/pulse repetition rates combinations) were tested at 170 kPa and resulted in similar Dox release as L170-50k, suggesting that duty cycle is the key parameter for release at low pressure (data not shown). The two pulses resulting in most release (L170-50k and L300-50k) were then tested for drug uptake, acute and 48h cytotoxicity.

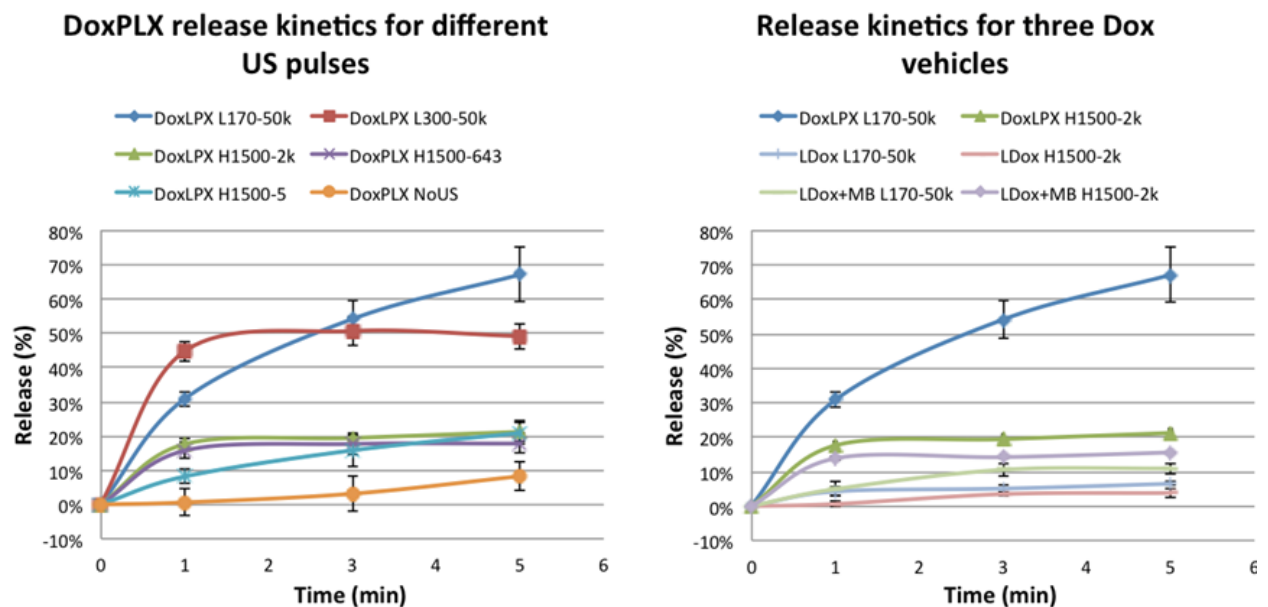


Figure 1: Kinetics of Dox fluorescence dequenching for DoxLPX exposed to different ultrasound pulses (a); and for DoxLPX, LDox co-injected with MB and LDox when exposed to US (n=3).

After 4h, cellular Dox uptake was highest for conditions associated with exposure to free Dox (Dox and DoxLPX+US) and significantly lower for conditions maintaining Dox encapsulated (LDox, DoxLPX without US and LDox+MB+US). L170-50k resulted in no acute toxicity but L300-50k resulted in significant acute toxicity in the presence of MB (Figure 2A). At 48h, exposure of DoxLPX to L170-50k pulse resulted in a significant increase in cytotoxicity, similarly to Dox exposure (Figure 2B). At 48h, for the L300-50k pulse, significant toxicity was found for conditions with free Dox exposure or in the presence of MB, suggesting a combination of drug and MB-US acute toxicity. Drug induced toxicity, calculated as the difference between cytotoxicity at 48h and acute toxicity, correlated with drug uptake ($r^2 > 0.7$, $p < 0.05$).

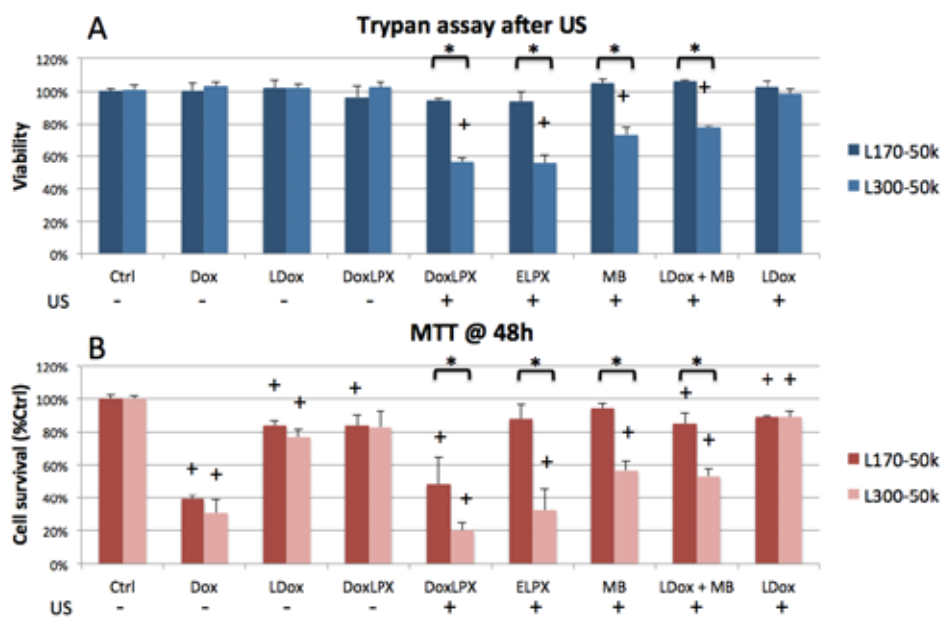


Figure 2: Cell viability after US exposure (Trypan Blue assay) and cell survival at 48h (MTT assay) (n=3); + p<0.05 vs Control, *p<0.05.

Discussion and conclusions

Using liposomal doxorubicin conjugated to polymer MB, we were able to produce a delivery vehicle that maintained drug encapsulated at 37°C and released drug after triggering by US. US pulses at 1 MHz with pressures of 170 and 300 kPa, released over 50% of loaded Dox in 3 minutes of US exposure. Pulses with the same energy, but at higher pressures (1500 kPa), only released up to 20% of encapsulated Dox. Conditions that released Dox lead to an increased cytotoxicity at 48h. Interestingly, MB co-injected with LDox did not release Dox when insonified, and did not lead to an increase in toxicity. Using low intensity pulses, our results did not support an improved cytotoxicity driven by an influx of Dox into the cells by sonoporation, but rather a cytotoxicity driven by drug release and diffusion into the cells, which was compounded, at 300 kPa, by an acute decrease in cell viability. Acute toxicity can potentially be desirable for drug delivery in tumoral microvasculature. Overall, this

approach seems promising for local delivery of anthracyclines to tumoral tissues with a potential reduction of systemic toxicity.

References

1. J. Lao, J. Madani, T. Puertolas, M. Alvarez, A. Hernandez, R. Pazo-Cid, et al., "Liposomal Doxorubicin in the treatment of breast cancer patients: a review," *J Drug Deliv*, vol. 2013, p. 456409, 2013
2. I. Lentacker, B. Geers, J. Demeester, S. C. De Smedt, and N. N. Sanders, "Design and evaluation of doxorubicin-containing microbubbles for ultrasound-triggered doxorubicin delivery: cytotoxicity and mechanisms involved," *Mol Ther*, vol. 18, pp. 101-8, Jan 2010
3. A. L. Klibanov, T. I. Shevchenko, B. I. Raju, R. Seip, and C. T. Chin, "Ultrasound-triggered release of materials entrapped in microbubble-liposome constructs: a tool for targeted drug delivery," *J Control Release*, vol. 148, pp. 13-7, Nov 20 2010
4. J. M. Escoffre, C. Mannaris, B. Geers, A. Novell, I. Lentacker, M. Averkiou, et al., "Doxorubicin liposome-loaded microbubbles for contrast imaging and ultrasound-triggered drug delivery," *IEEE Trans Ultrason Ferroelectr Freq Control*, vol. 60, pp. 78-87, Jan 2013

Gas-filled microbubbles used as an antigen delivery vehicle for vaccination

Jacques Terretaz¹, Gilles Bioley², Anne Lassus¹, Blaise Corthésy², François Tranquart¹

¹Bracco Suisse SA, Geneva research Center, Plan-les-Ouates, Switzerland

²R&D Laboratory, Immunology and allergy, University State Hospital (CHUV), Lausanne, Switzerland

Background

Vaccination is usually achieved by the delivery of antigenic entities (DNA, peptides or proteins), that are, due to their low immunological activities, generally formulated in adjuvanted delivery systems. Vehicles currently under development to deliver antigens comprise lipid-based systems (e.g. virosomes, liposomes, immunostimulatory complexes (ISCOMs), and others) or biodegradable synthetic polymer nano/microparticles (e.g. poly(lactide) (PLA), poly(lactide-co-glycolide) (PLGA), and others).

In this study we analyzed the ability of microbubbles to deliver the model antigen ovalbumin (OVA) both in vitro and in vivo without application of ultrasounds (US).

Methods

Microbubbles

Microbubbles (MB) composed of a shell of DSPC, palmitic acid and DSPE-PEG2000 entrapping perfluorobutane and nitrogen gases were prepared. Thiolation of OVA (20 mg/ml) was performed using a 10-fold molar excess of Traut's reagent in PBE for 1 h at room temperature. The final solution of thiolated OVA was coupled to DSPE-PEG2000-maleimide (Fig. 1).

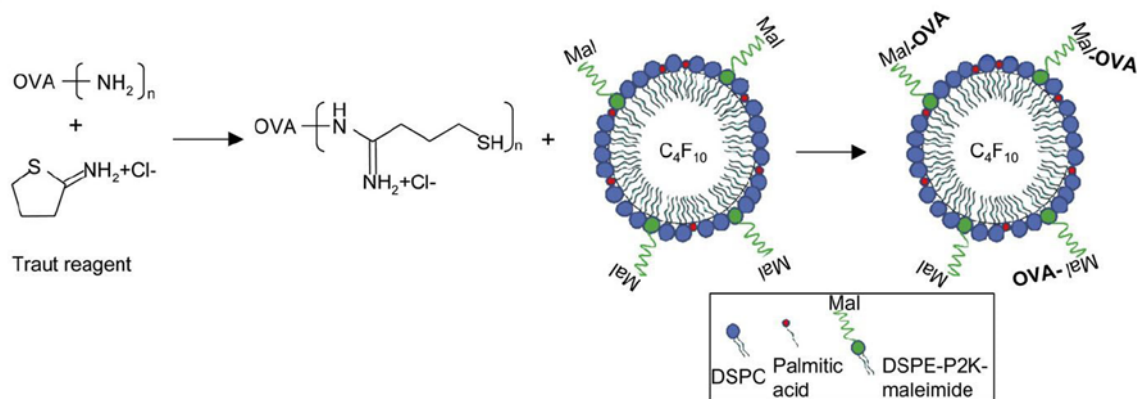


Figure 1: Schematic representation of thiolated OVA linkage to MB via maleimide

Incubation of cells with microbubbles

Human monocyte-derived dendritic cells (Mo-DC) were incubated for 2 h at 20,000 cells/well in mini tray culture plates in complete RPMI medium. Microbubbles were then added to the wells and the culture plates were inverted and incubated upside-down for 3 h. At the end of the incubation period, cells were collected, washed with PBS, and fixed with PBS-4% paraformaldehyde (PFA) on poly-L-lysine-treated glass slides. Cell surface staining was performed with a combination of biotinylated antibodies against human CD45 and streptavidin-Cy5. For intracellular staining, cells were first fixed with PBS-4% PFA, permeabilized with 0.2% Saponin in PBS-5% fetal bovine serum and then incubated with biotinylated antibody against human lysosomal-associated membrane protein-1 (LAMP-1), followed by incubation with streptavidin-Cy5. Slides were then mounted and analyzed with a confocal microscope.

Ultrasound imaging

MB were injected subcutaneously (s.c.) at the base of the tail and imaging of the site of injection and of the inguinal LN area was performed with a Vevo 2100 imaging system in contrast mode using an MS-250 probe at 18 MHz, 10% power. MB destruction was carried out with an IU22 scanner equipped with an L12-5 probe in contrast mode at 5 MHz. Images before and after MB destruction were captured at low mechanical index (MI $\frac{1}{4}$ 0.1), and MB were destroyed with a high mechanical index (MI $\frac{1}{4}$ 0.7).

In vivo MB administration and assessment of immune responses

Mice were immunized s.c. at the base of the tail with 8 μ g of OVA alone, in association with microbubbles or adsorbed on 1 mg alum in a total volume of 100 μ l, in the absence of US application. Three administrations at two-week intervals were performed and blood and spleens were collected two weeks after the last injection. Sera were analyzed for the presence of specific antibodies by ELISA. Splenic T cell responses were monitored by fluorescent dye-based proliferation assay, followed by flow cytometry analysis.

Mouse bacterial infection and determination of bacterial load

Frozen stocks of recombinant *Listeria monocytogenes* stably expressing OVA (Lm-OVA) were grown to mid log phase in brain-heart infusion broth. Bacterial numbers were determined by measuring the OD at 600 nm. 50,000 colony forming units (CFU) were injected in PBS intravenously. Lm-OVA burden in the spleen was analyzed on sacrificed animals 4 days after infection by plating splenic lysates and subsequently counting CFU..

Results

Phagocytosis of microbubbles by human Mo-DC

In a first step (1,2), the interaction of OVA-microbubbles with human Mo-DC was evaluated *in vitro* by incubating these cells in presence of microbubbles coupled with fluorescent OVA. We took advantage of the DQ:OVA derivative, whose fluorescence (Bodipy dye) is quenched by native OVA and is made detectable upon OVA degradation to assess internalization and processing of the antigen. As shown in Fig 2, co-incubation of human Mo-DC with DQ:OVA-microbubbles resulted in the appearance of fluorescence within the cells, that was in part co-localized with the lysosomal-associated membrane protein 1 (LAMP-1).

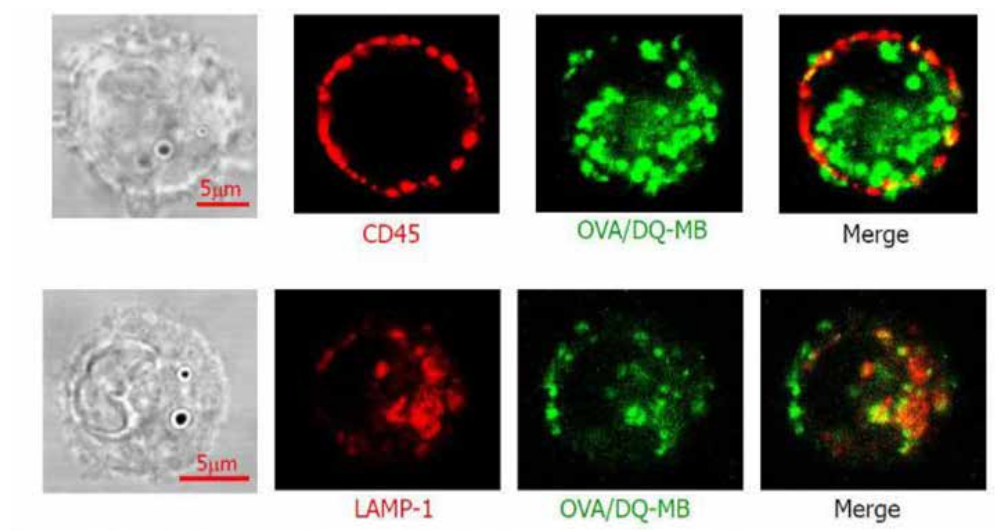


Figure 2: Incorporation of OVA:DQ-microbubbles into human dendritic cells

These results demonstrate that microbubbles deliver the antigen to DC *in vitro* and target it to the intracellular processing and presentation pathway.

In vivo immunization with OVA-microbubbles

The persistence of microbubbles after subcutaneous administration was assessed by ultrasound imaging. As shown in Fig. 3, contrast-enhanced ultrasound mediated visualization of injected MB by low mechanical index US pulse and signal persistence for up to 8 h.

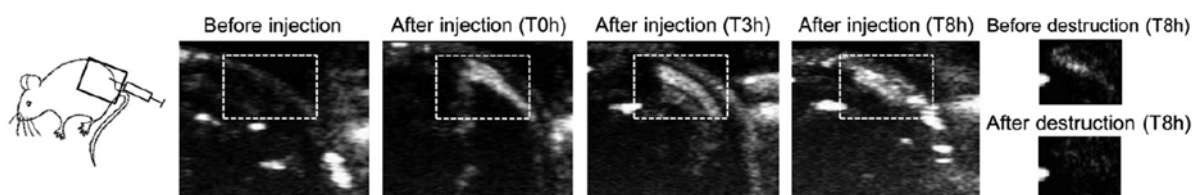


Figure 3: Persistence of microbubbles at the injection site after subcutaneous administration

No signal was observed locally in inguinal lymph nodes that drains the area of administration. This suggests that microbubbles were preferentially retained at the injection site where they were likely taken up by resident antigen presenting cells (such as DC) and not freely drained through the lymph.

OVA-specific antibodies and T cell responses after subcutaneous immunization were assessed by measuring the titers of OVA-specific IgG in sera of animals and splenic CD3⁺ T cell proliferation(2). Significant higher amounts of OVA-specific IgG and T cell proliferation were observed in all mice that had received OVA-MB compared to OVA alone. Injection of OVA adsorbed on alum generated similar immune responses (Fig. 4).

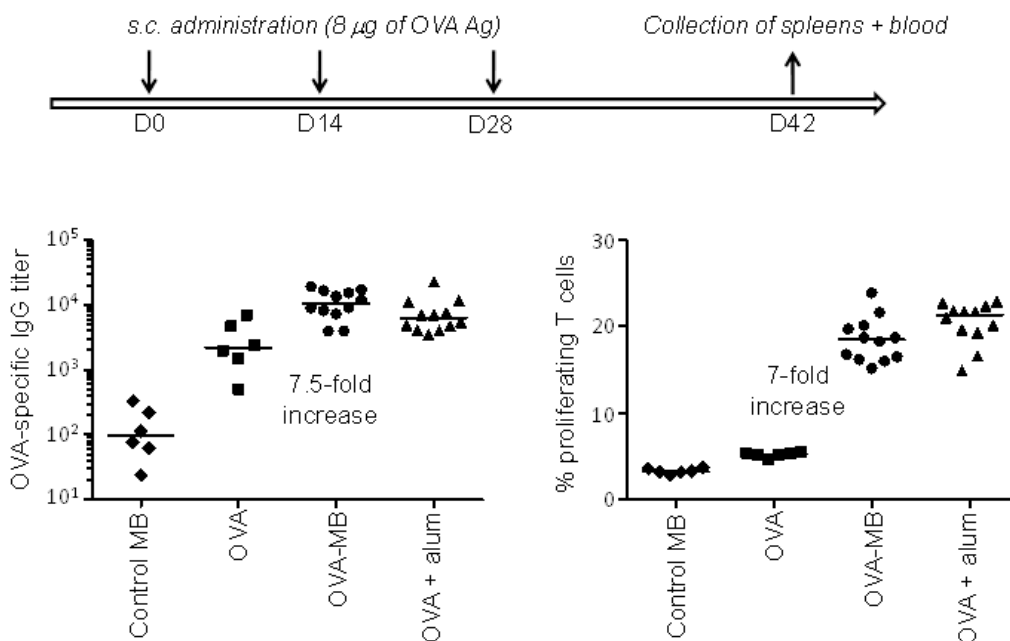


Figure 4: OVA-specific immune responses after subcutaneous immunization of mice with OVA, OVA-M) and OVA adsorbed on alum.

Effect of OVA-MB vaccination on mouse bacterial infection

To evaluate the efficiency of the immune responses resulting from administration of OVA-MB, we carried out a bacterial infection model (3). Mice immunized with OVA-MB were subsequently infected with a lethal dose of 50000 CFU / mouse of Lm-OVA to analyze the resulting protective effect of vaccination on infection.

Immunization of mice with OVA-MB before infection with Lm-OVA gave them a significant advantage over plain-MB (P-MB) administration in fighting infection. An approximately 120-fold reduction in the splenic bacterial load was observed in OVA-MB-immunized mice as compared to the control P-MB group (Fig. 5). These results demonstrate that administration of OVA-MB resulted in the induction of highly specific immune responses that were effective enough to partially protect mice against a subsequent systemic infection with a virulent recombinant bacterial strain expressing OVA.

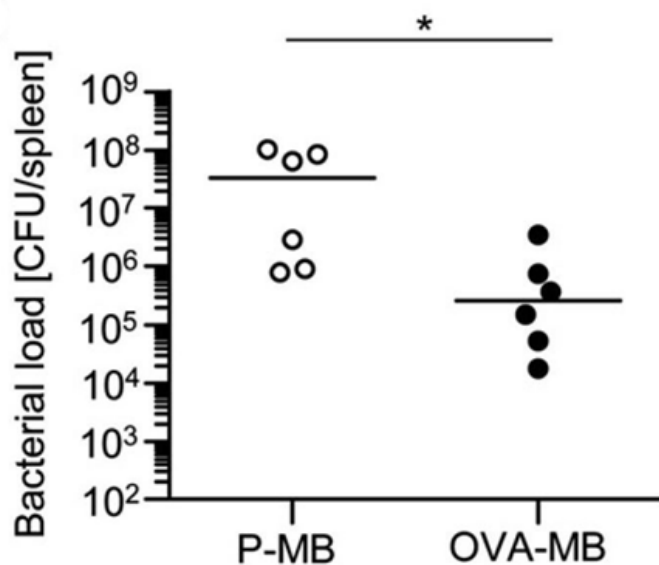


Figure 5: Bacterial load in the spleen analyzed 4 days after infection with Lm-OVA

Conclusions

These in vitro and in vivo results demonstrate that microbubbles might have a substantial impact on the immune system after a subcutaneous injection even without ultrasound activation. The marked reduction in *Listeria* burden seen after a high dose challenge in OVA-MB-vaccinated mice represents a proof of principle for the use of microbubbles as an immunostimulatory delivery system. Nonetheless, further developments of the technique are needed to optimize the structure of the microbubble shell and to enhance the efficacy of this approach. Routes and number of administrations are aspects that, together with optimization of microbubble formulations, are under investigation and may eventually lead to tailored microbubbles that are suitable for efficient vaccination.

References

1. Bioley G, Bussat P, Lassus A, Schneider M, Terretaz J, Corthesy B. The phagocytosis of gas-filled microbubbles by human and murine antigenpresenting cells. *Biomaterials* 2012;33(1):333-342
2. Bioley G, Lassus A, Bussat P, Terretaz J, Tranquart F, Corthesy B. Gas-filled microbubble-mediated delivery of antigen and the induction of immune responses. *Biomaterials* 2012;33(25):5935-5946
3. Bioley G, Zehn D, Lassus A, Terretaz J, Tranquart F, Corthésy B. The effect of vaccines based on ovalbumin coupled to gas-filled microbubbles for reducing infection by ovalbumin-expressing *Listeria monocytogenes*. *Biomaterials*. 2013;34(21):5423-5430

Improved delivery of nanomedicine in cancer tissue using ultrasound and a novel nanoparticle-microbubble platform

*Siv Eggen¹, Stein-Martin Fagerland¹, Yrr A Mørch², Rune Hansen³, Kishia Søvik¹,
Sigrid Berg³, Catharina de Lange Davies¹*

¹Dept of Physics, The Norwegian University of Science and Technology, Trondheim, Norway

²SINTEF Materials and Chemistry, Dept of Polymer Particles and Surface Chemistry, Trondheim, Norway

³SINTEF Technology and Society, Dept of Medical Technology, Trondheim, Norway

Systemic administration of chemotherapeutic drugs to treat solid tumours is characterized by systemic side effects, thus limiting the dosage. By encapsulating the drugs in pegylated nanoparticles (NPs), the exposure towards healthy tissue is reduced and a selective delivery of NPs to tumours can be achieved by passive accumulation of the NPs in the extracellular matrix of the tumour. This is caused by extravasation through the fenestrated tumour vasculature. However, the delivery of NPs throughout the tumour tissue is heterogeneous, and this limits the therapeutic response. The therapy can be improved by combining NPs and therapeutic ultrasound (US). The mechanisms behind this improvement, however, are unclear. The aim of this work was to combine US and a novel particle platform consisting of microbubbles (MBs) stabilized by polymeric NPs to improve the delivery of a hydrophobic model drug to tumour xenografts growing in mice. The microdistribution and uptake of NPs in tumour tissue exposed to US was compared with non-exposed tumours.

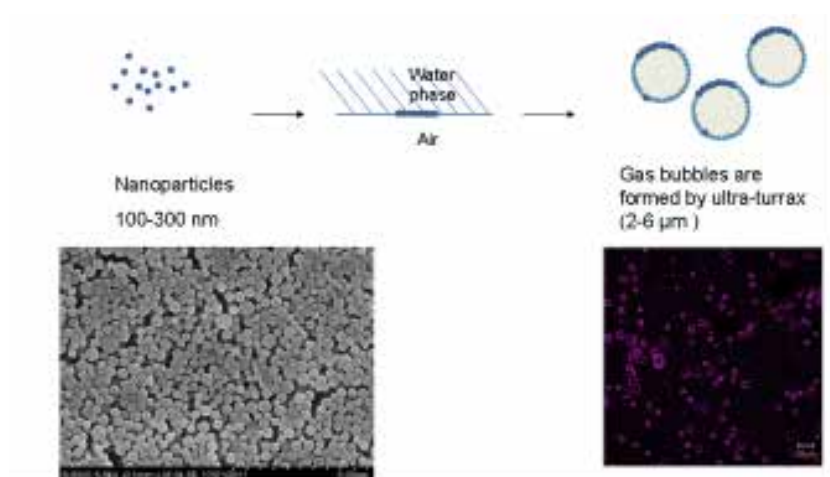


Fig: Schematic presentation of the NP-MB platform and electron microscopy of NPs and confocal laser scanning microscopy image of fluorescent NPs surrounding the MBs.

The NPs were synthesized from the biocompatible and biodegradable polymer poly(butyl-2-cyanoacrylate) (PBCA) in a one-step miniemulsion process. The NPs were coated with polyethylene glycol (PEG) to improve the circulation half-life and biodistribution. These NPs can form a shell around air bubbles by mixing the NP dispersion with bovine serum albumin and air using an ultra-turrax. This new NP-MB platform opens for an efficient interaction between the acoustic waves and the NPs in the presence of MBs.

Prostate cancer xenografts were grown subcutaneously on the hind leg in athymic mice. NPs containing the fluorescent dye Nile Red were administered intravenously, either as a solution of NPs or as NPs stabilizing MBs. Following administration, the tumours were exposed to focused US. Tumours given NP-MBs were exposed immediately afterwards to 1 MHz US with a duty cycle of 3 % and a mechanical index (MI) of 0.1 or 0.4. Tumours given NPs without MBs were exposed to either 300 kHz US with a duty cycle of 5 % and a MI of 2.4, or 5 MHz US with a duty cycle of 0.4 % and a MI of 0.7. US was given either 5 min or 24 hr after injection of NP to study the effect on extravasation and penetration through the extracellular matrix. The microdistribution of NPs and their distance from blood vessels were studied in frozen sections using confocal laser scanning microscopy. To visualize the blood vessels, fluorescent lectin was injected intravenously 5 min before the mice were euthanized.

In tumours where NP-MBs and US was given, the tumour uptake of NPs was improved and the uptake increased with increasing MI. In addition the distance from NPs to the closest blood vessel was increased in the tumour periphery in tumours exposed to low MI US. In tumours where only NPs and US was given, the tumour uptake of NP was higher when US was given shortly after NP administration, compared with US given the following day, demonstrating that US was important for extravasation of the NPs.

Successful chemotherapy for cancer patients requires that the therapeutic agents reach all the cancer cells and inactivates them, and the present results demonstrate that our new NP-MB platform, together with US exposure, improve the delivery of therapeutic agents and potentially improve the therapeutic outcome.

Can ultrasound and microbubbles induce fibrinolysis in vitro without rtPA?

B. Petit^{1,2}, Y. Bohren¹, P. Bussat¹, E. Gaud¹, F. Yan¹, E. Allémann² and F. Tranquart¹

¹Bracco Suisse S.A., Plan-les-Ouates, Geneva, Switzerland

²School of Pharmaceutical Sciences, University of Geneva, University of Lausanne, Geneva, Switzerland

Introduction

Acute ischemic stroke results from a cerebral vessel occlusion by a blood clot, which decreases or blocks the downstream blood supply, causing cerebral infarction leading to long term disability or death. Early treatments are intended to restore the cerebral blood flow in the ischemic brain to prevent major brain damage.

Currently, recombinant tissue plasminogen activator (rtPA) is the only thrombolytic drug approved for acute ischemic stroke treatment in Europe and in the United States of America [1]. However, due to exclusion criteria, only a few percent of patients are eligible for this treatment. Therefore, there is a real need for new therapeutic strategies in the management of acute ischemic stroke.

Sonothrombolysis (STL) uses ultrasound (US) and microbubbles (MB), to accelerate clot dissolution and blood vessel recanalization. Numerous recent studies have shown this technique may enhance clot lysis, both *in vitro* and *in vivo*, even without thrombolytic agent [2,3]. However, the underlying mechanisms of this approach remain unknown, especially concerning fibrinolysis. The present study was aimed to evaluate if the combination of US and MB without rtPA is sufficient to induce fibrin degradation in an *in vitro* blood clot model.

Methods

Human venous blood clots were prepared with ¹²⁵I-labeled fibrinogen. They were obtained after 6-hour incubation at 37 °C and stored at 4 °C between 1 and 7 days before use. The thrombus model was placed in a transparent PVC tube of 3.2 mm inner diameter filled with human plasma circulating at 21 mL/min. Clots were exposed to different combinations of rtPA (3 µg/mL, Actilyse[®], Boehringer Ingelheim, Germany), US and MB. A focused single-element transducer (1.6 MHz, Vermon, France) was used to sonicate the clots at 500 kPa. BR38 MB (Bracco Suisse SA, Switzerland) were infused into the system at a rate of 4x10⁵ MB/min.

Clot lysis was assessed as a function of time using a digital camera and radioactivity measurement (Cobra II gamma counter, Packard, USA). The first method allowed quantifying clot diameter loss over time by taking clot pictures every 5 min during the treatment [4]. Image processing and analysis were then performed with custom ImageJ and MATLAB® scripts. Fibrin degradation was determined by sampling 100 μ L of the plasma solution over 60 min and counting the release of radioactivity.

Results and discussion

Preliminary experiments conducted without rtPA showed that the area of the clot exposed to US progressively became translucent between 0 and 180 min (**Figure 1A**), indicating a progressive hemolysis. Further histological analysis confirmed the lysis of red blood cells and showed a fibrin-like structure in the translucent part of the clot exposed to US+MB (**Figure 1B**).

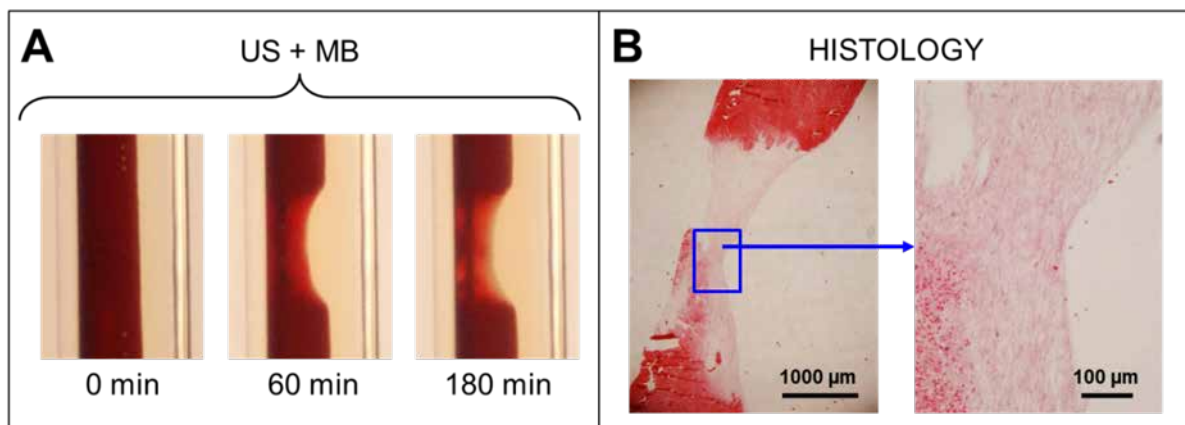


Figure 1: Observation of a human blood clot treated with US (1.6 MHz) and BR38 MB, without rtPA. (A) Photograph of clot lysis at different time points. (B) Hematoxylin and Eosin staining on longitudinal section of a clot after 60 min of exposure to US+MB; a large area depleted of red blood cells can be observed in the US+MB exposed area.

From these observations, experiments evaluating diameter loss and radioactivity release of STL-treated clots over 60 min were performed (**Figure 2**). Results showed an increase of fibrin degradation with US+MB+rtPA ($51.9\pm 2.9\%$) compared with rtPA alone ($43.7\pm 1.1\%$). This increase was in accordance with the larger diameter loss determined optically ($676\pm 22\mu\text{m}$ and $364\pm 55\mu\text{m}$ for rtPA+US+MB and rtPA, respectively). On the contrary, US+MB without rtPA, while inducing a significant clot diameter loss ($182\pm 42\mu\text{m}$, compared to control $26\pm 8\mu\text{m}$), did not induce any fibrin degradation ($0.4\pm 0.2\%$).

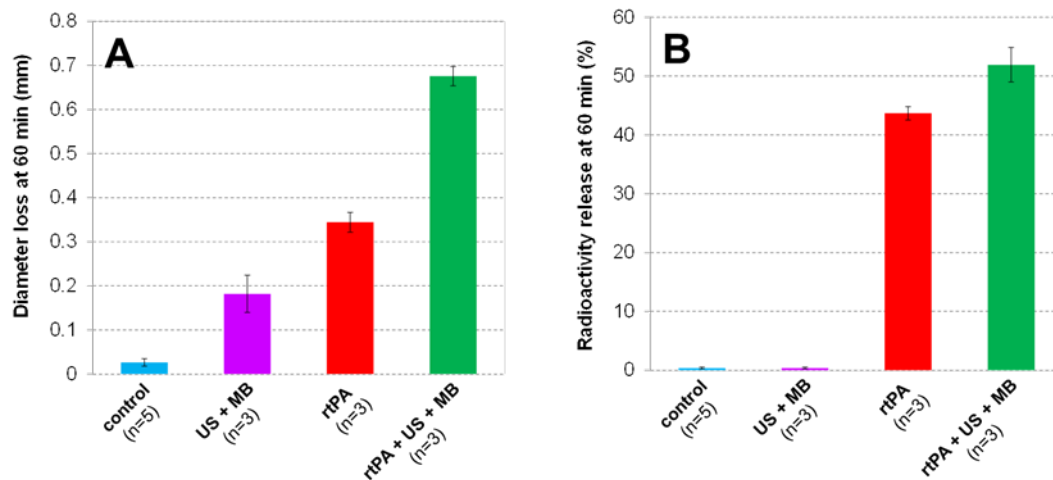


Figure 2: Lysis expressed as (A) diameter loss (mm) and (B) radioactivity release (%), at 60min, for ^{125}I -clots treated with different combinations of rtPA 3 $\mu\text{g}/\text{mL}$, US (1.6 MHz) and MB.

Conclusions

This study provides important information regarding the mechanisms involved in the STL process *in vitro*. Interestingly, the optical measurement and radioactivity release used for clot lysis assessment gave complementary information. It seems that in these *in vitro* conditions, the efficacy of STL using of combination of US and MB depends on the presence or absence of rtPA: in the absence of rtPA, STL induces hemolysis but not fibrinolysis; whereas in the presence of rtPA, both hemolysis and fibrinolysis occur. These results shall be put in perspective with *in vivo* studies [5], which pointed out that the local release of tPA might explain the positive effect of STL on clot lysis. From a clinical standpoint, the presence of endogenous tPA might thus play a key role in the success of an acute ischemic stroke treatment based on sonothrombolysis.

References

1. Adams HP Jr et al. Guidelines for the Early Management of Adults With Ischemic Stroke. *Stroke*. 38(5):1655-711 (2007)
2. B. Petit, F. Yan, F. Tranquart, E. Allémann. Microbubbles and ultrasound-mediated thrombolysis: a review of recent *in vitro* studies. *J. Drug Del. Sci. Tech.* 22(5):381-392 (2012)
3. Porter TR, Xie F. Can transcranial ultrasound and microbubble therapy ever enter the mainstream in acute stroke therapy? *Expert Rev Cardiovasc Ther.* 10(5):549-51 (2012)
4. B. Petit, E. Gaud, D. Colevret, M. Arditi, F. Yan, F. Tranquart, E. Allémann, *In vitro* sonothrombolysis of human blood clots with BR38 microbubbles. *Ultrasound Med Biol.* 38(7): 1222-1233 (2012)
5. Culp WC et al. Successful microbubble sonothrombolysis without tissue-type plasminogen activator in a rabbit model of acute ischemic stroke. *Stroke*. 42(8):2280-5 (2011)

Experimental evidence of the cytoskeleton involvement during cell sonoporation

Aya Zeghimi^a, Jean-Michel Escoffre^{a,b}, Ayache Bouakaz^a

^aInserm UMR 930 - Imaging and Brain, Université François Rabelais, Tours, France

^bPresent address: Imaging Division, UMC Utrecht, Utrecht, Netherlands

Introduction

The combination of ultrasound (US) and microbubbles for therapy, “sonoporation” proposes promising results in gene therapy [1]. However, the accurate mechanisms involved have to be elucidated. We have previously revealed that endocytic pathways such (caveolae-mediated endocytosis pathway) were stimulated after sonoporation [2]. It is currently admitted that these endocytic pathways were dependent on actin and tubulin cytoskeleton. The aim of our study was to investigate the effects of sonoporation on cytoskeleton. In this study, we attempt to define the effect of sonoporation on the actin and tubulin cytoskeleton of U-87 MG cells, but also their potential involvement during the sonoporation process.

Material and Methods

Cell Culture – U-87 MG human glioblastoma cells were grown as a monolayer in Dulbecco’s Modified Eagle’s Medium supplemented with 10% fetal calf serum and incubated at 37°C in humidified atmosphere with a 5 % CO₂ incubator. Forty-eight hours before sonoporation, the cells were seeded on 18 mm diameter glass cover slips and used at 80% confluence.

Ultrasound exposure conditions – Using Vevo SoniGene[®] (VisualSonics Inc., NL), adherent U-87 MG cells were insonated at 1 MHz sinusoidal US waves at 1 W/cm² acoustic intensity, 20 % duty cycle for 60 s. BR14[®] microbubbles (Bracco Research Geneva, Switzerland) were added at microbubbles/cell ratio of 5. These acoustic parameters were obtained as a result of a prior optimization experiment.

Membrane Permeabilization – The membrane permeabilization was assessed by using a non-permeant and fluorescent molecule, SYTOX[®] Green (600 Da, final concentration 1 µM) Immediately after US exposure, cells were harvested, resuspended in 500 µL PBS and then analyzed by flow cytometry. Fluorescence histograms were recorded with a flow cytometer and analyzed using the Kaluza software supplied by the manufacturer. A minimum of 10,000 events was analyzed to generate each histogram. To assess the cell mortality, propidium iodide was added at 0.5 µg/mL concentration to the cell suspension before flow cytometry analysis.

Inhibitors treatment – Cytochalasin D and nocodazole were used to inhibit the actin and tubulin polymerization, respectively. Before sonoporation, the cells were incubated with fresh cell medium containing 50 μ M of cytochalasin D and 10 μ M of nocodazole, for 1 hour at 37°C. These concentrations were identified through a series of cell cytotoxicity assays with various inhibitor concentrations.

Immunofluorescence – U-87 MG cells were fixed with 4% paraformaldehyde for 20 min at room temperature, immediately (0 min), 30 min and 60 min post-sonoporation. The cells were incubated with TRITC – (tetramethylrhodamine–5, 6 – isothiocyanate)-labeled phalloidin, used to stain the actin cytoskeleton. Tubulin antibody Alexa Fluor[®] 555 conjugate was used to label the microtubules. During the incubation with antibodies the cells were preserved in the moist chamber at room temperature in the dark. Afterwards, the antifading mounting medium containing DAPI (4', 6–Diamino–2–Phenylindole) was used to cover the slides, thus staining the nucleus. Confocal images were captured using Zeiss LSM510 confocal microscope with a 63x oil immersion lens.

Electron microscopy – The ultrastructural changes of plasma membrane were monitored by scanning electron microscopy (SEM). The cell samples were fixed and prepared using conventional osmium tetroxide staining [2]. Then, the cells were attached immediately (0 min) after sonoporation, in the presence of BR14[®] microbubbles. The samples were processed and coated by platinum sputtering (5 nm) and observed using a LEO DSM 982 SEM (Zeiss, Germany). The counting of permeation structures was performed over the entire surface of 10 cells per condition.

Results and Discussion

A sonoporation induced a permeabilization level of 60% as indicated by flow cytometry measurements. The morphology of sonoporated U-87 MG cells was examined post-exposure using confocal microscopy. As expected, control cells present typical polygonal-shaped actin and tubulin cytoskeleton, distributed into fibers and located in the peripheral cytoplasm adjacent to the cell margins. In contrast, immediately after sonoporation, insonified cells exhibited a depolymerization of actin and tubulin cytoskeleton. The latter results in diffuse and/or punctiform staining (Figure 1A), demonstrating that sonoporation alters the structures of actin microfilaments and microtubules.

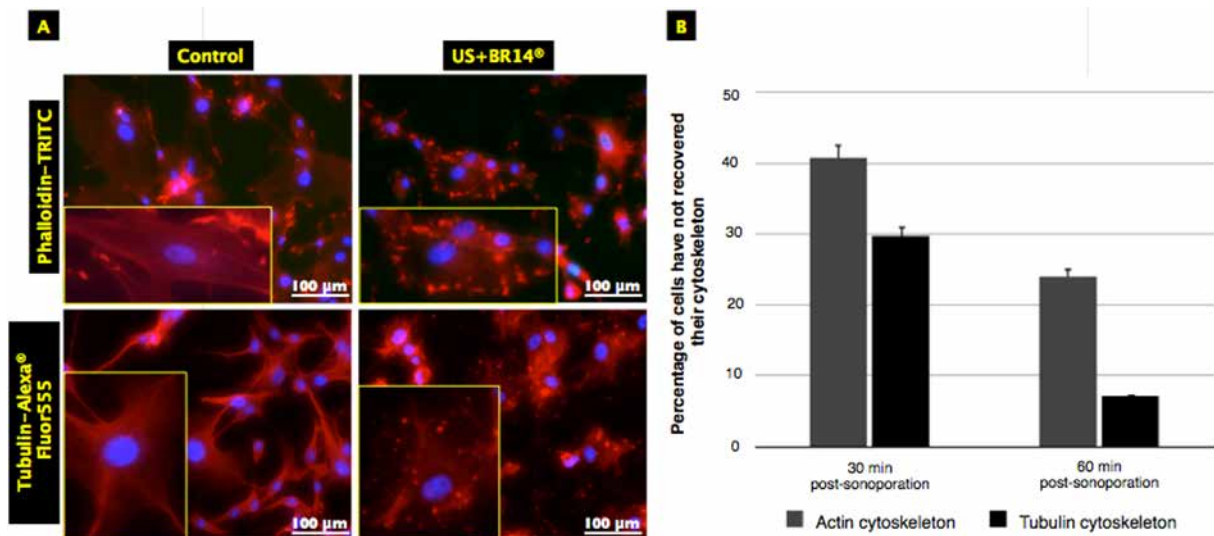


Figure 1: Effect of on actin and tubulin cytoskeleton of the U-87 MG cells. A. Immunofluorescence images depict control and sonoporated cells, with altered cytoskeleton (actin microfilaments and microtubules). B. Histograms of the percentage of cells with a normal cytoskeleton (actin and tubulin) 30 and 60 min post-sonoporation. N = 500 cells. The data are shown as the mean \pm SD.

Thereafter, in order to study the reversibility of the sonoporation effects on cytoskeleton, the cells were fixed 30 and 60 min post-sonoporation. The results (Figure 1B) show that, 30 min post-sonoporation, the percentage of cells with cytoskeleton disruptions decreases and approximately 60% and 70% of sonoporated cells recover the integrity of actin and tubulin cytoskeleton, respectively. This decrease is emphasized over time since \approx 8% of cells present a tubulin cytoskeleton disruption 60 min post-sonoporation. For actin cytoskeleton, this decrease is half compared to the cells 30 min post-sonoporation. These results give evidence that the effect of sonoporation on cytoskeleton is reversible, and suggest that actin cytoskeleton takes longer to get back up compared to tubulin one, following sonoporation.

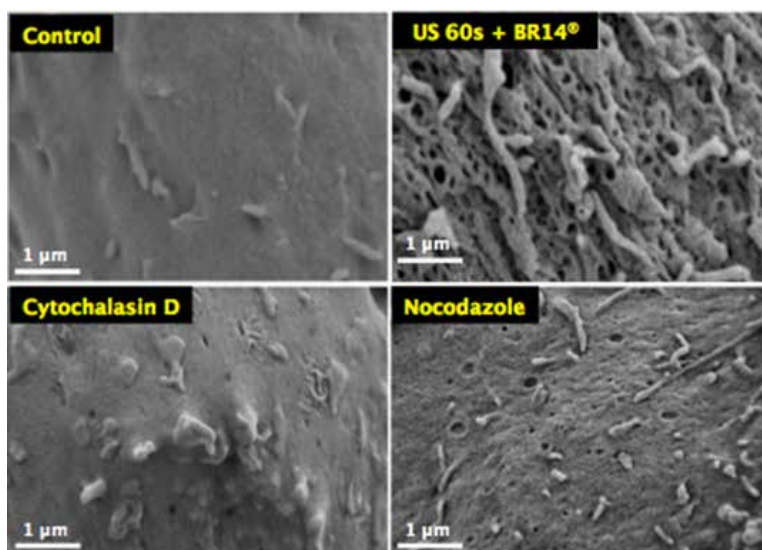


Figure 2: SEM photomicrographs of the morphology of the U-87 MG plasma membrane, for four conditions: Control cell, insonified cells (US 60s + BR14®) without any treatment, insonified cells treated with Cytochalasin D or Nocodazole. Cells were attached immediately post-sonoporation. N = 10.

The efficacy of drug treatments has been assessed using confocal microscopy. Visible actin microfilaments and microtubules were not observed after drug treatments (data not shown). These two inhibitors were used at concentrations that generate the depolymerization of the actin microfilaments and microtubules, while preserving high cell viability, $\approx 86\%$ after each treatment. The effects of inhibitors on the formation of permeation structures were assessed using SEM. Our results (Figure 2) showed that a cytochalasin D treatment induces a strong decrease in the number of permeation structures ($98.5 \pm 0.2\%$). Similarly, nocodazole also leads to decrease of the number permeation structures ($\approx 96\%$). However, this decrease is less pronounced compared to the cytochalasin D treatment. These data suggest that both actin and tubulin cytoskeleton are strongly involved in the membrane permeabilization. Indeed, it is currently admitted that the actin microfilaments could participate to the formation of invaginations, while microtubules are involved in the intracellular trafficking of vesicles.

As shown in figure 3, cytochalasin D and nocodazole lead to 87% and 58% decrease in permeabilization level, respectively.

Together, these results suggest the strong implication of cytoskeleton in the membrane permeabilization during sonoporation.

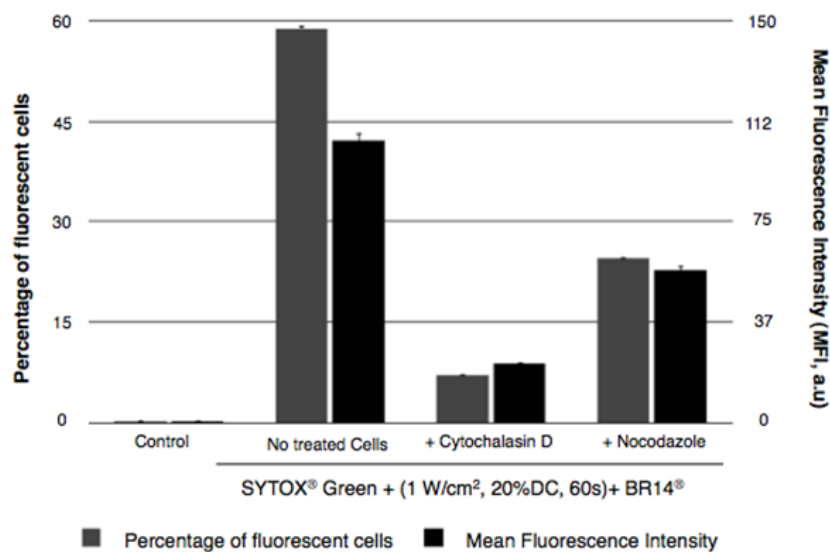


Figure 3: Effects of sonoporation on permeabilization level and efficiency with or without inhibitors treatment (cytochalasin D or nocodazole). The data are shown as the mean \pm SD.

Conclusions

It is well known that sonoporation increases the cell plasma membrane permeability, inducing cell membrane permeabilization. Here, we showed that both actin and tubulin cytoskeleton are transiently altered following sonoporation. We observe also a decrease in the membrane permeabilization after inhibitors treatment. These data suggest that cells cytoskeleton would be a leading player involved in sonoporation process. In addition, the cytoskeleton involvement could occur during the early stages of endocytosis (entry and transport of molecules). Further experiments are underway to investigate the role of cytoskeleton in the intracellular trafficking during sonoporation.

Acknowledgment

The authors wish to thank the members of the microscopy department for their technical assistance. We are also grateful to Bracco Research Geneva for supplying the contrast agents. This project was funded partly by the EU Project SONODRUGS (NMP4-LA-2008-213706).

References

1. I. Lentacker, I. De Cock, R. Deckers, SC. De Smedt, CT. Moonen, "Understanding ultrasound induced sonoporation: definitions and underlying mechanisms". *Advanced Drug Delivery Reviews* (2013)
2. A. Zeghimi, R. Uzbekov, B. Arbeille, J.M. Escoffre, A. Bouakaz, "Ultrastructural modifications of cell membranes and organelles induced by sonoporation.," in : *proceedings of the 2012, IEEE International Ultrasonics Symposium, Dresden, Germany, Oct. 2012*

ROMIUS: Reduction of microvascular injury utilizing sonolysis – study design and rationale

S.T. Roos MD, L. Juffermans PhD, P. Rafter MS, A. Patil PhD, N. van Royen MD PhD, A.C. van Rossum MD PhD, O. Kamp MD PhD

Rationale

The optimal treatment strategy in patients with acute ST-elevated myocardial infarction (STEMI) is immediate restoration of epicardial coronary blood flow. Currently, primary percutaneous coronary intervention (PCI) is the treatment of choice in STEMI patients, however, its widespread use is hampered by limited availability of specialized facilities and trained staff. Also, peripheral microvascular obstruction (MVO) often occurs, as part of the microvascular injury pathway. Therefore, there is need for simpler and low-risk methods for effective recanalization of thrombosed arteries that can be initiated early in the disease process and after initial primary PCI treatment.

Recently, in vivo studies using thrombo-occlusive canine and rabbit models demonstrated that ultrasound contrast agents (UCAs) enhance the thrombus dissolving effect of ultrasound, resulting in higher recanalization rates of occluded arteries. This was proven even without use of fibrinolytic agents. The Sonolysis study trial aimed to pretreat patients with STEMI using a combination of ultrasound and microbubbles with low dose fibrinolytic treatment. The goal of this study was to enhance epicardial reflow. This new study will aim to decrease MVO and reduce no-reflow effects. We hypothesize that under influence of ultrasound, UCAs enhance dissolution of thrombus due to cavitation in patients with acute STEMI premedicated with prasugrel, aspirin and heparin followed by bivalirudin and furthermore reduce the amount of microvascular obstruction that occurs after primary PCI. (Figure 1)

Methods

20 patients presenting with STEMI will undergo intravenous infusion of an UCA and diagnostic ultrasound (1.6MHz, MI 1.0 and pulse duration of 20 microseconds) for 15 minutes. Patients will also be treated with heparin, aspirin and prasugrel. Afterwards, PCI will be performed and bivalirudin will be administered. After primary PCI patients will receive an additional 30 minutes of ultrasound and UCA treatment. All patients will receive dual anti-platelet therapy in addition to normal STEMI protocol. During sonolysis treatment local echocardiographic imaging will be performed to observe cardiac function using the S5-1 Philips ultrasound probe. Additionally patients receive MRI in the first week following STEMI and echocardiography and MRI will be performed after 6 months.

Endpoints

Main goal of this study is the feasibility of the sonolysis procedure in this setting. Secondary endpoints consist of patient safety monitoring and cardiac function and recovery during follow up.

Conclusions

The ROMIUS study will be a feasibility study based on the original Sonolysis study. Positive findings may stimulate further research and technical innovations to described study protocol will determine feasibility of pre and post treatment of ultrasound and microbubbles in human STEMI patients treated with dual antiplatelet therapy.

Keywords

Sonolysis, MVO

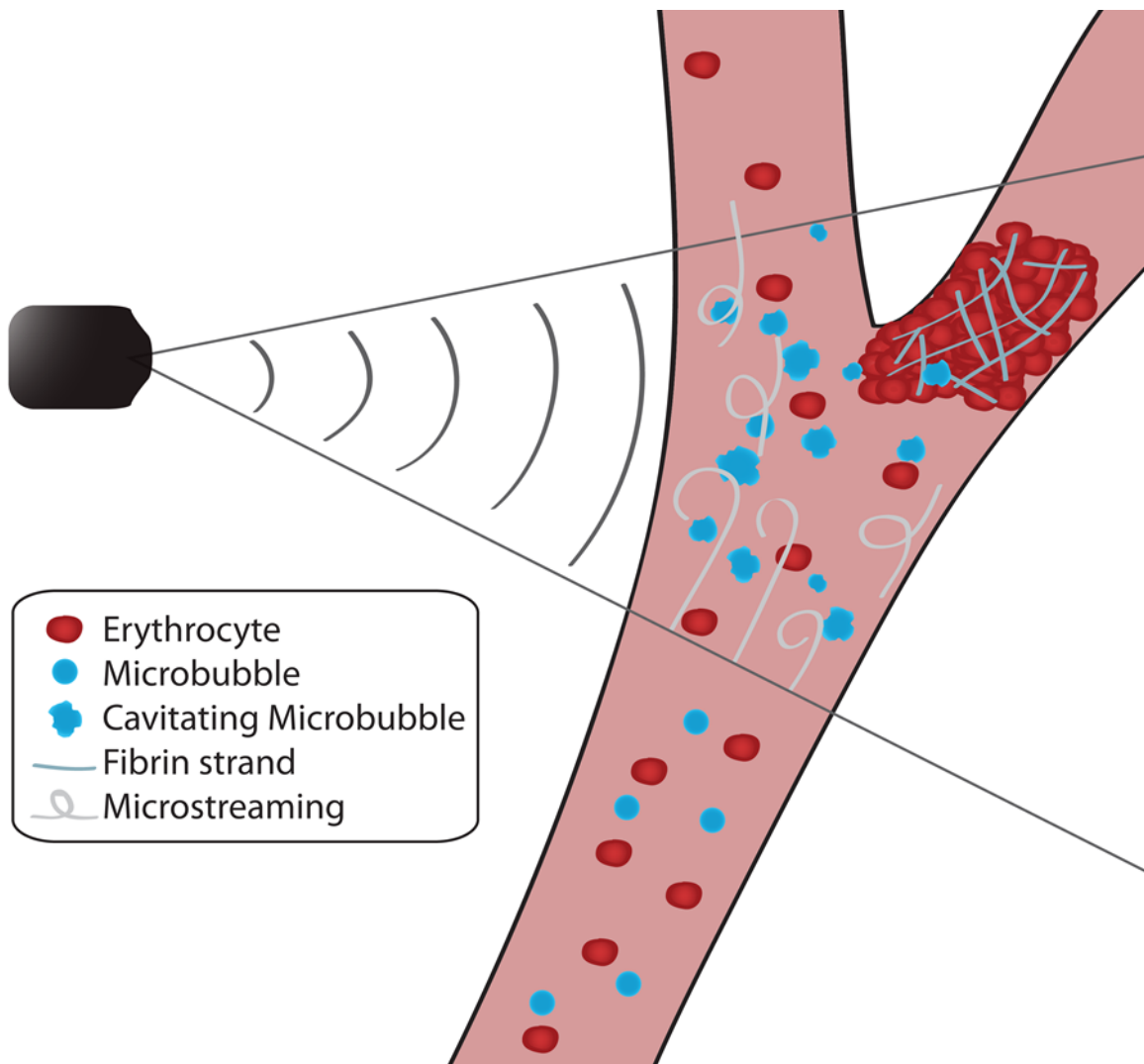


Figure 1: Cavitation of microbubbles occurs when ultrasound is applied in small microvascular vessels.

Improvement of accuracy of liver lesion DCEUS quantification using automatic respiratory gating

Damianos Christofides¹, Edward Leen² and Michalakis Averkiou¹

¹*Department of Mechanical and Manufacturing Engineering, University of Cyprus, Nicosia, Cyprus*

²*Imaging Department, Hammersmith Hospital, London, UK*

Introduction

Dynamic contrast enhanced ultrasound (DCEUS) has been used clinically to evaluate changes in the perfusion of lesions in the liver as a consequence of treatment with anti-angiogenic drugs[1], [2]. The perfusion patterns of the lesions can be modeled in order to extract quantification parameters like peak intensity (PI), area under the curve (AUC), rise time (RT) and mean transit time (MTT)[3].

Lesion perfusion quantification using DCEUS can be affected by many unwanted factors like signal saturation, acoustic shadowing, nonlinear propagation artifact and system settings. Respiration can also have a significant effect on liver lesion DCEUS quantification with various solutions being proposed in the literature[4]–[6].

This study investigates the errors that respiration introduces in the DCEUS quantification of liver lesions using a respiratory motion simulation model (RMSM). Also a method proposed for automatic respiratory gating (ARG)[6] is evaluated for its effectiveness in correcting for the errors introduced. Finally the RMSM is validated with clinical data by investigating the relationship between the respiratory amplitude and the quality of the fit of the DCEUS data onto the lognormal indicator dilution model[7].

Materials and method

Respiratory Motion Simulation Model

The RMSM was constructed in MATLAB (2012b, The MathWorks Inc., Natick, MA) for the purpose of simulating a dual contrast imaging mode acquisition. On the contrast side of the acquisition the lesion was modeled as a sphere of 20 pixels (px) radius inside a 300 by 300 px cube which modeled the parenchyma. The simulated lesion and parenchyma were perfused according to distinct lognormal indicator dilution models[7] with perfusion parameters derived from clinical data. On the tissue side of the acquisition a bright moving structure is modeled as a wedge inside of a 50% less bright cube measuring 300 by 300 px.

The imaging plane of the contrast side acquisition captured the lesion as a disk of varying position and radius to account for in-plane and out-of-plane motion respectively (figure 1). The position of the lesion was varied from its initial position by displacing its center by an offset vector $[Ar(t)]$ that was calculated according to equation (1) whereas the radius of the lesion $[r(t)]$ was varied using equation (2)

$$\overset{uu}{D}r(t) = A \left(\sin(0.4\rho t) \vec{i} + \sin(0.4\rho t) \vec{j} \right), \quad (1)$$

$$r(t) = \sqrt{20^2 - (7 \sin(0.4\rho t))^2}, \quad (2)$$

where t is the acquisition time and A is the amplitude of in-plane oscillations from the initial position which had a range between 0 and 36 px for creating simulations of different in-plane amplitude. On the tissue side of the imaging plane the bright wedge was captured as a rectangle (figure 1) whose position varies according to equation (1). Out-of-plane motion was modeled by varying the height of the rectangle [$h(t)$] according to equation (3),

$$h(t) = 20 + 3.5 \sin(0.4\rho t), \quad (3)$$

where t is the acquisition time.

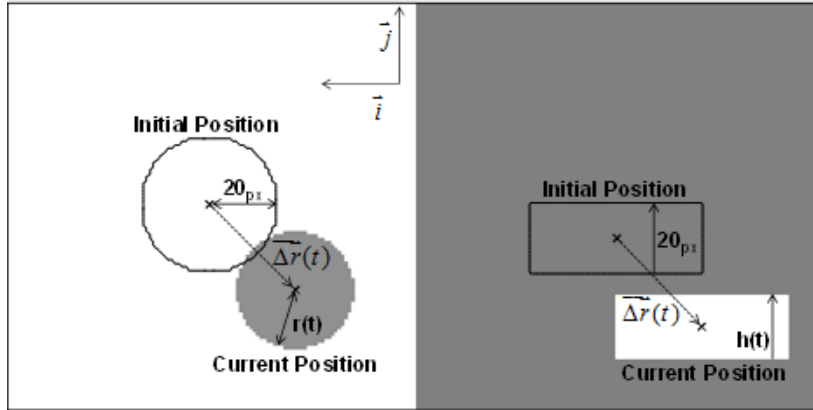


Figure 1: Screenshot from MATLAB of the simulated dual contrast imaging acquisition. On the left the DCEUS side of the acquisition is shown with the initial position of the lesion indicated (solid black line) and the current position of the lesion presented during its washout phase. On the right the tissue side of the acquisition is shown with the moving bright structure displaced from its initial position (solid black line).

The mean DCEUS linear intensity within a region-of-interest (ROI) delineating the initial lesion position was sampled across time to calculate the time intensity curve (TIC) of the lesion under the presence of respiratory motion. The lognormal indicator dilution model[7] was then fitted onto the lesion TIC extracted with and without ARG. Subsequently the RT, MTT, AUC and PI were extracted and compared with the set quantification parameters of lesion perfusion to calculate the percentage error caused by respiratory motion. The coefficient of determination of the lognormal model fit (R^2_{LN}) was calculated for both the ARG-processed and non-ARG-processed lesion TIC.

Clinical DCEUS acquisitions

The Philips iU22 scanner (Philips Medical Systems, Bothell, WA) was used to scan twenty two liver metastasis patients using dual contrast imaging mode. The lesion DCEUS TIC were extracted with and without the use of ARG[6] and the R^2_{LN} of the lognormal indicator dilution model was calculated.

Respiratory Amplitude

The effect respiration has on lesion TIC was quantified by evaluating its frequency spectrum and calculating the area under the respiratory range of 0.1-0.5Hz. The area under the respiratory range was then divided by the area under the 0-0.1Hz range which signifies the slower changing lesion perfusion signal (figure 2). This ratio was recorded as the respiratory amplitude (RA) metric.

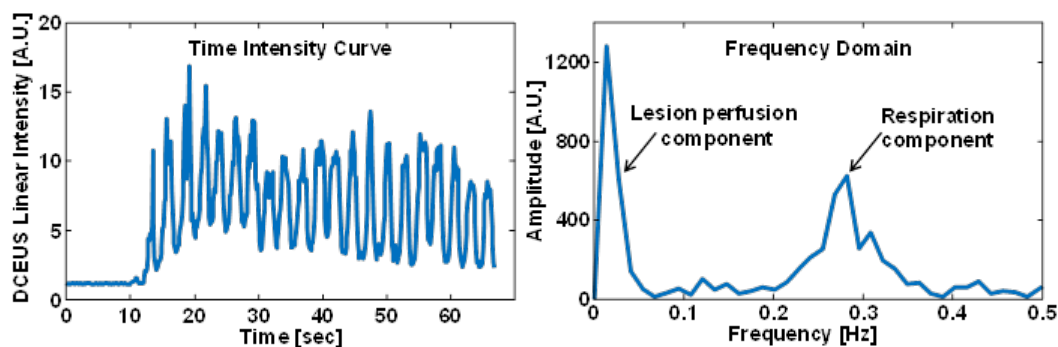


Figure 2: Example of the frequency spectrum (right) of a lesion TIC (left) with the lesion and respiratory components of the TIC indicated on the frequency spectrum.

Results

The results from the RMSM show that the average percentage error decreases with the use of ARG from a mean value of 45% to 17% for the RT, 11% to 5% for the MTT, 42% to 11% for the AUC and 41% to 9% for the PI (Figure 3).

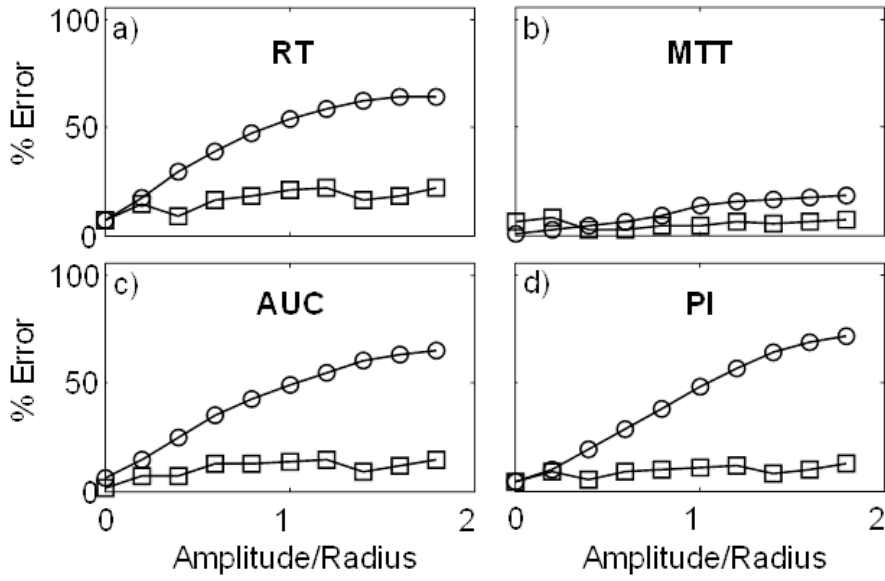


Figure 3: Simulation results for the percentage error between the acquired quantification parameters and the set quantification parameters with increasing respiratory in-plane amplitude without the use of ARG (circles) and with the use of ARG (squares) for the a) RT, b) MTT, c) AUC and d) PI.

The quality of fit of the lognormal indicator dilution model onto the lesion TIC correlates linearly with *RA* both for the patient data and the simulation with the Pearson's correlation coefficient decreasing by 37% with the use of ARG for the clinical data and 28% for the simulation (Figure 4).

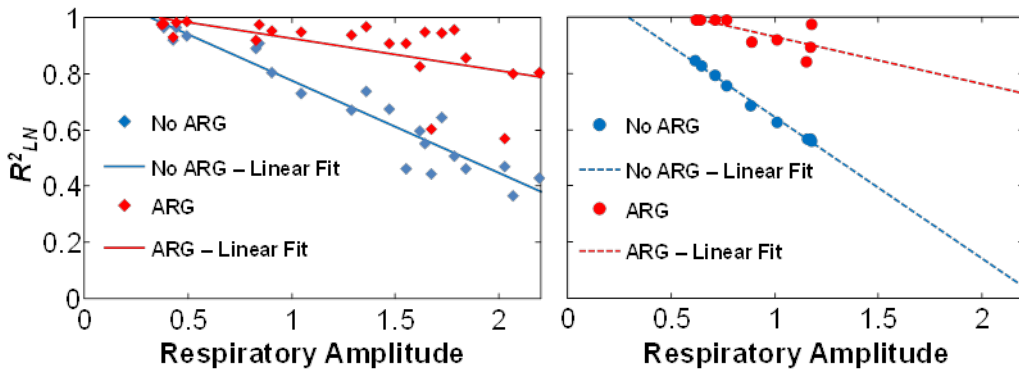


Figure 4: Relationship between the quality of fit and respiratory amplitude for the patient data (left) and the simulation (right).

Conclusion

The results from the simulation model show that ARG can reduce the absolute error between set and extracted DCEUS quantification parameters under the presence of respiratory motion thus increasing the accuracy of liver lesion DCEUS quantification parameters extracted.

The clinical relevance of the simulation model was validated by comparing the relationship between R^2_{LN} and RA derived from the RMSM and the clinical data with and without the use of ARG.

References

1. M. Averkiou, M. Lampaskis, K. Kyriakopoulou, D. Skarlos, G. Klouvas, C. Strouthos, and E. Leen, "Quantification of tumor microvasculature with respiratory gated contrast enhanced ultrasound for monitoring therapy.," *Ultrasound Med Biol*, vol. 36, no. 1, pp. 68–77, Jan. 2010
2. N. Lassau, S. Koscielny, L. Chami, M. Chebil, B. Benatsou, A. Roche, M. Ducreux, D. Malka, and V. Boige, "Advanced hepatocellular carcinoma: early evaluation of response to bevacizumab therapy at dynamic contrast-enhanced US with quantification--preliminary results.," *Radiology*, vol. 258, no. 1, pp. 291–300, Jan. 2011
3. E. Leen, M. Averkiou, M. Arditi, P. Burns, D. Bokor, T. Gauthier, Y. Kono, and O. Lucidarme, "Dynamic contrast enhanced ultrasound assessment of the vascular effects of novel therapeutics in early stage trials.," *Eur Radiol*, vol. 22, no. 7, pp. 1442–50, Jul. 2012
4. S. Mulé, N. Kachenoura, O. Lucidarme, A. De Oliveira, C. Pellot-Barakat, A. Herment, and F. Frouin, "An automatic respiratory gating method for the improvement of microcirculation evaluation: application to contrast-enhanced ultrasound studies of focal liver lesions.," *Phys Med Biol*, vol. 56, no. 16, pp. 5153–65, Aug. 2011
5. N. Rognin, R. Campos, J. Thiran, T. Messenger, P. Broillet, P. Frinking, M. Mercier, and M. Arditi, "A new approach for automatic motion compensation for improved estimation of perfusion quantification parameters in ultrasound imaging," in *Proceedings of the 8th French Conference on Acoustics*, 2006, pp. 61–65
6. D. Christofides, E. Leen, and M. A. Averkiou, "Automatic respiratory gating for contrast ultrasound evaluation of liver lesions.," *IEEE Trans Ultrason Ferroelectr Freq Control*, p. In-Print, Jun. 2014
7. C. Strouthos, M. Lampaskis, V. Sboros, A. McNeilly, and M. Averkiou, "Indicator dilution models for the quantification of microvascular blood flow with bolus administration of ultrasound contrast agents.," *IEEE Trans Ultrason Ferroelectr Freq Control*, vol. 57, no. 6, pp. 1296–310, Jun. 2010

Super-resolution localisation using single bubble acoustics and ultrasound

K. Christensen-Jeffries¹, O.M. Viessmann², M.X. Tang³, C. Dunsby² and R.J. Eckersley¹

¹Biomedical Engineering Department, Division of Imaging Sciences, King's College London, London SE1 7EH, UK

²Department of Physics, Imperial College London, London SW7 2AZ, UK

³Department of Bioengineering, Imperial College London, London SW7 2AZ, UK

The spatial resolution in US imaging is fundamentally limited by diffraction. Sub-diffraction imaging is a well-developed field in optical microscopy where methods have been developed to overcome the same fundamental physics through the localisation of many spatially separated photoactivatable fluorophores (Betzig et al. 2006).

Recently, this super-resolution process has been adapted to exploit contrast enhanced ultrasound (CEUS) imaging (Viessmann et al. 2013; Desailly et al. 2013). Since microbubbles are much smaller than the resolution cell of the scanner, it is assumed they act as point scatterers in the acoustic field and therefore their image is given by the point spread function (PSF) of the system. Dilute suspensions of microbubble contrast agents flowing through micrometer sized tube phantoms were imaged using pulse inversion imaging ensuring a sparse density of spatially isolated microbubble signals. By calculating the intensity weighted centre of mass of multiple spatially isolated microbubble signals and superimposing these located points, super-resolved microbubble location density maps were generated which can resolve the underlying structure containing these microbubbles.

This method is demonstrated using parallel and crossed-vessel phantoms where features smaller than the US system PSF full width half maximum in the lateral and axial directions respectively are resolved, shown in Figures 1 and 2. The angles between the crossed tubes in resulting super-resolution images match those measured to within 1. The computer detection algorithm was also shown to detect the number of single bubble signals predicted by Poisson statistics. Initial system characterisation experiments using a fixed 100 μm diameter brass wire and a US frequency of 2 MHz suggest that for an ideal stationary point scatterer the fundamental resolution limit of the unmodified clinical US system used could be in the range of 0.3 to 0.6 μm .

A computer simulation has been constructed which uses a model of the system PSF, the system noise, varying microbubble response and imaging parameters to investigate their effects on image acquisition. Numerous computer algorithms for the correct detection and localisation of individual bubble signals, such as using intensity and size thresholding and library-based comparative analysis, were tested on both experimental and simulated data. Super-resolution US imaging using the single microbubble method shows great potential to close this resolution gap, however the development, implementation and evaluation of super-resolution motion correction techniques and well as fast 3D acquisition to improve acquisition time is required for long-term development of this technique towards clinical application.

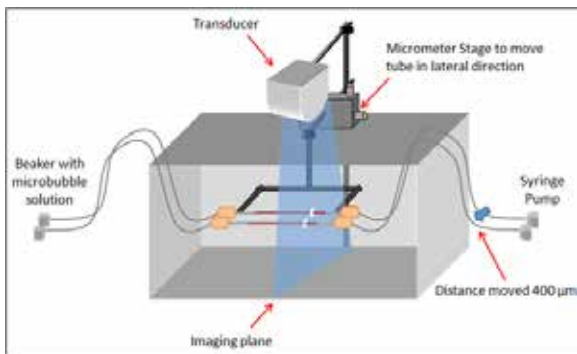


Figure 1a.

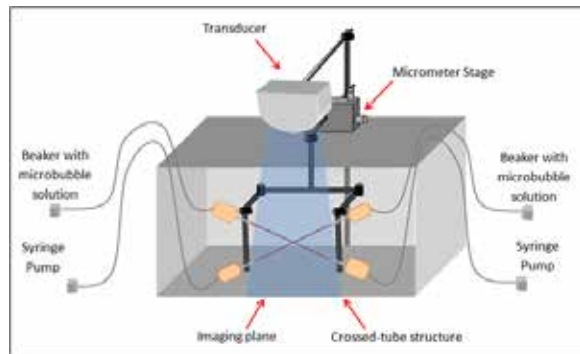


Figure 2a.

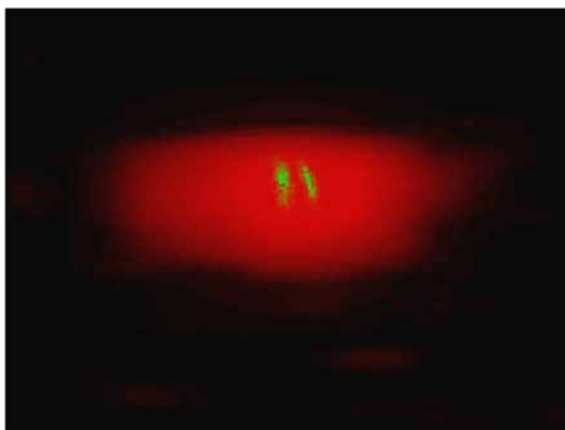


Figure 1b.

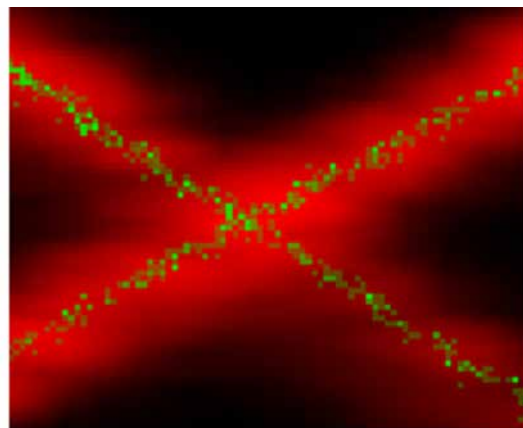


Figure 2b.

Acknowledgments

This research was supported in part by the EPSRC (EP/G038163/1) and the National Institute for Health Research (NIHR) Biomedical Research Centre at Guy's and St Thomas' NHS Foundation Trust and King's College London and the King's College London Medical Engineering Centre, funded by the Wellcome Trust and EPSRC. The views expressed are those of the author(s) and not necessarily those of the NHS, the NIHR or the Department of Health.

References

1. Betzig, E., Patterson, G. H., Sougrat, R., Lindwasser, O. W., Olenych, S., Bonifacino, J. S., Hess, H. F. (2006). *Imaging intracellular fluorescent proteins at nanometer resolution. Science (New York, N.Y.), 313(5793)*
2. Viessmann, O. M., Eckersley, R. J., Christensen-Jeffries, K., Tang, M. X., Dunsby, C. (2013). *Acoustic super-resolution with ultrasound and microbubbles.pdf. Physics in Medicine and Biology, 58(18), 6447*
3. Desailly, Y., Couture, O., Fink, M., Tanter, M. (2013). *Sono-activated ultrasound localization microscopy. Applied Physics Letters, 103(17), 103*

Attenuation correction and image normalisation improve quantification of ultrasound contrast enhancement in carotid artery adventitia in cancer patients after radiation therapy

W.K. Cheung¹, D.M. Gujral², B.N. Shah³, N.S. Chahal³, S. Bhattacharyya³, Y Yildiz¹, D. Cosgrove⁴, R.J. Eckersley⁵, K.J. Harrington², R. Senior³, C.M. Nutting², M.X. Tang¹

¹Department of Bioengineering, Imperial College, Exhibition Road, London, SW7 2AZ

²Head and Neck Unit, The Royal Marsden Hospital, 203 Fulham Road, London, SW3 6JJ, UK

³Department of Echocardiography, Royal Brompton Hospital, Sydney Street, London, SW3 6NP

⁴Imaging Department, Imperial College London, UK

⁵Division of Imaging Sciences, King's College London, UK

Background

Radiation therapy for cancer patients is known to promote atherosclerosis, and the growth of adventitial vasa vasorum is thought to be a precursor. Contrast-Enhanced Ultrasound (CEUS) has shown great potential in detecting and quantifying neovascularization [1]. However, currently quantification of contrast enhancement is significantly affected by many factors including spatially heterogeneous and patient specific attenuation [2][3]. The consequent high variations in the results affect the usefulness of such quantification in clinical applications.

Objective

This study is to evaluate whether an automatic attenuation correction and image normalisation technique can improve quantification of ultrasound contrast enhancement and better identify differences in carotid artery adventitial vasa vasorum between the irradiated and non-irradiated carotid arteries in head and neck cancer patients.

Methods

48 patients with head and neck cancer (HNC) treated with radiotherapy (unirradiated side as control) at least 2 years previously were recruited at the Royal Marsden Hospital. All patients had been prescribed a dose of at least 50 Gy to one side of the neck. CEUS image sequences were acquired on both sides of the neck with a clinical scanner (GE Vivid7 with a 9 MHz broadband linear array transducer).

Regions of interest (ROI) were selected in the lumen and in the adventitia of the far wall of the proximal common carotid artery (Figure 1). A novel algorithm was developed to estimate and correct attenuation artefact within the lumen which was then extended to regions beyond the lumen, including the adventitial vasa vasorum. The images were also normalised to improve the comparability between different patients. Average intensity within ROI between irradiated (RT) and non-irradiated (noRT)

arteries were calculated and compared. Statistical analysis was conducted to evaluate the difference in contrast enhancement between the irradiated and unirradiated sides.

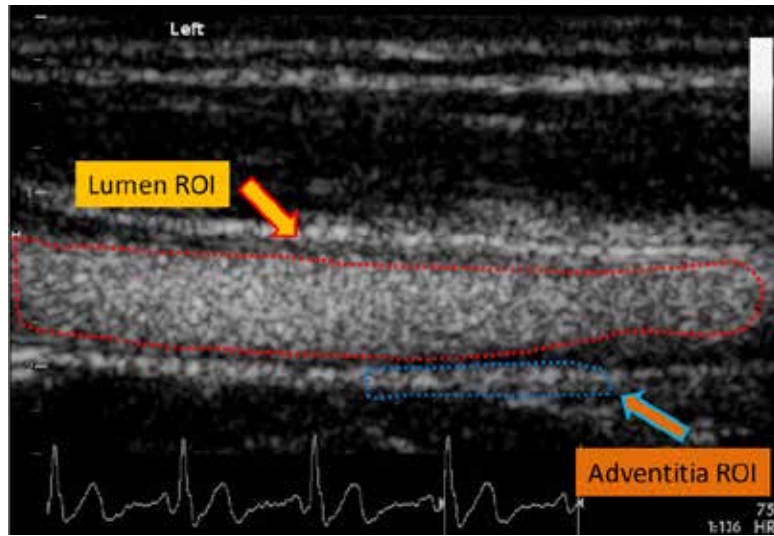
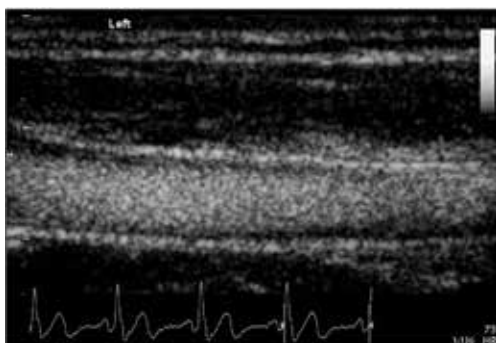


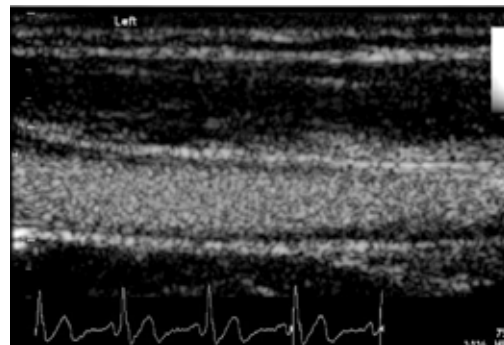
Figure 1: ROIs in the lumen (red line) and adventitia (blue line)

Results

The intensity of the lumen became more homogenous after attenuation correction and the visualization of contrast enhancement in adventitia was also improved (Figure 2B). The full width half maximum (FWHM) of the intensity histogram within the lumen was reduced from 0.51 (Figure 2C) to 0.11 (Figure 2D) after attenuation correction.



(A)



(B)

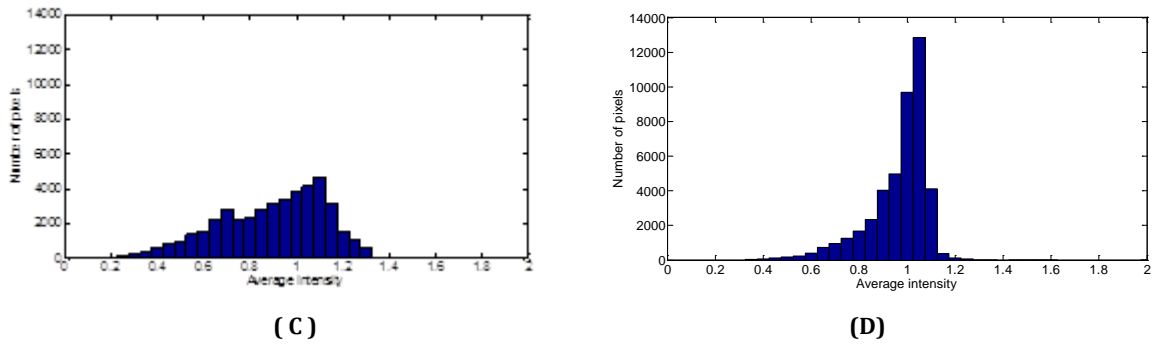


Figure 2: CEUS images of a carotid artery before (A) and after (B) attenuation correction, Histogram plot of average intensity within lumen before (C) and after (D) attenuation correction

There was no significant difference in average intensity between RT arteries (normalised mean \pm standard deviation 1.00 ± 0.03) versus noRT arteries (0.96 ± 0.02) ($p=0.06$). This difference becomes significant when the attenuation correction and image normalisation algorithm were applied (1.00 ± 0.08 for RT arteries vs 0.82 ± 0.05) ($p<0.005$) (Figure 3). The coefficient of variation in intensity difference between the two sides reduced from 3.51 to 2.30 after attenuation correction.

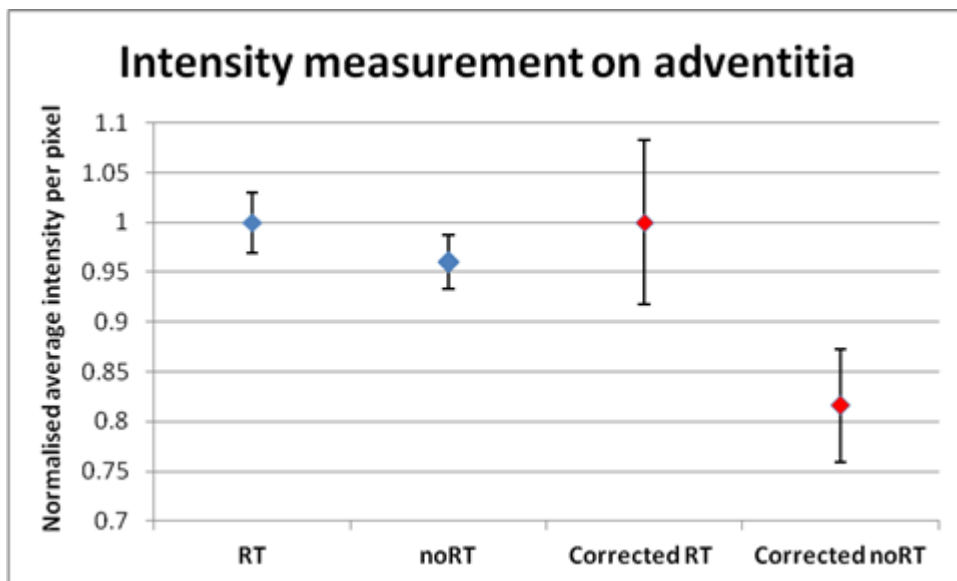


Figure 3: Comparison of average ROI intensity between RT and noRT arteries before and after attenuation correction and normalisation

Discussions and conclusions

Besides attenuation, nonlinear imaging artefacts [4-5] also commonly exist in CEUS images. Clinical examples of such artefacts have been recently reported [6-7]. In the present study, the quantification results will contain both desirable neovascularisation signals and undesirable nonlinear artefacts. As these artefacts are common to both sides, using noRT arteries as control has reduced the effect of such artefacts.

In conclusion, the attenuation correction and image normalisation method can significantly improve CEUS quantification and better identify differences in carotid artery adventitial vasa vasorum between the irradiated and non-irradiated carotid arteries in HNC patients.

References

1. Feinstein, S.B., *Contrast ultrasound imaging of the carotid artery vasa vasorum and atherosclerotic plaque neovascularization. Journal of the American College of Cardiology*, 2006. 48(2): p. 236-24.
2. Tang, M.X., et al., *Quantitative contrast-enhanced ultrasound imaging: a review of sources of variability. Interface Focus*, 2011. 1(4): p. 520-539
3. Tang, M.X., et al., *Attenuation correction in ultrasound contrast agent imaging: elementary theory and preliminary experimental evaluation. Ultrasound in Medicine and Biology*, 2008. 34(12): p. 1998-2008
4. Tang, M.X. and R.J. Eckersley, *Nonlinear propagation of ultrasound through microbubble contrast agents and implications for Imaging. Ieee Transactions On Ultrasonics Ferroelectrics and Frequency Control*, 2006. 53(12): p. 2406-2415
5. Tang, M.X., N. Kamiyama, and R.J. Eckersley, *EFFECTS OF NONLINEAR PROPAGATION IN ULTRASOUND CONTRAST AGENT IMAGING. Ultrasound In Medicine and Biology*, 2010. 36(3): p. 459-466
6. ten Kate, G.L., et al., *Far-Wall Pseudoenhancement During Contrast-Enhanced Ultrasound of the Carotid Arteries: Clinical Description and In Vitro Reproduction. Ultrasound in Medicine & Biology*, 2012. 38(4): p. 593-600
7. Stijn C.H. et al, *Far wall pseudo-enhancement: A neglected artifact in carotid contrast-enhanced ultrasound? Atherosclerosis, volume 229 issue 2 Pages 451-452, 2013*

Detecting the acoustic signatures of volatile phase-change perfluorocarbon agents

Paul S. Sheeran¹, Terry O. Matsunaga² and Paul A. Dayton¹

¹Joint Department of Biomedical Engineering, The University of North Carolina and North Carolina State University, Chapel Hill, NC, USA

²Department of Medical Imaging, University of Arizona, Tucson, AZ, USA

Perfluorocarbon phase-change agents have been proposed as a solution to many emerging problems in medical ultrasound. When activated by a thermal or rarefactional pressure source, the liquid core nucleates to form a gas bubble ideal for interaction with an ultrasound beam. Though many techniques are available for differentiating microbubble signals from surrounding tissue, few methods have been proposed to isolate signals unique to phase-change contrast agents. In the liquid state, the agents interact weakly with the ultrasound beam, and once converted the resulting bubbles act similar to conventional ultrasound microbubbles. In this study, we demonstrate that the physics of the vaporization event itself produce new acoustic signals that can be detected and isolated from both microbubble and tissue signals. High-speed brightfield video microscopy is used to show that, once vaporized with short acoustic pulses, agents composed of volatile perfluorocarbons overexpand and oscillate to a final resting diameter – producing new acoustic waves not related to the vaporization pulse. We next demonstrate that the size-dependent oscillation phenomenon can be detected using an ‘activate high’ (8 MHz), ‘listen low’ (1 MHz) technique. Results show that signal amplitude is dependent on choice of perfluorocarbon, and that by using a band-limited spectral processing technique, the signals can be easily distinguished from microbubble signals produced under identical conditions. Experimental relationships are developed between phase-change agent concentration and ultrasound rarefactional pressure. These results may be used for future physical studies, but may also be useful for development of phase-change agent imaging techniques.

Unique fracturing mechanism of polymer shelled microbubbles: Acoustic characterization and optical observation

*Dmitry Grishenkov^{1,2}, Satya V.V.N. Kotapalli¹, Verya Daeichin³, Frits Mastik³,
Nico de Jong^{3,4}*

¹*KTH, Royal Institute of Technology, School of Technology and Health, Department of Medical Engineering Stockholm, Sweden*

²*Karolinska Institute, Department of Clinical Science, Intervention and Technology Stockholm, Sweden*

³*Biomedical Engineering, Thoraxcenter, Erasmus MC, Rotterdam, the Netherlands*

⁴*Interuniversity Cardiology Institute of the Netherlands, Utrecht, the Netherlands*

Purpose

Getting information about, if and how tissue perfusion best can be quantified by contrast enhanced ultrasound (CEUS) is a challenge. The characteristics of the blood flow in the micro-capillaries can be estimated by destruction/replenishment method. This method is based on destruction of microbubbles (MBs) under insonification with high-energy ultrasound bursts. After destroying all MBs in the area of interest, perfusion can be studied by monitoring the reflow into this area of intact MBs circulating in the blood volume. As a result, it is of great importance to know not only the peak negative pressure above which the MBs fracturing occur, but also the mechanism and physical principal of MBs interaction with ultrasound wave of high amplitude.

Material and methods

We use a gas-filled MBs with an average diameter of 3 μm stabilized by a biocompatible poly vinyl alcohol (PVA) shell of about 300 nm (see Figure 1). This polymer based MBs are obtained by foaming a solution of PVA previously oxidized with sodium metaperiodate. The PVA chains are cross-linked during reaction occurring at the water/air interface. Resulting MBs has a gas core of air that allows them to efficiently scatter ultrasound waves.

Fracturing behavior was first evaluated using opto-acoustic set-up equipped with digital ultra-high speed camera, Brandaris-128, that manages to visualize and record radial oscillation of the MBs exposed to the acoustic wave of varied frequency and amplitude. The driving frequency was varied between 2 to 4 MHz, the peak negative pressure was approximately kept at 1 MPa. The suspension of the MBs was enclosed into OpticellTM chamber.

Then fracturing mechanism was further assessed using pure acoustic set-up, where two transducers 2.25 and 5 MHz were used as an emitter and receiver, respectively. The emitting transducer was driven to oscillation by a computer-controlled system for Study of Nonlinear Acoustic Phenomena (SNAP Mark

IV; Ritec Inc., Warwick, RI, USA). This system allows to set the excitation frequency, number of cycles and the pulse repetition frequency, PRF, of each pulse as well as to control the intensity of electrical signal exciting the transducer. This experimental setup simulates a harmonic imaging technique, where the detection is specific for the second or higher harmonic of the excitation frequency. The suspension of the MBs was introduced into the thin-walled cylindrical container and is gently stirred between the tests.

Results and discussion

The study was inspired by the optical observation where at low excitation pressure minor radial oscillation of the MBs shell takes place (Figure 2a). Interestingly that after arrival of first high-energy burst, MB shell does not fracture in several pieces but rather cracked locally and some encapsulated gas leaked out (Figure 2b). Consecutive high-energy bursts cause new portion of gas to escape from the MB, which is oscillating with higher order buckling modes (Figure 2c). After several of about 5 to 10 bursts all gas escapes from the encapsulating shell, which remain flattened with characteristic wrinkle (Figure 2d).

The acoustic test reveals evidence of completely novel not reported elsewhere fracturing behavior. When tests were performed at PRF equal to 500 or 100 Hz that corresponds to 0.2 and 1 ms respectively we have observed that after arrival of the initial high-energy burst scattered peak-to-peak amplitude, A_{pk-pk} , is increased but not to the absolute its maximum (Figure 2b). Only after approximately 10 consecutive high-energy bursts the maximum A_{pk-pk} was observed. Keeping in mind that thick PVA shell most probably contain some fraction of air between cross-liked PVA chains described above acoustic behavior might be attributed to the pumping the gas out from or through the shell in combination with the release from the core through the cracked part of the shell. We call it “pumping out” behavior. Figure 2a-d demonstrates the corresponding power spectra acquired from the recorded scattered signal. Typical pattern for gas bubble oscillation with sub- and ultra-harmonic signatures present in a power spectrum is reported (Figure 3b, c).

Conclusion

Novel fracturing mechanism that attributed only to the polymer shelled cross-linked MBs is reported. It was evident from both acoustical and optical tests that thick-shelled polymer MBs are not fragmented or destroyed by the first high-energy burst that would be characterized by maximum contrast enhancement. On the other hand PVA MBs require several closely spaced in time insonation pulses to provide maximum enhancement. This “pumping out” behavior is primarily due to the air molecules that are trapped between cross linked PVA chains that constitute the MB shell. Potentially these results can

contribute to the novel strategy of loading therapeutically gases such as nitric oxide, where the gas is trapped inside the shell but not encapsulated in a core.

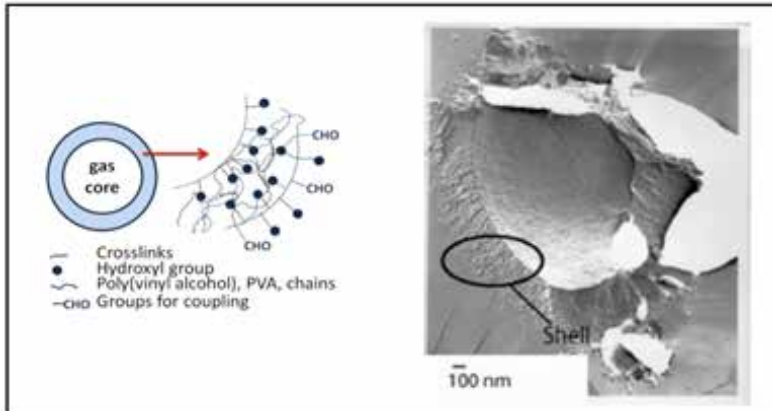


Figure 1: Left: Schematic representation of PVA MB. Right: Electron micrograph of freeze-fractured MB showing a microstructure of PVA microfibrils

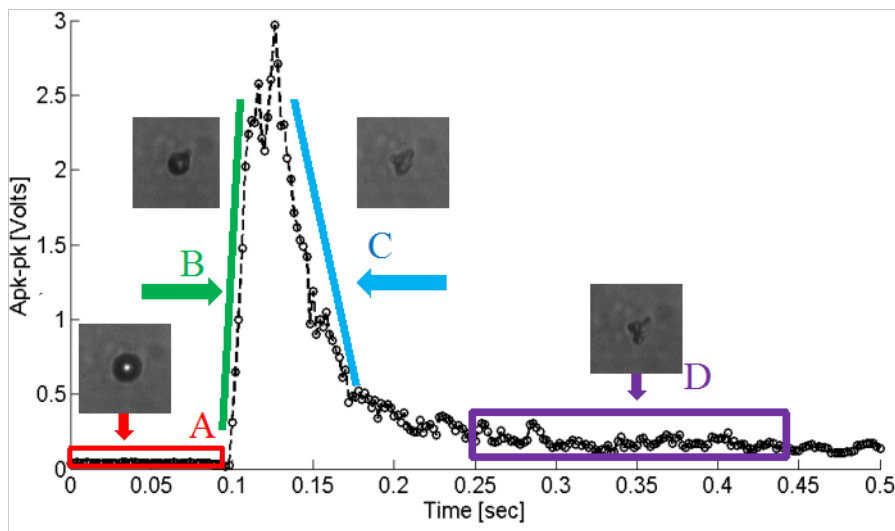


Figure 2: Maximum peak-to-peak amplitude of the scattered signal, A_{pk-pk} , versus time for peak negative pressure $P_{pk}=1$ MPa, pulse repetition frequency, PRF=500 Hz, and number of cycles, $N=10$.

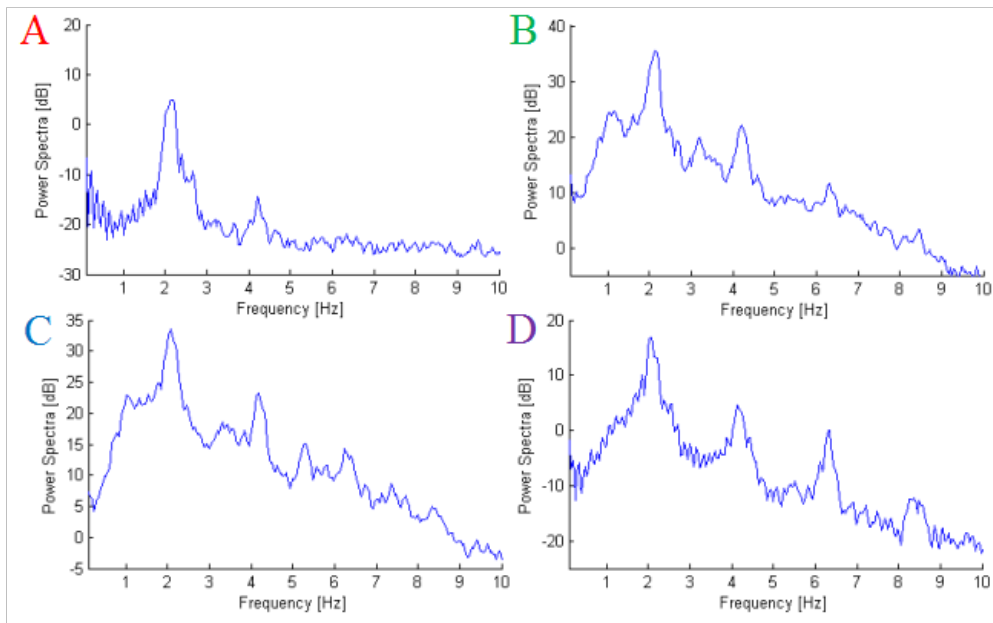


Figure 3: Average power spectra of the scattered time-domain signals for the corresponding regions in figure 2.

Impulse response of echogenic liposomes

*Jason L. Raymond¹, Ying Luan¹, Tom van Rooij¹, Shao-Ling Huang²,
David D. McPherson², Nico de Jong¹, Christy K. Holland³*

¹*Department of Biomedical Engineering, Erasmus MC, Rotterdam, the Netherlands*

²*Department of Internal Medicine, University of Texas Health Science Center, Houston, USA*

³*Department of Internal Medicine, University of Cincinnati, Ohio, USA*

Introduction

Echogenic liposomes (ELIP) are currently under development as theragnostic ultrasound contrast agents for the diagnosis and treatment of cardiovascular disease. ELIP formulations differ from other commercially available ultrasound contrast agents primarily in shell material and gas content. ELIP have a phospholipid bilayer shell that includes a small amount of cholesterol to increase membrane rigidity, and are echogenic due to the presence of air, which is entrapped and stabilized by the lipid during the rehydration process [1]. The exact location of the entrapped air in ELIP has not been fully ascertained, and may be due to air pockets stabilized by lipid monolayers within the liposome, or by the lipid bilayer shell. Our goal is to develop a more complete understanding of the dynamics and shell properties of ELIP, which will contribute to further optimization of ELIP as a theragnostic agent.

We recently reported measurements of the linear viscoelastic shell properties of ELIP using a broadband acoustic substitution technique [2]. The objective of the present study was to investigate the response of individual ELIP to a broadband acoustic pulse using optical methods. The damping coefficient was estimated from experimentally measured radius-time curves obtained using the Brandaris 128 fast-framing camera and are compared to our previously reported measurements.

Materials and Methods

ELIP suspensions were prepared by reconstituting 10 mg/mL lyophilized lipid powder using air-saturated, filtered water at room temperature as described by Huang [1]. The suspension was diluted (~100x) into PBS with 0.5% albumin solution, loaded into an Opticell, and placed in a 37 °C water bath for optical measurements. A microscope with a 60x water-immersion objective and 2x magnifier was used to image the dynamics at ~15 Mfps using the Brandaris 128 fast-framing camera [5].

A focused broadband PVDF transducer (25 mm focal distance; Precision Acoustics) was used to generate acoustic pulses with a center frequency of ~4.5 MHz and pulse duration of approximately 0.33 μ s (1.5 cycles). ELIP were acoustically excited by a 500 kPa peak-positive pressure pulse followed by a 500 kPa peak-negative pressure pulse after a delay of 3 μ s. Each particle was exposed to both positive and negative pulses in order to obtain free-response radius-time curves which were analyzed separately.

Determination of the damping coefficient by impulse response decay time

Linearization of a suitable bubble dynamics equation (such as the one proposed by Marmottant et al.[3]) yields the equation of motion for a damped oscillator. The solution can be written in terms of an oscillatory signal with a decaying exponential envelope of the form:

$$x(t) = A(t) \cos(\omega_d t + \phi), \quad A(t) = e^{-(\delta/2)\omega_0 t} \quad (1)$$

If the amplitude envelope is measured, the damping time constant can be readily determined by fitting a line to the logarithm of the envelope, with a slope given by:

$$\frac{d(\log A(t))}{dt} = \frac{\delta\omega_0}{2} = \frac{1}{\tau} \quad (2)$$

In this study, the envelope was determined by taking the magnitude of the analytic signal formed using the discrete Hilbert transform of $x(t)$. The damping coefficient was then deduced from the decay time constant using (2). An example of the damping analysis is shown in Figure 1.

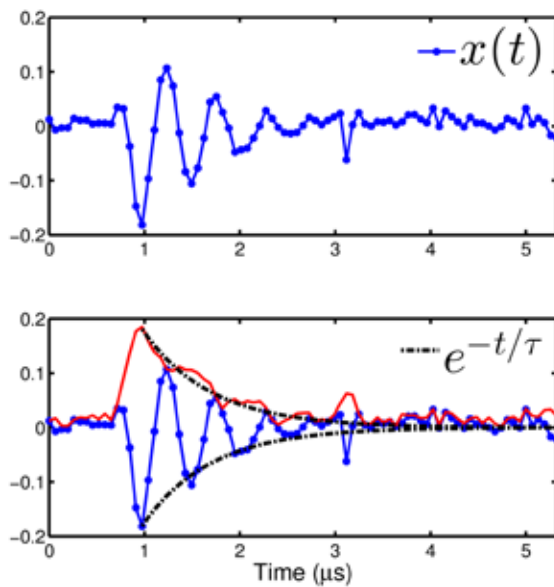


Figure 1. Schematic of the damping analysis. (a) Radius-time response of a single ELIP measured using the fast-framing camera. (b) The amplitude decay envelope (-) is calculated using the discrete Hilbert transform; the time constant is obtained by fitting an exponential decay (-.-) to the envelope using equation (2). For this example $\tau = 0.71 \mu\text{s}$.

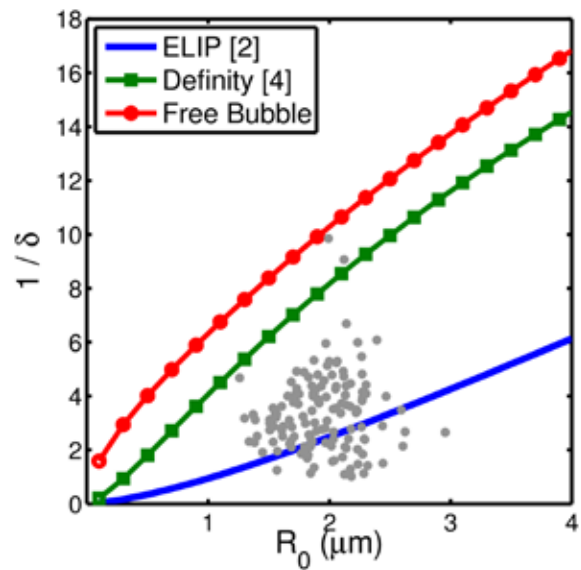


Figure 2. Graph of the measured damping coefficient for 140 ELIP particles. The damping coefficients previously reported for ELIP [2] and Definity [4] as well as for a free bubble are also shown.

Results

A total of 140 (69 peak-positive, 71 peak-negative) radius-time curves for single ELIP particles with equilibrium radii between ~ 1.25 and $3.0 \mu\text{m}$ were analyzed. For a small percentage of particles, the resting radius before and after the acoustic pulse was different (due to acoustically-driven growth or dissolution). Only particles for which the final radius was the same as the initial radius were analyzed in this study ($\Delta x < 0.2 \mu\text{m}$). Results for the damping coefficients are shown in Figure 2. Overall, our results for individual ELIP are consistent with our previous measurement obtained using a broadband attenuation technique [2]. The spread of the individual data points for ELIP may indicate the presence of multilamellar liposomes, where the damping depends on the number of lipid bilayers. Radius- and time-dependent damping mechanisms may also play a role and need to be investigated further.

Conclusions

This study demonstrates a simple method to estimate the damping coefficient for individual ELIP using experimentally measured radius-time curves. The decay time constant and natural frequency of oscillation are determined based on the free response of the particle following excitation by a short acoustic pulse. The non-dimensional damping coefficients estimated for 140 individual response curves compare well with our previously determined shell properties for ELIP at 37°C . However, the natural frequency of oscillation was lower than expected based on our previous measurements. This may be due to the much higher pressure (500 kPa) used in this study compared with our previous measurements (33 kPa in ref. [2]). In conclusion, this study provides additional confirmation of the damping introduced by the ELIP shell, for example as compared with Definity as shown in Figure 2. This is an important parameter which will be further investigated to determine the release profiles of individual ELIP in response to destruction pulses.

Acknowledgements

JLR was supported by a fellowship from the Whitaker International Program administered by the Institute of International Education (IIE). The authors would like to thank Robert Beurskens and Frits Mastik from the Dept. of Biomedical Engineering, Erasmus MC for technical assistance.

References

1. Huang S. *Ultrasound-responsive liposomes*. In: Weissig V, ed. *Liposomes: methods and protocols*. New York, NY: Humana Press, 2010.
2. Raymond JL, Haworth KJ, Bader KB, Radhakrishnan K, Griffin JK, Huang S-, McPherson DD, Holland CK. *Broadband Attenuation Measurements of Phospholipid-Shelled Ultrasound Contrast Agents*. *Ultrasound Med Biol* 2013.
3. Marmottant P, van Der Meer S, Emmer M, Versluis M, de Jong N, Hilgenfeldt S, Lohse D. *A model for large amplitude oscillations of coated bubbles accounting for buckling and rupture*. *J Acoust Soc Am* 2005;118:3499-505.
4. Faez T, Goertz D, de Jong N. *Characterization of Definity™ Ultrasound Contrast Agent at Frequency Range of 5-15 MHz*. *Ultrasound in Medicine and Biology* 2011;37:338-42.
5. *Brands 128 ultra-high-speed imaging facility: 10 years of operation, updates and enhanced features*. Gelderblom E, Vos HJ, Mastik F, Faez T, Kokhuis T, van der Steen AFW, de Jong N, Lohse D, and Versluis M. *Rev. Sci. Instrum.* 83, 103706 (2012).

Basic bolus kinetics explored in an ex vivo liver machine perfusion model

Maria-Louisa Izamis, Christina Keravnou, Damianos Christofides, Ed Leen,
Mike Averkiou*

*Department of Mechanical and Manufacturing Engineering, University of Cyprus, Nicosia, Cyprus
Imaging Department, Hammersmith Hospital, London, UK

Introduction

Dynamic contrast enhanced ultrasound (DCEUS) can quantify perfusion for critically useful diagnostic and prognostic metrics in the characterization of disease states and therapy monitoring. The measurements depend on the complex passage of contrast agent through fast-moving arteries, a stagnantly slow microcirculation, and a low-pressure venous system. Characterizing the flow through this varying architecture in order to construct useful, clinically-applicable algorithms is typically first tested *in vitro* using flow phantoms. These constructs, generally comprised of single passages of rubber tubing through which the contrast is pumped, have very little physiological relevance. To overcome this limitation, we have developed an artificial body with an artificial blood supply to sustain an animal or human donor organ *ex vivo*. This “machine perfusion” device subsequently enables several hours of stable experimentation with the organ of interest. Here we explore basic bolus kinetics in the machine perfusion of a porcine liver model.

Methods

Ex Vivo Liver Machine Perfusion. Healthy porcine livers were procured from the local abattoir and sustained for up to 6 hrs with *ex vivo* machine perfusion. The circuit comprised an organ chamber from which 6L of asanguineous perfusate was circulated through an oxygenator prior to being split into pressure-controlled inputs for each of the portal vein ($P_{PV} < 5\text{mmHg}$) and hepatic artery ($P_{HA} 50\text{--}100\text{mmHg}$). Hepatic stability was ascertained with half-hour interval measurements of bile production, oxygen consumption, and sustained vascular perfusion. The circuit provided individual syringe port access to each of the hepatic vessels so that contrast could be administered to either the portal vein (PV) or hepatic artery (HA).

DCEUS imaging. To monitor the microcirculation of a specific region, a linear array probe (Philips iU22, L9-3) was held in a fixed position on the liver with a mechanical arm. The region was chosen with a preliminary bolus of contrast to the PV and HA to ascertain it contained a cross-sectional view of each input vessel, a hepatic vein (HV), and well-perfused parenchyma. The impact of changing bolus concentration (C) on time-intensity curves (TICs) was evaluated first. The impact of various changes in

physiological flow rates on TICs was subsequently evaluated. For instance, in mimicking such conditions as tumor angiogenesis HA flow was increased and the PV flow was decreased while maintaining an overall constant total flow to the liver.

Contrast agent administration. Unlike the action of the lungs *in vivo*, the perfusion system is not equipped with a filtering system. We therefore chose BR38 (Bracco Suisse SA, Geneva, Switzerland) contrast agent over the clinically available Sonovue since its microbubbles are more tightly distributed with fewer large microbubbles. For each experiment, a new vial of BR38 was utilized. Contrast was serially diluted for an array of different concentrations; a total volume of 0.5ml was administered each time first to the PV and then to the HA. Image loops of 40sec were captured for each injection with “Contrast side/side” (contrast/tissue) mode. High MI imaging was used to eliminate remaining microbubbles between injections and a waiting time of 2 minutes between flow rate changes was allowed for the flow to reach its new equilibrium.

Image quantification. Data analysis of the image loops was conducted by defining 3 regions of interest (ROIs) around the input vessel, HV, and parenchyma (Pa) using commercial quantification software (QLAB version 8.1; Philips Medical System, Bothell, WA, USA). The TICs were exported and analyzed in MATLAB (MathWorks, Inc., Natick, MA, USA). For each TIC, the parameters Peak Intensity (PI), Area Under the Curve (AUC), Rise Time (RT) and Mean Transit Time (MTT) were recorded.

Results

Since trends in the HA and PV, as well as in the intra- and inter-liver variations, were similar, only the HA and inter-liver results are shown for brevity and clarity.

In Intensity vs. Concentration experiments, a linear increase in PI and AUC was observed in the input vessel, the HV, and Pa as bolus concentration increased (Figure 1). For the higher concentrations considered ($>0.2\%$), signal saturation due to acoustic shadowing was observed in the PV. Although there was some noise in the data at very low contrast concentrations ($<0.1\%$), RT and MTT values did not change with contrast concentration. Evaluation of the parenchyma was challenging in general for two reasons. Firstly, at such high imaging resolutions identifying regions that were devoid of major vessels became challenging, and secondly, because contrast washout never reached zero. Rather, a persistent background noise remained that produced spurious AUC and MTT results. These results were subsequently excluded from the present analyses.

In the flow rate results presented here, the HA flow rates ranged from 150ml/min to 400ml/min, a 2.7x increase. As HA flow rates increased, AUC, RT and MTT declined in the HA, while the PI values remained steady. The Pa demonstrated trends similar to the HA while in the HV the trends were less consistent.

Discussion

The results observed here support the long-standing correlation that intensity and contrast concentration is predominantly linear; an optimal range of concentration appears to exist between 0.1‰ and 0.25‰. In the results for the PV injection (not shown here), signal saturation was observed above a concentration of 0.2‰ due to acoustic shadowing, a phenomenon that is well described in the literature.

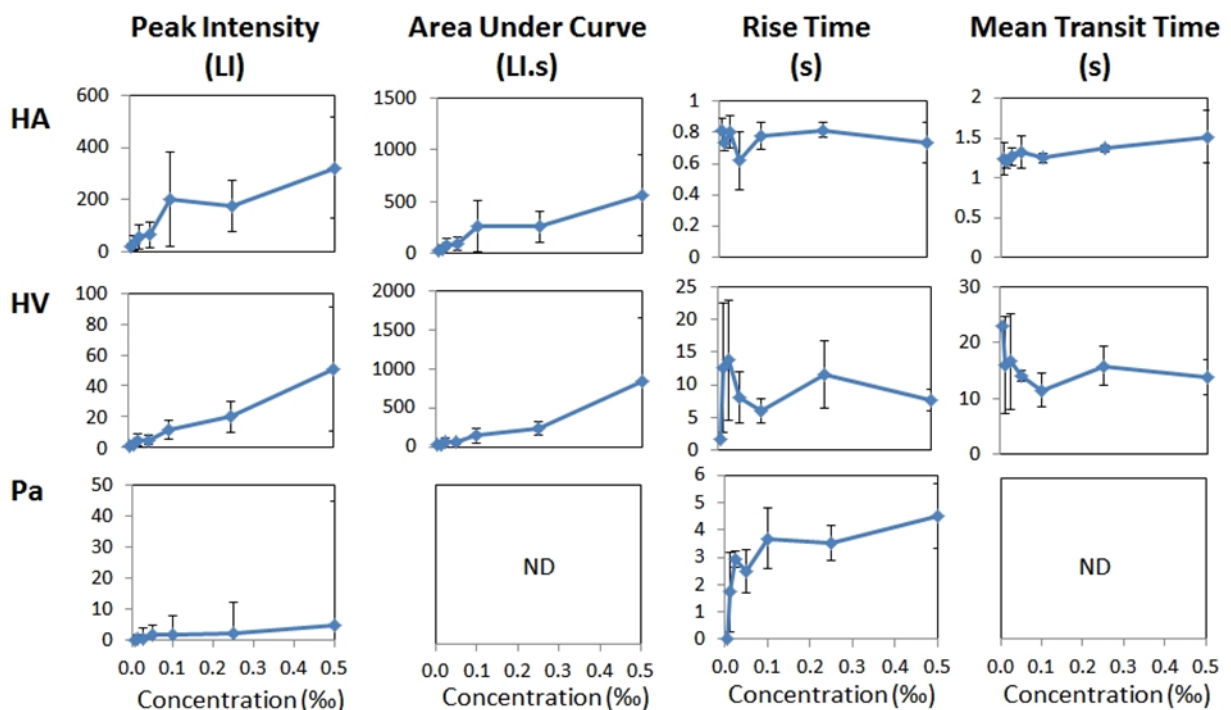


Figure 1: TICs produced from HA-injections of isolated livers in machine perfusion demonstrate linear profiles of PI and AUC vs. Concentration regardless of which region of tissue is evaluated. Both BR38 and SonoVue produce similar trends.

At concentrations lower than 0.1‰ noise becomes problematic for BR38 as reflected in the variability seen in the RT and MTT vs. C curves. The hepatic veins however, have I vs. C trends that are generally linear across the range of concentrations. These readily-located vessels could perhaps be a choice consideration for ROI placement when evaluating the state of the microcirculation since their TICs characterize the trajectory of the contrast through hepatic architecture. This is especially useful when considering that flow in the parenchyma is generally challenging to quantify since the regions which are not perfused by input tributaries are small, and generally produce poor signal to noise ratios.

Flow rate experiments demonstrate that changes in flow rate produce no changes in the PI, while RT, MTT and AUC decline as flow rate increases, as also suggested by indicator dilution theory.

Conclusions

In conclusion, a linear relationship between intensity and contrast concentration is a rational assumption, particularly within a small range of concentrations. The two limits of the above relationship are signal noise at low concentrations and acoustic shadowing at high concentrations. Further, the impact of flow rate increase on ultrasound quantification appears to be a general decline in AUC, RT and MTT, while the PI stays roughly the same. Finally, flow in the HV tree appears to be an easily measured quantity that is representative of flow in the microcirculation.

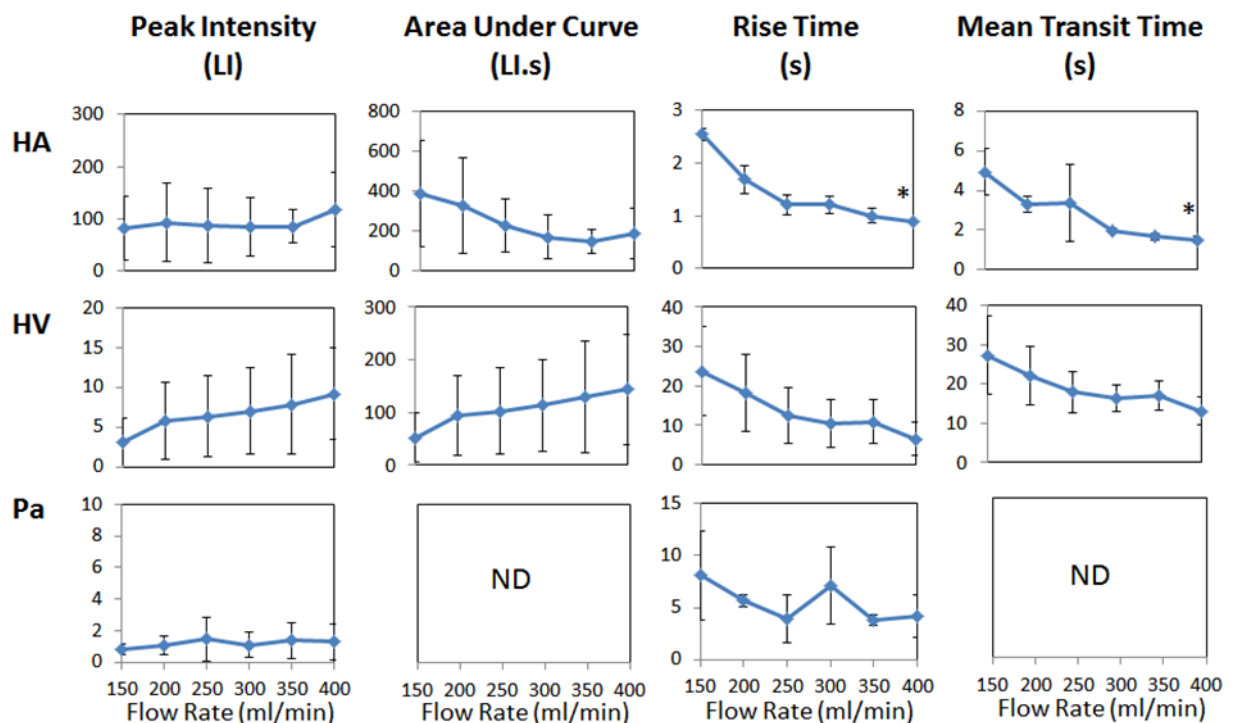


Figure 2: Large changes in HA flow rate, within physiological values, produce negligible changes in PI, while AUC, RT and MTT values appear to decline. *Values at 400ml/min are significantly reduced compared to values at 150ml/min ($p < 0.05$).

Acknowledgements

This work was co-funded by the European Regional Development Fund and the Republic of Cyprus through the Research Promotion Foundation (Project: DIDAKTOR/0311/78). BRACCO is also acknowledged for providing the BR38 contrast agent that was used in these studies.

Influence of DSPC versus DPPC on acoustical responses of lipid-coated microbubbles

Tom van Rooij¹, Ying Luan¹, Guillaume Renaud¹, Antonius F.W. van der Steen^{1,2}, Nico de Jong^{1,2}, Klazina Kooiman¹

¹Biomedical Engineering, Erasmus MC, Rotterdam, the Netherlands

²Interuniversity Cardiology Institute of the Netherlands, Utrecht, the Netherlands

Background

Microbubbles (MB) have been used for diagnostic CEUS imaging for several decades and they are also promising for molecular ultrasound imaging and therapy. Different lipid coatings and compositions can be chosen, however, exact influences on acoustical responses remain unclear [1]. The most commonly used lipid-coated MBs for diagnostic CEUS are Definity (Lantheus Medical Imaging) and SonoVue (Bracco Imaging), for which different varieties of lipids were applied for the coating. For Definity, DPPC is used as one of the shell lipids encapsulating a C₃F₈ gas core [2], whereas for SonoVue DSPC is used in combination with a SF₆ gas core [3]. More recently, the research agent BR14 (Bracco) was introduced as a successor for SonoVue with a similar shell composition, but with a C₄F₁₀ gas core for increased stability [4].

We previously studied two types of homemade MBs with high-resolution 4Pi confocal laser scanning microscopy by changing the main shell lipid; either DSPC or DPPC was used [5]. The only structural difference between the C16-phospholipid DPPC and the C18-phospholipid DSPC are two C-atoms in the hydrophobic acyl chain. For DSPC MBs the lipids were heterogeneously distributed throughout the shell, whereas DPPC MBs showed a homogeneous distribution. Therefore it was hypothesized that these different microstructures would result in different acoustical behaviour as well. We aimed to characterise MB oscillation behaviour and estimate shell properties using the Brandaris 128 high-speed camera. Additionally, we want to use these findings to determine which type would be best suited for CEUS imaging and to select the most promising MB type for molecular imaging.

Methods

Biotinylated lipid-coated MBs with a C₄F₁₀ gas core were made by sonication [6]. The coating was composed of 59.4 mol% DSPC or DPPC, 35.7 mol% PEG-40 stearate, 4.1 mol% DSPE-PEG(2000), and 0.8 mol% DSPE-PEG(2000)-biotin.

Dynamics were captured using the Brandaris 128 high-speed camera [7] operated at ~15 million frames per second. MB spectroscopy was performed [8], with transmit frequencies from 1 to 4 MHz using a broadband single element PVDF transducer. A 10-cycle sine wave burst was applied at 10 and 20 kPa peak-negative pressure to determine frequencies of maximum response and to estimate shell properties of 31 DSPC and 33 DPPC MBs, and at 50 kPa to study non-linear behaviour of 15 DSPC and 14 DPPC MBs.

Results

The acoustical stability of each MB was quantified by means of the diameter change throughout the experiment (33 excitations within a time interval of 80 ms). At 10 and 20 kPa, both MB types were acoustically stable. At 50 kPa, however, shrinkage was significant for both types with mean (\pm SD) diameter decreases of 4.4% (\pm 2.6) for DSPC and 9.2% (\pm 6.0) for DPPC.

Frequencies of maximum response were significantly higher for DSPC MBs at 10 and 20 kPa (Fig. 1). The 20 kPa data in Fig. 1 were fitted to a linearization of the Marmottant model [8] and the elasticities of the coatings were estimated to be $\chi_{DSPC} = 0.26 (\pm 0.13)$ N/m and $\chi_{DPPC} = 0.06 (\pm 0.06)$ N/m. Shell damping at 20 kPa increased with diameter for both bubble types, but was not significantly different with mean values of $\delta_{DSPC} = 0.22$ and $\delta_{DPPC} = 0.25$. Shell viscosities were derived from the shell damping values, resulting in similar mean shell viscosities of $\kappa_{DSPC} = 1.0 \cdot 10^{-8}$ kg/s and $\kappa_{DPPC} = 0.8 \cdot 10^{-8}$ kg/s.

Non-linear properties were evaluated at 50 kPa by means of subharmonic- and second harmonic frequencies. Subharmonics were present in 4 out of 15 (27%) DSPC and 10 out of 14 (71%) DPPC MBs. For use as contrast agents the emitted subharmonic acoustic pressures must be detectable with ultrasound scanners as well. The acoustic pressures were calculated at 2 cm from the MBs [9], resulting in subharmonic pressures for DPPC MBs around the detection limit of 1 Pa [10] and for DSPC even below 0.6 Pa (Fig. 2A), making subharmonic imaging challenging. Since the MB diameter scales quadratically with the emitted pressure, the larger mean diameter for DPPC, 6.4 μ m as compared to 5.1 μ m for DSPC, may partly explain the higher pressures. Second harmonics were comparable between both MB types; 10 out of 15 (67%) DSPC and 11 out of 14 (79%) DPPC MBs showed second harmonics, with mean diameters of 5.0 μ m for DPPC and 5.4 for DSPC. At 2 cm distance from the MB emitted pressures were well above the detection limit, up to values of 6.5 Pa (Fig. 2B).

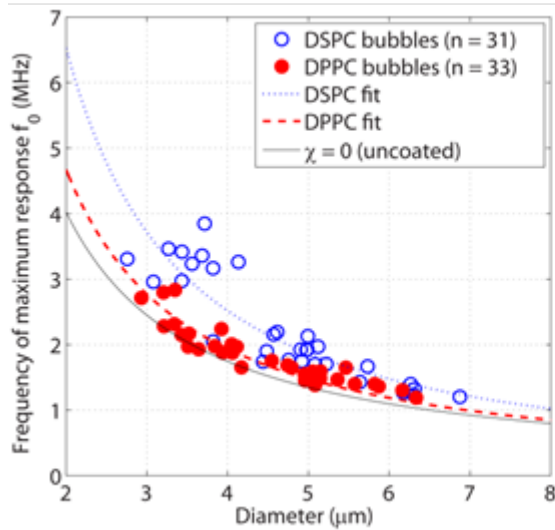


Fig. 1: Frequencies of maximum response at 20 kPa plotted versus the diameter of DSPC and DPPC MBs. Shell elasticities were estimated from the data fitted to a linearization of the Marmottant model [8]. The continuous black line represents an uncoated bubble with shell elasticity $\chi = 0$.

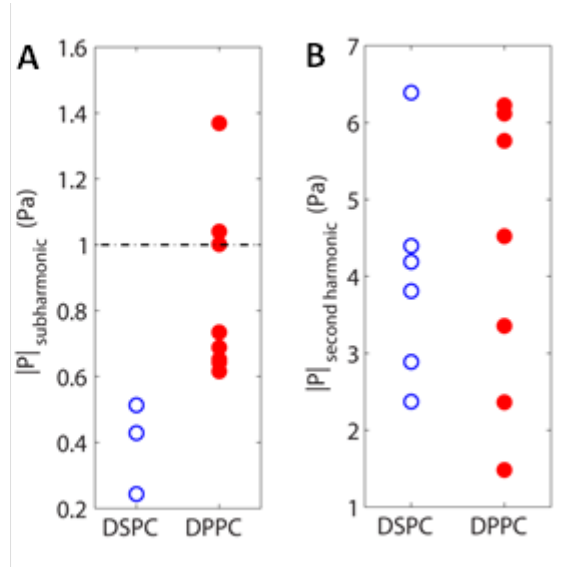


Fig. 2: Calculated theoretical acoustic pressures [9] emitted by **A)** subharmonic and **B)** second harmonic oscillations at 2 cm distance of DSPC (blue open circles) and DPPC (red closed circles) MBs.

Conclusion

This *in vitro* study shows that changing the main shell component of lipid-coated MBs does affect the acoustic responses. We found a lower stability, more subharmonic behaviour, and a lower elasticity for DPPC MBs. As compared to Definity (DPPC) and BR14 (DSPC), elasticities were lower with values of $\chi = 0.5 - 1$ N/m for Definity [11] and $\chi = 0.54$ N/m for BR14 [8]. Viscosities on the other hand, were comparable with both commercial bubbles with $\kappa = 10^{-8} - 10^{-9}$ kg/s [8, 11].

For CEUS and molecular imaging, MBs need to be distinguishable from tissue based on their non-linear oscillations and amplitudes must be sufficiently high for detection. Based on their second harmonic response, both MB types are suited for non-linear imaging and with emitted pressures measurable at 2 cm, e.g. carotid imaging could well be performed. When stability of DPPC can be increased and higher excitation pressures are used, subharmonic imaging of DPPB MBs might become possible. Nevertheless, based on these data our DSPC MBs seem more suitable for CEUS. For molecular imaging, other aspects like ligand loading and binding force need to be considered as well.

Acknowledgements

This work is supported by NanoNextNL, a micro and nanotechnology consortium of the Government of the Netherlands and 130 partners. The authors thank Frits Mastik, Michiel Manten, and Geert Springeling from the Department of Biomedical Engineering, Erasmus MC for technical assistance.

References

1. Kwan, JJ, et al., *Adv Colloid Interface Sci*, vol. 183-184, pp. 82-99, 2012
2. Helfield, BL, et al., *Ultrasound Med Biol*, vol. 38, pp. 846-63, 2012
3. Schneider, M, et al., *Invest Radiol*, vol. 30, pp. 451-7, 1995
4. Schneider, M, et al., *Invest Radiol*, vol. 32, pp. 410-7, 1997
5. Kooiman, K, et al., in *IEEE Ultrasonics Symposium Proceedings, Dresden, Germany*, 2012
6. Klibanov, AL, et al., *Invest Radiol*, vol. 39, pp. 187-95, 2004
7. Chin, TC, et al., *Rev Sci Instrum*, vol. 74, pp. 5026-5034, 2003
8. van der Meer, SM, et al., *Journal of the Acoustical Society of America*, vol. 121, pp. 648-56, 2007
9. Emmer, M, et al., *IEEE Trans Ultrason Ferroelectr Freq Control*, vol. 56, pp. 2370-9, 2009
10. van Neer, PL, et al., *IEEE Trans Ultrason Ferroelectr Freq Control*, vol. 57, pp. 455-68, 2010
11. Helfield, BL, et al., *Journal of the Acoustical Society of America*, vol. 133, pp. 1158-68, 2013

Acoustic bubble sorting of ultrasound contrast agents

Tim Segers, Nico de Jong and Michel Versluis*

*Physics of Fluids Group,
MIRA Institute of Biomedical Technology and Technical Medicine,
and MESA+ Institute of Nanotechnology
University of Twente, The Netherlands*

**Biomedical Engineering, Thoraxcentrum, Erasmus MC, Rotterdam, The Netherlands*

Ultrasound contrast agents resonate to the driving pressure pulse transmitted by the clinical ultrasound system. These systems operate at a narrow bandwidth optimized for the ultrasound transducer. Due to the large size distribution of commercially available UCA only a small selection of bubbles contributes to the echo signal. Thus the sensitivity in diagnostic imaging can be improved by narrowing down the size distribution. Moreover, a fully resonant bubble population of drug-loaded agents will be much more efficient in the local delivery to target cells. Finally, for the use of targeted molecular imaging with ultrasound it would be highly beneficial to discriminate adherent bubbles from freely floating ones, which can be achieved through spectral differences through a resonance shift of the adherent bubbles of a single size. For all these reasons it is of great interest to devise a method to inject only the resonant bubbles.

Here, we present a simple lab on-a-chip method to sort a population of microbubbles on-chip using a traveling ultrasound wave. A bubble in a traveling pressure wave experiences a net acoustic radiation force that pushes the bubble in the direction of wave propagation. The magnitude of the radiation force is bubble size-dependent through resonance; bubbles close to resonance experience the largest force. We use the radiation force to sort bubbles in a microfluidic channel made in polydimethylsiloxane (PDMS) with an embedded piezo transducer. The use of a low-pressure travelling continuous ultrasound wave allows for a finite net displacement of the bubbles during multiple cycles, whereas the ultrasound frequency allows for size-selectivity through resonance.

The contrast agent suspension is hydrodynamically focused between two co-flows to produce a bubble train with large enough spacing between the bubbles to minimize bubble-bubble interactions (Fig. 1). Figure 2 shows the measured displacement for contrast agent bubbles (BR-14) of different sizes sorted in a 2 MHz traveling ultrasound wave. The solid lines shows the displacement modeled by the Marmottant model coupled to a translation model incorporating the instantaneous radiation force, the drag force and the added mass force. The modeled displacement is in good agreement with the experimental data for typical shell parameters adapted from literature. The bubbles are sorted by their acoustic property rather than to their size, which can be directly observed from the scatter of data in the

figure; two bubbles having the same size can have a different surface phospholipid concentration resulting in a very different acoustical behavior.

The sorted bubbles were harvested from the chip and characterized by scattering and attenuation measurements over a frequency range from 0.7 MHz to 5.5 MHz and for acoustic pressures of 10, 25, 50 and 100 kPa, see Fig. 3. A comparison will be presented between scatter and attenuation measurements of native BR-14 bubble populations and the acoustically sorted agent. The scatter and attenuation results of the enriched agent shows a stronger resonance behavior and the correlation of the echoes from the enriched population was significantly greater confirming that the acoustic response of the sorted agent is much more homogeneous than that of the native agent. The proposed sorting strategy is highly efficient for the injection of a smaller dose, yet highly resonant, enriched bubble suspension for preclinical small animal imaging, for targeted molecular imaging using ultrasound, and for drug and gene delivery applications.

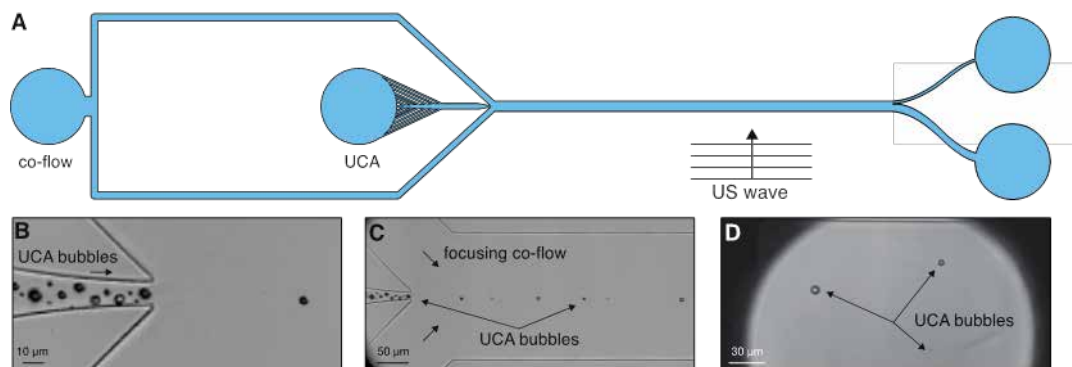


Figure 1: Acoustic bubble sorter for the sorting of UCAs. (A) shows the design. A microbubble suspension is hydrodynamically focused between two liquid co-flows (B) shows the formation of a bubble train (C). (D) A traveling acoustic wave pushes the bubbles in vertical direction downstream of the channel.

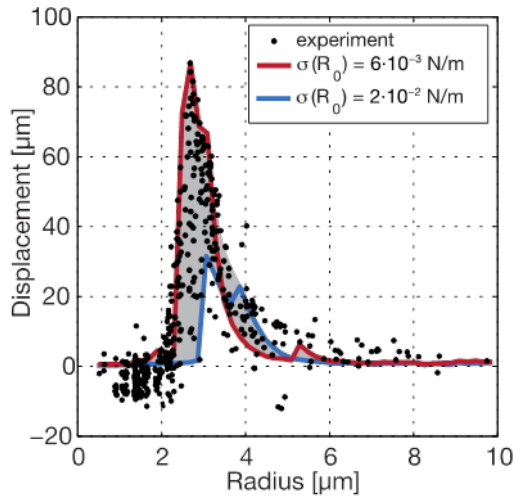


Figure 2: Experimentally obtained displacement of UCA bubbles as a function of the bubble size (dots). The red line shows the modeled displacement of coated bubbles with an initial surface tension of 6×10^{-3} N/m and the blue line shows the modeled displacement for a initial surface tension of 2×10^{-2} N/m. Varying the initial surface tension between these two values (gray area) show excellent agreement with the measured displacement.

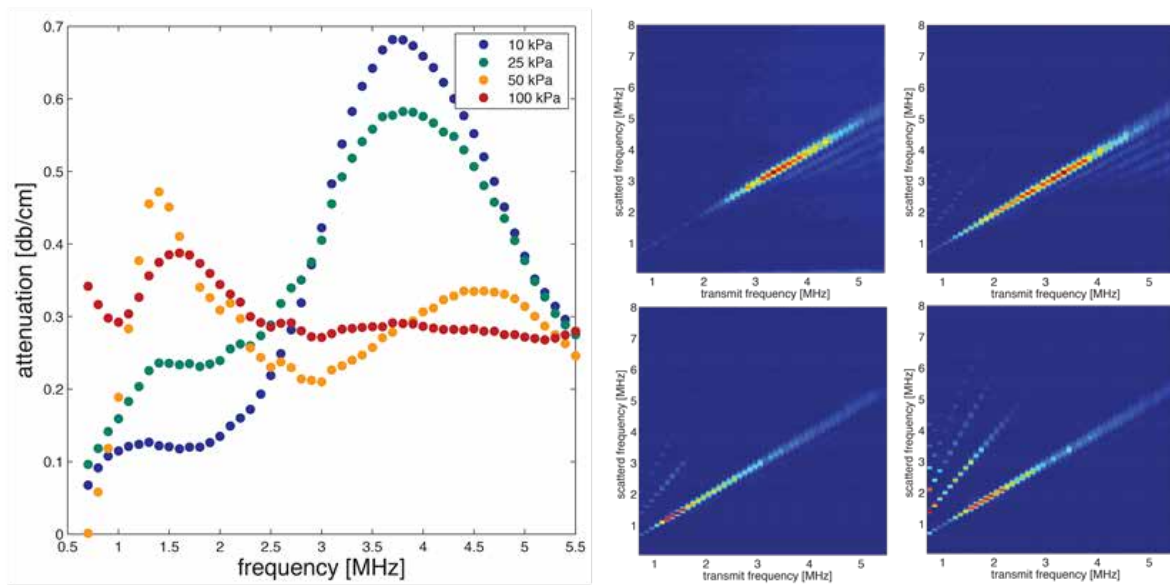


Figure 3: Frequency-dependent attenuation and scattering of the acoustically sorted agent measured at pressures of 10, 25, 50, and 100 kPa.

Stable nonlinear dynamics of free-floating lipid-coated microbubbles

Ying Luan¹, Guillaume Renaud¹ and Nico de Jong^{1,2}

¹Biomedical Engineering Thoraxcenter, Erasmus Medical Center, Rotterdam, the Netherlands

²Acoustical Wavefield Imaging, Delft University of Technology, the Netherlands

Background

Lipid-coated microbubbles have been used extensively for contrast-enhanced ultrasound imaging and have been proposed for ultrasound-mediated drug delivery. The stability of the microbubbles maintained by the lipid coating is crucial for the diagnostic usage. However, the shedding of lipids and subsequent destruction of microbubbles is essential for the therapeutic purpose. Single microbubble characterizations found that the subsequent acoustic response of single microbubbles can be altered by microbubble dissolution and lipid shedding [1-3]. We present a statistical study of the stability of the dynamic response of single free-floating microbubbles. Forty two short modulation sine bursts at 1 MHz were applied to each microbubble, and the corresponding 42 dynamic responses were measured with an acoustical camera [4].

Materials and Methods

Two focused ultrasound field was established using a 30 MHz probing wave (200 kPa peak amplitude) and a 1 MHz modulation sine wave (25, 100 or 200 kPa). For each recording, a long sine burst as a probing wave (800 μ s duration) and 42 modulation sine bursts (10 μ s duration, 3 μ s interval) were sent simultaneously. A second 30 MHz center-frequency transducer was employed to collect the signal scattered from single microbubbles (1:1,000,000 dilution in 250 mL water tank) passing through the transmitted 30 MHz focused beam. A thousand responses of single free-floating DSPC-based homemade microbubbles were measured at each acoustic pressure. Parameters obtained from the 42 consecutive modulation bursts were calculated and compared. The parameters include radial strain at fundamental frequency (R_f) and the second/third harmonic frequency (R_{2f} , R_{3f}), the ratio of radial excursion in expansion over that in compression (EoC) and the dc offset [5] in the time-domain response .

Results

The present data shows very minor variations when excited 42 times by the same 1 MHz sine burst for all the applied pressures. Because of the stable vibrational response of microbubbles along the 42 excitations, all parameters derived were averaged 42 times and the results are illustrated as follows. First, R_{2f} (Figure 1 left) and R_{3f} (Figure 1 right) increase with R_f until a plateau is reached at the R_f ~30%. Second, the dc offset increases monotonically with the radial strain at the fundamental frequency

R_f (Figure 2 left). EoC varies with R_f (Figure 2 right) - microbubbles tend to exhibit symmetrical oscillations at low radial strain ($R_f < 5\%$); compression dominant oscillations at moderate radial strain ($10\% < R_f < 20\%$), and expansion dominant oscillations at large radial strain ($R_f > 20\%$).

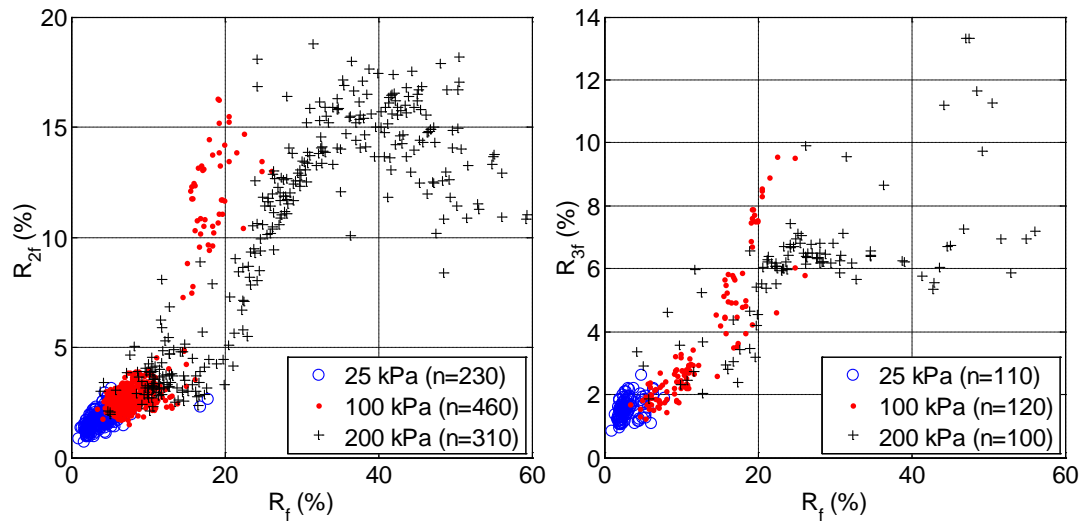


Figure 1: Left: radial strain at the second harmonic frequency (R_{2f}); Right: radial strain at the third harmonic frequency (R_{3f}) as a function of radial strain at the driving frequency (R_f). n indicates the number of microbubbles selected.

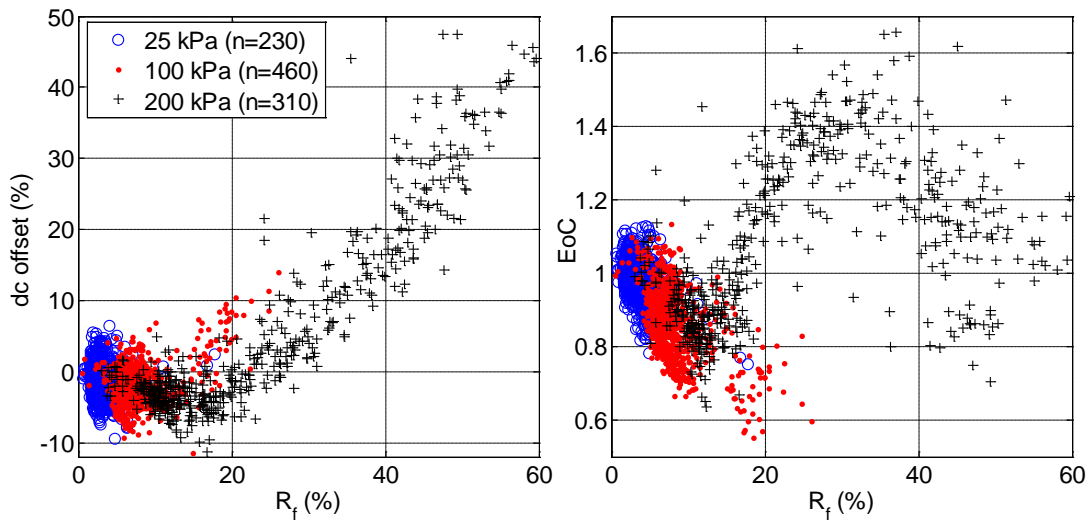


Figure 2: Left: dc offset in the radial response as a function of radial strain at the fundamental frequency (R_f), and Right: the ratio of radial excursion in expansion over that in compression (EoC) as a function of R_f .

Conclusions

This *in vitro* study demonstrates the stability of the dynamic radial response of free-floating microbubbles exposed to 42 successive 10 μ s excitations at 1 MHz with a peak pressure of 25 to 200 kPa observed within 800 μ s. This is crucial for applications like diagnostic imaging. The nonlinearity (R_{2f} , R_{3f} , dc offset) and asymmetry (EoC) of oscillations increase with the radial strain at the driving frequency (R_f), but show a plateau for a radial strain of ~40% and ~20% for R_{2f} and R_{3f} , respectively.

Acknowledgement

The authors thank Tom Kokhuis for providing the microbubble samples. This work was supported by Dutch Heart Foundation project PARISk (Grant No. 01C-202) and European Union FP7 project SonoDrugs (3C).

References

1. Borden, M.A., et al., Influence of lipid shell physicochemical properties on ultrasound-induced microbubble destruction. *Ieee Transactions on Ultrasonics Ferroelectrics and Frequency Control*, 2005. 52(11): p. 1992-2002
2. Thomas, D.H., et al., The acoustic signature of decaying resonant phospholipid microbubbles. *Phys Med Biol*, 2013. 58(3): p. 589-99
3. Marmottant, P., et al., A model for large amplitude oscillations of coated bubbles accounting for buckling and rupture. *Journal of the Acoustical Society of America*, 2005. 118(6): p. 3499-3505.
4. Renaud, G., et al., An "acoustical camera" for *in vitro* characterization of contrast agent microbubble vibrations. *Applied Physics Letters*, 2012. 100(10)
5. Sijl, J., et al., "Compression-only" behavior: a second-order nonlinear response of ultrasound contrast agent microbubbles. *J Acoust Soc Am*, 2011. 129(4): p. 1729-39

Temporal aspects of membrane permeability induced by cavitating microbubbles

Bart Lammertink¹, Roel Deckers¹, Gert Storm², Chrit Moonen¹, Clemens Bos¹

¹Division Imaging, University Medical Center Utrecht, The Netherlands

²Pharmaceutical Sciences, Utrecht University, The Netherlands

Introduction

Therapeutic ultrasound (US) has been shown to facilitate intracellular delivery of drugs or genes that are not readily taken up by cells. However, there is no consensus on the underlying mechanism [1]. One of the unknown aspects of US induced internalization is the time during which the cell membrane is permeable for e.g. low molecular weight drugs. Previous studies show contradicting results, ranging from seconds [2] up to 8 hours [3] of increased permeability. In this study, the temporal window of US-mediated membrane permeability of human breast cancer cells was investigated.

Methods

MDA-MB-468 (ATCC) cells were grown in DMEM + 10% FBS. Two days before US experiments, cells were cultured in OptiCells (Thermo Scientific). Sytox Green was used as a marker of membrane permeability. In each OptiCell, four regions were sonicated in the presence of 1.4×10^7 microbubbles/ml (SonoVue, Bracco), and after a certain time interval ($t = -30$ min, -1, -2, -3, and -24 hours), fresh medium containing Sytox Green and microbubbles was added. Next, two more regions were sonicated ($t=0$) as a positive control. Cells were sonicated at 1.5 MHz, 1 kHz PRF, 10% DC, 1.0 MPa p-p for 5 seconds in a 37°C water bath. Bright light and fluorescence images of the sonicated areas were taken before and after sonication, and cells were counted using ImageJ. Twenty-four hours post-sonication, viability of (non-)sonicated cells was assessed using an MTT-assay.

Results

Compared to the control area, all time intervals show increased uptake of Sytox Green after ultrasound exposure (Fig. 1).

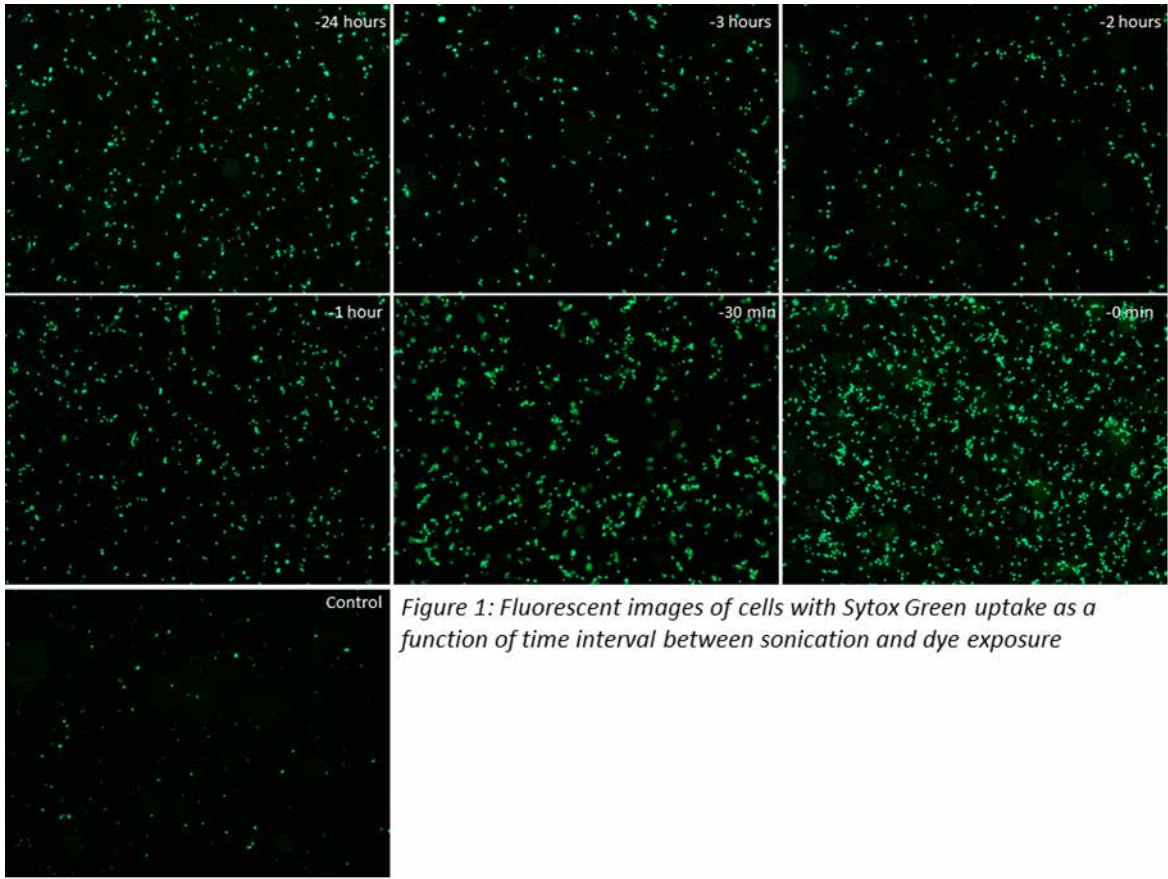


Figure 1: Fluorescent images of cells with Sytox Green uptake as a function of time interval between sonication and dye exposure

However, after 1 hour the time-interval related decrease in Sytox Green-positive cells does not continue and similar numbers of stained cells are seen for timepoints -2, -3 and -24 hours (Figure 2). The number of Sytox Green positive cells when sonicated in the presence of the dye ($t=0$) was used as the positive control and set at 100%.

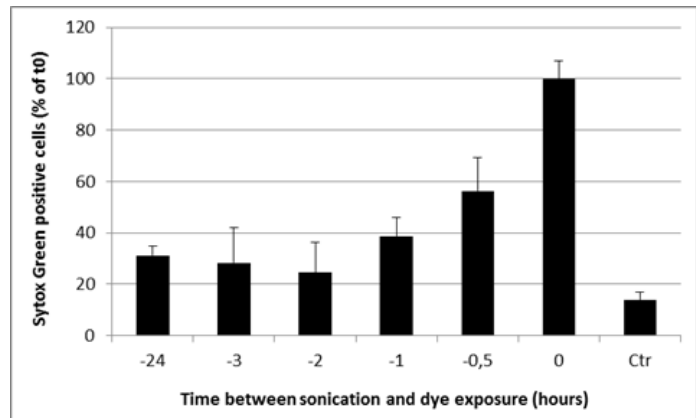


Figure 2: Cells with Sytox Green uptake as a percentage of positive control ($t=0$).

When cells are exposed to the dye 30 minutes after ultrasound sonication, 55% of the cells that would have taken up the dye at $t=0$ are Sytox Green positive. This percentage decreases to 40% for $t= -1$ hour and 25% for $t= -2, -3$ and -24 hours.

With increasing time interval between sonication and dye exposure, the percentage of Sytox Green positive cells does not decrease to the value of the control cells. This observation suggests irreversible membrane damage, which is confirmed by the viability assay (Fig. 3).

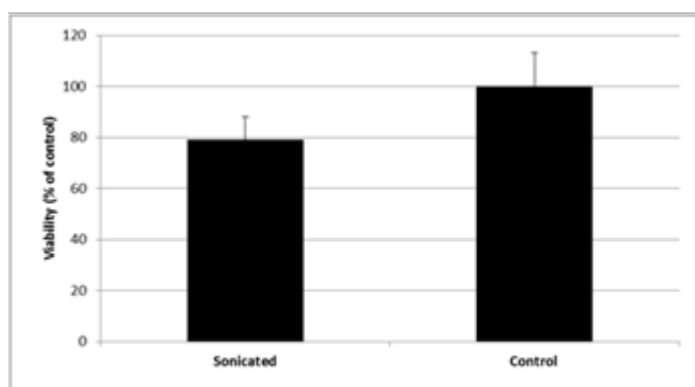


Figure 3: Viability of sonicated cells, compared to unsonicated cells.

Conclusions

Up to 1 hour post-sonication there remains intracellular uptake by reversible membrane permeabilization of the cell-impermeable dye Sytox Green. After 1 hour, the dye uptake seems to be related to irreversible membrane damage. This is supported by the viability assay, which shows reduced cell viability after ultrasound exposure.

References

1. V. Frenkel, *Adv Drug Deliv Rev*, 2008
2. S. Mehier-Humbert et al., *J Control Release*, 2005
3. A. Yudina et al., *Mol Imaging Biol*, 2010

Sonoporation dynamics at different acoustic pressures

*Ilya Skachkov¹, Tom J.A. Kokhuis^{1,2}, Ying Luan¹, Antonius F.W. van der Steen^{1,2},
Nico de Jong^{1,2}, Klazina Kooiman¹*

¹*Dept. of Biomedical Engineering, Thoraxcenter, Erasmus MC, Rotterdam, the Netherlands*

²*Interuniversity Cardiology Institute of the Netherlands, Utrecht, the Netherlands*

Background

Vibrating microbubbles (MB) can increase cell membrane permeability, also known as sonoporation. This can be reversible or irreversible. When irreversible, it causes severe cell damage and death [1]. Different therapeutic approaches may require different grades of sonoporation and there is always a balance between effectiveness and cell damage. The aim of this study was to investigate how targeted MB (tMB) and non-targeted MB (ntMB) effect cell membrane permeability at different ultrasound (US) settings. We studied sonoporation dynamics real-time by correlating propidium iodide (PI) uptake dynamics to MB behaviour.

Methods

Human umbilical vein endothelial cells were cultured in OptiCells as previously reported [2]. Lipid-coated MB were made by sonication [3]. For tMB, CD31-antibody was conjugated via avidin-biotin bridging [4]. MB were added 5 min prior to sonication at a ratio of 4 MB per cell. Sonoporation dynamics were studied at 150 kPa (n=1), 300 kPa (n=3) and 500 kPa (n=3). A 1 MHz single pulse was applied with varying amount of cycles (1,000, 2,000, 5,000, 1,0000, and 20,000 cycles). MB dynamics were recorded at 2,000 fps (RedLake, MotionPro, San Diego, CA). PI was used to assess cell membrane permeability and studied for 3 min after insonification (5 sec interval) with AxioCam MRc camera (Carl Zeiss B.V., Sliedrecht, the Netherlands). We distinguished between fast and slow PI uptake by defining fast uptake as the fluorescence intensity signal reaching the plateau within 5 seconds after US application. Slow PI uptake was defined as the fluorescence intensity signal reaching the plateau between 5 and 180 seconds after US application. Cell viability was assessed 1 hour after ultrasound treatment by adding Calcein-AM 30 min after US application. A minimum of 2,000 cells for each condition were analysed.

Results

Figure 1 shows that there was no difference in the sonoporation efficiency between ntMB and tMB insonified at 150 kPa for all studied amount of acoustic cycles. At 300 kPa, we found a significant difference between ntMB and tMB for 1,000 and 2,000 cycles; the tMB induced more sonoporation. tMB also caused higher sonoporation efficiencies at 500 kPa for the highest amount of cycles, namely 20,000 cycles. When cells were sonoporated, we observed different nuclear PI uptake dynamics (see figure 2A + 2B), ranging from fast (defined as up to 5 sec after US application) to slow (defined as 5-180 sec after US application) increases in nuclear PI uptake. This could suggest different size and amount of cell membrane pores formed. The studies at lower acoustical pressures, showed less fast PI uptake for both tMB and ntMB. At 150 kPa and 20,000 cycles fast PI uptake accounted for 17.6% of all sonoporation events for tMB and 7.4% for ntMB, while at 1,000 cycles this was 12% and 11%. At 500 kPa, this was $27.7\pm 5.4\%$ for tMB and $19.3\pm 4.1\%$ for ntMB at 20,000 cycles and 11% at 1,000 cycles for both tMB and ntMB. At lower acoustic pressures, we expect less irreversible sonoporation. This suggests that the fast PI uptake is correlated to irreversible sonoporation. The cell viability assay revealed that cell death was lower than the amount of sonoporated cells, for example $38\pm 5.2\%$ for tMB and $20\pm 3.1\%$ for ntMB at 20,000 cycles and 500 kPa, thereby supporting that partial reversible sonoporation did occur.

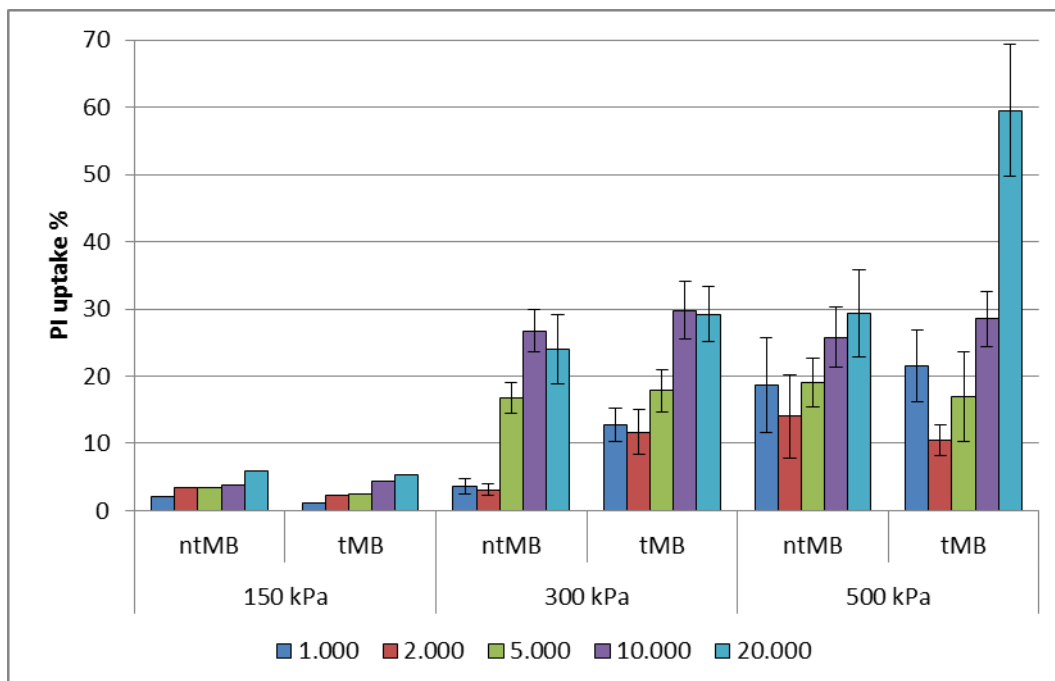


Figure 1. Propidium iodide uptake by HUVEC cells after ultrasound and microbubble treatment.

The MB dynamics revealed that MB displacement was high in the vicinity of cells with fast PI uptake and was much lower for cells with slower PI uptake. This suggests a direct correlation between MB activity and reversible or irreversible sonoporation. We also observed that cells were not sonoporated when no MB were in their vicinity.

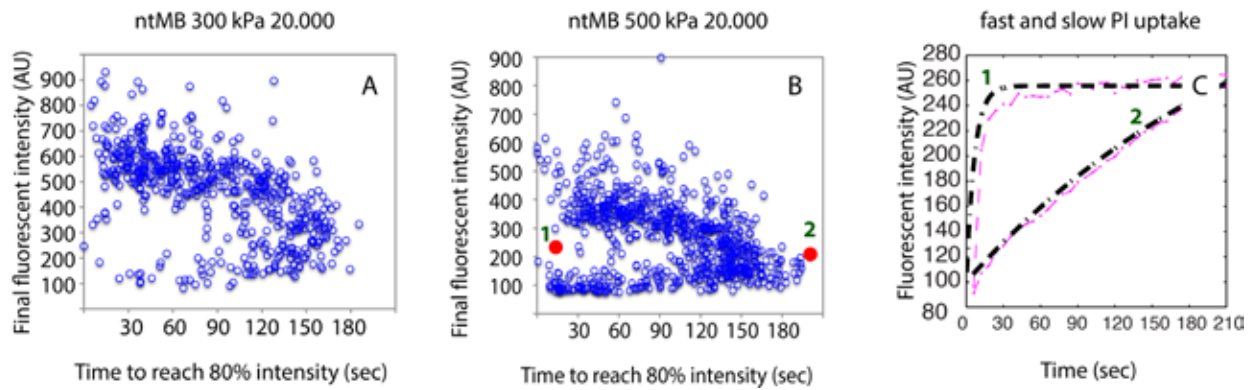


Figure 2: Nuclear propidium iodide (PI) fluorescence intensity dynamics upon insonification for ntMB. A+B: time PI reaches 80% of maximum intensity for individual cells at two different acoustic pressures; C: example of PI intensity increase for cells labelled 1 and 2 in B.

Conclusion

In conclusion, this study shows the feasibility of studying sonoporation dynamics real-time by correlating PI uptake dynamics to MB behaviour. This will contribute to unravelling the mechanism of sonoporation and can be used to improve drug delivery.

Acknowledgements

Authors would like to thank, Michiel Manten, Robert Beurskens and Geert Springeling from the department of Biomedical Engineering, Erasmus MC for their assistance.

References

1. Hernot et al, *Adv Drug Deliv Rev* 2008, 60(10):1153
2. Kooiman et al, *J Control Release* 2011, 154:35
3. Klibanov et al, *Invest Radiol*, 2004, 39:187; [4] Lindner et al, *Circulation*, 2001, 104:2107

***In vivo* acoustic imaging of large albumin stabilized microfluidic-produced microbubbles**

*Ali H Dhanaliwala**, *Adam J Dixon**, *Dan Lin**, *Alexander L Klibanov[^]*, *John A Hossack**

**Department of Biomedical Engineering. [^] Department of Medicine – Cardiovascular division
University of Virginia, Charlottesville, VA, USA*

Introduction

Microfluidic production of stable microbubbles for ultrasound contrast exhibits precise control over microbubble diameter with the penalty of low production rate. Conversely, increased production rates can be achieved but at the cost of microbubble stability. To overcome these issues, we propose microbubble production directly within the vasculature via a catheter-sized microfluidic device. *In situ* production may eliminate the need for high microbubble production rates, as fewer microbubbles are lost during administration and circulation; as well as the need for long stability, as the microbubbles need only survive a short distance from the catheter tip to the site of interest. Furthermore, by intentionally producing short-lived microbubbles, larger diameters can be explored since microbubble dissolution can be relied upon to reduce the risk of gas emboli. As a step towards this goal, we injected microfluidic produced microbubbles directly into a mouse tail vein in order to investigate whether a microfluidic device can produce microbubbles of sufficient quantity and longevity to produce ultrasound contrast.

Methods

Microbubbles were fabricated using a flow-focusing microfluidic device (FFMD) and comprised 100% nitrogen gas stabilized with 3% bovine serum albumin (BSA) and 10% dextrose[1]. The microbubbles were injected into wild-type C57 Bl/6 mice (n = 18 imaging sessions) by directly connecting the output channel of the FFMD to a previously placed tail vein catheter for 10 s. There were no washing, concentrating, or storage steps prior to administration. Short-axis images of the right and left ventricle were acquired with a high frequency small animal scanner. Microbubble diameter and production rate within the FFMD were monitored optically with a high speed camera connected to an inverted microscope.

Results and Discussion

Microbubble with diameters between 10 and 20 μm and with production rates between 200,000 and 800,000 microbubble/s were all successfully imaged (Fig 1). No correlation was observed between microbubble diameter, production rate, and image intensity. Microbubbles were observed in both the right and left ventricles; however, on average, image intensity in the left ventricle was 18% of the

intensity observed in the right ventricle. The median rise time, duration, and decay time within the right ventricle were 2.9, 21.3, and 14.3 s, respectively. Each mouse was imaged three times with one hour separating the first and second injection and one week separating the second and third injection. All mice survived the procedure with no obvious issues respiration or heart rate issues.

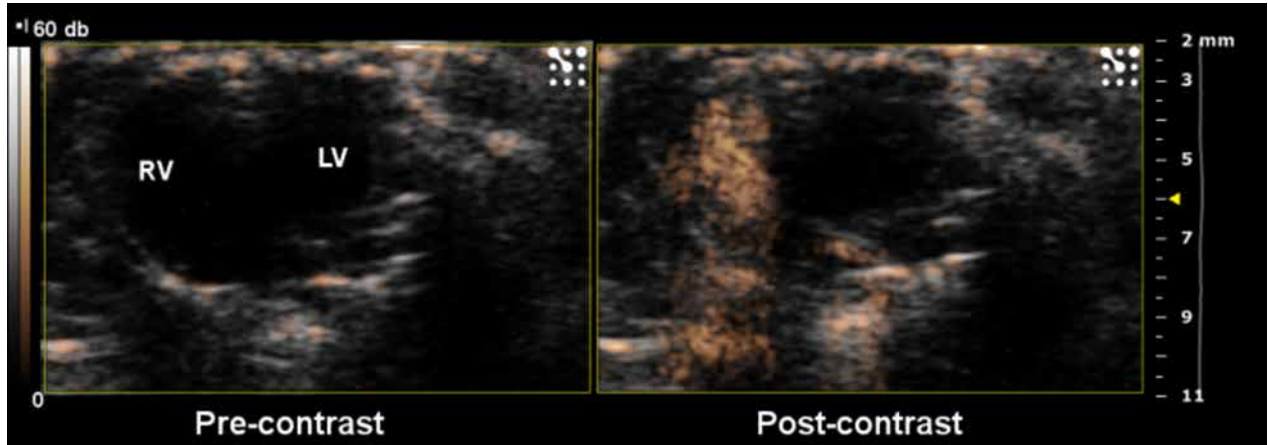


Figure 1: Pre and post-contrast images of the right (RV) and left (LV) ventricle following injection of 14 μm diameter microbubbles produced at a rate of 714,000 microbubbles/s. Images were acquired at 12.5 MHz, 10% power, and 60 dB dynamic range. The nonlinear contrast mode (orange) is overlaid atop the B-mode (gray).

Conclusions

Microfluidic produced microbubbles provided adequate image contrast *in vivo* despite low production rates and low stability. Furthermore, we were able to utilize large diameter microbubbles without any obvious physiological effects. Overall, we demonstrated a successful first step towards our goal of microbubble production directly within the vasculature.

References

J. L. Chen, A. H. Dhanaliwala, A. J. Dixon, A. L. Klibanov, and J. A. Hossack, "Synthesis and characterization of transiently stable albumin-coated microbubbles via a flow-focusing microfluidic device," *Ultrasound Med. Biol.*, vol. In Press, Sep. 2013

Recruitment of endocytosis in ultrasound-mediated drug delivery: A real-time study

*Marc Derieppe¹, Katarzyna Rojek¹, Baudouin Denis de Senneville^{1,2}, Clemens Bos¹,
Chrit Moonen¹*

¹*Imaging Division, University Medical Center Utrecht, Utrecht, the Netherlands*

²*IMB, UMR 5251 – CNRS – Université Bordeaux 1 – INRIA, Bordeaux, France*

Introduction

Sonoporation of cell membrane by means of ultrasound (US) waves, usually in the presence of microbubbles, proves to be an asset for local drug delivery strategies since it may locally facilitate the uptake of anticancer agents. However, transport mechanisms recruited in uptake by the cells after exposure to US remain unclear. Previous studies showed that endocytosis was involved in the uptake of macromolecules [1] and small molecules (MW lower than 4 kDa) [2]; however, the observations were made at a single, fixed, time point. Here, we propose to use Fibered Confocal Fluorescence Microscopy (FCFM) [3][4] to evaluate in real-time the involvement of clathrin- and caveolin- mediated endocytosis upon US exposure by using endocytosis inhibitors.

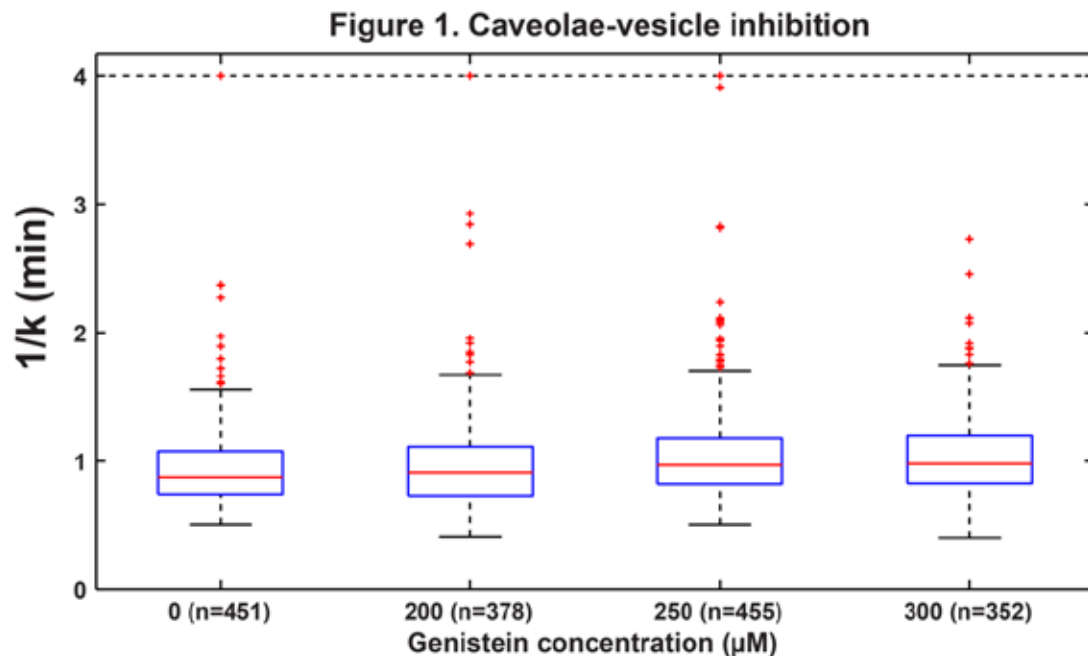
Methods

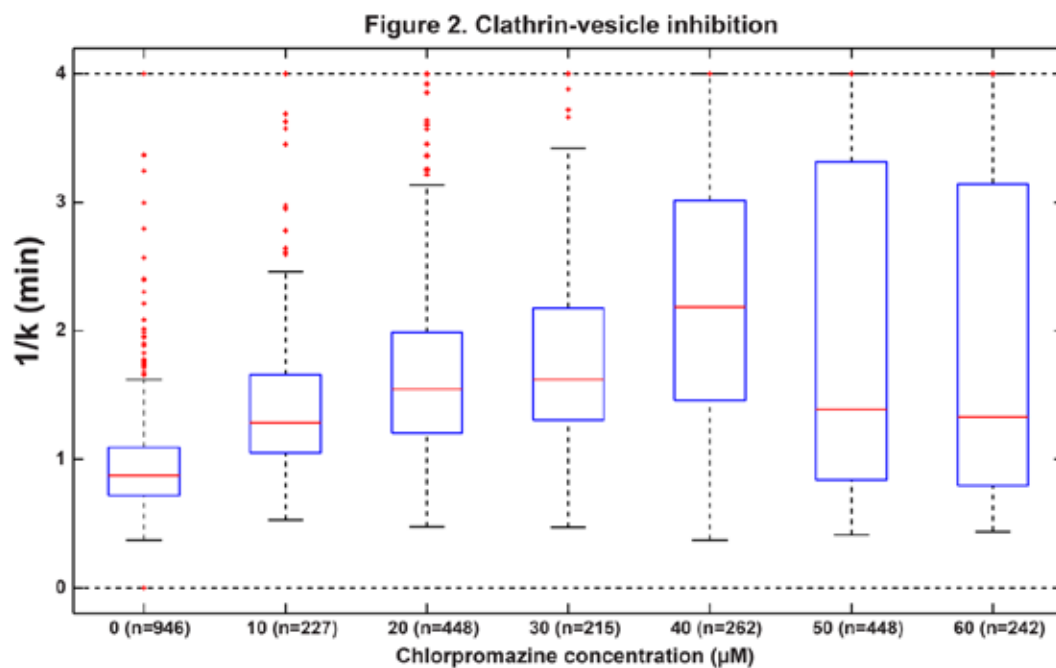
C6 rat glioma cells were preincubated for 30 minutes with either chlorpromazine (CTZ), an inhibitor of clathrin-mediated endocytosis, or genistein (GEN), inhibiting the caveolin-mediated pathway. Inhibitor cytotoxicity was assessed, varying concentration (CTZ from 10 to 60 μ M - GEN from 200 to 300 μ M) and incubation time (30 minutes, but also 1.5 and 3 hours, to control for increased exposure for the duration of the experiment), via XTT viability assay. For the sonoporation experiments, uptake of SYTOX Green fluorescent dye was triggered with 1.4 MHz US, (0.5 MPa p-p, Duty Cycle 10%, Pulse Repetition Frequency 1kHz), in the presence of Sonovue at 20 microbubbles per cell. After detecting and tracking the nuclei, uptake in each nucleus was monitored in real-time using FCFM, as described in [3] and [4], and uptake rates were obtained from fitting a two-compartment model to the fluorescence intensity data. Statistical analyses were performed using Mann-Whitney test; results are expressed as median (interquartile range).

Results

Cells incubated with endocytosis inhibitors expressed a lower SYTOX Green uptake rate k after sonoporation. First, GEN inhibition resulted in a shallow but significant (MW, $p < 0.05$) reduction of SYTOX Green uptake rate $1/k$ from 52.4s (20.1s, $n=451$) (no treatment) to 0'54" (0'22", $n=378$), 0'58" (0'21", $n=455$) and 0'58" (0'22", $n=352$) for 200 μ M, 250 μ M and 300 μ M of GEN, respectively (Fig 1).

CTZ had a higher inhibitory effect on SYTOX Green uptake rate than GEN. A significant (MW, $p < 0.05$) uptake rate reduction was observed from 0'52" (0'22", $n=946$) without treatment to 1'17" (0'36", $n=227$), 1'32" (0'46", $n=448$), 1'37" (0'52", $n=215$), and 2'11" (1'33", $n=262$) for 10 μ M, 20 μ M, 30 μ M, 40 μ M. CTZ had a higher inhibitory effect on SYTOX Green uptake rate than GEN. A significant (MW, $p < 0.05$) uptake rate reduction was observed from 0'52" (0'22", $n=946$) without treatment to 1'17" (0'36", $n=227$), 1'32" (0'46", $n=448$), 1'37" (0'52", $n=215$), 2'11" (1'33", $n=262$) for 10 μ M, 20 μ M, 30 μ M, and 40 μ M of CTZ, respectively (Fig. 2), indicating that clathrin-mediated endocytosis was recruited in sonoporated cells. An abrupt increase of the uptake rate was noticeable at CTZ concentrations higher than 40 μ M, suggesting a loss of cell membrane integrity: 1'23" (2'28", $n=448$) and 1'20" (2'21", $n=242$) for 50 μ M and 60 μ M, respectively.





Conclusion

Model drug uptake kinetics of C6 cells after sonoporation can be studied in real-time using FCFM. A reduction of US-mediated uptake rate was observed in response to GEN and especially CTZ incubation. The data provide evidence for involvement of, in this case primarily clathrin-mediated, endocytosis in US-mediated uptake of drugs.

References

1. Meijering *et al.*, *Circ. Res.*, 2009
2. Zeghimi *et al.*, *ESUCI*, 2013
3. Derieppe *et al.*, *Mol. Imaging Biol.*, 2012. [4] Derieppe *et al.*, *EMIM*, 2013

Development of integrin $\alpha\beta3$ -targeted microbubbles based on clinically available ultrasound contrast agent

Kentaro Otani

*Department of Regenerative Medicine and Tissue Engineering,
National Cerebral and Cardiovascular Center Research Institute, Suita, Japan*

Background and Aim

Phagocytosis of apoptotic cells is carried out through bridging of phosphatidylserine (PS)-expressing apoptotic cells and integrin $\alpha\beta3$ -expressing phagocytes with lactadherin. The aim of this study was to examine whether microbubbles targeted to integrin $\alpha\beta3$ could be produced by conjugating a PS-containing clinically available ultrasound contrast agent with lactadherin (**Figure 1**).

Methods

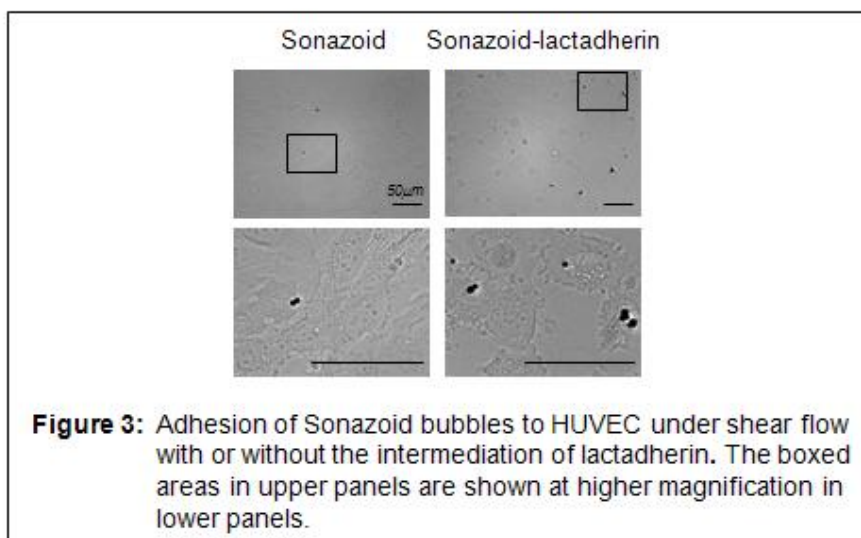
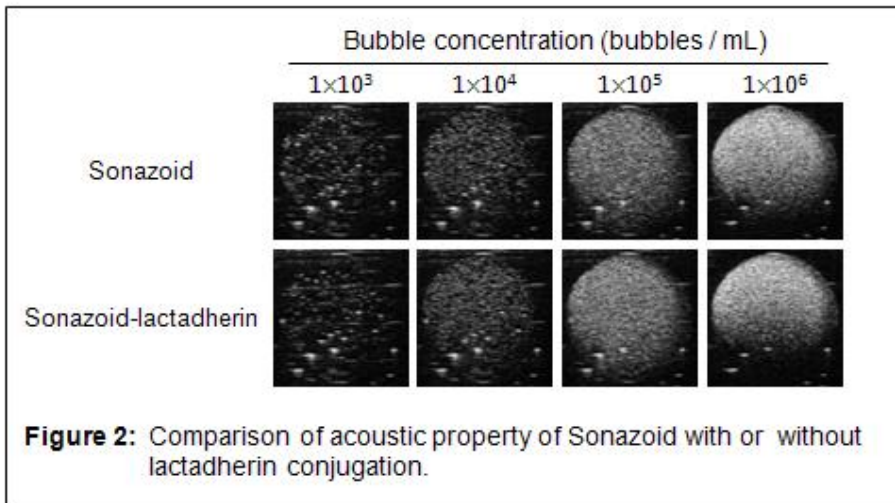
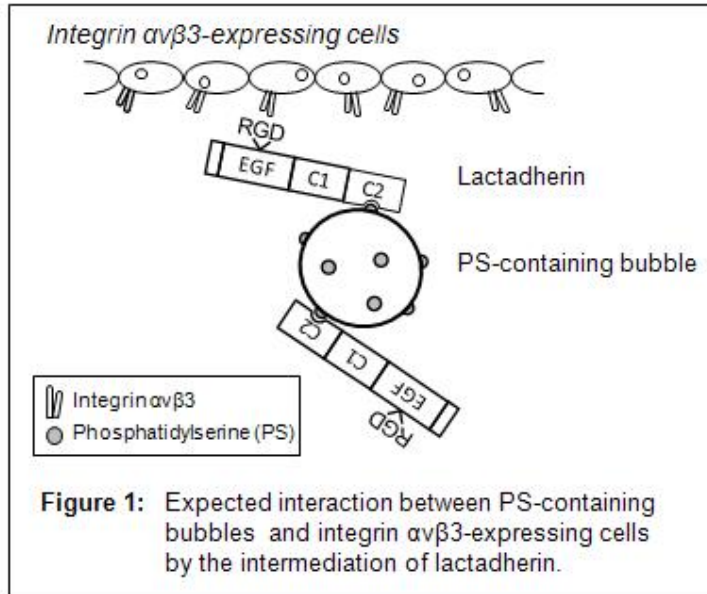
PS-containing perfluorobutane-filled microbubbles (Sonazoid) were incubated with R-phycoerythrin (PE) labeled-lactadherin, and the presence of PE-positive bubbles was examined by FACS analysis. Secondly, the attachment of lactadherin to integrin $\alpha\beta3$ -expressing cell (human umbilical vein endothelial cell; HUVEC) was also examined by FACS analysis. Finally, the adhesion of Sonazoid bubbles to HUVEC was examined using a parallel plate flow chamber. The number of adherent bubbles with or without the intermediation of lactadherin was compared.

Results

By increasing the dose of lactadherin, the number of PE-positive Sonazoid bubbles became larger. It was noteworthy that the mean diameter of Sonazoid bubbles did not change even after conjugating with lactadherin (2.90 ± 0.04 vs. 2.81 ± 0.02 μm). Furthermore, the acoustic property of Sonazoid bubbles was not influenced by the conjugation with lactadherin (**Figure 2**). The binding between lactadherin and HUVEC was also confirmed by the FACS analysis. The parallel plate flow chamber study revealed that the number of Sonazoid bubbles adherent to HUVEC was increased about five times by the intermediation of lactadherin (12.1 ± 6.0 to 58.7 ± 33.1 bubbles) (**Figure 3**).

Conclusion

Our study demonstrated that the development of integrin $\alpha\beta3$ -targeted Sonazoid bubbles could be feasible by the intermediation of lactadherin. Because integrin $\alpha\beta3$ is well-known to play a key role in angiogenesis, the lactadherin-bearing Sonazoid bubbles has feasibility as a clinically translatable targeted ultrasound contrast agent for angiogenesis.



Endocardial border delineation capability of a multimodal polymer-shelled contrast agent

Malin K. Larsson^{a,}, Matilda Larsson^{a,b}, Greg Nowak^c, Gaio Paradossi^d, Lars-Åke Brodin^{a,c}, Birgitta Janerot Sjöberg^{a,c}, Kenneth Caidahl^b, Anna Bjällmark^{a,b}*

^aDepartment of Medical Engineering, School of Technology and Health, KTH Royal Institute of Technology, Stockholm, Sweden

^bDepartment of Molecular Medicine and Surgery, Karolinska Institutet, Solna, Sweden

^cDepartment of Clinical Science, Intervention and Technology, Karolinska Institutet, Stockholm Sweden

^dDepartment of Chemical Sciences and Technologies, Università di Roma Tor Vergata, Rome, Italy

Background

A novel polymer-shelled contrast agent (CA) with high mechanical and chemical stability was recently developed [1]. In excess to its ultrasound properties, it also supports targeted and multimodal imaging [2-4]. Even though these new possibilities have the potential to lead to new methodologies and approaches for non-invasive diagnosis, it is important that the fundamental diagnostic features in contrast-enhanced ultrasound are preserved. The aim of this study was therefore to examine the clinical use of the polymer-shelled CA by analyzing the left ventricular endocardial border delineation capability in a porcine model. In addition, physiological effects due to CA injections were studied.

Methods

The endocardial border delineation capability was assessed in a comparative study, which included three doses (1.5 ml, 3 ml and 5 ml, [5x10⁸ MBs/ml]) of the polymer-shelled CA and the commercially available CA SonoVue[®] (1.5 ml, [2-5x10⁸ MBs/ml]). Ultrasound images of the left ventricle were evaluated manually by blinded observers (n=3) according to a 6-segment model, in which each segment was graded as 0=not visible, 1=barely visible or 2=well visible, as well as semi-automatically by a segmentation software. Furthermore, duration of clinically useful contrast enhancement and changes in physiological parameters were evaluated.

Results

For the highest dose of the polymer-shelled CA, the obtained segment scores, time for clinically sufficient contrast enhancement and semi-automatic delineation capability were comparable to SonoVue[®]. Moreover, neither dose of the polymer-shelled CA did affect the physiological parameters.

Conclusion

This study demonstrated that the polymer-shelled CA can be used in contrast-enhanced diagnostic imaging without influence on major physiological parameters.

References

1. G. Paradossi, F. Cavalieri, E. Chiessi, V. Ponassi, and V. Martorana, "Tailoring of physical and chemical properties of macro- and microhydrogels based on telechelic PVA," *Biomacromolecules*, vol. 3, pp. 1255-62, Nov-Dec 2002
2. T. B. Brismar, D. Grishenkov, B. Gustafsson, J. Harnmark, A. Barrefelt, S. V. Kothapalli, S. Margheritelli, L. Oddo, K. Caidahl, H. Hebert, and G. Paradossi, "Magnetite nanoparticles can be coupled to microbubbles to support multimodal imaging," *Biomacromolecules*, vol. 13, pp. 1390-9, May 14 2012
3. A. A. Barrefelt, T. B. Brismar, G. Egri, P. Aspelin, A. Olsson, L. Oddo, S. Margheritelli, K. Caidahl, G. Paradossi, L. Dahne, R. Axelsson, and M. Hassan, "Multimodality imaging using SPECT/CT and MRI and ligand functionalized ^{99m}Tc -labeled magnetic microbubbles," *EJNMMI Res*, vol. 3, p. 12, 2013
4. R. Villa, B. Cerroni, L. Vigano, S. Margheritelli, G. Abolafio, L. Oddo, G. Paradossi, and N. Zaffaroni, "Targeted doxorubicin delivery by chitosan-galactosylated modified polymer microbubbles to hepatocarcinoma cells," *Colloids Surf B Biointerfaces*, vol. 110, pp. 434-42, Oct 1 2013

A method for calculating acoustic pressure in the liver using linear measurements in water

Christina P. Keravnou, Maria-Louisa Izamis and Michalakis A. Averkiou

Department of Mechanical and Manufacturing Engineering, University of Cyprus, Nicosia, Cyprus

Introduction

Novel therapeutic methods such as sonoporation, sonothrombolysis and other recent gene and drug delivery techniques make use of the combined effects of ultrasound and microbubbles. The ultrasound pressure used in therapy varies according to the specific application and often nonlinear effects are encountered. The ratio of nonlinearity and attenuation parameters of the tissue of interest highly affects the delivered pressure during therapy sessions. In this work a method for calculating in-situ pressure in liver was developed and evaluated using the attenuation coefficient and linear water measurements. In addition, the range of validity of this method was examined with a nonlinear theoretical model.

Methods

Linear extrapolation method: The proposed linear extrapolation method was implemented using Eq. (1)

$$p = \frac{V_2}{V_1} p_l e^{-\alpha x}, \quad (4)$$

where p is the extrapolated in-situ pressure, V_2 is any transmit voltage, V_1 is the low transmit voltage used for linear measurements, p_l is the measured low amplitude pressure at the region of interest, α is the attenuation coefficient and x is the distance of the source from the region of interest. The method was validated by comparing the extrapolated values with actual measurements of the acoustic pressure after propagation through samples taken from ex-vivo machine perfused livers.

Theoretical Model: Nonlinear propagation and dissipation are competing phenomena since nonlinearity causes distortion to the wave by generating harmonics, while attenuation reduces the harmonics resulting from nonlinear effects. Nonlinear theory was used to find the range of validity of the extrapolation method, as Goldberg number (the nonlinearity–attenuation ratio, I) changes. Simulations were performed using a time-domain numerical solution of the KZK parabolic wave equation [1 – 2] for a medium gain source ($G= 6.7$) at 2 MHz.

Attenuation measurements: The porcine liver attenuation coefficient value that was required for Eq. (1) was measured in a water tank, using a C5-1 curve-linear array connected to a clinical imaging system (model: iU22, Phillips Medical Systems, Bothell, WA, USA). A large amplitude pulse (MI>1) was sent and after propagation through a container filled with water, the pulse was received by a 0.4 mm membrane hydrophone (Precision Acoustics Ltd, Dorchester, UK). The same procedure was repeated when porcine liver sample was placed in the container. Ultrasonic attenuation of porcine liver as a function of frequency was calculated via the difference of the spectra [Fig. 1(b)] of the two propagated pulses [Fig. 1(a)] at each harmonic component.

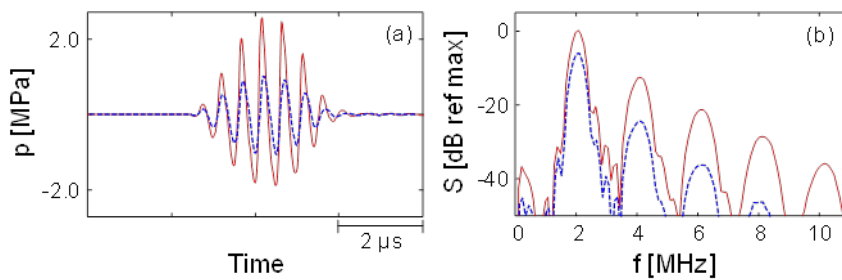


Figure 1: Time waveforms (a) and spectra (b) of a high amplitude pulse after propagation through water (solid line) and porcine liver (dashed line).

For tissues, the frequency-attenuation dependence may be approximated by a power law, where the exponent is assumed to be between 1 and 2 [3] depending on tissue's composition and biochemical environment [4]. The measured values of α for each f were fitted to Eq. (2),

$$a = a_0 f^n, \quad (5)$$

where a_0 is the attenuation coefficient at 1 MHz, and n is the power exponent for the tissue measured.

Tissue samples: The attenuation coefficient of ex-vivo machine perfused livers was measured. Porcine livers were procured from a local abattoir. Livers were flushed with 7L of ice cold Lactated Ringers through both the portal vein and hepatic artery. The organs were stored in ice and transported to the laboratory where they were connected to the machine perfusion system. The perfusion was monitored via Contrast Enhanced Ultrasound (CEUS) imaging. After 3 hours of perfusion a sample was carefully dissected from the organ while avoiding letting air in the vessels and used to perform the measurements.

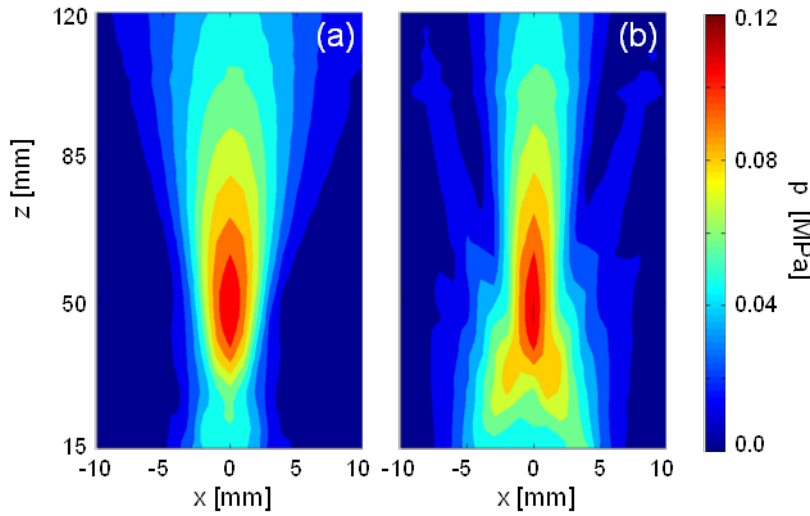


Figure 2: Measurements of low amplitude beam profiles of C5-1 probe; (a) scan plane and (b) elevation plane.

Linear lossless acoustic field measurements: The low amplitude acoustic field ($MI \leq 0.07$) produced by the C5-1 curve linear array was also measured to be used in Eq. (1). The measurements were taken in de-ionized water using a resolution of 3 mm in the axial direction and 1 mm in the transverse direction to create a two dimensional beam profile [Fig. 2]. Thus, the extrapolation method could be applied for any point in the field.

Results

The attenuation in Np/m as a function of frequency for porcine liver tissue in the range of 2 – 8 MHz is shown in Fig. 3. An attenuation coefficient (α_0) of 9.05 Np/m/MHz and an exponent (n) of 0.73 was calculated from the fit of attenuation measurements. The goodness of the fit using Eq. (2) was $R^2 = 0.99$.

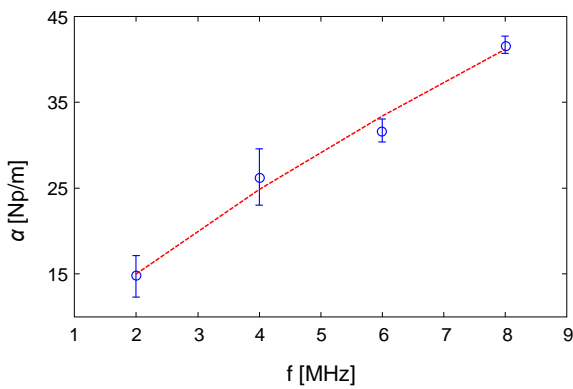


Figure 3: The attenuation (Np/m) as a function of frequency (MHz). The average of the three measurements is shown in circles (o), while the fit is shown in dashed line.

Figure 4 shows KZK simulations for different nonlinearity coefficients, $0 \leq N \leq 1.6$ ($N = \bar{x}/d$, where \bar{x} is the shock formation distance), for 2 different cases of attenuation ($\alpha = 4$ Np/m, $\alpha = 16$ Np/m). It was observed that as the Goldberg number (Γ) decreases, better agreement between the extrapolated values and the simulations is achieved.

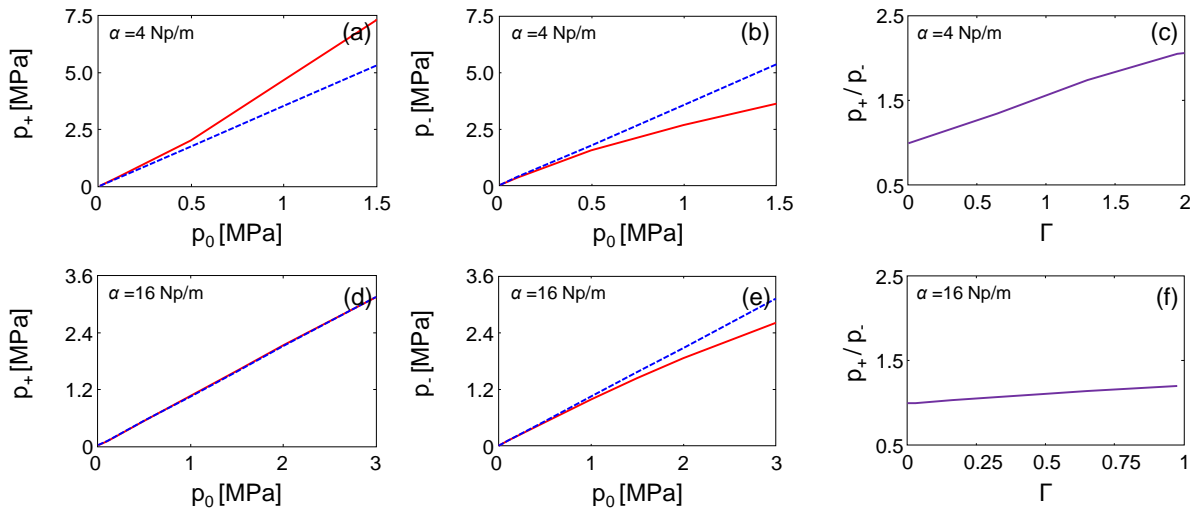


Figure 4: Comparison of extrapolated values (dashed line) and KZK simulations (solid line) for different source pressures and different attenuation coefficient. (a-b) $\alpha = 4$ Np/m, (d-e) $\alpha = 16$ Np/m. The effect of Γ on p_+/p_- is shown in (c-f).

Figure 5 shows the comparison between extrapolated and measured pressures. Larger deviations (>25%) between measurements and extrapolated values were observed at higher input voltages (>125V, >MI=2.0) where the pulses were very distorted due to nonlinear propagation. However, the method was accurate for the range of MIs that a diagnostic ultrasound operates (MI<1.9).

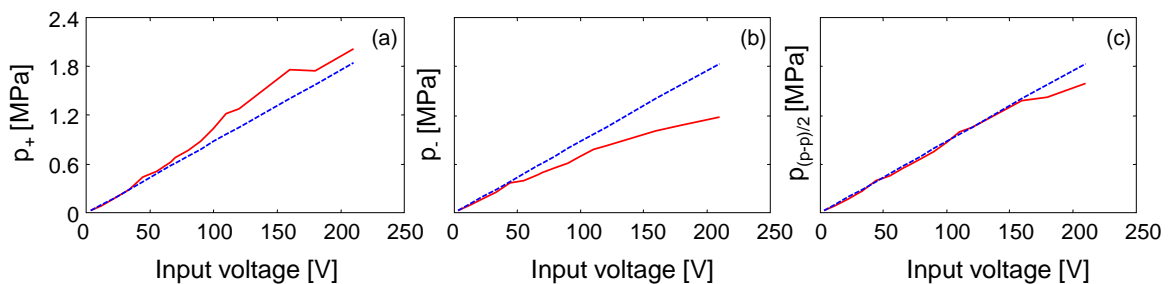


Figure 5: Comparison of extrapolated (dashed line) and measured pressures in porcine liver (solid line) for different amplitudes. Peak positive (a), peak negative pressure (b), and $p_{(p-p)/2}$ (c). The input voltages range (3 - 210 V) corresponds to MIs = 0.07 - 2.1.

Conclusions

A method for calculating in-situ pressure in tissues based on low amplitude measurements in water has been presented and validated. The method requires the attenuation coefficient of tissue. Porcine liver attenuation was accurately measured in the range of 2–8 MHz.

Extrapolated values of acoustic pressures in porcine liver were in good agreement with measurements in the range $0 \leq MI \leq 2.1$. From theoretical simulations of nonlinear propagation we have found that for Goldberg numbers up to about 1, where the p_+/p_- ratio is less than about 1.5, the method gives accurate estimates of the in-situ pressure.

Acknowledgements: This work was co-funded by the European Regional Development Fund and the Republic of Cyprus through the Research Promotion Foundation (Project: DIDAKTOR/0311/78).

References

1. V. P. Kuznetsov, "Equation of nonlinear acoustics," *Sov Phys Acoust*, vol. 16, pp. 467–470, 1970
2. R. V. Khokhlov and E. A. Zabolotskaya, "Quasi-plane waves in the non-linear acoustics of confined beams," *Sov Phys Acoust*, vol. 15, pp. 35–40, 1969
3. F. A. Duck, "Acoustic properties of tissue at ultrasonic frequencies," in *Physical properties of tissue : a comprehensive reference book*, London; San Diego: Academic Press, 1990
4. F. Dunn, P. D. Edmonds, and W. Fry, "Absorption and Dispersion of Ultrasound in Biological Media," in *Biological engineering*, H. P. Schwan, Ed. New York: McGraw-Hill, 1969

Influence of serum on gene delivery using microbubble-assisted ultrasound

Jean-Michel Escoffre^{a,b}, Anthony Novell^{a,c}, Aya Zeghimi^a, Ayache Bouakaz^a

^aInserm UMR 930, Université François Rabelais de Tours, PRES Centre-Val de Loire Université, Tours, France

^bPresent address: Imaging Division, UMC Utrecht, Utrecht, Netherlands

^cPresent address: Joint Dept. Biomedical Engineering, North Carolina State University, Chapel Hill, USA

Rationale and aim

Plasmid DNA molecules (pDNA) is a highly attractive molecule for gene therapy, genetic vaccination and immunotherapy provided that an efficient, safe and targeted delivery can be achieved. While microbubble-assisted ultrasound can provide an advantageous and safe gene delivery method for *in-vitro* and *in-vivo* applications, its use appears restricted by the relative low delivery efficiency compared to viral vectors[1]. Nevertheless, the currently available data indicates that the potential of this method for pDNA delivery could be improved further. This optimization could be achieved by controlled and targeted pDNA delivery and by finding ways to deliver a greater amount of pDNA into the targeted cells. This method has demonstrated various degrees of successes in increasing the transfection efficiency. This difference in transfection efficiency might have different origins, especially the presence of serum, in cell medium and in blood during the *in-vitro* and *in-vivo* sonoporation, respectively. The aim of this present study is to investigate the influence of serum on *in-vitro* pDNA delivery using microbubble-assisted ultrasound.

Material & Methods

Human glioblastoma U-87 MG cells were resuspended in cell medium supplemented with a concentration range of serum (0-50%). The cell suspension (5×10^5 cells in 1.5 mL) was placed in the polystyrene cuvette. 7.5 μ g pDNA (*i.e.* transfection assay) or 100 μ M propidium iodide (*i.e.* permeabilization assay) and 7.1 μ L of SonoVue microbubbles (microbubble-to-cell ratio of 5) were added 1 min before ultrasound application. Subsequently, in a deionized water tank at 37°C, the cell suspension was exposed to 1 MHz sinusoid ultrasound waves with a pulse repetition period of 100 μ s, 40 cycles per pulse, and for 30 s[2], with a peak negative pressure of 400 kPa. Forty-eight hours later, transfection level was assessed by flow cytometry. The cell viability was evaluated using a methylthiazolyldiphenyltetrazolium bromide colorimetric assay. After 15 min incubation at 37°C, the percentage of permeabilized cells was assessed by flow cytometry. The microbubble sonodestruction was monitored and quantified as previously described[3]. The effect of increasing the concentration of serum on pDNA topology was monitored by agarose gel electrophoresis.

Results

In the present study, *in-vitro* results showed that a low serum concentration (*i.e.*, $\leq 1\%$) induced a significant increase in transfection level (Figure 1A) through an increase of cell viability (Figure 1B). However, a high serum concentration (*i.e.*, $\geq 5\%$) resulted in a significant decrease in transfection cells (Figure 1A), which is not associated with a loss of cell viability (Figure 1B), neither a decrease of membrane permeabilization (data not shown) nor an inefficient microbubble sonodestruction (data not shown).

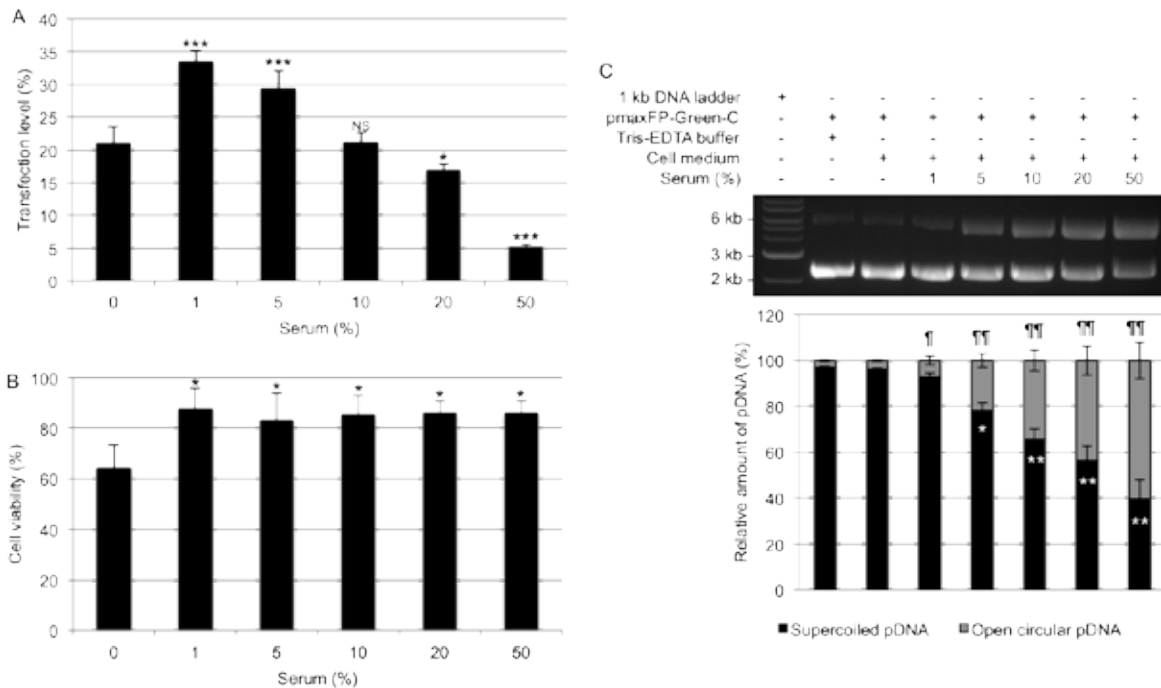


Figure 1: Effect of increasing the concentration of serum on transfection level (A), cell viability (B) and pDNA topology (C).

Serum is known to exhibit an intrinsic DNase activity. Hence, pDNA was incubated for 1 min (*i.e.*, under the same conditions used in the previously described experiments) in the presence or not of serum. The incubation of pDNA in cell culture medium without serum did not change significantly the proportions of supercoiled ($96 \pm 1\%$) and open circular forms ($4 \pm 1\%$) ($p > 0.05$) compared to Tris EDTA buffer. However, the fraction of supercoiled pDNA significantly decreased with increasing serum concentration ($p < 0.05$). In our experimental conditions, no linear pDNA and fragments were detected. These data demonstrate that serum modifies the topology of pDNA. The topology of pDNA changes in the same way after treatment by microbubble-assisted ultrasound (data not shown) than reported in Figure 1C. No significant difference was observed between these two experimental conditions. Thus, these results show that the combination of ultrasound and SonoVue microbubbles has no impact on the topology of pDNA in our experimental conditions. However, our comparative study

demonstrates that the decrease in transfection level was positively correlated to the decrease in the proportion of supercoiled pDNA (Pearson's correlation coefficient, 0.99).

Conclusions

In summary, the serum affects the efficacy of pDNA delivery using microbubble-assisted ultrasound by acting on the pDNA topology. In order to get an efficient *in-vitro* pDNA delivery using microbubble-assisted ultrasound, low serum concentration (*i.e.*, 1%) is required to preserve pDNA topology and to act as protector of cell viability.

Acknowledgement

This project was funded by the EU FP7 Project SONODRUGS (NMP4-LA-2008-213706), Inserm (AB) and Foundation Thérèse and René Planiol (JME). The authors thank Bracco Research Geneva for supplying the microbubbles.

References

1. *Escoffre JM, Zeghimi A, Novell A, Bouakaz A (2013) Curr. Gene Ther., 13:2-14*
2. *Escoffre JM, Novell A, Piron J, Zeghimi A, Doinikov A, Bouakaz A (2013) IEEE Trans. Ultrason. Ferroelectr. Freq. Control., 60:46-52*
3. *Lamanauskas N, Novell A, Escoffre JM, Venlauskas M, Satkauskas S, Bouakaz A (2013) J. Drug. Target., 21:407-414*

Ultrasound and cationic microbubble induced local delivery of microRNA-based therapeutics both *in vitro* and *in vivo*

Rick F.J. Kwekkeboom¹, Zhiyong Lei², Sylvia J.P. Bogaards¹, Eric Aiazian^{3,4}, Otto Kamp⁴,
Walter J. Paulus¹, Joost P.G. Sluijter², René J.P. Musters¹

¹Department of Physiology, VU University Medical Center, Van der Boechorststraat 7, 1081 BT, Amsterdam, the Netherlands

²Department of Experimental Cardiology, University Medical Center Utrecht, P.O. Box 85500, 3508 GA, Utrecht, the Netherlands

³Axle International, Nieuwe Uitleg 28, 2514 BR, the Hague, the Netherlands

⁴Department of Cardiology, VU University Medical Center, De Boelelaan 1117, 1081 HV, Amsterdam, the Netherlands

MicroRNAs are involved in many pathological processes and are a promising class of molecules to therapeutically target. However, therapeutic molecules influencing the activity of these microRNAs lack successful delivery vehicles. In the present study, the use of cationic ultrasound-responsive microbubbles (MB) and their ability to deliver microRNA blockers and mimics was studied *in vitro* and *in vivo*. MB successfully delivered microRNA blockers into various intracellular compartments of primary isolated human endothelial cells. Different ultrasound protocols led to variable transfection percentages with the most successful protocol resulting in transfection of 18% of the total number of endothelial cells. At the same time, ultrasound+MB+microRNA blocker treatment reversibly weakened the integrity of endothelial cell monolayers using low mechanical index (MI=0.1) ultrasound. However, low mechanical index (MI=0.2) ultrasound activated MBs lost their capability of microRNA delivery *in vivo* (figure 1A), probably due to the dampening effect of blood on MB oscillation. The capability of MB to locally deliver microRNA based therapeutics was restored by using high mechanical index (MI=1.8) ultrasound, leading to a local 2.8-fold increase of delivered microRNA to treated tissue (Figure 1A).

Furthermore, tissue distribution of miRNA blockers to the muscles of mouse hind-limbs was confined to the arteries and capillaries in the untreated limbs, whereas after treatment with high mechanical index (MI=1.8-1.9) both at 2 MHz and 14 MHz a much more diffuse pattern of tissue distribution was observed (Figure 1B). Our findings suggest that MB can be used in combination with US to increase local tissue penetration of miRNA therapeutics into skeletal muscle after i.v. injection.

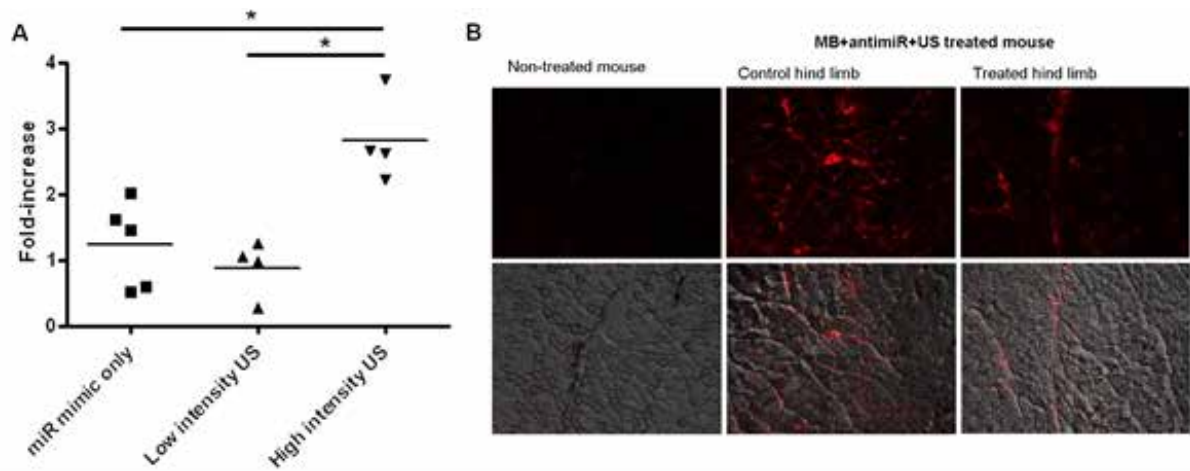


Figure 1: miR mimic delivery (A) and miRNA blocker delivery (B) *in vivo*. A) miRNA from both treated and non-treated hind-limbs was isolated after US+MB delivery of miRNA mimics. miRNA levels were determined by qPCR and the fold-increase of miRNA presence in treated hind-limbs compared to non-treated hind-limbs was compared. B) Fluorescently tagged miRNA blockers (antimiR) were delivered using MB+US to the hind-limb of mice. Muscles from both US-treated as non-treated legs were isolated, frozen and cryosectioned. Both dark- and bright-field images of these cryosections cryosections were subsequently taken to analyze the localization of delivered antimiRs.

This research forms part of the Project P1.05 LUST of the research program of the BioMedical Materials institute, co-funded by the Dutch Ministry of Economic Affairs. The financial contribution of the Nederlandse Hartstichting is gratefully acknowledged.

The use of self-made microbubbles for contrast-enhanced ultrasound imaging in dogs: Potential for image-guided drug delivery *in vivo*

K. Vanderperren, S. Cool, H. Haers, E. Stock, C. Fina, L. Duchateau, N. Sanders, J.H. Saunders

*Department of Veterinary Medical Imaging and Small Animal Orthopaedics,
Faculty of Veterinary Medicine, Ghent University, Belgium*

Ultrasound-mediated drug delivery is currently under extensive investigation because of its interesting clinical potential. Moreover, the ability to prepare drug-containing microbubbles (MB) allows one to image the drug delivery vehicle in real time. It has been demonstrated that unloaded MB and doxorubicin liposome-loaded MB could be used for contrast ultrasound-guided drug delivery *in vitro*.¹ The aim of this study was to investigate the use of self-made MB for imaging the canine spleen *in vivo* by comparing it with the commercial Sonovue.

Five experimental beagles with no evidence of splenic disease, were imaged using contrast harmonic ultrasound after injection of self-made MB and Sonovue. The self-made MB consist of a C₄F₁₀ gas core surrounded by a lipid shell made of dipalmitoylphosphocholine (DPPC) and 1,2-distearoyl-*sn*- glycerol-3-phosphoethanolamine-N-(polyethylene glycol)-2000 (DSPE-PEG2000). Microbubbles were prepared by shaking a vial containing a solution of these lipids, using a Capmix. All dogs received three separate bolus injections of 0.3 ml/10 kg of both contrast media. Time-pixel intensity curves (MPI) were generated for 3 selected regions in the spleen. Mean values of baseline intensity (BI), peak intensity (PI), area-under-curve (AUC), arrival time (AT), time-to-peak (TTP), wash-in (W_{in}) and wash-out (W_{out}) were determined. Statistical analysis was performed.

No differences were found for TTP, W_{in}, BI and AT between self-made MB and Sonovue. On the other hand, significant increase in PI (43.6 MPI vs. 15.17 MPI), and AUC (1746.83 MPI vs. 663.94 MPI), and faster W_{out} (-0.3 MPI/sec vs. -0.06 MPI/sec) was found for self-made MB compared to Sonovue.

Our results demonstrated that our self-made MB can be used for diagnostic purposes *in vivo* with better image quality but a lower stability compared with Sonovue. As similar imaging properties were found for doxorubicin liposome-loaded MB, contrast ultrasound-guided drug delivery *in vivo* could have potential for clinical purposes.

References

Escoffre JM et al. (2013) Doxorubicin liposome-loaded microbubbles for contrast imaging and ultrasound-triggered drug delivery. Trans Ultrason Ferroelectr Freq Control. 60:78-87.

Denoising of contrast-enhanced ultrasound movies based on a multiplicative model

Avinoam Bar-Zion¹, Charles Tremblay-Darveau², Melissa Yin³, Dan Adam¹ and F. Stuart Foster^{2,3}

¹*Department of Biomedical Engineering, Technion - Israel Institute of Technology, Haifa, Israel*

²*Department of Medical Biophysics, University of Toronto, Toronto, Ontario, Canada*

³*Sunnybrook Health Sciences Centre, Toronto, Ontario, Canada*

Background

Speckle noise is an inherent characteristic of dynamic contrast-enhanced ultrasound (d-CEUS) cines and ultrasound images in general. Currently, maximum intensity persistence (MIP) is the only widely accepted processing method enabling the visualization of vasculature using d-CEUS imaging. A different approach has been used for speckle removal from B-mode ultrasound images. In this approach, a multiplicative model for formation of speckled images is adopted and the log transform is applied in order to convert this multiplicative noise to additive noise. Two main characteristics distinguish between d-CEUS images and B-mode images in this context: First, the resulting additive noise is not only non-Gaussian but its distribution is determined by the concentration of microbubbles within each resolution cell, at a given time. Second, due to the random spatial distribution of microbubbles inside the vasculature, the multiplicative noise in consecutive d-CEUS images is independent, facilitating its removal.

Methods

In this work, log-transformed d-CEUS cines are processed within the framework of temporal-domain wavelet denoising. A pre-processing step is performed, which locally removes low value outliers and enables the use of standard denoising methods, optimized for Gaussian white noise. The main advantage of using wavelet shrinkage in the present context is its ability to estimate ultrasound contrast agents' (UCA) concentration over time adaptively, without assuming a model or predefining the signal's degree of smoothness. Wavelet Shrinkage is compared against cumulative MIP, Temporal Compounding and Log-normal model fitting, in a series of numerical simulations, *in-vitro* flow-phantom experiments and *in-vivo* and *ex-vivo* scans. All experiments were performed using MicroMarker™.

Results

Phantom experiments, in which UCA concentration and flow velocities were kept stable, showed a 50% reduction, when compared to MIP, of the spatial coefficient of variation factor, using Wavelet shrinkage. These results hold over a wide range of UCA concentrations (0.001%-1%). Dynamic phantom experiments, including bolus injection of UCA, demonstrated improved estimation of the time-intensity curve using Wavelet shrinkage, when compared to Log-normal model fitting ($r = 0.95$ vs. $r = 0.86$). As a result, perfusion parameters, calculated using these methods, are notably different. In the *in-vivo* and *ex-vivo* tests, the proposed approach resulted in improved noise removal, reflected by lower MSE throughout the scan (see figure I), and enhanced spatial resolution (see Table I). Moreover, the proposed method enables the investigation of the wash-out phase that is not depicted in cumulative MIP movies. The wash-out phase is especially important in the context of d-CEUS imaging with targeted microbubbles.

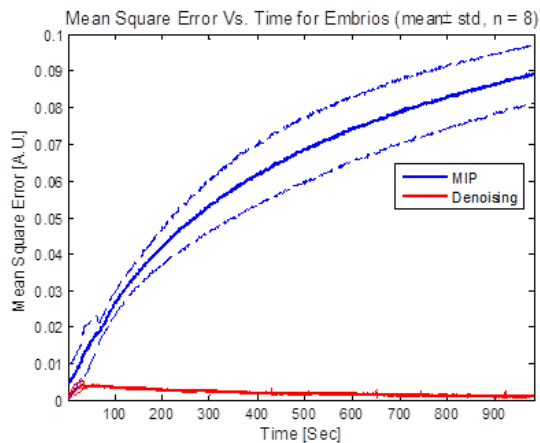


Fig. 1: MSE vs. time in *ex-vivo* embryo experiments.

TABLE I
Resolution Gain Obtained Using Wavelet Shrinkage compared to MIP

	Axial Resolution Ratio	Lateral Resolution Ratio
<i>In-vivo</i> hind-limb LS174T tumors N=6	1.93±0.42	1.56±0.10
<i>In-vivo</i> hind-limb PC3 tumors n=6	2.04±0.41	1.78±0.14
<i>Ex-vivo</i> Mouse Embryos n=8	2.58±0.31	1.28±0.07

Which harmonic gives the highest CTR and SNR?

D. Peruzzini^{1,2}, D. Bera², P. Tortoli¹, N. de Jong², H.J. Vos²

¹*MSD lab, Department of Information Engineering, University of Florence, Italy*

²*Biomedical Engineering, Thorax Centre, Erasmus MC, Rotterdam, The Netherlands*

Introduction

In ultrasound contrast agent (UCA) imaging, the contrast to tissue ratio (CTR) in second harmonic imaging suffers from nonlinear effects due to ultrasonic wave propagation in tissue. It can be expected that third or fourth harmonic imaging suffers less from these nonlinear propagation effects in tissue, while the nonlinear response of the ultrasound contrast agent retains its amplitude for these higher harmonics. This study investigates the CTR and signal to noise ratio (SNR) in a tissue/vessel mimicking phantom with standard UCA concentrations, and a custom dual-frequency probe [1] connected to a commercially-available ultrasound imaging machine.

Materials and Method

The dual-frequency probe, developed earlier for tissue harmonic imaging, has interleaved transmit (N=44, fc=1 MHz) and receive (N=44, fc = 3.5MHz) elements. All elements are addressed separately through a custom-programmed commercial ultrasound machine (SonixTOUCH, Ultrasonix - Analogic Ultrasound, Richmond, BC, Canada). Real-time imaging is provided during the measurements while beam formed RF data is stored for further offline processing.

The model consisted of a custom tissue mimicking phantom with a UCA-filled cavity of 1 cm diameter. The phantom was designed to produce realistic tissue scattering. The attenuation was characterized at 3 dB/cm at 1 MHz, and 4 dB/cm at 3 MHz. In a separate hydrophone measurement, the probe was found to produce 900 kPa peak-negative pressure at the focus in water at 6 cm depth at 1 MHz. This corresponds to 110 kPa pressure (MI = 0.11) in the phantom at the location of the UCA when taking the phantom's attenuation into account. Such pressure value is known, and verified, to be non-destructive for the UCA. Notably, the amplitude of the 3rd harmonic is 40 dB below the fundamental level in water with these transmit settings, indicating that nonlinear propagation at the higher harmonics is expected to be negligible in the tissue phantom. BR14 (Bracco, Geneva) contrast agent is diluted in a 1:2000 ratio to mimic clinical concentration.

Results

Figure 1 shows the images that were produced from the beam formed RF data, based on single frames. The data was temporally filtered around the fundamental, 2nd, 3rd and 4th harmonic, respectively, with 1-MHz band pass filters. The images were normalized to have equal signal power in an area in the centre of the image. The UCA-filled cavity is clearly observed, and tissue speckle is only visible in the top areas. UCA RMS levels are obtained from the right encircled areas, while tissue levels are obtained from the left encircled area, after averaging over 140 frames to reduce noise. Table 1 summarizes the CTR and signal to noise ratio (SNR) for the harmonics. The CTR values are similar to those reported earlier for contrast superharmonic imaging *in-vitro* and *in-vivo* [2]. Note that the tissue levels were below the noise levels for the 3rd and 4th harmonic, even after the frame averaging step, and only lower limits can be provided for the CTR.

Discussion

The results show that the CTR of the 3rd harmonic is higher than that of the 2nd, but the SNR is lower for the 3rd harmonic. This shows that noise is the limiting factor for the UCA detection when using the higher harmonics, not tissue signal, which is contrary to 2nd harmonic imaging in practice. The result implies that a 3rd harmonic, or superharmonic, imaging system needs careful tuning, settings optimization and, possibly, coded excitation with nonlinear compression algorithms to increase the SNR.

Table 1: Measured values, in dB

harmonic number	1	2	3	4
SNR	21	23	18	11
CTR	21	36	>>38	>32

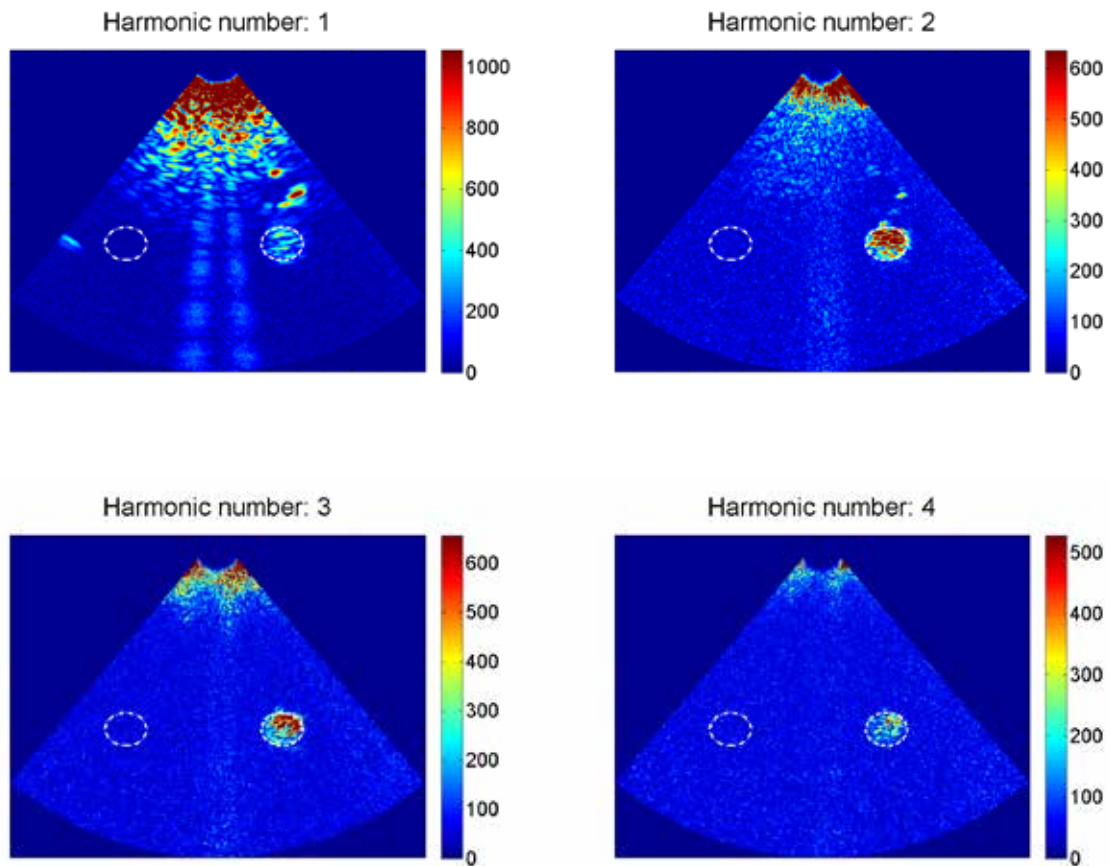


Figure 1: B-mode frames of the phantom with UCA-filled cavity, filtered around the 1st to 4th harmonic frequency

References

1. van Neer, P. L.; Matte, G.; Danilouchkine, M. G.; Prins, C.; van den Adel, F.; and de Jong, N., "Superharmonic imaging: development of an interleaved phased-array transducer". *IEEE Transactions on Ultrasonics, Ferroelectrics and Frequency Control*, 57(2), pp. 455-468, 2010
2. Bouakaz, A.; Krenning, B.J.; Vletter, W.B.; ten Cate, F.J.; and de Jong, N., "Contrast superharmonic imaging: a feasibility study". *Ultrasound in Medicine & Biology*, 29(4), pp. 547-553, 2003

Theoretical and experimental observations of lipid shedding

C.J. Harfield¹, Y. Luan², N.C. Ovensden³, N. de Jong^{2,4} and E. Stride¹

¹*Institute of Biomedical Engineering, Department of Engineering Science, University of Oxford, UK*

²*Erasmus Medical Center, Rotterdam, the Netherlands*

³*Department of Mathematics, University College London, UK*

⁴*Delft University of Technology, the Netherlands*

Interest in coated microbubbles as agents for therapeutic and quantitative imaging applications has increased the need for accurate characterization of their acoustical behavior. A number of recent studies have demonstrated that the properties of the coating of phospholipid-coated bubbles may change significantly, even of the timescale of a single ultrasound pulse [1, 2]. In particular, the phenomenon of “lipid shedding” has been observed, whereby material is expelled from the bubble surface when it oscillates under ultrasound exposure. This may have significant implications for the utility of microbubbles for both diagnostic and therapeutic applications, since the subsequent acoustic response of the bubble may be altered and/or therapeutic molecules attached to the bubble surface may also be released. A theoretical model has been utilized in previous work by the authors to examine the relationship between the concentration of surfactant molecules on the bubble surface and shedding [2]. A threshold for shedding has been hypothesized corresponding to a reduction in bubble surface area during compression.

In this study we compare the theoretical results with high speed fluorescence microscopy footage of single bubbles undergoing lipid shedding[3]. We perform a theoretical sensitivity study to determine whether the composition of the bubble coating affects the probability of shedding and the quantity of material shed for a range of ultrasound exposure conditions. We also examine the influence of a nearby rigid boundary upon shedding behavior.

The results indicate that varying the bubble shell composition does affect the occurrence and degree of shedding, and hence that any shedding threshold will be entirely bubble dependent. The presence of a wall also affects the onset and degree of shedding by shifting the effective resonance frequency and changing the net change in surface area during oscillation, so this must be taken into account when comparing theory and experiment. The total mass of lipid shed appears to reach a constant level in the theoretical simulation at a ratio of oscillation amplitude to initial bubble size corresponding to the experimentally observed “threshold” for the onset of lipid shedding. The implications of these observations for understanding the underlying mechanisms and their potential exploitation in therapeutic applications will be discussed.

References

1. Borden, M.A., et al., *Influence of lipid shell physicochemical properties on ultrasound-induced microbubble destruction. Ieee Transactions on Ultrasonics Ferroelectrics and Frequency Control*, 2005. 52(11): p. 1992-2002
2. O'Brien, J.P., N. Ovenden, and E. Stride, *Accounting for the stability of microbubbles to multi-pulse excitation using a lipid-shedding model. J Acoust Soc Am*, 2011. 130(4): p. EL180-5
3. Gelderblom, E.C., *Ultra-high-speed fluorescence imaging*, 2012: Enschede. p. 144

Sono-activated ultrasound localization microscopy (SAULM): Basic principles, theoretical limits and simulations

Yann Desailly, Olivier Couture, Mathias Fink, Mickael Tanter

Institut Langevin (ESPCI, INSERM, CNRS), Paris, France

In optics, localization microscopy has brought tremendous improvements as it yields images with a resolution down to $\lambda/15$ (or 45 nm for 650 nm wavelength). These techniques are based on the stochastic activation of luminescent sources to create single spots. In ultrasound, punctual sources of echo can be found when microbubbles are imaged with ultrafast plane wave imaging at several thousand frames per second. To achieve such frame rate, plane waves are emitted and their echoes are recorded on all of the channels all at once. Hence, a single emission can be used to obtain an entire image. Since microbubbles are acting as independent echoes on differential ultrafast imaging, they can then be localized with a precision far beyond the diffraction limit. We present here the theoretical limits of SAULM, computed both with an analytical model and simulation.

Experiments to explore the resolution limit of SAULM were performed on microbubbles flowing through 40 μm microfluidic channels. These channels were observed with a 1.75 MHz 128 elements transducer matrix. The channels were 22 times smaller than the wavelength and they were separated by at most one wavelength. The system is imaged at 1000 frames per second and echoes of bubbles are isolated by looking at fast changes between each images. Bubble echo yields individual parabola on the reception matrix, which can then be fitted with a propagation model of the acoustical wave to find the location of the source.

The error made on these resulting coordinates can be predicted with an ad-hoc analytical model. To assess the validity of the model, the predicted errors are compared to simulation data. The resolution of SAULM is dependent on the number of elements of the transducer, the electronic noise of the scanner and the axial / lateral distances. For a 1.75 MHz 128 elements matrix transducer, we predict that the maximum resolution will be 69 micrometers. This resolution improves in a \sqrt{N} fashion with respect of the number of transducers and reduces proportionately with the noise. These predicted values compares well with the resolution obtained experimentally, since the width of a 40 μm channel, was measured as 80 μm (fig 1).

Figure 1 demonstrates that the resolution of SAULM is better than the diffraction-limited focused imaging. At higher frequency, we predict that the resolution could eventually attain 10 microns (with a 10 MHz 256 transducer matrix). Therefore, it could become possible to distinguish bubbles flowing inside microvessels.

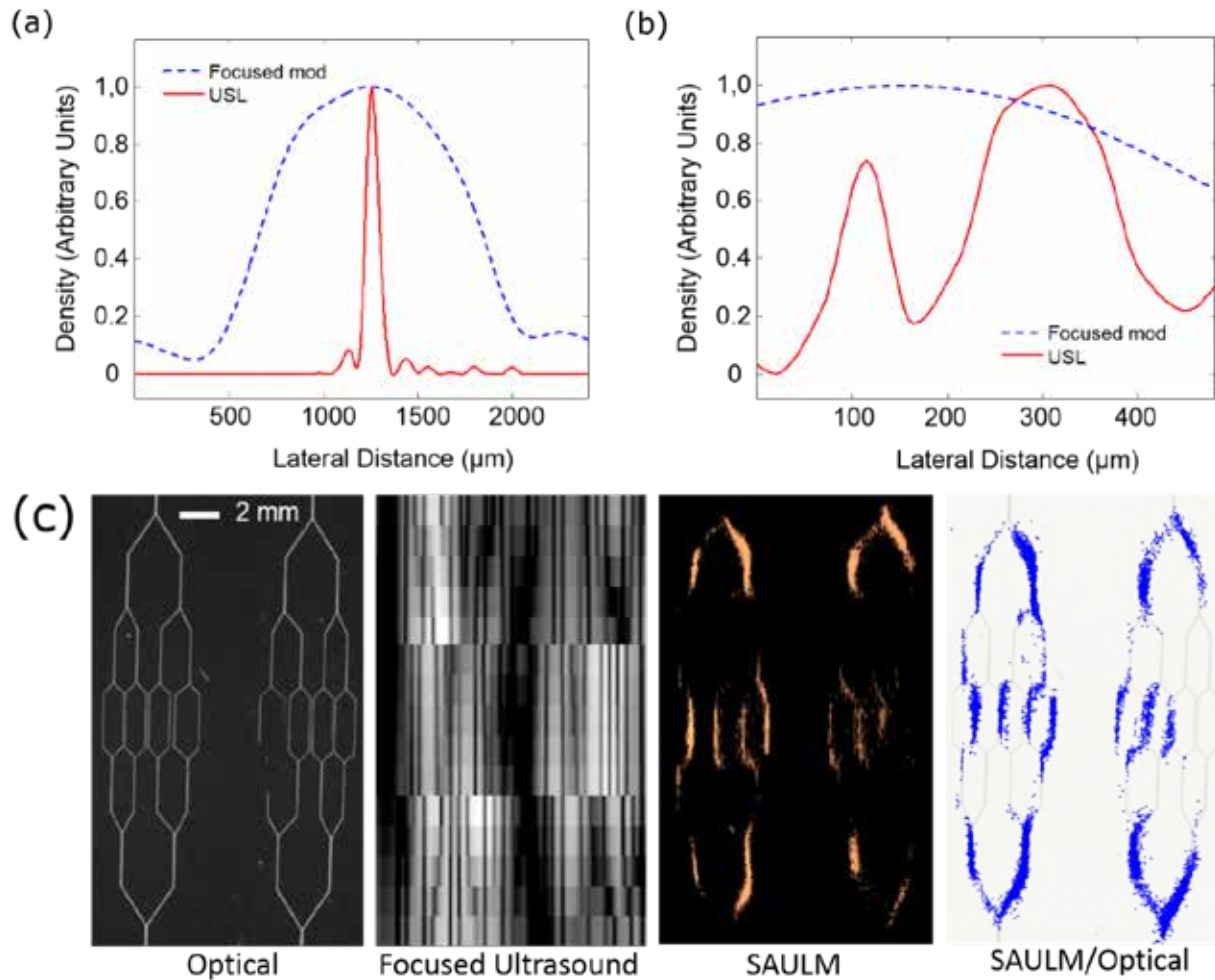


Figure 1: SAULM grant images with a resolution 13-fold higher than standard echography techniques (a) The full width at half maximum formed by one channel is 80 μm with SAULM whereas it is 1100 μm with standard focused imaging (b) Two channels separated by 200 μm are distinguishable with SAULM. (c): Comparison between fluorescence microscopy, standard echography, SAULM and all the localized sources superimposed with optical image (from left to right); the correlation coefficient between the optical image and the standard ultrasonic image is 0.11; the correlation coefficient between the optical image and the SAULM image is 0.22

Contrast-enhanced angiogenesis imaging by mutual information analysis

N. Bouhouch^{1,2}, L. Demi¹, M. Kuenen^{1,2}, H. Wijkstra^{2,1}, T. Tjalkens¹, M. Misch¹

¹*Eindhoven University of Technology, Dept. of Electrical Engineering, the Netherlands*

²*Academic Medical Center, University of Amsterdam, Dept. of Urology, the Netherlands*

Introduction

The key role of angiogenesis in cancer growth has motivated extensive research aiming at non-invasive cancer detection by blood perfusion imaging methods [1], e.g. using dynamic contrast-enhanced ultrasound (DCE-US). However, the results are limited due to the complex relationship between angiogenesis and blood perfusion.

Recently, contrast ultrasound dispersion imaging (CUDI) has been proposed as an alternative method for imaging angiogenesis. Determined by the geometrical properties of the microvascular architecture, dispersion may in fact be more suitable for detecting angiogenic processes than perfusion.

Two different approaches have been proposed so far to perform CUDI by analysis of ultrasound-contrast-agent (UCA) indicator dilution curves (IDCs). Following the intravenous injection of an UCA bolus, DCE-US imaging is performed. From the obtained image sequence, IDCs are extracted that measure the acoustic intensity at each pixel as a function of time. After proper linearization, the recorded IDCs are linearly correlated with the UCA concentration evolution. The first approach estimates dispersion by fitting each IDC by a convective-dispersion model [2]. The second approach is based on an indirect estimation of dispersion, achieved by means of spatiotemporal analysis of the measured IDCs by linear similarity measures such as spectral coherence [3, 4].

Here, we present a development of the second approach by inclusion of nonlinear similarity measures based on information theory. In particular, mutual information is adopted as a new similarity measure. As opposed to linear similarity measures, mutual information also allows the exploration of nonlinear connectivity between IDCs. The estimation of the mutual information at each pixel permits building a parametric dispersion map based on both linear and nonlinear similarity.

Similar to the previous CUDI methods, the presented approach was tested for localization of prostate cancer (PCa). This choice is motivated by the high incidence of this form of cancer as well as by the lack of reliable imaging methods for prostate cancer diagnosis. A preliminary validation was therefore

performed in 21 datasets recorded from 9 patients referred for radical prostatectomy because of proven PCa at the Academic Medical Center, University of Amsterdam, the Netherlands.

Methodology

After an intravenous injection of a 2.4-ml SonoVue® (Bracco, Milan, Italy) bolus, its passage through one plane in the prostate is imaged using an iU22 ultrasound scanner (Philips Healthcare, Bothell, WA) equipped with either a C8-4v or C10-3v probe. Power modulation imaging was adopted at a frequency of 3.5 MHz and a mechanical index of 0.06. Local dispersion is then estimated by means of mutual information analysis applied to IDCs as obtained from neighboring pixels.

A kernel is designed that determines the pixels that are considered to estimate the local mutual information at a particular location. A 3x3 mm kernel size is adopted in order to achieve an optimal balance between diagnostic resolution and reliability. In fact, angiogenesis is required for tumors to grow beyond 2-3 mm in diameter. Therefore, to detect early angiogenic processes, a resolution of at least 3 mm should be achieved. A square shape was chosen to estimate mutual information independently of the blood perfusion direction.

The discrete mutual information, here indicated by the symbol I , as defined by Shannon [5], can be written as follows:

$$I(X^{N-1}, C) = \sum_{x \in X} \sum_{c \in C} p_{X^{N-1}, C}(x^{N-1}, c) \text{Log}_2 \left(\frac{p_{X^{N-1}, C}(x^{N-1}, c)}{p_{X^{N-1}}(x^{N-1}) p_C(c)} \right), \quad (1)$$

$$p_{X^{N-1}}(x^{N-1}) = \sum_{c \in C} p_{X^{N-1}, C}(x^{N-1}, c), \quad (2)$$

$$p_C(c) = \sum_{x \in X} p_{X^{N-1}, C}(x^{N-1}, c) \quad (3)$$

The random variable C represents the IDC, expressed in gray-level video density, obtained at the kernel's central pixel. The IDCs of all other pixels, except the central one, are defined as the random vector X^{N-1} . N is the total number of pixels in the kernel.

From these equations, it can be noticed that the mutual information, $I(X^{N-1}, C)$, is a function of the joint distribution of the two random variables X^{N-1} and C . This is given by the joint probability mass function (PMF), $p_{X^{N-1}, C}(x^{N-1}, c)$, which can be expressed as

$$p_{X^{N-1}, C}(x^{N-1}, c) = p_C(c) \prod_{i=1}^{N-1} p_{x_i, C}(x_i | c) \quad (4)$$

where $P_{x_i|c}(x_i|c)$ is the conditional PMF of the IDC obtained at the kernel's i^{th} pixel given c , the IDC obtained at the kernel's center. In Eq. (4), the IDCs in X^{N-1} are assumed to be mutually independent and only dependent on c . This assumption, which may not be realistic, is made to focus the analysis on the local dependency between the central pixel and its surroundings. Moreover, this assumption reduces the complexity for computing the joint PMF of X^{N-1} and c .

To improve the SNR of measured IDCs, the raw data of the echographic video was pre-filtered temporally and spatially. Temporally, a low-pass filter with cut-off frequency at 0.5 Hz was adopted, because the IDC bandwidth in the prostate is limited to frequencies up to 0.5 Hz. Spatially, a Gaussian low-pass filter with standard deviation of 0.5 mm to increase the SNR while maintaining sufficient resolution for angiogenesis detection. Given that the original pixel size is 3 times smaller than the spatial resolution, low-pass filtering enables spatial downsampling of each frame by factor 3, which significantly reduces the computation time.

The mutual information analysis is then performed. First, the kernel center is placed at the pixel where the mutual information must be computed. Then, the kernel IDCs are mapped to the probabilistic domain using Eq. (4). Mutual information is then calculated and its value stored at the central pixel's coordinates. By applying this procedure for all pixels, a mutual-information map is generated for each imaging plane.

This method was validated by comparing mutual information maps to histology results in 21 datasets recorded from 9 patients that were referred to radical prostatectomy at the Academic Medical Center, University of Amsterdam, the Netherlands. After cutting the prostate in 4-mm thick slices, a pathologist marked the presence of PCa [6]. Figure 1 shows an example of a dispersion map obtained by mutual information analysis and its corresponding histology slice. Two regions of interests (ROIs) larger than 0.5 cm^2 , representing healthy and cancerous tissue, were determined on the basis of the histology results and applied on the ultrasound mutual information maps to evaluate the performance of the proposed method for PCa localization.

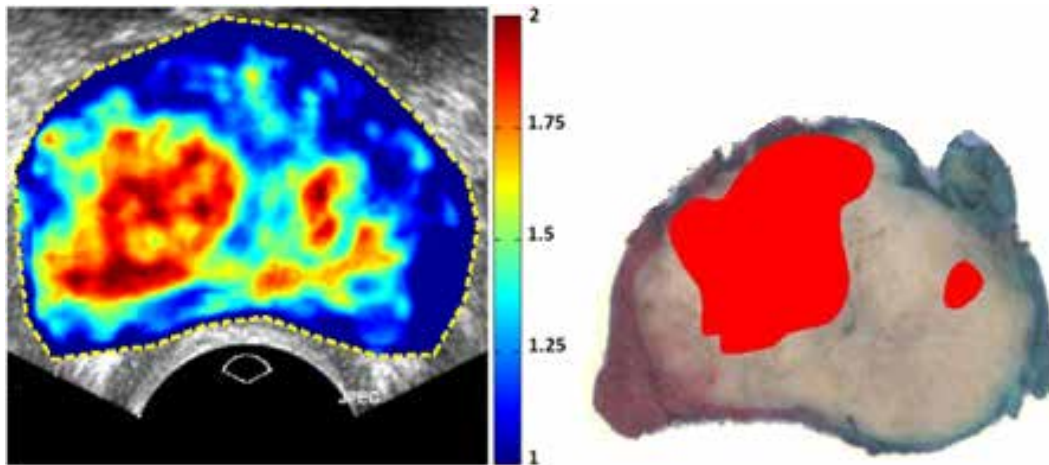


Figure 1: Dispersion map obtained by mutual information analysis (left) and corresponding histology slice.

Results

Pixel classification using the presented method resulted in a sensitivity and specificity equal to 81% and 87%, respectively. The receiver-operating characteristic (ROC) curve area was 0.92. When applied to the same dataset, CUDI by coherence analysis resulted in sensitivity, specificity, and ROC curve area equal to 78%, 80%, and 0.87, respectively.

Conclusions

CUDI by mutual information shows promising results for PCa localization. To confirm this method's clinical value, further validation with a larger dataset is needed.

References

1. G. Russo, M. Mischi, W. Scheepens, J. J. de la Rosette, and H. Wijkstra, "Angiogenesis in prostate cancer: onset, progression and imaging," *BJU international*, vol. 110, no. 11c, pp. E794–E808, 2012
2. M. P. J. Kuenen, M. Mischi, and H. Wijkstra, "Contrast-ultrasound diffusion imaging for localization of prostate cancer," *Medical Imaging, IEEE Transactions on*, vol. 30, no. 8, pp. 1493–1502, 2011
3. Mischi, M. P. J. Kuenen, and H. Wijkstra, "Angiogenesis imaging by spatiotemporal analysis of ultrasound contrast agent dispersion kinetics," *Ultrasonics, Ferroelectrics and Frequency Control, IEEE Transactions on*, vol. 59, no. 4, pp. 621–629, 2012
4. M. P. J. Kuenen, T. Saidov, H. Wijkstra, and M. Mischi, "Contrast-ultrasound dispersion imaging for prostate cancer localization by improved spatiotemporal similarity analysis," *Ultrasound in Medicine & Biology*, vol. 39, no. 9, pp. 1631–1641, 2013
5. T. M. Cover and J. A. Thomas, *Elements of information theory*. John Wiley & Sons, 2012
6. R. Montironi, T. V. der Kwast, L. Boccon-Gibod, A. V. Bono, and L. Boccon-Gibod, "Handling and pathology reporting of radical prostatectomy specimens," *Eur. Urol.*, vol. 44, no. 6, pp. 626–636, 2003

Maximum-likelihood estimation for quantitative analysis in dynamic contrast-enhanced ultrasound

*Maarten Kuenen^{1,3}, Ingeborg Herold^{2,1}, Erik Korsten^{2,1}, Jean de la Rosette³,
Hessel Wijkstra^{1,3} and Massimo Mischi¹*

¹*Dept. of Electrical Engineering, Eindhoven University of Technology, The Netherlands*

²*Dept. of Anesthesiology, Catharina Hospital, Eindhoven, The Netherlands*

³*Dept. of Urology, Academic Medical Center, University of Amsterdam, The Netherlands*

Introduction

Dynamic contrast-enhanced ultrasound (DCE-US) has established itself as a minimally invasive imaging method that provides real-time functional information at a very high spatial and temporal resolution 1. While DCE-US was primarily developed for visualization of the heart function 1, the strong potential of DCE-US has also been recognized in application areas such as cancer detection 2, vascular diseases 1 and ischemia 2.

Many of these applications involve the injection of a small microbubble bolus injection. The subsequently recorded DCE-US image sequences can be analyzed quantitatively by extracting time-intensity curves (TICs), which measure the acoustic intensity in a region of interest (ROI) in the DCE-US image as a function of time 2. Common TIC models adopted for estimation of physiological parameters, such as the local density random walk (LDRW), lognormal, and gamma-variate models, offer both a physiological and a statistical interpretation of the observed TIC shape 3, 4, 5. These models are typically fitted to TICs by nonlinear least-squares (NLS) regression, as NLS provides optimal parameter estimation results in case of additive white noise. However, since TICs obtained by DCE-US feature multiplicative noise 3, 6, NLS may not be the optimal method for parameter estimation.

In this abstract, we describe an alternative method for TIC parameter estimation that exploits the statistical nature of TIC models 7. To this end, the TIC model is interpreted as the probability density function of the microbubble transit-times. A measured TIC is considered as the observed histogram of this probability distribution. Parameter estimation is then performed by maximizing the likelihood of observing the measured TIC. Semi-analytical solutions are derived for the LDRW, lognormal, and gamma-variate models and an adaptation is proposed to deal with microbubble recirculation. The proposed method is compared to NLS in simulations and in experimentally measured TICs. The *in vivo* feasibility of the method is also shown

Maximum-likelihood estimation

The mathematical model adopted for TIC fitting is defined by a probability density function $p(t)$, which describes the probability for each microbubble to arrive at the detection location at time t as function of the parameters \mathbf{q} . In this abstract, the LDRW, lognormal, or gamma-variate models are considered to formulate $p(t)$. If K independent microbubble transit-times $t(k)$ are observed, the logarithm of the likelihood of observing these transit-times can be written as function of \mathbf{q} as

$$\ln(L(\mathbf{q})) = \ln \prod_{k=1}^K p(t(k) | \mathbf{q}) = \sum_{k=1}^K \ln(p(t(k) | \mathbf{q})) \quad (6)$$

In reality, the individual transit-times $t(k)$ cannot be observed. Instead, a TIC is measured that relates linearly to the microbubble concentration [8]. Therefore, a TIC can be interpreted as the the observed histogram of $p(t)$, i.e., the amount of observed microbubbles $C(n)$ at N different discrete-time samples n (with time step Δt). We can rewrite the log-likelihood of (1) in terms of $C(n)$ as

$$\ln(L(\mathbf{q})) = \sum_{n=1}^N C(n) \ln(p(n\Delta t | \mathbf{q})). \quad (7)$$

Maximum-likelihood (ML) parameter estimation is then performed by finding those parameters \mathbf{q} that maximize (2), as for example shown in Figure 1. This problem can be solved partially analytically for the LDRW, lognormal, and gamma-variate models: if the injection time parameter t_0 is known, a closed-form solution is available [7]; if t_0 is unknown, it is the only parameter to be estimated numerically by maximization of (2).

This approach requires the complete transit-time distribution to be observed. In practice, however, microbubble recirculation often masks the tail of the transit-time distribution. In this case, closed-form solutions are no longer valid. After discarding the overlapping TIC time segment and truncating the transit-time distribution, ML estimation can still be performed [7].

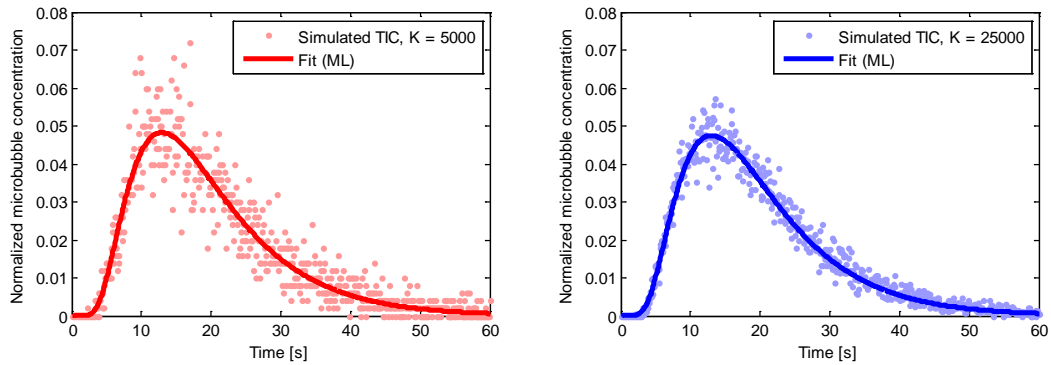


Figure 1 TICs obtained by random LDRW sampling for $K = 5000$ (left) and $K = 25000$ (right) and the corresponding fits based on ML estimation. The parameter K determines the signal-to-noise ratio (SNR) of the simulated TICs.

Data acquisition and performance evaluation

Simulated TICs were obtained by random sampling of $p(\underline{\theta}|t)$ for the LDRW, lognormal, and gamma-variate models. Different values of K were chosen to simulate different signal-to-noise ratios (SNRs). For all TICs and all models, the parameter estimation accuracy by the proposed ML method was compared to that obtained by NLS regression. To this end, the relative bias and standard deviation [%] was evaluated for all parameters $\underline{\theta}$. The performance was evaluated for fitting the complete TIC as well as the truncated TIC, from which the tail (<30% of the peak value) was discarded. In addition, the sensitivity to the truncation time was evaluated.

An experimental validation was performed with 79 TICs that were measured using an *in vitro* hydrodynamic setup at the Catharina Hospital (Eindhoven, The Netherlands) 9. Harmonic imaging (2.7-5.4 MHz) was performed at a mechanical index of 0.2 with an iE33 ultrasound imaging system (Philips Healthcare, Andover, MA) and a transesophageal X7-2t probe. QLAB acoustic quantification software was used to obtain linearized TICs from five differently-sized ROIs. Analogous to the parameter K in the simulations, the ROI size influences the SNR of the TIC (see Figures 1 and 2). Because the true parameter values were unknown, the precision was evaluated by the relative standard deviation [%] among parameters estimated from TICs obtained using different ROI sizes. The sensitivity to the truncation time was also evaluated.

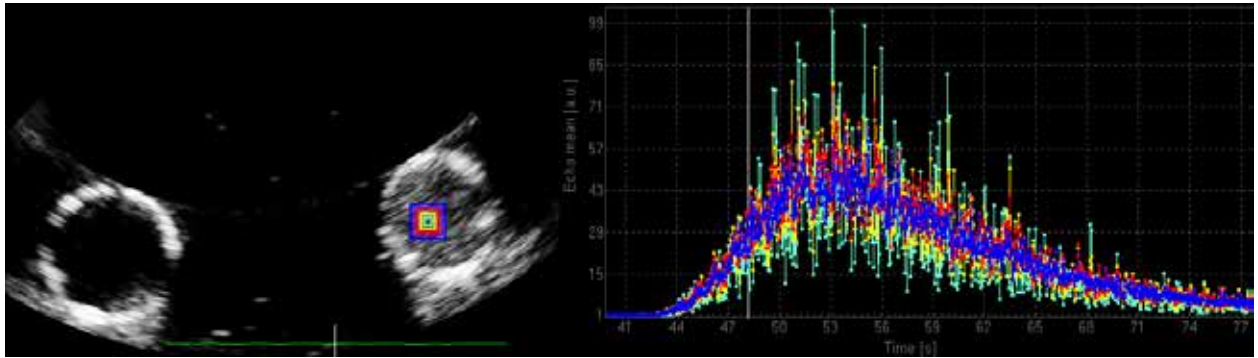


Figure 2: DCE-US measurement of acoustic TICs in an in vitro set-up. On the left, two tubes for inflow (left) and outflow (right) of microbubbles are shown. For this study, outflow TICs were obtained from the square ROIs shown in the image. The associated TICs are shown on the right.

The method was also tested on *in vivo* data obtained from the prostate microcirculation. 19 DCE-US datasets were obtained from 9 patients who underwent radical prostatectomy at the Academic Medical Center, University of Amsterdam (The Netherlands). DCE-US imaging was performed using an iU22 imaging system (Philips Healthcare, Bothell, WA) equipped with either a C8-4v or C10-3v probe. Power modulation imaging was performed at 3.5 MHz and a mechanical index of 0.06. Based on the histology ground truth, two TICs were extracted from each data set in 5x5-mm ROIs to represent healthy tissue and cancer. For several TIC parameters estimated by LDRW model fitting, the ability to discriminate between healthy tissue and cancer was evaluated for both ML and NLS by the area under the receiver-operating-characteristic (ROC) curve.

Results

In all studies, the determination coefficient for TIC fitting was approximately equal for ML and NLS. In the simulations, both methods fitted the TICs without a significant estimation bias. Both for fitting the complete and the truncated TIC, and for all TIC models, the TIC shape parameters estimated by ML were approximately two times (1.36-2.68x) more precise and 17-48% less sensitive to the truncation time than those estimated by NLS.

A similar result was found in the experimental data: the precision obtained by ML was 1.82-2.69 times superior to that obtained by NLS. The sensitivity of ML parameter estimation to the truncation time was 17-63% lower than that of NLS.

In the *in vivo* study, the ROC curve area obtained by ML was 0.13, 0.04, and 0.03 higher than by NLS for the TIC parameters τ , full-width at half-maximum, and wash-in time, respectively, and 0.02 lower than by NLS for the mean transit-time.

Discussion and conclusions

A maximum-likelihood algorithm is presented for quantitative DCE-US analysis. This algorithm, which exploits the statistical interpretation of TIC models, provides a superior parameter estimation precision both in simulated and in experimental data. Moreover, feasibility of the algorithm for use with *in vivo* data is shown.

In the future, the ML algorithm could be extended to implement system identification methods for e.g. volume quantification [9]. Because of its general nature, the ML algorithm could also be tested in other imaging modalities. Furthermore, the ML estimation algorithm may be combined with alternative algorithms that are designed for DCE-US-specific noise [6].

References

1. Feinstein, S. B., et al, Contrast-enhanced ultrasound imaging, *J. Nucl. Cardiol.*, 17, pp. 106-112, 2010
2. Cosgrove, D. and Lassau, N., Imaging of perfusion using ultrasound. *Eur. J. Nucl. Med. Mol. Imaging*, 37 (Suppl 1), pp. S65-S95, 2010
3. Kuenen, M. P. J., Mischì, M., and Wijkstra, H., Contrast-ultrasound diffusion imaging for localization of prostate cancer, *IEEE Trans. Med. Im.*, 30 (8), pp. 1493-1502, 2011
4. Hudson, J. M., Karshafian, R., and Burns, P. N., Quantification of flow using ultrasound and microbubbles: A disruption replenishment model based on physical principles, *Ultrasound Med. Biol.*, 35 (12), pp. 2007-2020, 2009
5. Mischì, M., Den Boer, J. A., and Korsten, H. H. M., On the physical and stochastic representation of an indicator dilution curve as a gamma variate, *Physiol. Meas.*, 29, pp. 281-294, 2008
6. Barrois, G., et al, A multiplicative model for improving microvascular flow estimation in dynamic contrast-enhanced ultrasound (DCE-US): theory and experimental validation, *IEEE Trans. Ultrason, Ferroelect. Freq. Control*, 60 (11), pp. 2284-2294, 2013
7. Kuenen, M. P. J., et al, Maximum-likelihood estimation for indicator dilution analysis, *IEEE Trans. Biomed. Eng.*, in press, e-version available at <http://dx.doi.org/10.1109/TBME.2013.2290375>
8. Lampaskis, M. and Averkiou, M., Investigation of the relationship of nonlinear backscattered ultrasound intensity with microbubble concentration at low MI, *Ultrasound Med. Biol.*, 36 (2), pp.306-312, 2010
9. Herold, I. H. F., et al, Volume quantification by contrast-enhanced ultrasound: an in-vitro comparison with true volumes and thermodilution, *Cardiovascular Ultrasound*, 11 (36), 2013

A high throughput device for measuring single microbubble response to ultrasound excitation

Paul Rademeyer, Joshua Owen, Ming-Wei Chang, Eleanor Stride

Institute of Biomedical Engineering, University of Oxford, United Kingdom

Microbubbles are well established as ultrasound contrast agents (UCA) due to their highly non-linear response to ultrasound excitation. They have also shown significant promise in a wide range of therapeutic applications. Unfortunately, despite the development of numerous theoretical models, their behaviour is difficult to predict quantitatively due to the complexity of their behaviour and lack of techniques for measuring their physical properties. Better understanding of a microbubble's response to ultrasound and its environment is crucial for the optimisation of current contrast enhanced ultrasound imaging techniques, therapeutic applications, fabrication methods and the validation of theoretical models.

Significant insights have been obtained over the past 2 decades through characterisation techniques including: high speed imaging, optical and acoustic scattering measurements, fluorescence and atomic force microscopy. There remain, however three significant challenges that have not yet been addressed together by a single technique: 1) Enabling a high throughput for large sample analysis 2) Isolation of microbubbles away from physical boundaries or each other and 3) Control and measurement of the ultrasound excitation for each microbubble. This work presents a device that combines optical and acoustical techniques to overcome these experimental challenges.

The experiment, figure 1, works by isolating microbubbles from a dilute suspension and entraining them in a hydrodynamically focussed flow, thereby avoiding any boundary and/or bubble interactions. Laser scattering measurements (408 nm, 0.5mW) are then used to detect and size a microbubble as it enters the focal region of an ultrasound transducer which is simultaneously triggered in order to measure the acoustic scattering from the bubble at a given (variable) frequency and peak negative pressure. Results from an initial study, figure 2, are presented, showing the potential of this technique for comparing different types of microbubble (in this case of varying composition) with a view to optimising their performance for contrast enhanced ultrasound imaging. The data demonstrate that whilst composition significantly affects acoustic response, there is also considerable variation in response across each microbubble population.

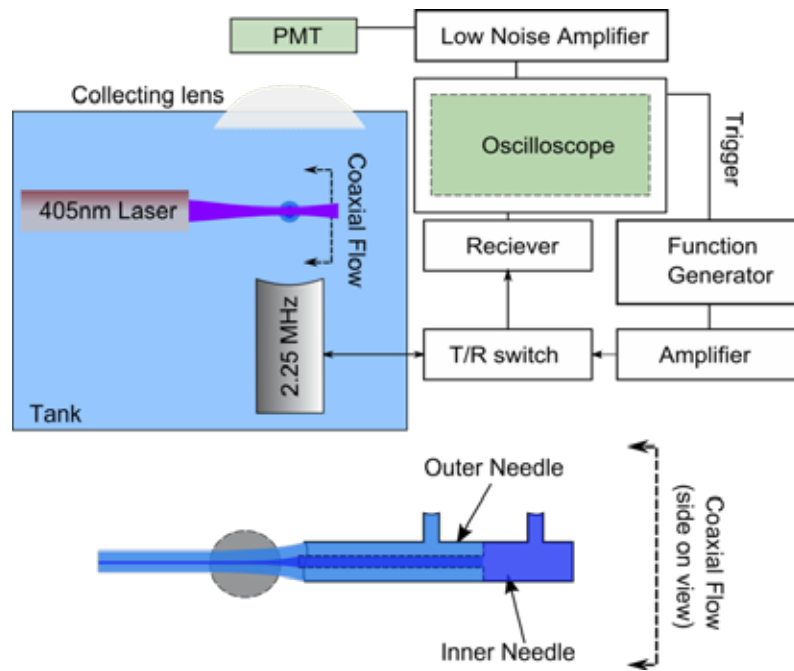


Figure 1: Schematic setup of simultaneous acoustic and optical measurement from single isolated microbubbles.

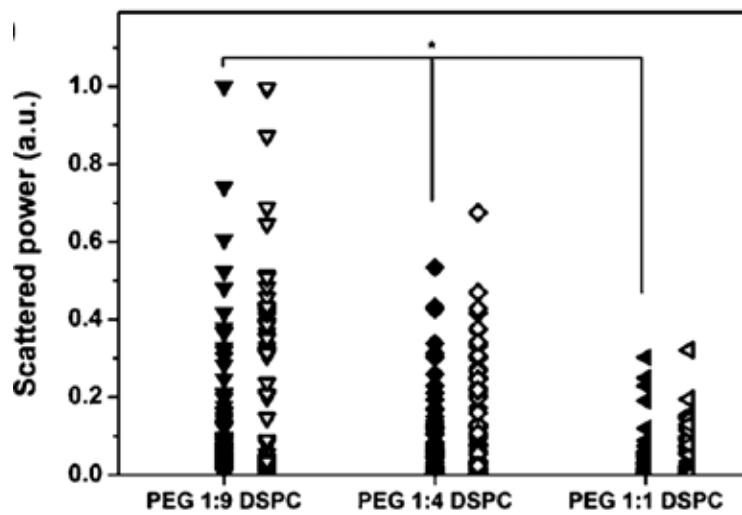


Figure 2: Normalized scattered power at the fundamental excitation frequency (2.25MHz) from bubbles coated with different composition surfactant mixtures ($n = 150, 80, 69$) ($* \chi^2 < 0.05$). Experimental results (closed symbol) are shown compared with those from simulations (open symbol) obtained using a modified Rayleigh Plesset equation for the measured size distribution and assuming a coating elastic modulus and viscosity respectively of 70 MPa and 507cP (1:9), 40 MPa and 426 cP (1:4), 10 MPa and 337 cP (1:1).

Numerical study on nonlinear oscillation and translation of an insonified microbubble

K.Omiya, H.Kubo, K.Terada, T.Sugiura

Mechanical Engineering, Faculty of Science and Technology, Keio University, Japan

Introduction

Insonified microbubbles (MBs) strongly reflect the ultrasonic for difference between the acoustic impedance of encapsulated gas in them and surrounding liquid. By making use of this characteristic, MBs are applied as contrast agents in medical field. Insonified MBs show complex nonlinear behavior under the ultrasonic excitation, thus irradiated waves also take complex forms. In many cases of past researches, the governing equations are derived by assuming spherically symmetrical oscillation. However, it is experimentally reported that MBs can oscillate nonspherically and translate. Therefore, it is significant clarifying how such complex behaviors occur. In this study, we simulated motion of an insonified MB by computational fluid dynamics solving numerically the governing equations by using C-CUP (CIP-Combined Unified Procedure) method.

Method

In the present simulation, we assume that the model is an axisymmetric gas-liquid two-phase flow. The gas phase is arranged in liquid phase as a MB and pressure pulsation is given from the left side of the computational domain, as shown in Fig.1. We adopt the equation of continuity, the Navier-Stokes equation and the energy equation considering the compressibility. Additionally, we use the density functional method to distinguish differences in physical properties of the gas and liquid phases. By calculating the advection equation for the density function, we are able to capture the gas-liquid interface. Furthermore, we adopt C-CUP method which can solve gas-liquid two-phase flow simultaneously. First calculating the advection terms by CIP (Cubic-Interpolated Pseudo-Particle) method, C-CUP method calculates the Poisson equation for the pressure field, which is not advection type.

Results

Fig.2 shows a time history of the pressure pulsation behind the MB and its wavelet transformation indicating the dominant frequency of received signal. The incident pressure amplitude is 100kPa; the incident frequency is 2.4MHz which is twice larger than the natural frequency of a MB of radius 3 μ m. The subharmonic component arises in the irradiated pressure wave, though it does not arise under the pressure amplitude 30kPa. Fig.3 and Fig.4 show distributions of pressure and axial flow velocity along the z axis, respectively. The horizontal axis indicates the location along the z axis nondimensionalized

by the diameter of the MB. Fig.5 shows the velocity vector distributions around the MB. As shown in Fig.4 (a) and Fig.5 (a), when the MB is expanded, surrounding liquids flow isotropically to the center of the MB. Additionally, as shown in Fig.3 (a), the pressures before the MB and that behind the MB are almost the same. As shown in Fig.4 (b) and Fig.5 (b), when the MB is compressed, surrounding liquids flow asymmetric to the center of the MB. Also, as shown in Fig.3 (b), the pressure in front of the MB is larger than that at the back of the MB. For these reasons, while the MB is compressed, the MB translates down and the front of the MB slightly dents as found in Fig.5 (b).

Conclusion

In this study, we simulated dynamics of an insonified MB by using an axisymmetrical gas-liquid two-phase flow model. Obtained results show the subharmonic component arises in radiated waves from a MB when the pressure amplitude of the incident wave exceeds a critical value. Additionally, we confirmed that a MB translates mainly while it is compressed.

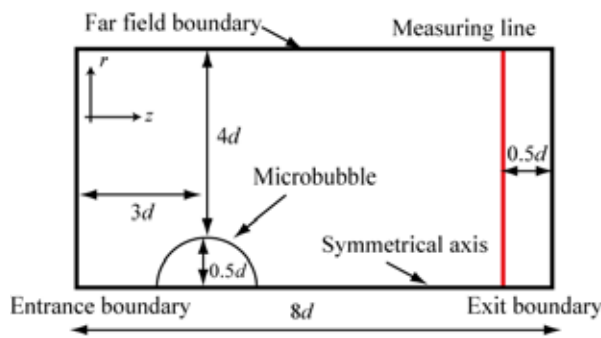


Fig.1 A schematic of computational domain

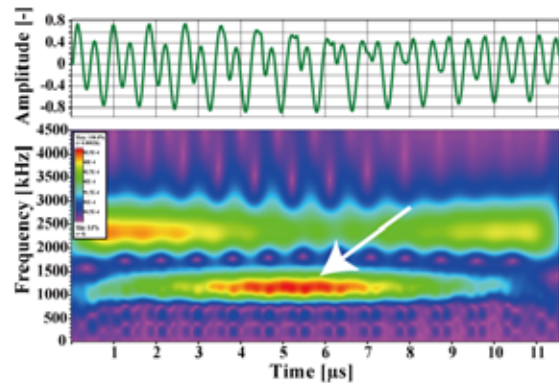


Fig.2 Time history of pressure pulsation behind microbubble and its wavelet transformation under pressure amplitude 100kPa, and incident frequency 2.4MHz (The white arrow shows the subharmonic component.)

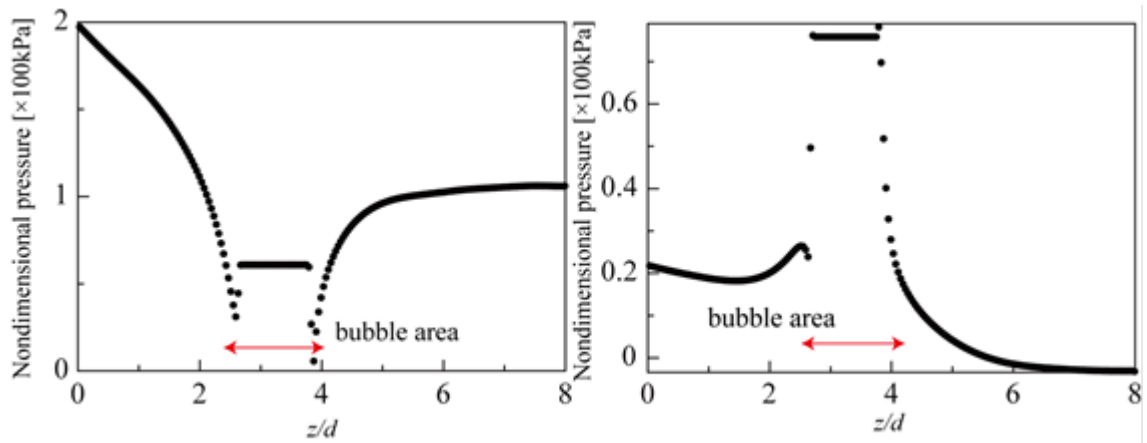


Fig.3 Pressure distributions along the z axis; (a)MB expansion , (b)MB compression

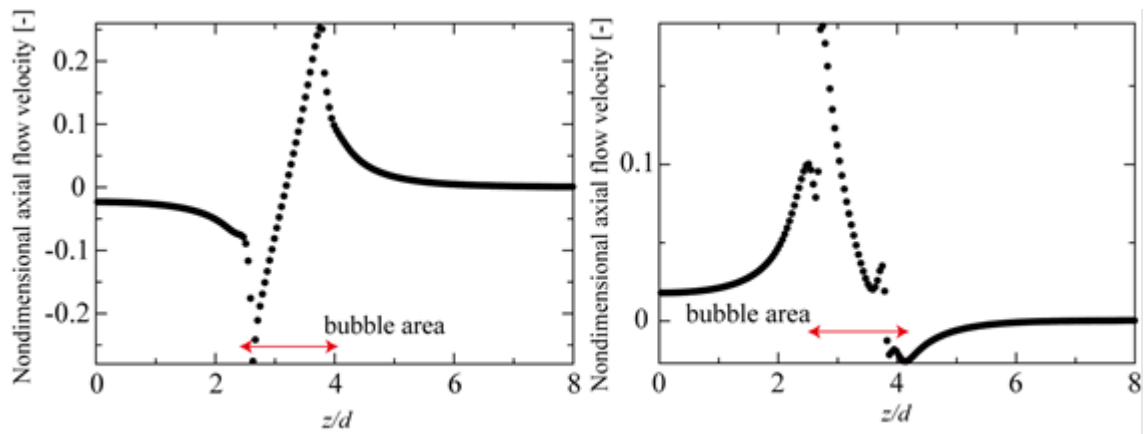


Fig.4 Axial flow velocity distributions along the z axis; (a)MB expansion , (b)MB compression

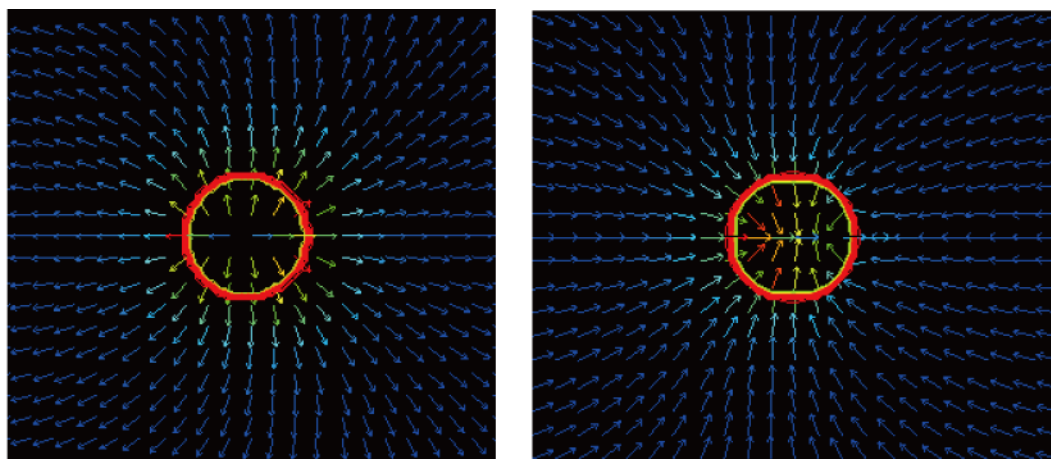


Fig.5 Velocity distributions around the MB ; (a)MB expansion , (b)MB compression

Pinched flow fractionation for ultrasound contrast agent enrichment

Maarten P. Kok, Tim Segers and Michel Versluis

*Physics of Fluids Group,
MIRA Institute of Biomedical Technology and Technical Medicine,
and MESA+ Institute of Nanotechnology
University of Twente, Enschede, The Netherlands*

Lipid monolayer-coated microbubbles are used as contrast agents in medical ultrasound imaging. Commercially available microbubble contrast agents are produced with techniques that result in a large size distribution. The acoustic (nonlinear) response of these contrast agents, or echo, strongly depends on the resonance frequency of the bubbles, which in turn is directly related to the microbubble diameter. Clinical ultrasound systems operate at a narrow bandwidth, optimized for the ultrasound transducer in use. Due to the small response of bubbles at off-resonance sizes, the contrast response would substantially improve, using a narrow size distribution of a well-controlled bubble size.

Here we present a novel, low-cost, lab-on-a-chip method for the separation of microbubbles by size, based on a microfluidic separation technique termed pinched flow fractionation (PFF)[1]. The operating principle of PFF is illustrated in Fig. 1. The microbubbles are introduced into a narrow channel (called the pinched segment), where the microbubbles are pinned to the wall by a co-flow from a buffer inlet channel (flow ratio of approximately 50:1). As the pinched segment expands into a broader segment, the distance from the center of the microbubbles to the wall is extended through microfluidic amplification. Thus, the microbubbles are separated by size.

A suspension of UCA microbubbles (sizes ranging from 0.5 to 8 μm) was used to investigate the separation performance of the microfluidic sorting chips made in polydimethylsiloxane (PDMS). Figure 2 shows the resulting positions of bubbles in the broadened segment as a function of their size, showing that this method can be successfully used to separate microbubbles by size. Due to the broad, continuous size distribution of the microbubbles, they are ideally suited to characterize the separation method over a broad range of particle sizes. We investigated the influence of several parameters, such as flow rates and pinched segment length, in which we find significant deviations from previously established models by Yamada et al.[1] and Vig and Kristensen[2].

Next, we designed a sorting device to extract microbubbles with a radius of 3 μm . Fig. 3 shows the resulting size distribution. Sorted microbubbles were then acoustically characterized using a setup comprised of three ultrasound transducers to measure both attenuation and scattering simultaneously, see Figs. 4 and 5. The results were compared to those found for native ultrasound contrast agent, showing a significantly improved response.

Parallelization of the sorting method may result in a way to enrich microbubble populations, leading to an order of magnitude increase in sensitivity of contrast-enhanced ultrasound imaging techniques, without the need for externally powered sorting devices.

References

1. Yamada, M.; Nakashima, M.; Seki, M. *Pinched Flow Fractionation: Continuous Size Separation of Particles Utilizing a Laminar Flow Profile in a Pinched Microchannel*, *Anal. Chem.* 2004 Vol. 76, 5465
2. Vig, A.L.; Kristensen, A. *Separation Enhancement in pinched flow fractionation*, *Applied Physics Letters* 2008, Vol. 93, 203507

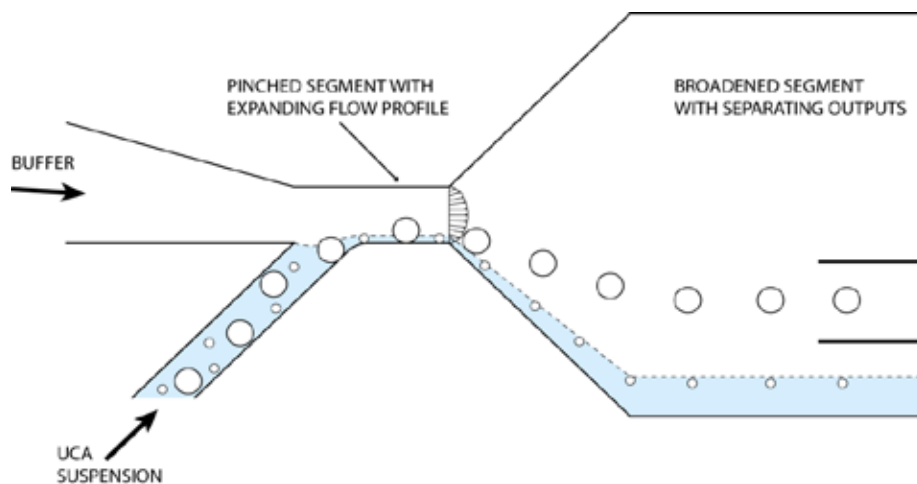


Figure 1: Schematic view of the lab-on-chip device used to sort microbubbles. The bubbles enter the pinched segment (width 12 μm). Bubbles then separate due to the expansion of the channel, to be sorted into exit channels positioned in the broadened segment (width 300 μm).

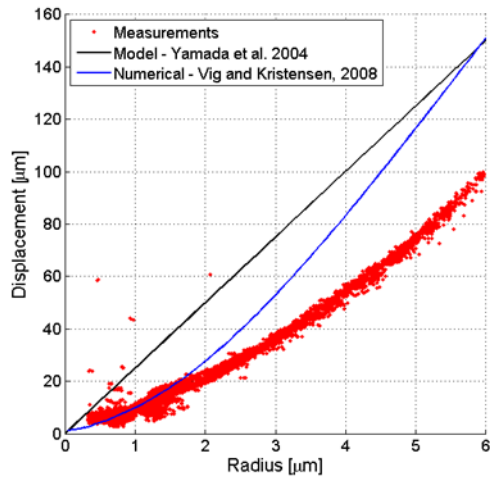


Figure 2 - Distance from the lower wall in the broadened segment as a function of the bubble size. The sorting principle is evident, however, significant deviation from models in the literature [1,2] is observed.

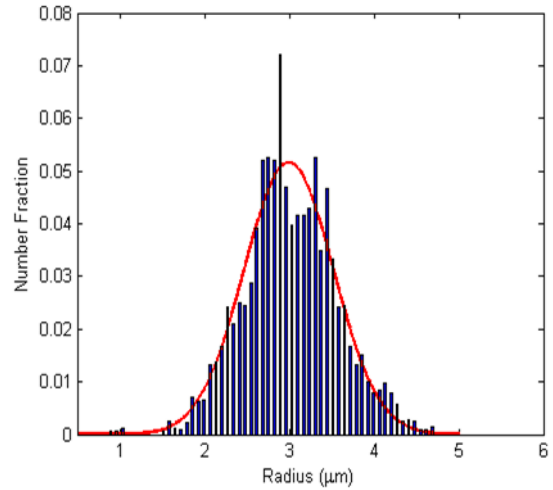


Figure 3 - Size distribution of microbubbles obtained from the PFF device.

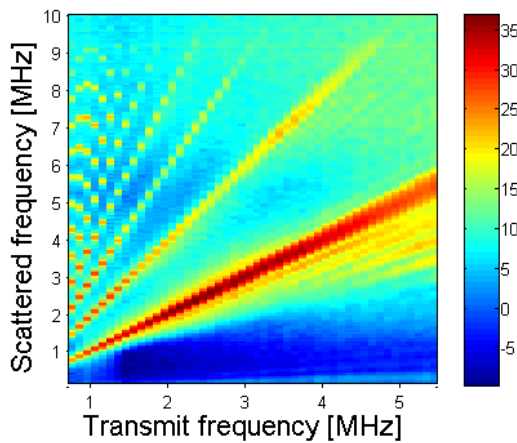


Figure 4: Scattered power as a function of the transmitted frequency (in dB re: noise level). UCA was insonified with a 16-cycle ultrasound pulse at 35kPa, at a PRF of 100Hz. The maximum scattered power of the fundamental frequency occurs at 2.2MHz. Higher harmonics can clearly be observed.

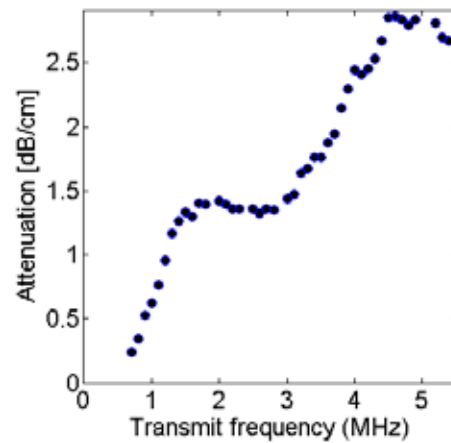


Figure 5: Attenuation as a function of the transmitted frequency for sorted ultrasound contrast agent. The results show a high attenuation at the higher frequencies. This indicates that the bubbles smaller than the resonant size at a given transmit frequency attenuate the signal significantly, while not significantly contributing to the echo.

Adapting amplitude modulation to plane-wave Doppler imaging

Charles Tremblay-Darveau¹, Ross Williams², Laurent Milot², Matthew Bruce³ and Peter N. Burns^{1,2}

¹Department of Medical Biophysics, University of Toronto, Toronto, Ontario, Canada

²Sunnybrook Health Sciences Centre, Toronto, Ontario, Canada

³Supersonic Imagine, Aix en Provence, France

Introduction

Ultrasound synthetic images acquired with a single plane wave have higher frame rates ($<7.7\text{kHz}$ assuming a depth of 10 cm) than conventional scanners ($<60\text{ Hz}$). Such frame rates permit the combined use of pulse inversion (PI) and Doppler (also known as pulse inversion Doppler [1]), without compromising the ensemble length, which would result in reduced SNR and flow sensitivity. It was previously shown by our group [2] that this allows the display of perfusion and large vessel flow simultaneously. While Doppler is useful for resolving large vessels from the perfusion background, our ability to detect perfusion behind the hyperechoic tissue signal is still intrinsically limited by the contrast-to-tissue ratio (CTR) achieved with the contrast sequence used (e.g. how well we suppress the tissue echo while keeping the microbubble signal). PI isolates the even harmonics of the microbubble echoes, but imperfect phase inversion in the transmitters of clinical scanners often hinders proper tissue signal cancellation, limiting the CTR achieved with PI. On the other hand, amplitude modulation (AM) selectively images microbubble non-linearity by a sequence of pulses with different acoustic amplitude. As AM does not rely on phase inversion and is usually accomplished by apodisation of the transmit array, it often yields better tissue cancellation and improved CTR, albeit at the cost of resolution (fundamental signal from the third order non-linearity). While there is an advantage in adapting AM to Doppler processing, the reasoning behind PI-Doppler (PID), namely that an inverted phase can be re-expressed as a π phase shift leading to a separation of the non-linear from the linear signal in the Doppler spectrum, does not obviously hold for AM. In this work, we show that it is possible to combine AM and Doppler processing if the AM Doppler vectors are *a priori* renormalized on an appropriate basis. Under such conditions, a straightforward Doppler analysis analogous to PID can then be used. *In-vitro* proof of principle is first presented to validate this claim, followed by *in-vivo* perfusion measurements in a rabbit kidney.

Method

An AM modulation Doppler vector is acquired by repeatedly insonicating the microbubbles with ‘full’ (+1) and ‘half’ (+1/2) amplitude pulses. The echoes are then scaled by a factor 2 for the ‘half’ amplitude pulse as shown in Figure 1. The linear signal, unaffected by the amplitude modulation, is centred around 0Hz in the Doppler spectrum. In contrast, the nonlinear signal does not perfectly align even after renormalization, resulting in a periodic oscillation centred at Nyquist frequency. A similar approach can also be employed for amplitude modulation pulse inversion (AMPI or CPS, pulse 1 = +1, pulse 2 = -1/2) and PI as long as the appropriate normalization is used. This was first tested *in vitro* by measuring the flow of both bubbles and a linear scatterer (cornstarch) in a tissue-mimicking phantom containing a wall-less vessel (2% weight ratio of agar in water with graphite scatterers at a concentration of 25g per Litre of water, corresponding to an attenuation coefficient of 0.3dB/[cmMHz] [3]). Plane-waves of 1 cycle at 4.5MHz center frequency were emitted using an *Aixplorer* scanner (Supersonic Imagine, Aix-en-Provence, France) with an 8MHz centre frequency linear array probe at a pulse repetition frequency of 2000Hz. AM, AMPI and PI Doppler were then performed *in-vivo* in a New Zealand white rabbit. *Definity* (10 μ L/kg bolus) was used in all experiments.

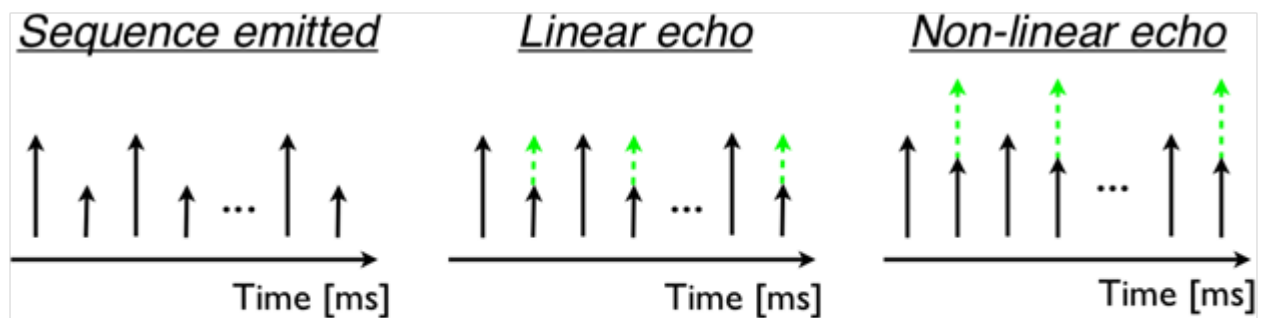


Figure 1: Proposed amplitude modulation Doppler processing scheme. A sequence of ‘full’ and ‘half’ amplitude pulses is emitted. The received echo is then multiplied by 2 for the ‘half’ amplitude pulses. The linear echo then does not experience periodic oscillation between the different amplitude pulses (a consequence of linearity), and is therefore centered around 0Hz in the Doppler spectrum. This does not hold for the non-linear echo, which is centered at the Nyquist frequency.

Results

a) In-vitro proof of principle

Figure 2 shows the Doppler spectra of the normalized AM, AMPI and PI sequences for both flowing linear scatterers (a) and flowing microbubbles (b). The linear echo is preserved around 0Hz for both cornstarch and microbubbles for all sequences. On the other hand, the non-linear signal component (around the Nyquist frequency) is much stronger for *Definity* than for cornstarch. The residual non-linear signal in cornstarch is attributed to non-linear propagation. The proposed method therefore allows to separate moving tissue from moving microbubbles for all contrast sequences.

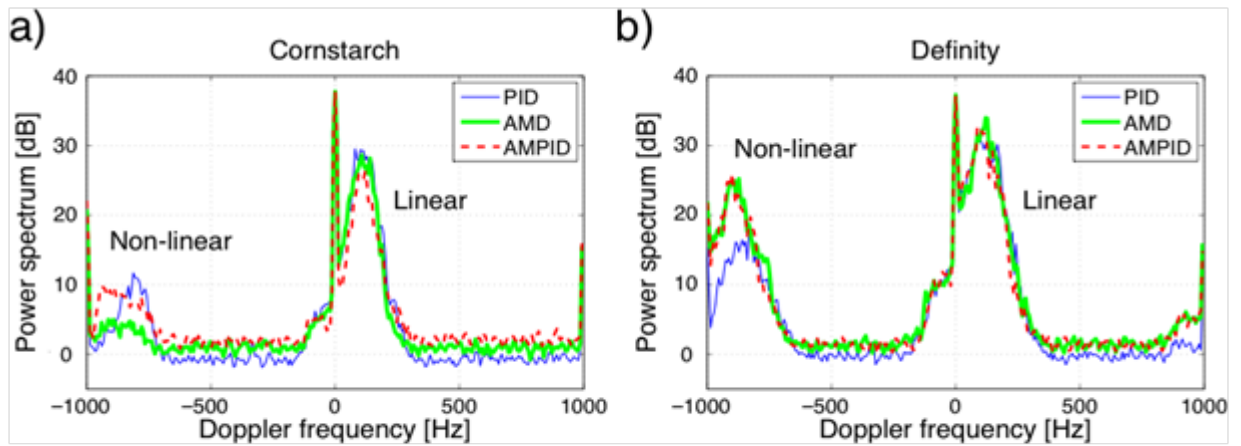


Figure 2: AM, PI and AMPI Doppler spectra for cornstarch (a) and Definity microbubbles (b). The non-linear signal in the 600Hz to 1000Hz range, e.g. in proximity of the Nyquist frequency, is much stronger for Definity than cornstarch.

b) In-vivo demonstration in a rabbit kidney

The perfusion of a rabbit kidney is imaged using AM, AMPI and PI Doppler, keeping the same anatomic plane for all cases. Figure 3 shows the resulting power Doppler image, depicting artery and vein morphology, and perfusion images (green colormap), sensitive to the presence of bubbles independently of their velocity. All images highlight similar vascular patterns. While AM does appear to have a lower resolution compared to PI and AMPI, the excitation frequency could be increased to recover resolution as most of the non-linear echo occurs at the fundamental.

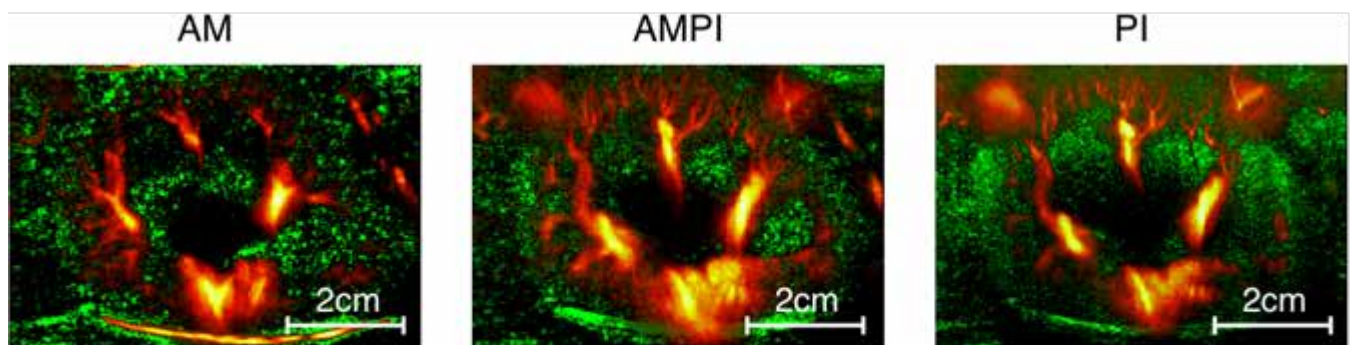


Figure 3: Contrast-enhanced images (green colormap) of a rabbit kidney overlaid by the AM, PI and AMPI Doppler (hot colormap). All contrast-enhanced sequences show similar vascular patterns.

Conclusion

Contrast-enhanced amplitude modulation imaging can be adapted to Doppler processing, allowing the separation of the echo of moving microbubbles from moving tissue. As AM, AMPI and PI perform differently under different imaging conditions, this work opens the path to new trade-off opportunities in contrast-enhanced Doppler imaging.

References

1. *D. Simpson, C. Chin, P. Burns. IEEE transactions on ultrasonics, ferroelectrics, and frequency control (1999) vol. 46 (2) pp. 372-382*
2. *C. Tremblay-Darveau, R. Williams, L. Milot, M. Bruce, P. Burns . IEEE International Ultrasonics Symposium (2012), pp. 1315-1318*
3. *M. Burlew, E. Madsen, J. Zagzebski, R. Banjavic, S. Sum. Radiology (1980), vol. 134 (2) pp. 517-520*

Microbubbles as stable drug-loadable structures toward targeted, triggered drug delivery

Sally A. Peyman*, Radwa H. Abou-Saleh*, Nicola Ingram**, Gemma Marston**,
P. Louise Coletta** and Stephen D. Evans *

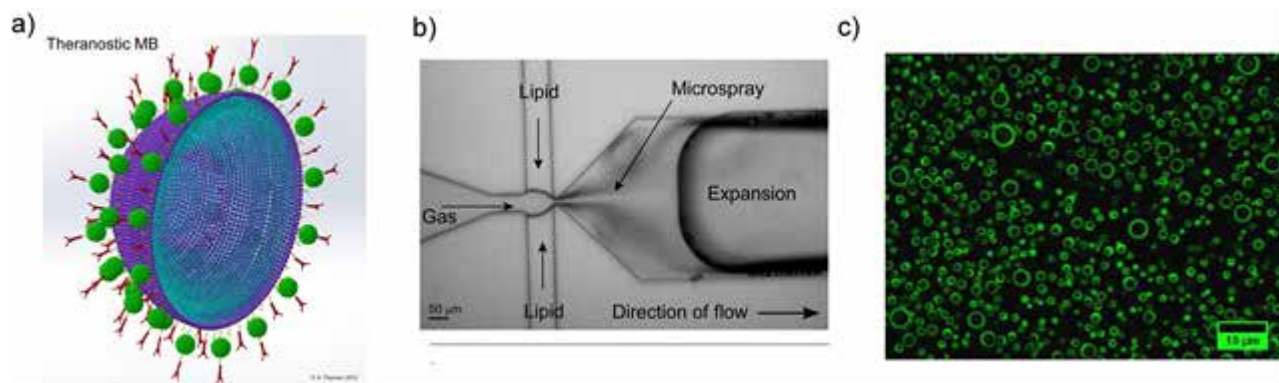
*School of Physics and Astronomy, University of Leeds, UK. LS2 9JT

**Leeds Institute for Molecular Medicine, St James's Hospital, Leeds, UK. LS9 7TF

Micron-sized, lipid stabilised bubbles of gas have been used as image enhancers for ultrasound (US) for over 30 years[1]. In recent years interest has bloomed in coupling the diagnostic properties of MBs with drug delivery techniques to produce theranostic agents (figure 1a). MBs loaded with drugs are targeted with antibodies to diseased cells and MB accumulation monitored using US. The US destruction pulse is delivered to destroy the MBs and thus release the drug in the immediate region of the diseased cell, creating a truly targeted, triggered drug delivery vehicle.

Microfluidics has been utilised to produce highly monodisperse populations of μf -MBs with polydispersity index below 5% [2]. However, such approaches inherently suffer from low bubble concentrations, usually $< 10^7$ MBs/mL while conventional MBs used for contrast-US are in the range of 10^{10} MBs / mL. We demonstrated a new flow-focusing (FF) microfluidic design featuring a 3D expansion in the exit channel which facilitated a new microspray formation regime (figure 1b) [3]. The microspray regime boosts the concentration of μf -MBs to $>10^9$ MBs / mL in 6 minutes, equating to a μf -MB production rate of 2.5 MHz per chip. MB stability remains a huge challenge to MB diagnostic and drug delivery approaches, we have greatly improved our *in vitro* μf -MB lifetimes from 60 minutes to >3 hours (cell culture media at 37°C) and also the *in vivo* signal from these μf -MBs in the aorta of a mouse model in which μ -MBs showed excellent longevity, surpassing lifetimes of some commercially available MBs.

We have reported the on-chip surface functionalisation of the MBs with drug-loaded liposomes in a one-step approach[3]. Complex surface architectures self-assembled as μ -MBs were formed using streptavidin-biotin linkage and this approach has now been used to successfully load Doxorubicin, Irinotecan and Luciferin onto μf -MB carriers (figure 1c). Functionalised μf -MBs concentrations remained $> 10^9$ / mL and production times < 10 minutes. In addition, many anti-cancer drugs that have been developed have hydrophobic properties and as a result cannot be administered systemically. Our current work explores the possibility of delivering hydrophobic drugs inside Lipid-Oil-Nano-Droplets (LONDS) attached to the μf -MB surface. Recent work has demonstrated the successful loading of Combretastatin A-4 into LOND structures using triacetin as a carrier oil.



References

1. E. G. Schutt, D. H. Klein, R. M. Mattrey and J. G. Riess, *Angewandte Chemie-International Edition*, 2003, 42, 3218-3235
2. K. Hettiarachchi, E. Talu, M. L. Longo, P. A. Dayton and A. P. Lee, *Lab on a Chip*, 2007, 7, 463-468
3. S. A. Peyman, R. H. Abou-Saleh, J. R. McLaughlan, N. Ingram, B. R. G. Johnson, K. Critchley, S. Freear, J. A. Evans, A. F. Markham, P. L. Coletta and S. D. Evans, *Lab on a Chip*, 2012, 12, 4544-4552

Acoustic droplet vaporization is initiated by superharmonic focusing

*Oleksandr Shpak¹, Martin Verweij², Hendrik J. Vos^{2,3}, Detlef Lohse¹, Nico de Jong^{2,3}
and Michel Versluis¹*

¹*Physics of Fluids group, MIRA Institute of Biomedical Technology and Technical Medicine, MESA+ Institute of Nanotechnology, University of Twente, Enschede, the Netherlands*

²*Biomedical Engineering, Erasmus MC, Rotterdam, the Netherlands*

³*Acoustical Wavefield Imaging, Delft University of Technology, Delft, The Netherlands*

Background, motivation and objective

Ultrasound can be used to phase-transition liquid droplets into gas bubbles – a process known as acoustic droplet vaporization (ADV). These droplets are composed of a volatile perfluorocarbons, such as perfluoropentane (PFP, 29°C boiling point). A PFP emulsion does not spontaneously vaporize when injected in vivo at 37°C. However, upon exposure to ultrasound above certain acoustic pressure amplitude, the PFP within the emulsion is vaporized. This opens up the possibilities in a wide variety of diagnostic and therapeutic applications, such as tumor imaging, localized drug delivery, and embolotherapy. However, the physical mechanisms underlying the ultrasound-triggered nucleation are largely unexplored. Here we show that acoustic droplet vaporization is initiated by a combination of two phenomena: highly nonlinear distortion of the acoustic wave before it hits the droplet and focusing of the distorted wave by the droplet itself.

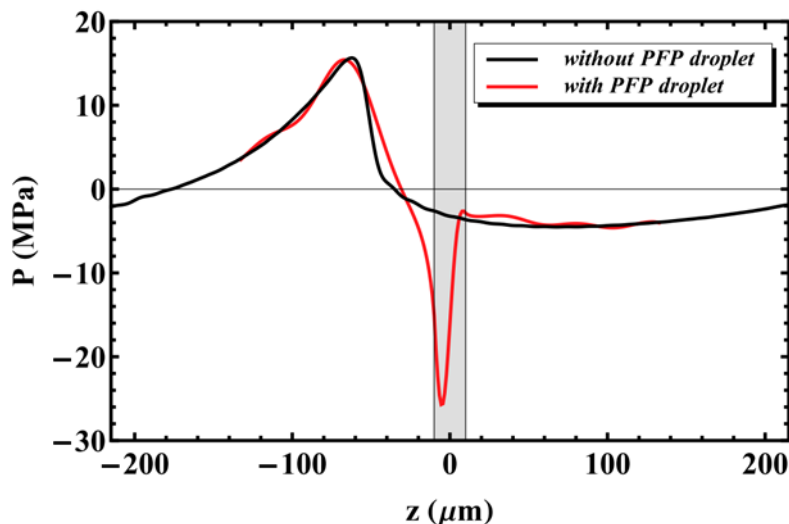


Fig. 1: Snapshot of the superharmonic focusing effect within a spherical droplet. The black line represents the acoustic pressure waveform on the axis of symmetry ($\theta = 0$) as a function of the coordinate along the US propagation direction in the absence of a droplet. The red solid line is the focused pressure in the presence of the droplet. The snapshot is taken right at the moment of minimum focused pressure. The horizontal axis displays one full wavelength in the medium outside the droplet. The gray shaded region depicts the position of the droplet $R = 10 \mu\text{m}$. The focusing spot lies around $z = -0.4 R$ and the pressure is amplified 5.8 times compared with the incident acoustic pressure -4.5 MPa .

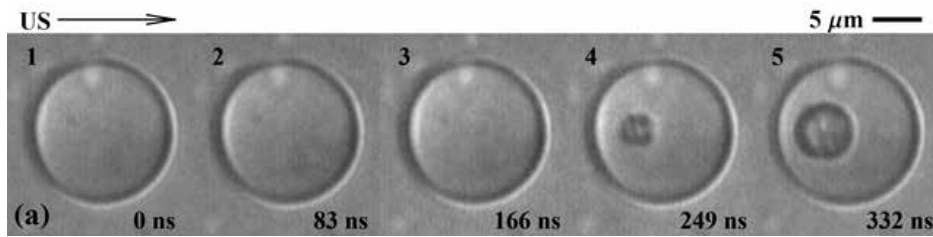


Fig. 2: A set of consecutive images showing acoustic droplet vaporization of a 7.4- μm -radius PFP droplet taken at a frame rate of 12.6 million frames per second. The droplet is triggered by an eight-cycle, 5-MHz frequency ultrasound pulse. The nucleation at the focusing spot is initiated between frames 3 and 4. Frames 4 and 5 show the subsequent vapor bubble growth.

Results and discussion

At high excitation pressures, nonlinear distortion causes significant superharmonics with wavelengths of the order of the droplet size. These superharmonics strongly contribute to the focusing effect on a droplet sphere. The example of the focused wave is theoretically calculated and plotted in Fig. 1 in spatial coordinates in the propagation direction, along the axis of symmetry. The black line represents one wavelength of the wave, $\lambda = 438\mu\text{m}$, in the absence of a droplet. The red line represents the same wave in the presence of an $R = 10\mu\text{m}$ droplet. The position of the droplet is indicated by the gray shaded region in Fig. 1. The red curve shows the pressure right at that particular time instant when the maximal negative pressure is reached over the full period $2\pi = \omega$. It can be observed that a focused pressure of -26 MPa is achieved within the droplet for an incoming wave with a peak negative pressure of -4.5 MPa. A nearly six fold increase in peak negative pressure amplitude is observed in a concentrated region on the proximal side around $z = -0.4 R$. The pressure amplification factor in the focusing spot as well as its location depend on the input parameter values (i.e., frequency, pressure amplitude, transducer geometry and size), which prescribe the propagation distance to the focal point. The higher the pressure, the more nonlinear the wave becomes. The focusing effect strongly depends on the frequency as well. Here two effects come into play. First, the nonlinear propagation depends on frequency and, second, there is a strong coupling between the frequency and the droplet size owing to diffraction on a sphere. Our interpretation is validated with experimental data (see example on Fig. 2) captured with an ultrahigh-speed camera on the positions of the nucleation spots, where we find good agreement with the theoretical prediction.

Conclusion

Acoustic droplet vaporization is initiated by the focusing of the superharmonics of a nonlinearly distorted acoustic wave within the droplet. In the parameter range considered, the focusing leads to up to a ten-fold increase of the incident peak negative pressure in a well-defined focusing spot. The location of the focusing spot as well as the focusing strength depends on the frequency of the incident wave and on the size of the droplet. A higher frequency, and vice versa a larger droplet radius, i.e. a smaller wavelength compared to the droplet size, leads to a more pronounced focusing effect and

consequently leads to smaller pressure amplitudes required for activation. Nonlinear propagation is shown to have a crucial role in ADV. It causes distortion of the pressure waveform and the resulting superharmonics are highly focused within the spherical droplet. Thus, the transducer geometry, as well as the parameters of nonlinearity of the propagating medium have an effect on the focusing strength and the position of focusing. The super harmonic focusing effect derived from a theoretical diffraction model is compared to experimental results. First, the dependence of the activation threshold on various system parameters, such as pressure amplitude, frequency and droplet size are discussed in the framework of recent experiments by various research groups. Secondly, temporal and spatial nucleation maps obtained with the ultra-high speed camera were compared in the context of the present theoretical work and were found to agree very well with the theory.

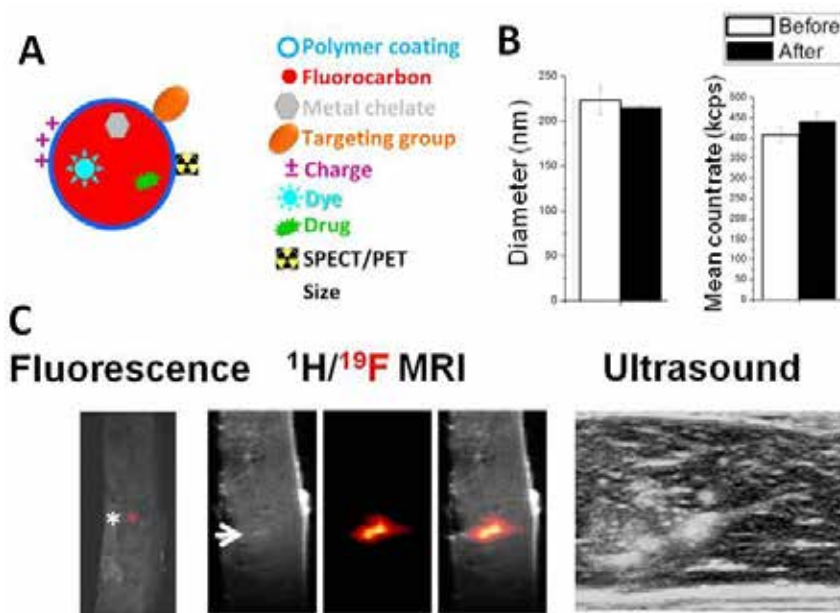
Clinically-relevant, customizable agents for multimodal imaging

M. Srinivas¹, C.L. de Korte¹, G. Lajoinie², M. Versluis², C. G. Figdor¹, I.J.M. de Vries¹

¹Radboud UMC, Nijmegen, the Netherlands
²University of Twente, Twente; the Netherlands

We have developed an imaging agent that combines the ability for frequent, real-time imaging of ultrasound with the quantitative ability of ¹⁹F MRI for use in clinical personalized medicine applications, such as cellular therapeutics. The agent consists of a polymer-entrapped liquid perfluorocarbon (PFC) for long-term cell tracking using multimodal imaging¹. The particles can be readily customized (Fig. A) in terms of size (200-1000nm), content (e.g. drug, fluorescent dye) and coating (e.g. targeting antibody, radionuclide), and are suitable for clinical and preclinical applications such as cell tracking and drug delivery.

Importantly, unlike microbubble ultrasound contrast agents, these particles are extremely stable and do not appear to be affected by ultrasound (B); they are therefore suitable for longitudinal, multimodal imaging.



Methods

Particles are synthesized and imaged as described². Briefly, for (C) ¹⁹F MR images were acquired at 11.7T (Bruker) using a RARE sequence with 512 averages, TR/TE of 960/46ms, 64x32 matrix and 4mm isotropic voxels. Ultrasound imaging was carried out using a Philips SONOS 7500 scanner with a

linear array transducer (11-3L) at a centre frequency of 7.5MHz.

Results & discussion

We have previously shown that these particles perform extremely well for ^{19}F MR imaging³, in terms of low toxicity and high signal intensity. The agents are very stable, both to long term storage and other stresses, such as cell labeling and probe sonication (**B**; dynamic light scattering data on particle diameter and mean count rate shown before and after exposure to 30 seconds of probe sonication). The particles can also be stored without significant change in diameter, ^{19}F content or mean count rate for at least 6 months. Fig. **C** shows 2 million labeled primary monocyte-derived human dendritic cells, as currently used in clinical cellular therapeutics, injected in an ex vivo tissue sample. The labeled cells are readily detected using fluorescence, MR and ultrasound imaging.

The mechanism of acoustic contrast generation is unclear, since it appears from ultra high-speed imaging experiments that the liquid PFC core does not vaporize during insonation, including probe sonication. This is further corroborated by ^{19}F NMR, dynamic light scattering and electron microscopy data (not shown here).

Conclusion

The novel agent is not affected by ultrasound energy, including exposure to probe sonication, and can be used to label primary human therapeutic cells, without any significant changes to their physical or functional properties, such as expression of cell surface markers or migratory and stimulatory ability. Labeled cells can be detected using multiple imaging modalities (**C**). All components of the particles have previously been used in humans, and the particles can be synthesised for clinical use. Thus, these particles are very promising for clinical multimodal imaging applications, particularly cell tracking and targeted therapeutics, with broader preclinical applications.

References

1. Srinivas M, de Vries IJ, Cruz JL, de Korte CL, Figdor CG. *Contrast agents for imaging* (filed 09/2012)
2. *Biomaterials* 31(27):7070-7, 2010
3. *Biomaterials* 33(34): 8830-40, 2012

Ultrasound molecular imaging enhancement by Volumic Acoustic Radiation Force (VARF)

Nicolas G. Rognin ¹, Sunil Unnikrishnan ², Alexander L. Klibanov ²

¹Toshiba Medical Research Institute USA, Inc., Redmond, WA, USA

²Cardiovascular Division, University of Virginia, Charlottesville, VA, USA

Clinical potential

Ultrasound molecular imaging can potentially improve outcomes of oncological practice in the future. Possible clinical applications range from tumor detection to quantitative therapy monitoring, where early determination of patient response to an anti-cancer drug treatment plays a crucial role in terms of survival.

Ultrasound molecular imaging uses intravenous administration of targeted microbubbles decorated with a specific ligand on their surface. As a result, they adhere to tumor vasculature (endothelium) overexpressing a biomolecule for which the specific ligand has a high affinity. Such adhesion of targeted microbubbles to endothelium makes tumor detection conspicuous in ultrasound contrast images.

Objective

To enhance adhesion, it was demonstrated in the literature that acoustic radiation force (ARF) [1] (“pushing” targeted microbubbles towards endothelium) was effective for 2D imaging [2] and also slice by slice [3]. Generalization of ARF in 3D called “Volumic Acoustic Radiation Force (VARF)” is promising; in particular for prostate gland that can be entirely scanned with a clinical endocavity 3D transducer. Our objective was to validate ultrasound molecular imaging enhancement by VARF.

Materials and Methods

In vitro

Acoustic parameters were implemented into a modified clinical ultrasound imaging system Aplio™ XG (Toshiba Medical Systems, Otawara, Japan) equipped with a mechanically swept convex array transducer (PVT-681MV). To maximize the effect of VARF while minimizing destruction of microbubbles, optimal acoustic parameters (**Table 1**) were defined using a suspension of agitated microbubbles in a glass beaker.

Adhesion of targeted microbubbles with VARF compared to Native mode (without VARF) was assessed in flow conditions using the *in vitro* setup of **Figure 1**. The biomolecule VCAM-1 (known to be overexpressed in tumor vasculature) was our target. Targeted ultrasound contrast agent was based on

biotinylated microbubbles conjugated to anti-VCAM-1 antibody using streptavidin. The targeted microbubbles were infused in a parallel plate flow chamber (IBIDI, Martinsried, Germany) coated with murine VCAM-1 (3 µg/ml). Flow was set to reflect physiological conditions in tumors (wall shear stress at 0.6 dyne/cm²).

Parameter	Volumic Acoustic Radiation Force	Imaging
Frequency [MHz]	3.6	5.5
Number of cycles	64	-
Duty cycle [%]	15	-
Acoustic pressure [kPa]	30	140
Focus depth [cm]	-	1
Mode	Plane wave	Contrast
Volume rate [Hz]	4	1
Exposure duration [min]	1	-

Table 1: Optimal acoustic parameters.

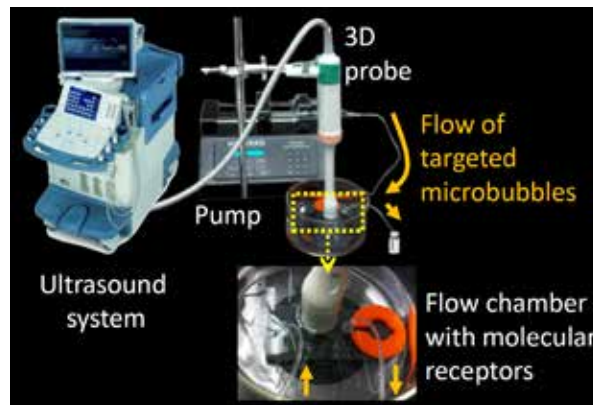


Figure 1: *In vitro* setup.

In vivo

Pre-clinical validation in a small animal model (non-xenograft mouse tumor hind leg tumor) was performed in triplicate. Two types of ultrasound contrast agents were injected as bolus ($\sim 2 \times 10^6$ particles): targeted microbubbles (same as *in vitro*) and control microbubbles with no ligand.

Volumic quantification

Enhancement ratio (VARF / Native) was computed in 3D to evaluate the gain in microbubble adhesion with VARF. Seven 7 minutes after injection, microbubble accumulation (average over 20 seconds) was quantified in a volume of interest outlining the flow chamber (*in vitro*) or the tumor (*in vivo*). Any

remaining circulating microbubbles were removed by subtraction of post-destruction value (average over 20 seconds), obtained after destruction of microbubbles by high acoustic intensity in 3D (Mechanical Index=1.42).

Results

The **Figure 2a** shows a typical example of contrast kinetics in tumor. Corresponding contrast images at 7 minutes in VARF and Native modes are shown on **Figures 2b** and **2c**, respectively. In the bar graph of **Figure 3a**, enhancement ratio for targeted microbubbles was 6.1 *in vitro* (SD = 2.1, n = 3) and 4.1 *in vivo* (SD = 2.3, n = 3). For control microbubbles, it was 0.8 *in vivo* (SD = 0.1, n = 3). Furthermore, a volume rendering method was developed to show added value of VARF. Notably, volume fusion (VARF in red hues and Native in cyan hues) of **Figure 3b** allows delineating additional vessels compared to the Native volume of **Figure 3c**.

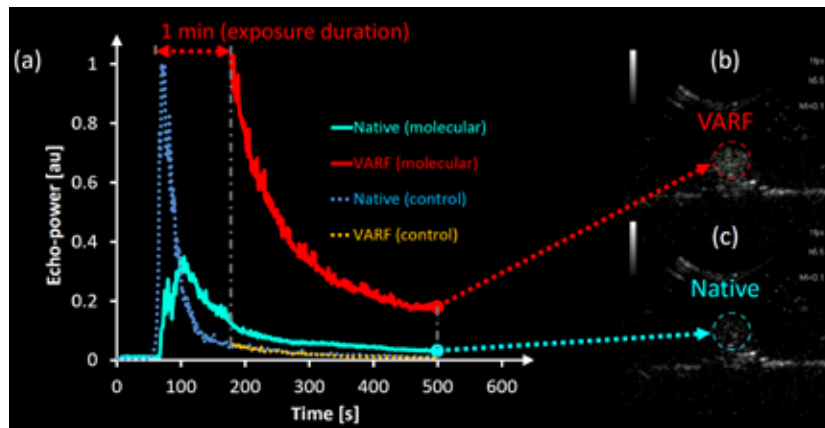


Figure 2: (a) *in vivo* contrast kinetics in tumor, corresponding contrast images at 7 min (b) with VARF and (c) Native.

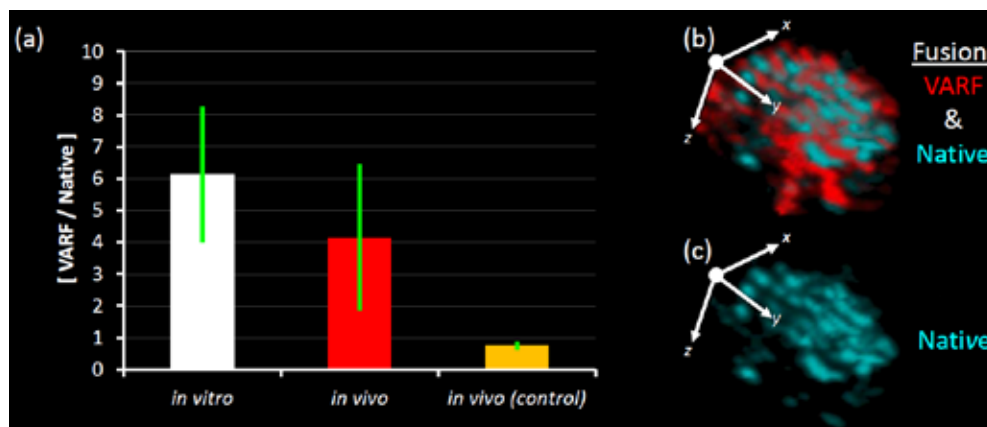


Figure 3: (a) enhancement adhesion ratio of microbubbles, volume rendering of (b) additional enhancement with VARF in red hues compared to (c) Native in cyan hues.

Conclusion

In our study, pre-clinical in vivo validation of VARF (enhancement ratio of 4.1) was demonstrated with a clinical ultrasound imaging system equipped with a 3D transducer, offering potential implementation into the clinic. Further processing will include advanced 3D quantification to fully characterize the vascular network of tumoral tissue.

Acknowledgments

The authors would like to thank Ms. Y. Kanayama, Mr. G. Guenette, Mr. R. Woods and Mr. C. Sanders from Toshiba for their technical support.

References

1. Dayton P, Klibanov AL, et al. Acoustic radiation force in vivo: a mechanism to assist targeting of microbubbles. *Ultrasound Med Biol.* 1999;25(8):1195-201
2. Frinking PJ, Tardy I, et al. Effects of acoustic radiation force on the binding efficiency of BR55, a VEGFR2-specific ultrasound contrast agent. *Ultrasound Med Biol.* 2012;38(8):1460-9
3. Gessner RC, Streeter JE, et al. An in vivo validation of the application of acoustic radiation force to enhance the diagnostic utility of molecular imaging using 3-d ultrasound. *Ultrasound Med Biol.* 2012;38(4):651-60

Effects of molecule size and microbubble affinity on delivery

Jason Castle

GE Global Research, Niskayuna, NY 12309, USA

A preliminary investigation on the roles of agent size (molecular weight) and bubble-binding affinity play in delivery of agents to a target *in vivo* was carried out by the research team at GE GR. To accomplish this, a systematically varied set of model compounds were designed and synthesized. The team established a matrix in which the delivery of different molecular weight PEGylated cyanine dyes could be directly compared. Two different dyes were functionalized - one with high affinity for microbubbles and one with relatively low affinity. Bound to these were two different PEG chain lengths, with molecular weights of 20,000 g/mole and 550 g/mole. These compounds were used to evaluate the delivery of structurally similar large molecules and small molecules, in both good bubble-binding as well as weaker bubble-binding scenarios. Each of these agents was delivered with an ultrasound system via microbubble cavitation (MI~1.3) within the liver.

To test this system the team developed several methods to semi-quantify fluorescence retention in the liver of rats following perfusion. First, the whole liver was imaged, and this was followed by a dye extraction process of tissue disruption and cell lysis to free sequestered agent. Using calibration curves generated from liver samples spiked with known concentrations of agent, the data from the dye extraction procedures was used to estimate the amount of agent delivered to the liver.

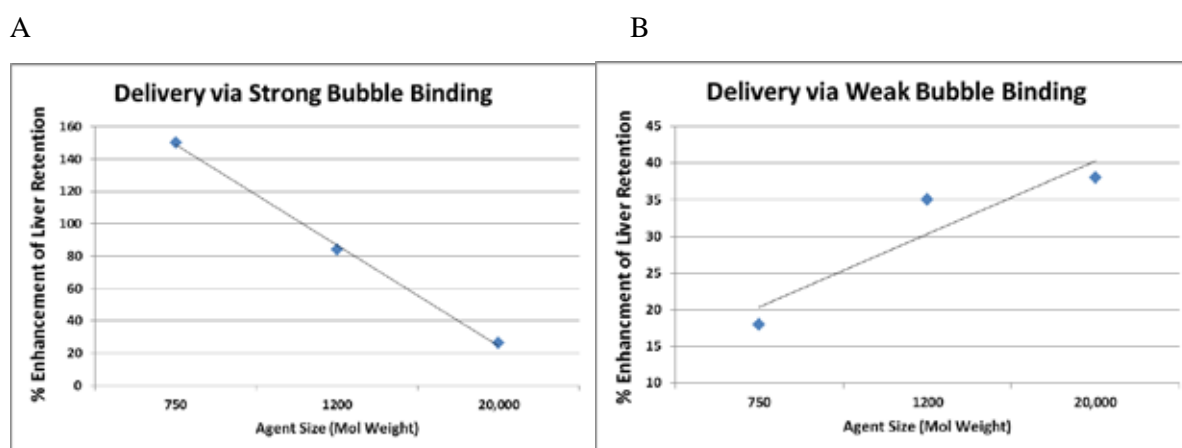


Figure 1. Delivery of agents with high and low affinity for microbubble. A) Comparison of retention of three agents of different molecular weights. Each of these had an equal amount of Cy5 dye which acts as both a fluorescent label as well as a strong binder to our microbubble. B) Comparison of retention of three agents of different molecular weights. These had an equal amount of Cy5** dye, which again acts as a fluorescent label however its properties make it a weak binder to our microbubble.

The retention profiles are quite different both in magnitude as well as the effect of size. Several theories as to why this occurs will be explained - it is not only a function of bubble affinity but also the pharmacokinetics and pharmacodynamics of agent and target organ. This information has implications for therapeutic design. It follows from these results that a close examination of not only the properties of drug to be delivered but also the target organ and the microbubble used is required. A custom regimen may be required for UTMD success.

Our presentation will walk through the results of size/binding affinity effects on delivery as well as our calculations of increased agent retention as a result of microbubble drug delivery.

Protocol:

- U/S targeted microbubble delivery of agent to rat liver.
- 1 hr incubation period.
- 100 mL saline cardiac perfusion to remove agent remaining systemic circulation.
- Whole liver imaging on fluorescence detector.
- Dye extraction and fluorescence detection by spectrophotometer

Intravital microscopy of localized stem cell delivery using microbubbles and acoustic radiation force

*T.J.A. Kokhuis^{1,2}, I. Skachkov¹, B.A. Naaijens^{2,3}, L.J.M. Juffermans^{2,4}, O. Kamp^{2,5},
A.F.W. van der Steen^{1,2,6}, M. Versluis⁷ and N. de Jong^{1,2,6}*

¹*Biomedical Engineering, Thorax Center, Erasmus MC, Rotterdam, the Netherlands*

²*Interuniversity Cardiology Institute of the Netherlands, Utrecht, the Netherlands*

³*Department of Pathology, VU University Medical Center, Amsterdam, the Netherlands*

⁴*Department of Physiology, VU University Medical Center, Amsterdam, the Netherlands*

⁵*Department of Cardiology, VU University Medical Center, Amsterdam, the Netherlands*

⁶*Delft University of Technology, Delft, the Netherlands*

⁷*Physics of Fluids, University of Twente, Enschede, the Netherlands*

Introduction

Stem cell therapy has the ability to regenerate and repair damaged cardiac tissue after a myocardial infarction [1,2]. Besides the potential to replace lost cardiomyocytes, stem cells have been shown to stimulate angiogenesis and to secrete a protein cocktail which promotes tissue repair [3,4]. However, cardiac regenerative therapy is currently hampered by the low number of stem cells that are delivered at the area at risk. Typically, only a small fraction of the transplanted cells engrafts within the infarcted area, limiting the effect of stem cell therapy. To improve the lodging of stem cells we have proposed a new technique in which stem cells are decorated with functionalized microbubbles [5], creating echogenic complexes called “StemBells” (Fig. 1A-C). StemBells vibrate in response to incoming ultrasound waves [6], making them very susceptible to a net acoustic force known as the (primary) acoustic radiation force [7]. Ultrasound can therefore be used to propel the StemBells from the centerline of the vessel to the wall in order to facilitate binding and extravasation to the surrounding tissue. In this study we investigated the feasibility of manipulating StemBells acoustically after injection employing a chicken embryo model.

Materials and Methods

Fertilized White Leghorn chicken eggs (*Gallus gallus domesticus*) were incubated for 5 days in a humidified incubator at 37°C. For the experiment, the embryo was taken out of the eggshell and transferred to the experimental setup connected to the microscope (see figure 1D), equipped with an AxioCam MRc color camera (Carl Zeiss B.V., Sliedrecht, the Netherlands). The chicken embryo was embedded in a water bath which was kept at 37°C throughout the experiment using a heating element controlled by a thermostat. The water tank was also holding the 1 MHz single element PZT transducer (V303, Panametrics Inc., Waltham, MA, USA) used for the application of the acoustic radiation force. The optical and acoustical foci were aligned prior to each experiment. The embryo could be manoeuvred independently from the water tank and microscope in all directions facilitating change of

the region of interest during the experiment. A custom made catheter was placed into one of the vitelline veins, upstream from the microscopic field of view, after which a small amount of StemBells was infused.

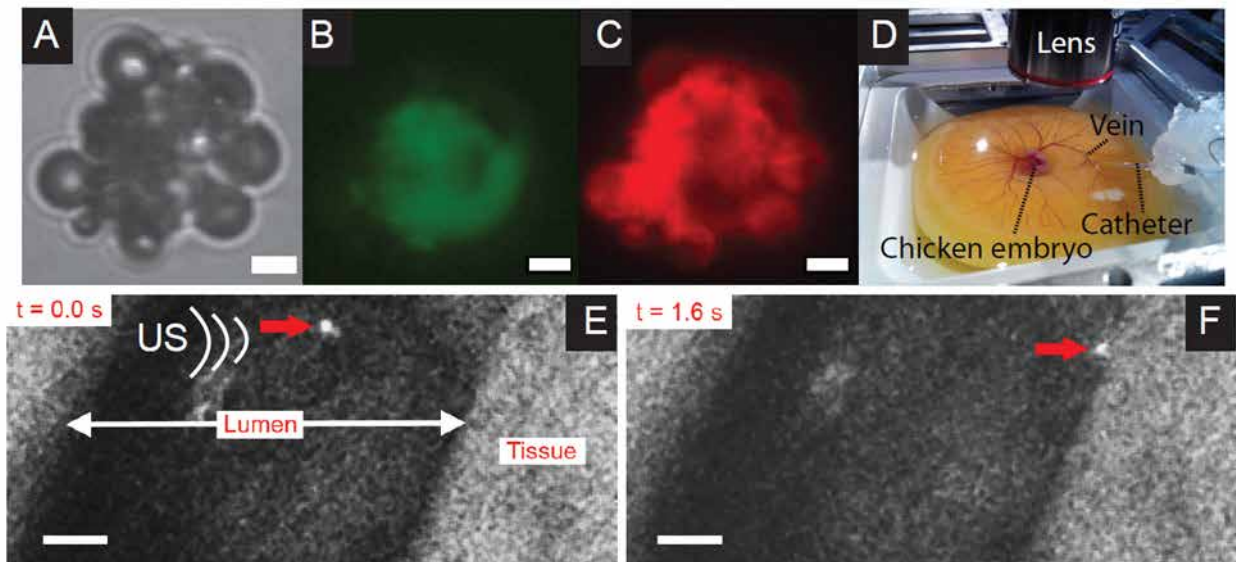


Fig. 1:(A) Brightfield image of a StemBell. Corresponding (B) CellTrackerGreen (showing the stem cell within) and (C) DiI (surrounding CD90-targeted microbubbles) fluorescence images. The scale bar corresponds to 5 μm . (D) Chicken embryo with infusion catheter (E) Fluorescence snapshot of a StemBell (indicated by the arrow) flowing through a 500 μm sized vessel, just before ultrasound application. (F) Acoustic radiation force displaced the StemBell (arrow) to the right vessel wall, opposite to the location of the transducer. The scale bar corresponds to 100 μm .

Shortly after, as soon as the fluorescently labeled StemBells started to pass by, image acquisition in combination with ultrasound application was triggered. Due to the placement of a catheter, multiple infusions and recordings could be done in a single vessel in a short time period.

Results

The model allowed for direct optical observation of the effects of acoustic radiation force on the StemBells *in vivo*. An example is shown in figure 1E-F; panel E shows a snapshot of a StemBell flowing by (indicated by the arrow) just before ultrasound application ($t = 0$ seconds). Ultrasound application (1 MHz, $P_{-} = 450$ kPa, 10% duty cycle) propels the StemBell within 1 second over a distance of 250 μm to the vessel wall opposite to the position of the transducer. A snapshot of the StemBell in contact with the wall at $t = 1.6$ seconds is shown in panel F. Peak translational velocities measured were ~ 50 $\mu\text{m/s}$ for an acoustical pressure $P_{-} = 200$ kPa and ~ 300 $\mu\text{m/s}$ for $P_{-} = 450$ kPa. The acoustic radiation force had no effect on the trajectory of stem cells only.

Conclusion

Using intravital microscopy in a chicken embryo, we have demonstrated that acoustic radiation force and microbubbles can be used for localized stem cell delivery. This technique therefore offers potential to increase the homing of stem cells to the diseased cardiac microvascular endothelium after a myocardial infarction.

Acknowledgments

This project was funded by the Dutch Technology Foundation (STW). The authors would like to thank Geert Springeling, Robert Beurskens, Frits Mastik, Michiel Manten and Klazina Kooiman for their assistance.

References

1. Houtgraaf, J.H. et al. *First experience in humans using adipose tissue-derived regenerative cells in the treatment of patients with ST-segment elevation myocardial infarction. J. Am. Coll. Cardiol.* 59, 539-540 (2012)
2. van Dijk, A. et al. *Reduction of infarct size by intravenous injection of uncultured adipose derived stromal cells in a rat model is dependent on the time point of application Stem Cell Res.* 7, 219-229 (2011)
3. Silva, G.V. et al. *Mesenchymal stem cells differentiate into an endothelial phenotype, enhance vascular density, and improve heart function in a canine chronic ischemia model. Circulation* 111, 150-156 (2005)
4. Tang, Y.L. et al. *Autologous mesenchymal stem cell transplantation induce VEGF and neovascularization in ischemic myocardium. Regul. Pept.* 117, 3-10 (2004)
5. Juffermans, L.J.M et al. *Directing adipose derived stem cells to the area at risk in the heart after myocardial infarction using targeted microbubbles 15th European symposium on Ultrasound Contrast Imaging, 21-22 January 2010, Rotterdam, The Netherlands*
6. Kokhuis, T.J.A. et al. *Characterization of microbubble-loaded stem cells for targeted cell therapy. Proc. IEEE Ultras Symp 2013*
7. Leighton, T.G. *The acoustic bubble. Academic Press, London, 1994*

Correction of nonlinear propagation artefact in contrast enhanced ultrasound imaging

Y Yildiz¹, R.J. Eckersley², M.X. Tang¹

¹Department of Bioengineering, Imperial College, Exhibition Road, London, SW7 2AZ, UK

²Division of Imaging Sciences, King's College London, UK

Background

Contrast enhanced ultrasound (CEUS) imaging with microbubbles is a promising tool in a wide range of clinical applications including cardiovascular diseases and cancer. CEUS imaging relies on detecting nonlinear bubble echoes over background tissue. However, nonlinear propagation of ultrasound in tissue containing bubbles causes tissue echoes to become nonlinear and consequently CEUS imaging techniques which rely on linear cancellation of tissue echoes cannot differentiate between tissue and microbubble echoes resulting in misclassification of tissue as microbubble echoes [1-3]. This type of artifact is common and significantly affects CEUS imaging both qualitatively and quantitatively. Especially at frequencies higher than the resonance frequency of microbubbles in e.g. vascular or pre-clinical imaging, the sensitivity of bubble detection is reduced and a higher Mechanical Index (MI) is often used to generate sufficient bubble signals, causing more nonlinear artefact. Some recent studies have reported the clinical presence of such artefacts and some method to reduce the artefacts [4-8]. In this study a new method is proposed to correct for this artefact.

Methods

Ultrasound image formation is described as a convolution between a tissue scattering distribution (TSD) and the point spread function (PSF) of the imaging system with added measurement noise. It is assumed that a B-mode image at fundamental frequency contains mostly tissue signal.

The proposed method estimates the underlying TSD by deconvolving the known PSF from acquired B-mode RF data. The TSD is in turn convolved with an estimated nonlinear PSF to generate nonlinear tissue echoes (artefact) which are then removed from the CEUS image to generate a corrected microbubble specific image.

The proposed method was tested both in simulation and on laboratory phantoms. Using a clinical prototype scanner (Toshiba AplioXG), RF data of a tissue mimicking phantom with a microbubble solution filled wall-less vessel was acquired.

Results

Figure 1 and 2 show original and corrected Pulse Inversion (PI) images of the phantom at the same intensity range. This set was acquired with 0.1mL/L concentration of Sonovue at 0.3MI with a transmit center frequency of 4MHz. In the original PI image the intensity of the tissue region below the vessel, representing artefact, is comparable to the intensity of the microbubble region whereas in the corrected image the intensity of this region is significantly reduced while the strength of the microbubble signal remains relatively unchanged. Figure 3 shows the detected radio frequency signal in the original versus corrected PI image in the center column of the image. Figure 4 displays the Contrast to Tissue Ratio (CTR) of the original and corrected PI images. The increase in CTR ranges from 8.5 to 10dB and on average, CTR is improved by 9.2 +/-0.6 dB at this concentration. Work is ongoing to further evaluate the performance of the method.

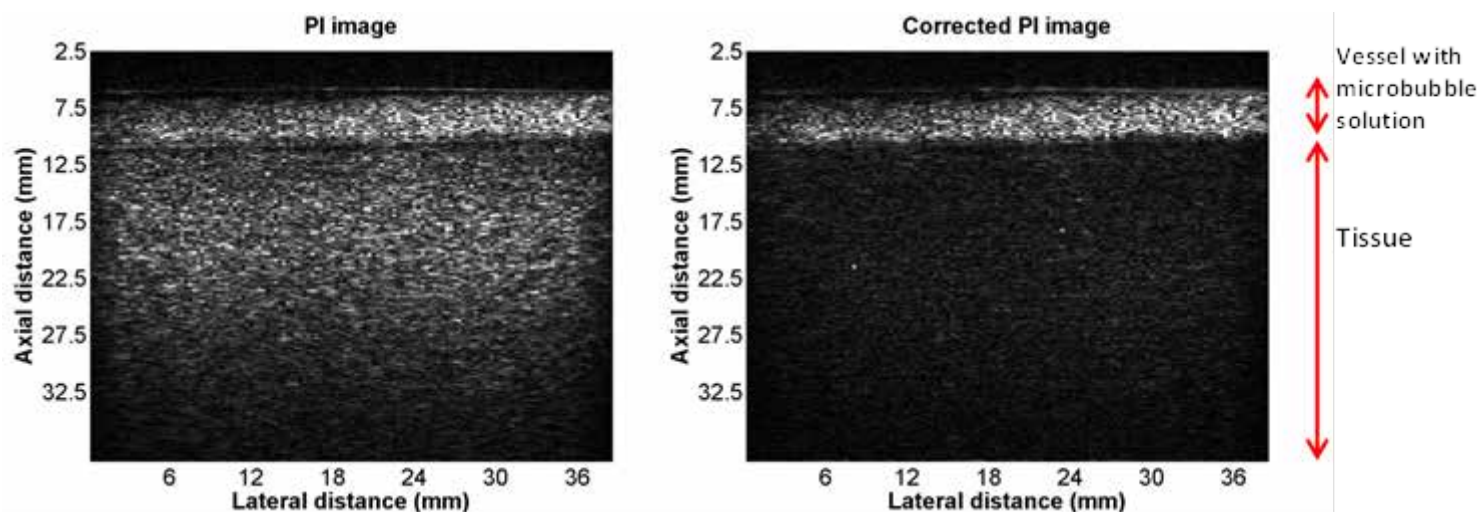


Figure1: Original PI Image of a micro bubble filled vessel with tissue underneath.

Figure2: Corrected PI image, where nonlinear artefact in the tissue regions is significantly reduced.

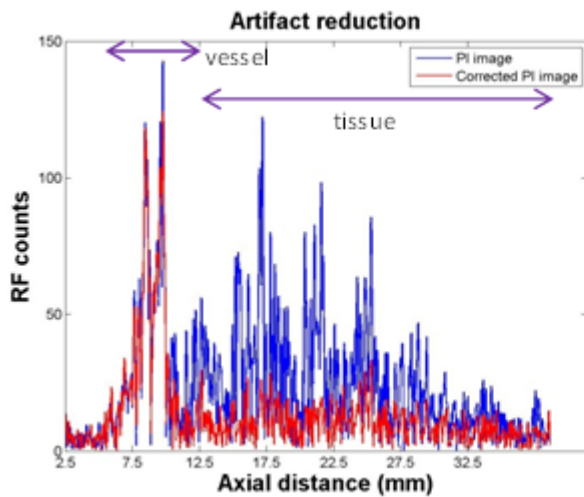


Figure3: Radio frequency signal of a column in the original versus corrected PI image

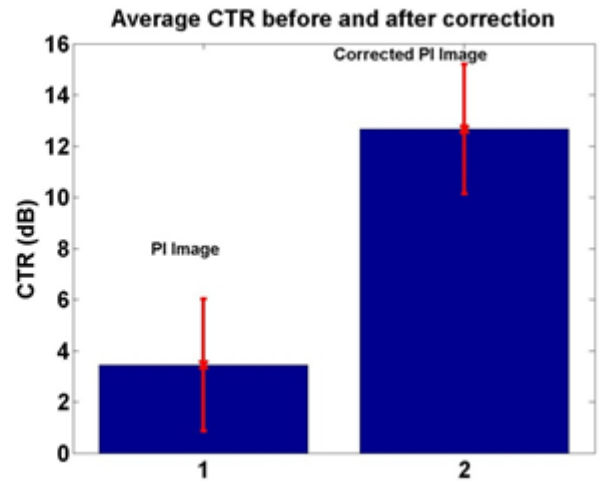


Figure4: Contrast to Tissue Ratio(CTR) for the original and corrected images. CTR increases significantly after correction.

The developed method is shown to be able to reduce nonlinear propagation artefacts in CEUS imaginand improve CTR by more than 9dB on a tissue mimicking phantom.

References

1. Tang, M.X. and R.J. Eckersley, *Nonlinear propagation of ultrasound through microbubble contrast agents and implications for Imaging. Ieee Transactions On Ultrasonics Ferroelectrics and Frequency Control*, 2006. 53(12): p. 2406-2415
2. Tang, M.X., N. Kamiyama, and R.J. Eckersley, *EFFECTS OF NONLINEAR PROPAGATION IN ULTRASOUND CONTRAST AGENT IMAGING. Ultrasound In Medicine and Biology*, 2010. 36(3): p. 459-466
3. Tang, M.X., et al., *Quantitative contrast-enhanced ultrasound imaging: a review of sources of variability. Interface Focus*, 2011. 1(4): p. 520-539
4. ten Kate, G.L., et al., *Far-Wall Pseudoenhancement During Contrast-Enhanced Ultrasound of the Carotid Arteries: Clinical Description and In Vitro Reproduction. Ultrasound in Medicine & Biology*, 2012. 38(4): p. 593-600
5. Stijn C.H. et al, *Far wall pseudo-enhancement: A neglected artifact in carotid contrast-enhanced ultrasound? Atherosclerosis*, volume 229 issue 2 Pages 451-452, 2013
6. Yu, H.J., et al., *Pseudoenhancement Within the Local Ablation Zone of Hepatic Tumors Due to a Nonlinear Artifact on Contrast-Enhanced Ultrasound. American Journal Of Roentgenology*, 2010. 194(3): p. 653-659
7. G Renaud et al *Counter-propagating wave interaction for contrast-enhanced ultrasound imaging*, 2012 *Phys. Med. Biol.* 57 L9
8. Pasovic, M, et al., *Second harmonic inversion for ultrasound contrast harmonic imaging. Physics in Medicine and Biology*, 2011.56(11): p. 3163-3180

Evaluation of carotid plaque perfusion using DCEUS

Michalakis Averkiou¹, Damianos Christofides¹, Brahman Dharmarajah², Ankur Thapar², Alun Davies² and Edward Leen²

¹Department of Mechanical and Manufacturing Engineering, University of Cyprus, Nicosia, Cyprus

²Imaging Department, Hammersmith Hospital, London, UK

Introduction

Dynamic contrast enhanced ultrasound (DCEUS) can be used in the clinic as a complementary technique to color Doppler ultrasound in the assessment of carotid atherosclerosis[1]. Studies have been conducted using DCEUS that found a difference in the perfusion of carotid plaques between symptomatic and asymptomatic patients[2]–[4]. Also the examination of microbubble tracking techniques[5] holds promise for the future.

In this study the perfusion of carotid plaques is evaluated both qualitatively and quantitatively in order to investigate differences in the perfusion between symptomatic and asymptomatic patients.

Materials and Method

The carotids of twenty-four (24) patients were imaged using the L9-3 probe of the Philips iU22 ultrasound platform (Philips Medical Systems, Bothell, WA). The patients were injected with 2ml of Sonovue (Bracco s.p.a., Milan, Italy) and one minute ultrasound loops were acquired and saved as DICOM files.

Offline blinded analysis was performed by extracting the DICOM files from the Philips iU22 onto a workstation equipped with the QLAB commercial quantification software (version 8.1, Philips Medical Systems, Bothell, WA). Quantitative perfusion assessment was performed using a binary grading system: 0 represented less than 50% of carotid plaque area contained moving microbubbles and 1 represented more than 50% of carotid plaque area contained moving microbubbles. Static reflectors within the plaques were not considered as valid microbubble signal.

For the qualitative DCEUS analysis a region-of-interest (ROI) was drawn around the plaque. Care was taken to delineate the plaque without including any portion of the lumen signal due to the potentially large amplitude differences between the lumen DCEUS signal and the signal from the plaque. The mean intensity DCEUS signal from within the ROI containing the plaque was sampled across time to generate the time intensity curve (TIC) of the carotid plaque. The mean TIC signal amplitude after the arrival of the microbubbles into the plaque ROI was calculated.

Results

The mean DCEUS intensity signal from the plaques was significantly higher for asymptomatic patients than symptomatic patients (Figure 1).

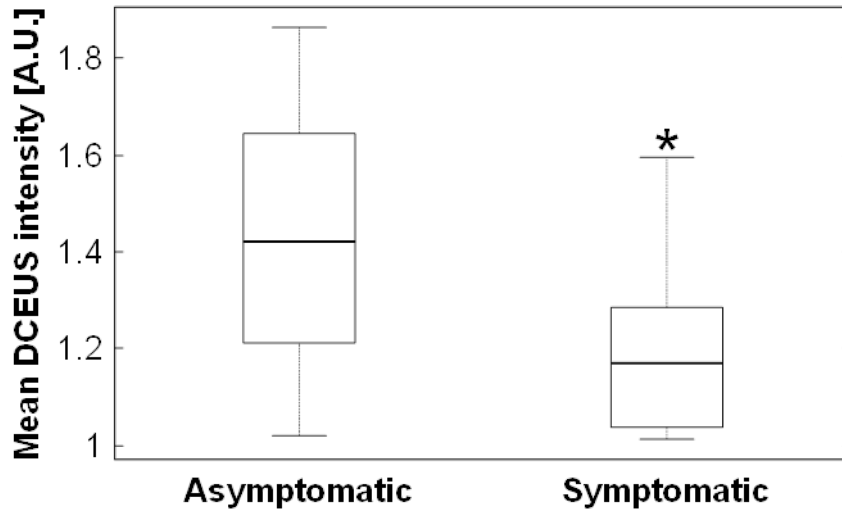


Figure 1: Boxplots of the mean DCEUS intensity signal within the carotid plaques after the arrival of the microbubbles between asymptomatic and symptomatic patients. Notation: * signifies $P < 0.1$, Power > 0.8

The qualitative analysis results showed that only 25% (3/12) of asymptomatic patients had a score of 0 in comparison to 67% (8/12) of symptomatic patients.

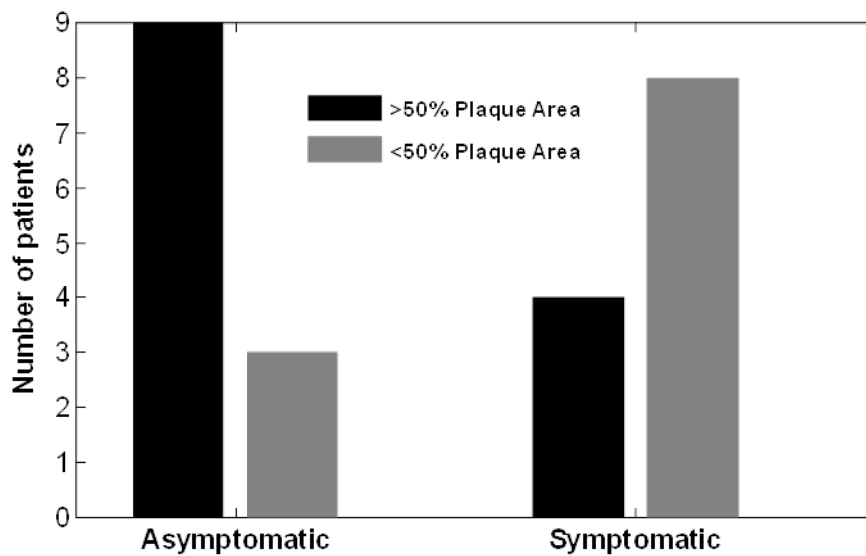


Figure 2: Qualitative DCEUS perfusion scores of asymptomatic and symptomatic patients.

Conclusion

The results of this study suggest that patients with perfused carotid plaques have a lower risk of having symptoms compared to patients with carotids plaques that are less perfused, contrary to previously published results.

References

1. J. Shalhoub, D. R. J. Owen, T. Gauthier, C. Monaco, E. L. S. Leen, and A. H. Davies, "The use of contrast enhanced ultrasound in carotid arterial disease.," *Eur. J. Vasc. Endovasc. Surg.*, vol. 39, no. 4, pp. 381–7, Apr. 2010
2. D. Staub, S. Partovi, A. F. L. Schinkel, B. Coll, H. Uthoff, M. Aschwanden, K. A. Jaeger, and S. B. Feinstein, "Correlation of carotid artery atherosclerotic lesion echogenicity and severity at standard US with intraplaque neovascularization detected at contrast-enhanced US.," *Radiology*, vol. 258, no. 2, pp. 618–26, Feb. 2011
3. P.-T. Huang, C.-C. Chen, W. S. Aronow, X.-T. Wang, C. K. Nair, N.-Y. Xue, X. Shen, S.-Y. Li, F.-G. Huang, and D. Cosgrove, "Assessment of neovascularization within carotid plaques in patients with ischemic stroke.," *World J. Cardiol.*, vol. 2, no. 4, pp. 89–97, Apr. 2010
4. L. Xiong, Y.-B. Deng, Y. Zhu, Y.-N. Liu, and X.-J. Bi, "Correlation of carotid plaque neovascularization detected by using contrast-enhanced US with clinical symptoms.," *Radiology*, vol. 251, no. 2, pp. 583–9, May 2009
5. A. Hoogi, D. Adam, A. Hoffman, H. Kerner, S. Reisner, and D. Gaitini, "Carotid plaque vulnerability: quantification of neovascularization on contrast-enhanced ultrasound with histopathologic correlation.," *AJR. Am. J. Roentgenol.*, vol. 196, no. 2, pp. 431–6, Feb. 2011

CEUS in rheumatology

**B. Raffener¹, A. Coran², V. Beltrame², L. Cipria¹, L. Bernardi¹, C. Botsios¹, L. Punzi¹,
E. Grisan³, R. Stramare²**

¹Rheumatology Unit, Department of Medicine, University of Padova

²Radiology, Department of Medicine, University of Padova

³Department of Information Engineering, University of Padova

Musculoskeletal ultrasonography has become an established imaging technique in rheumatology for diagnosis, prognosis and follow-up with great impact on therapeutic decisions especially in rheumatoid arthritis (RA).¹ By adding color and power Doppler ultrasonography (CDUS/PDUS) to clinical examination a better differentiation between active and inactive joint (2) and between low disease activity and remission is obtained (3). In fact angiogenesis in synovial tissue correlates with disease activity, and is closely linked to joint destruction more than synovial hypertrophy itself (4).

Contrast-enhanced ultrasonography (CEUS) is even more accurate in differentiating between active and inactive synovitis than CDUS/PDUS, and identifies profound remission after therapy (5,6). The measurement of overall synovial thickness and synovia/effusion ratio related to active synovitis is significantly improved after the administration of contrast medium (7). CEUS was found to be more useful than the unenhanced PD to detect arthroscopically evident hypervascularization of synovial villi (8). CEUS allows therefore a significant improved quantification of intensity and extension of vascularization compared to PDUS in both semiquantitative and computer-aided measurement (9).

CEUS demonstrated same sensitivity as contrast-enhanced MRI (CE-MRI) in assessing synovitis in painful joints of RA patients (10). Moreover CEUS resulted highly sensitive and specific in detecting MRI demonstrated sacroileitis (11). Some studies demonstrated superiority of CEUS compared to CE-MRI in detecting synovitis (12,13). Because US contrast medium persists in the vascular bed, there is no leakage into the extra-synovial compartments. Whereas delayed MRI sequences may show synovial effusion enhancement secondary to gadolinium diffusion rather than to active synovitis (14).

Most studies about CEUS issued evaluation of disease activity in RA, but further applications are being developed for the next future. CEUS allows non-invasive dynamic study of synovial perfusion differentiating among different arthritis forms by reflecting distinct vascularization patterns identified in biopsy specimens. Computer-aided software systems can analyze CEUS derived parameters and determine a more objective validation of disease activity and entity influencing drastically prognosis and therapeutic interventions (15).

References

1. Backhaus M. New developments in joint ultrasonography. *Z Rheumatol* 2006;65(8):700-7
2. Szkudlarek M. Power Doppler ultrasonography in the metacarpophalangeal joints of patients with rheumatoid arthritis. *Arthritis Rheum* 2001;44:2018-23
3. Foltz V. Power Doppler ultrasound, but not low-field magnetic resonance imaging, predicts relapse and radiographic disease progression in rheumatoid arthritis patients with low levels of disease activity. *Arthritis Rheum* 2012;64:67-76
4. Firestein GS. Starving the synovium: angiogenesis and inflammation in rheumatoid arthritis. *J Clin Invest* 1999;103(1):3-4
5. Klauser A. The value of contrast-enhanced color Doppler ultrasound in the detection of vascularization of finger joints in patients with rheumatoid arthritis
6. Stramare. Evaluation of finger joint synovial vascularity in patients with rheumatoid arthritis using contrast-enhanced ultrasound with water immersion and a stabilized probe. *J Clin Ultrasound* 2012;40(3):147-54
7. Klauser A. The IACUS study group. Contrast enhanced gray-scale sonography in assessment of joint vascularity in rheumatoid arthritis: results from the IACUS study group. *Euro Radial* 2005;15(12):2404-10
8. Fiocco UJ. Contrast medium in power Doppler ultrasound for assessment of synovial vascularity: comparison with arthroscopy. *Rheumatol* 2003;30(10):2170-6
9. Klauser A. Contrast-enhanced ultrasonography for the detection of joint vascularity in arthritis - subjective grading versus computer-aided objective quantification. *Ultraschall in Med* 2011;3:31-37
10. Raffener B. Validity of contrast-enhanced ultrasound (CEUS) in the detection of synovial inflammation in rheumatoid arthritis compared to Power Doppler in contrast-enhanced MRI controlled pilot study. *Eular* 2013: FRI0477
11. Klauser A. Feasibility of second-generation ultrasound contrast media in the detection of active sacroileitis. *Arthritis Care Res* 2009;61:7909-16
12. Song IH. Knee osteoarthritis efficacy of a new method of contrastenhanced musculoskeletal ultrasonography in detection of synovitis in patients with knee osteoarthritis in comparison with magnetic resonance imaging. *Ann Rheum Dis* 2008;67:19
13. Lee SH. Quantitative assessment of synovial vascularity using contrastenhanced power Doppler ultrasonography: correlation with histologic findings and MR imaging findings in arthritic rabbit knee model. *Korean J Radiol* 2008;9:45
14. Turetschek K. Tumor microvascular changes in antiangiogenic treatment: assessment by magnetic resonance contrastmedia of different molecular weights. *J Magn Reson Imaging* 2004;20:138
15. Raffener B. Dynamic automated synovial imaging (DASI) for differentiating between rheumatoid arthritis and other forms of arthritis: automated versus manual interpretation in contrast-enhanced ultrasound. *Eular* 2013: FRI0478

Perivascular venous vascularization on contrast-enhanced ultrasound (CEUS) is correlated with inflammation in patients with acute deep vein thrombosis

Mathias Kaspar, MD; Stephan Imfeld, MD, PhD; Markus Aschwanden, MD; Heiko Uthoff, MD; Daniel Staub, MD

Department of Angiology, University Hospital Basel, Petersgraben 4, CH-4031 Basel, Switzerland

Introduction

Deep venous thrombosis (DVT) is a common vascular condition that is associated with significant morbidity and mortality. Despite appropriate anticoagulant therapy, the post-thrombotic syndrome (PTS) occurs in up to 50% of patients after DVT. However, little is known about PTS and the factors that contribute to its development. To date, it remains unclear who will develop PTS after DVT, and who will benefit from compression therapy. Recently, several experimental and clinical studies suggest that the inflammatory process at the time of DVT play also an important role in thrombus formation and resolution, and may promote destruction of venous valves and thereby induce valvular reflux, subsequently leading to the development of PTS.

Contrast-enhanced ultrasound (CEUS) is emerging as a valuable imaging modality that complements and enhances conventional vascular ultrasound imaging, particularly to image the microvascular perfusion e.g. in perivascular tissue.

Therefore, the purpose of this study was to assess the presence and degree of systemic inflammatory markers and perivascular hypervascularization using CEUS as an indicator of perivenous inflammation in patients with acute DVT.

Methods

Consecutive patients with acute unilateral proximal DVT (involving the popliteal vein or proximal veins) were included. Diagnosis of DVT was performed by standard compression and duplex ultrasound using a Philips iU22 ultrasound scanner (Bothel, WA) equipped with a linear array L9-3 MHz probe. At baseline, after 2 weeks and 3 months CEUS imaging of the thrombosed popliteal vein as well as the normal popliteal vein at the contralateral side was evaluated using a standardized cross-sectional view after bolus injection of 2.5ml of SonoVue™ (Bracco, Milan, Italy). Perivascular contrast-enhancement was analyzed using QLAB software (Philips; Bothel, WA) to quantify maximal video intensity within the first minute (arterial phase) after bolus contrast injection in a region of interest of 5x5mm (**Figure**).

The level of inflammatory markers as von Willebrand factor (vWF:Ag) and high sensitive C-reactive protein (hsCRP) were determined at each visit. The degree of edema of the leg with DVT was calculated by subtraction the volume of the lower extremity of the non-affected side form the affected side, by volumetry using an automated 3D volume measurement system (Bauerfeind®, Zeulenroda-Triebes, Germany).

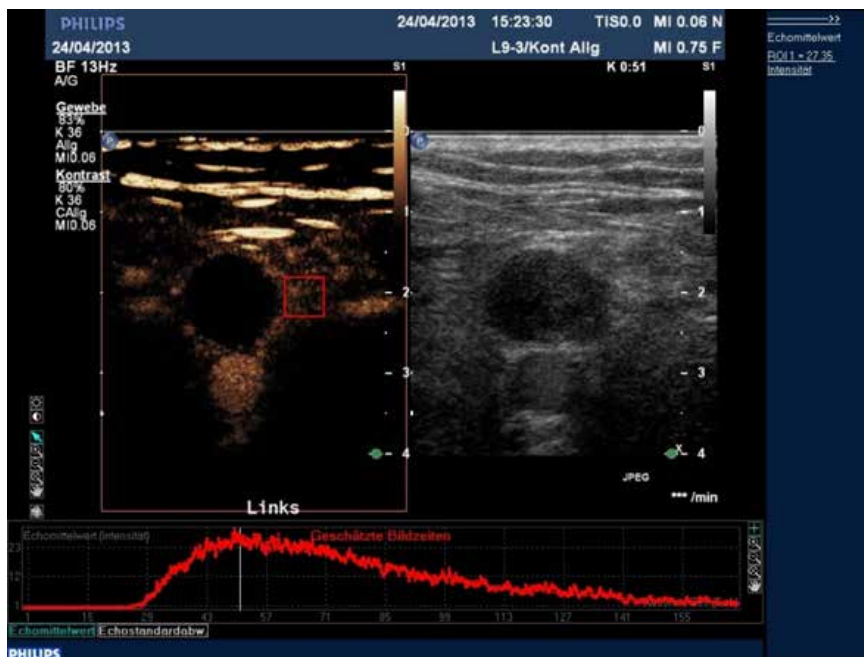


Figure: Perivascular enhancement of a thrombosed popliteal vein with corresponding time-intensity-curve.

Results

The results of 19 patients (mean age 55 ± 12 years, 18 males) are listed in the Table:

Variables	Baseline	2 weeks	P-Value [‡]	3 months	P-Value [‡]
hsCRP [mg/l]	21.2 (9.5-44.9)	2.5 (1.7-4.6)	<0.001	2.2 (0.8-5.3)	0.001
vWF:Ag [%]	226 (181-266)	180 (141-209)	0.009	139 (125-213)	0.004
Edema [l]	0.52±0.41	0.37±0.38	0.003	0.30±0.21	0.019
Perivascular enhancement [dB]	18.2 (11.2-26.3)	24.2 (14.6-32.5)	0.136	5.7 (3.9-9.7)	0.001
Ratio [¶]	8.3 (3.7-14.6)	4.7 (3.0-13.6)	0.463	1.5 (0.7-4.7)	0.002

Data are expressed as median (IQR) or mean±SD, ¶Ratio of perivascular enhancement in affected to that of the non-affected leg.

‡Wilcoxon-Test or paired T-Test compared with baseline value

The level of systemic inflammatory markers and leg edema are elevated at baseline and decrease significantly within the first two weeks, and remain low after 3 months. Perivascular enhancement on CEUS is elevated at baseline and remains high during the initial 2 weeks and decreases significantly after three months.

Conclusion

Vascularization assessed by CEUS is significantly more pronounced in the perivascular tissue of the thrombosed vein compared to the non-affected vein. Vascularization decreases from baseline to 3 months follow-up and this course correlates also with the decrease of the systemic inflammatory markers, supporting the fact that DVT is associated with vessel wall inflammation. Inflammation with pronounced perivascular vascularization might play an important role in promoting endothelial vessel wall damage and destruction of venous valves, subsequently leading to the development of PTS after DVT. Therefore, our results could lead to novel approaches to interrupt the natural history of PTS.

Prevalence of subclinical atherosclerosis and intraplaque neovascularization in patients with familial hypercholesterolemia

Stijn C.H. van den Oord†, MD; Zeynetin Akkus†, MSc;
Jeanine E. Roeters van Lennep‡, MD, PhD; Johan G. Bosch†, PhD;
Antonius F.W. van der Steen†, PhD; Eric J.G. Sijbrands‡, MD, PhD;
Arend F.L. Schinkel*, MD, PhD*

**Dept. of Cardiology, Thoraxcenter, Erasmus Medical Center, Rotterdam, the Netherlands*

†Dept. of Biomedical Engineering, Thoraxcenter, Erasmus Medical Center, Rotterdam, the Netherlands

*‡Division of Pharmacology, Vascular and Metabolic Diseases, Dept. of Internal Medicine,
Erasmus Medical Center, Rotterdam, the Netherlands*

Purpose

Patients with heterozygous familial hypercholesterolemia (FH) are at severely increased risk of developing atherosclerosis at relatively young age. The purpose of this study was to assess the prevalence of subclinical atherosclerosis and intraplaque neovascularization (IPN) in patients with FH, using contrast-enhanced ultrasound (CEUS) of the carotid arteries.

Methods

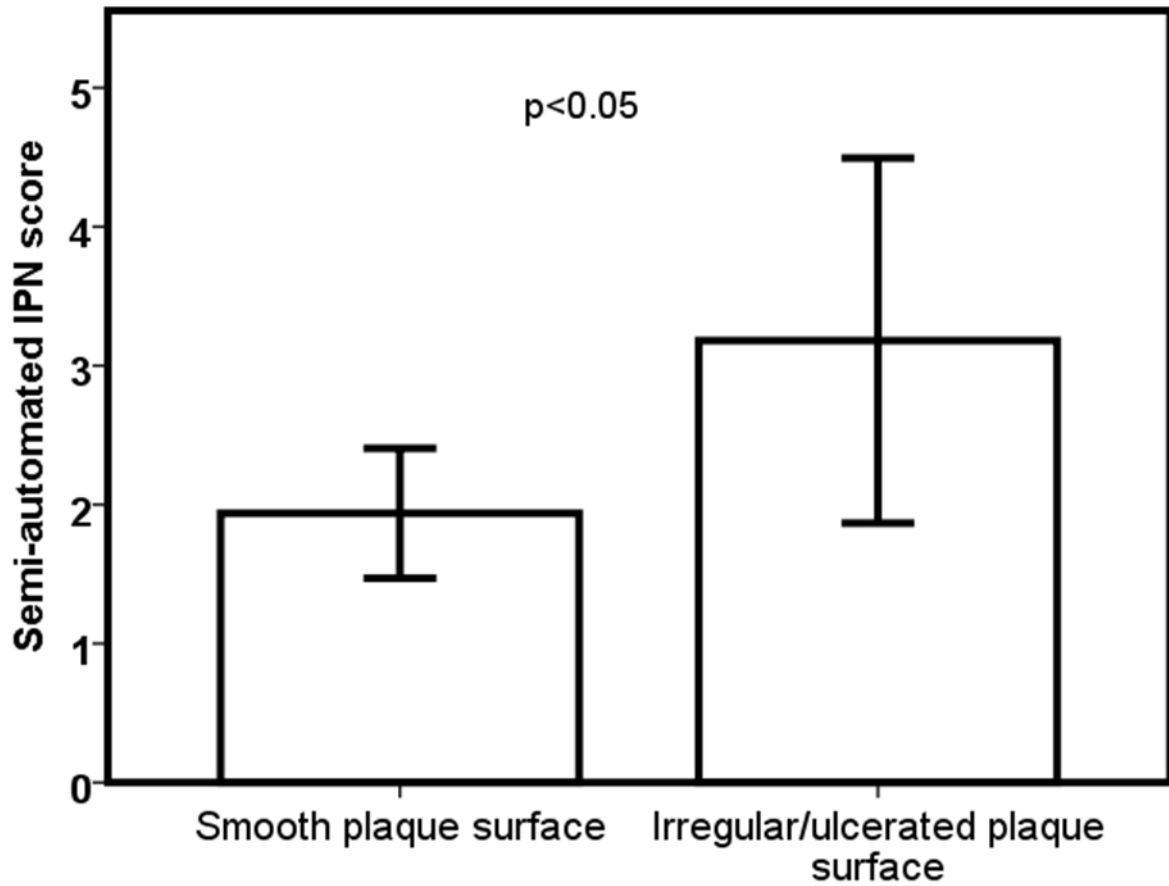
The patients had no cerebrovascular symptoms and underwent bilateral carotid ultrasound and CEUS to evaluate the presence of subclinical atherosclerosis and IPN. Far wall plaques were excluded for assessment of IPN due to a hindering pseudo-enhancement artifact. IPN was assessed in near wall plaques using a visual grading scale and dedicated semi-automated quantification software. Mann-Whitney U test was performed to compare the output of the semi-automated software in groups.

Results

The study population consisted of 69 patients (48% women, mean age 55 ± 8 years, mean LDL 143 ± 66 mg/dl). Carotid plaque was present in 62 patients (90%). A total of 49 patients had plaques that were eligible for the assessment of IPN: 7 patients (14%) had no IPN, 39 (80%) had mild to moderate IPN and 3 (6%) had severe IPN. Individual carotid artery analysis (n=68) showed that plaques with irregular or ulcerated surface (n=18) had significantly more IPN than plaques with a smooth surface (n=50) ($p < 0.05$) (figure 1).

Conclusion

Carotid ultrasound demonstrated atherosclerotic plaque in 90% of asymptomatic patients with FH without known atherosclerosis. IPN assessed with CEUS, was present in 86% of these patients. Irregular and ulcerated plaques exhibited significantly more IPN than plaques with a smooth surface.



Ultrasound-based measurement of molecular marker concentration in large blood vessels

Shiyang Wang*, F. William Mauldin Jr*, Alexander L. Klibanov[^], John A. Hossack*

*Department of Biomedical Engineering
[^]Department of Medicine – Cardiovascular division
University of Virginia, Charlottesville, VA, USA

Introduction

In ultrasound molecular imaging, targeting ligands are conjugated to microbubbles, allowing the microbubbles to attach to specific regions of the vascular endothelium through a specific ligand-receptor interaction. In order to increase the binding efficacy, especially in large blood vessels, acoustic radiation force (ARF) is frequently applied.

State-of-the-art ultrasound-based molecular imaging techniques typically involve some combination of nonlinear microbubble detection and elimination of freely circulating microbubble (e.g. low-pass interframe filtering or pre- and post-burst subtraction). These techniques have demonstrated success in small blood vessel environments (e.g. tumor) *in vivo* and in large blood vessels *ex vivo*. However, these methods lack quantitative measures of receptor concentration and typically require both a target and control group in order to normalize for non-specific binding. Consequently, the current protocols for ultrasound-based targeted molecular imaging have limited clinical efficacy.

To address these limitations, we have developed a new imaging protocol involving a novel modulated ARF-based imaging sequence, which enables the detection of targeted adhesion of microbubbles without the need for separate control measurements. In addition, the feasibility of quantitative measurements of molecular marker concentration has been demonstrated in large blood vessel environments, *in vitro*.

Methods

Flow phantoms with 4 mm diameter channels were used to mimic large blood vessels in human. Targeted channels were incubated with streptavidin solution (1 – 50 $\mu\text{g}/\text{mL}$) for 12 h followed by a 10 min incubation with 5% BSA. Control channels were incubated with BSA alone for 12 h. The surface concentration of streptavidin was determined using Eu^{3+} -labelled streptavidin and dissociation-enhanced time-resolved spectrofluorometry. Biotinylated lipid shelled microbubbles diluted in isotonic saline to a concentration of $0.5 \times 10^6/\text{mL}$ were injected through the channels at a flow velocity of 6 cm/s. The modulated ARF-based imaging sequence was designed to have three sections – 10 s of imaging (4.5 MHz frequency, 4Hz frame rate), 70 s of imaging plus ARF applied (4.5 MHz frequency,

5 kHz PRF; $10 \text{ s} \leq t < 80 \text{ s}$), and 100 s of imaging ($80 \text{ s} \leq t \leq 180 \text{ s}$) – showing the baseline, rise, and decay of adherent microbubble concentration along the bottom channel wall (Fig. 1A). Signal magnitude curves were obtained by calculating the average signal magnitude over time within the ROI located at the center of the bottom channel wall. The residual-to-saturation ratio (R_{resid}) parameter:

$$R_{\text{resid}} = \frac{M_{\text{resid}} - M_{\text{init}}}{M_{\text{sat}} - M_{\text{init}}} \cdot 100\% \quad (8)$$

where M_{init} and M_{resid} are the initial and residual signal magnitudes and were measured directly from the signal magnitude curve at $t = 5 \text{ s}$ and $t = 180 \text{ s}$, respectively; and M_{sat} is the saturated signal magnitude after reaching steady-state was used to separate specific binding from non-specific adhesion. The detection sensitivity was defined as the minimum detectable increment of molecular marker concentration using the modulated ARF-based imaging sequence.

Results

Signal magnitude curves observed with application of the modulated ARF-based imaging sequence are presented in Fig. 1B. With application of ARF (10 – 80 s), the signal magnitude for both control and targeted channels exponentially approached a steady-state magnitude. After cessation of ARF (80 – 180 s), the residual signal magnitude of targeted channels were significantly higher than that of control channels ($p < 0.001$, $n = 10$). R_{resid} values of targeted channels ($60.4\% \pm 17.7\%$) were significantly higher than those of control channels ($-1.3\% \pm 1.1\%$) ($p < 0.001$, $n = 10$). In addition, R_{resid} value was observed to be linear with streptavidin concentration (Fig. 1C, $R^2 = 0.99$). Under these parameters, the minimum observed detection sensitivity was determined to be $1.3 \times 10^3 \text{ molecules}/\mu\text{m}^2$.

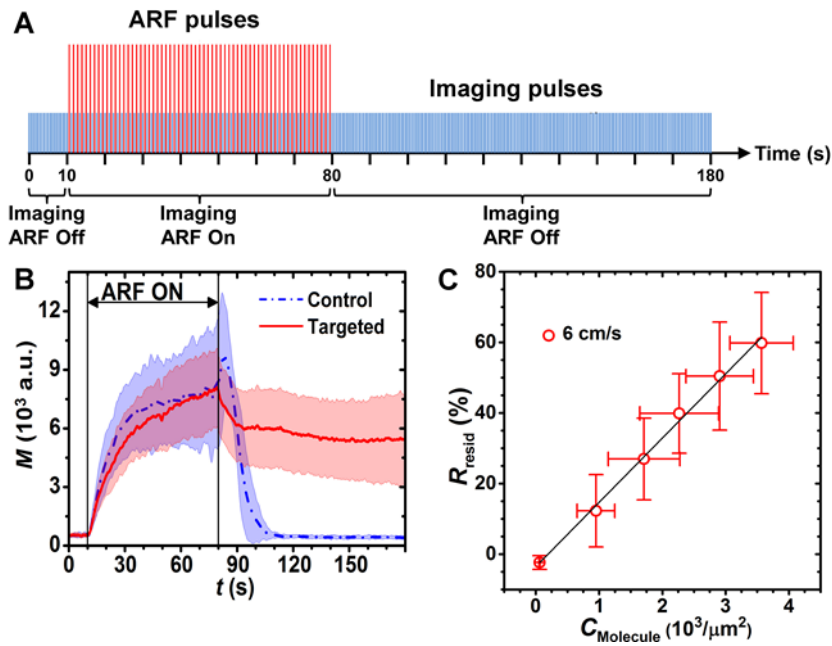


Figure 1: (A) Diagram of the custom designed modulated ARF-based imaging sequence. Imaging and ARF pulses are represented with blue and red colors, respectively. The amplitudes of imaging and ARF pulses are not to scale. (B) Averaged signal magnitude curves for control channels (blue) and targeted channels (red). Blue and red solid lines indicate the mean values from 10 trials. Light color shadows indicate the corresponding error bars at the range of [mean \pm standard deviation]. (C) Relationships between the residual-to-saturation ratio (R_{resid}) and corresponding surface concentration of streptavidin at flow velocities of 6 cm/s. Black line is a weighted linear fit.

Discussion & Conclusion

The residual-to-saturation ratio (R_{resid}) was observed to be an excellent quantitative parameter for detection of targeted adhesion without the need for separate control measurements. R_{resid} provides a quantity that was linearly proportional to the percentage of remaining specifically bound adherent microbubbles along the vessel wall. In addition, R_{resid} was also demonstrated to provide quantitative measurements of molecular marker concentration in large blood vessel environments. These results suggest that modulated ARF-based imaging sequence and extraction of the R_{resid} parameter have potential for use in targeted molecular imaging and as a means to achieve quantitative measures of ligand concentration in real-time, using relatively short imaging protocols (< 5 min) that do not require separate control experiments or waiting periods.

Perfusion imaging in the eighties: Has the goal been reached?

Folkert J. ten Cate MD

Thoraxcenter , Erasmus MC, Rotterdam, the Netherlands

When the microbubbles for use in echocardiography were developed most investigators at that time felt that a significant step forwards has been accomplished. This expectation was based on the fact that if myocardial perfusion could be determined clinically Echocardiography would have been a real competitor for the standard perfusion method at that time which was either Thallium- or TC nuclear imaging.

Many investigators worked on different aspects of the method. Several physical problems have to be solved, among them stabilization of microbubbles, shell characteristics and the influence on imaging of using several gasses to fill the microbubbles. Among many people the work of Nico de Jong and coworkers have been essential in the knowledge of the physical properties of micro bubbles and its interaction with ultrasound.

Others, like the work of Sanjiv Kaul and coworkers produced many seminal papers to show the usefulness of myocardial contrast echo as it was mentioned , for myocardial perfusion and coronary flow in the experimental setting.

Also from this group Kevin Wei showed how one could get a quantitative measure of myocardial perfusion using his destruction- inflow concept.

Steve Feinstein and coworkers showed myocardial perfusion in the cathlab in clinical patients and the Rotterdam group showed also a relation between myocardial washout of echo contrast and coronary stenosis in stable patients with angina pectoris.

Furthermore the yearly contrast echo symposia , the bubble course in Chicago led by Steve Feinstein and the Rotterdam contrast course led by Nico de Jong and Folkert ten Cate brought clinical researchers, industry and academic physicists together to detect the secrets of micobubbles and perfusion.

Two big, expensive trials one from The Point company and recently the Bracco Phoenix trial have been set up to show the usefulness of myocardial perfusion echo in clinical medicine. The Point trial was not accepted by the FDA . The reasons of this decision were not known.

The Bracco European trial has been published in JACC in 2013. There are no data known at this moment whether the company will go for FDA or EMEA approval.

Also there is the Accuspheres trial which is under investigation of EMEA as far as this author knows now.

Why then with all this work and research is myocardial perfusion not a clinical technique for everyday use at this moment.

To answer this question some other aspects have to be mentioned which has not helped its widespread use: the black Box warning and the EMEA warning in Europe to prevent the use of Sonovue in the first 7 days after an acute coronary symptom. The development of the International Contrast Ultrasound Society was put up to make Echocontrast more popular among clinicians.

But this author will present also his personal opinion why myocardial perfusion is not widespread used in clinical echocardiography.

This has to do with reimbursement. Now the cheapness of an Echoexam as compared to a Nuclear exam has worked contraproductive because one was not used to spend more money for an echo exam.

Furthermore even at these days the method is not fully standardized so that a low specificity still exists.

Also there was a lot of scepticism of the editors of main journals to publish echo perfusion clinical data.

In summary;

Myocardial echo perfusion has not reached its enormous expectations . Many causes can be seen of which lack of standardization and reimbursement issues to the opinion of this author are the most important.

The influence of blood on targeted microbubbles

Joshua Owen, Paul Rademeyer & Eleanor Stride

Institute of Biomedical Engineering, University of Oxford, Oxford, UK

Numerous targeting strategies for ultrasound contrast agents have been developed. Targeted microbubbles with moieties attached to the surface have been designed to image inflammation [1-3], angiogenesis [4, 5] and to both detect and treat thrombi [6, 7] and tumours [8-10]. Despite promising in vitro results, however, clinical translation has been limited especially for therapeutic applications and efficient targeting of microbubbles in vivo is still a considerable challenge [11].

One factor, which is likely to have an effect on targeting, relates to the characteristics of blood. Blood is a particulate suspension, containing ~40 % volume of particles mainly consisting of deformable red blood cells or erythrocytes. As such it is significantly different to water or saline – the fluids typically used in in vitro testing. Remarkably few studies however test targeted microbubbles in flowing blood prior to conducting experiments in vivo. The aim of this study was to investigate the effect of blood on two different targeting strategies: biochemical and magnetic.

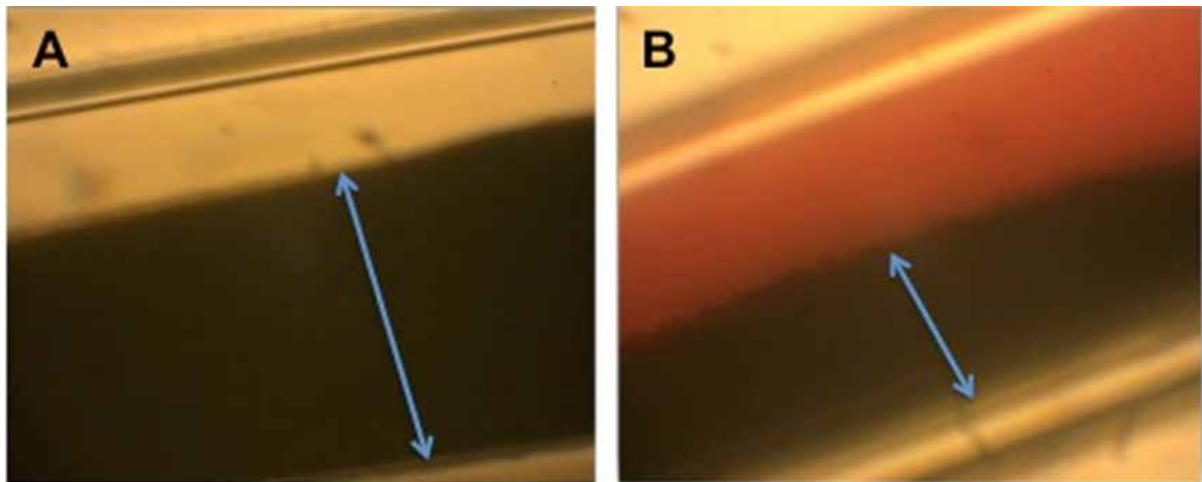


Figure 1: Optical microscope images (40 x magnification) of capillary tubes (200 μm ID), under the influence of a magnetic field, showing the number of magnetic microbubbles targeted in A) PBS and B) blood under the same flow conditions. Use of blood causes a decrease in the number of successfully targeted magnetic microbubbles.

A 200 micrometre internal diameter capillary tube was suspended in a water tank attached to a high precision syringe pump and imaged using a 40 x water immersion microscope. The tube could be coated with avidin or a magnetic field could be brought in close proximity. The capillary was perfused with either magnetic microbubbles or biotin-coated microbubbles in water and the number of bubbles retained at a given flow rate was observed and quantified. Blood was then substituted for water and the difference in targeting examined. Each set of experiments was repeated three times.

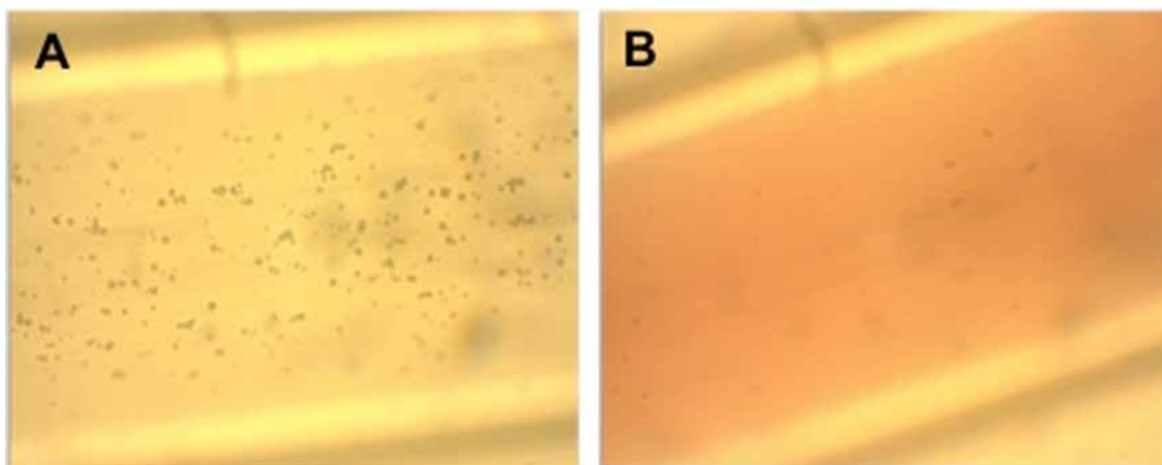


Figure 2: Optical microscope images (40 x magnification) of avidin coated capillary tubes (200 μm ID) showing the number of biotinylated microbubbles targeted in A) PBS and B) blood under the same flow conditions. Use of blood causes a significant decrease in the number of successfully targeted microbubbles.

The results showed that blood has a significant impact on targeting efficiency. A 90% decrease in targeting occurred for biochemically-targeted microbubbles and a 70 % decrease for magnetically targeted microbubbles. There may be a number of reasons for this. It seems likely that collision with erythrocytes is an important factor in the reduction in targeting seen in this study. The presence of cells in the suspension will both impede bubble motion, reducing the number of bubbles that can accumulate in a given time period; and potentially shield target sites in the case of biotinylated bubbles preventing adhesion. Collisions could also potentially detach adherent bubbles. No aggregation of bubbles and erythrocytes was observed in the experiments but this is another factor to consider which has shown to be important with certain types of nanoparticle. Further experimentation is required to find what elements of blood have the greatest impact and to develop strategies to overcome them; but the fact that these two very different methods of targeting suffered substantial reductions in efficiency in the presence of blood demonstrates the importance of utilising appropriate models when developing targeting strategies. It also supports the hypothesis that blood contributes significantly to the drop in targeting efficiency reported between *in vitro* and *in vivo* studies.

References

1. Villanueva, F.S., et al., Microbubbles targeted to intercellular adhesion molecule-1 bind to activated coronary artery endothelial cells. *Circulation*, 1998. 98(1): p. 1-5
2. Takalkar, A.M., et al., Binding and detachment dynamics of microbubbles targeted to P-selectin under controlled shear flow. *Journal of Controlled Release*, 2004. 96(3): p. 473-482
3. Fisher, N.G., et al., Influence of microbubble surface charge on capillary transit and myocardial contrast enhancement. *Journal of the American College of Cardiology*, 2002. 40(4): p. 811-819
4. Leong-Poi, H., et al., Assessment of endogenous and therapeutic arteriogenesis by contrast ultrasound molecular imaging of integrin expression. *Circulation*, 2005. 111(24): p. 3248-3254
5. Ellegala, D.B., et al., Imaging tumor angiogenesis with contrast ultrasound and microbubbles targeted to $\alpha\beta3$. *Circulation*, 2003. 108(3): p. 336-341
6. Xie, F., et al., Diagnostic ultrasound combined with glycoprotein IIb/IIIa-targeted microbubbles improves microvascular recovery after acute coronary thrombotic occlusions. *Circulation*, 2009. 119(10): p. 1378-1385
7. Alonso, A., et al., In vivo clot lysis of human thrombus with intravenous abciximab immunobubbles and ultrasound. *Thrombosis Research*, 2009. 124(1): p. 70-74
8. Willmann, J.K., et al., Dual-targeted contrast agent for US assessment of tumor angiogenesis in vivo. *Radiology*, 2008. 248(3): p. 936-944
9. Korpany, G., et al., Monitoring response to anticancer therapy by targeting microbubbles to tumor vasculature. *Clinical Cancer Research*, 2007. 13(1): p. 323-330
10. Weller, G.E.R., et al., Ultrasonic imaging of tumor angiogenesis using contrast microbubbles targeted via the tumor-binding peptide arginine-arginine-leucine. *Cancer Research*, 2005. 65(2): p. 533-539
11. Ferrara, K., R. Pollard, and M. Borden, Ultrasound microbubble contrast agents: Fundamentals and application to gene and drug delivery. *Annual Review of Biomedical Engineering* 2007. 9: p. 415-447

Ultrasound molecular imaging of transient acute myocardial ischemia with a new multi-selectins targeted ultrasound contrast agent: Correlation with the expression of selectins

Jean-Marc Hyvelin, Isabelle Tardy, Maria Costa, Patricia Emmel, Delphine Colevret, Philippe Bussat, Mathew von Wronski, Catherine Botteron, Peter Frinking, Thierry Bettinger and François Tranquart

Bracco Suisse S.A., Geneva Research Center and Manufacturing Site, Plan-les-Ouates / Geneva, Switzerland

Objectives

Diagnosis of chest pain suggestive of myocardial ischemia remains challenging especially in patients presenting with symptoms of acute coronary syndrome (ACS) and an initial normal ECG and/or an inconclusive troponin test. A hallmark of ischemia/reperfusion (I/R) is the rapid activation of endothelial cells, which is characterized by the expression of inflammatory adhesion molecules, such as P- and E-selectin. Ultrasound molecular imaging (USMI) can provide evidence of inflammation at the molecular level for cardiovascular diseases. In this context, we and others, have demonstrated that microbubbles (MB) targeted with antibodies against P-selectin can successfully image the inflammatory status of the endothelium [1]. In this context we developed an ultrasound contrast agent (UCA) functionalized with a recombinant P-selectin glycoprotein ligand-1 analog (PSGL-1, a ligand that recognizes both P- and E-selectin) that is covalently attached to the lipid shell of the MB, a step mandatory for clinical translation of targeted UCA [2]. We hypothesized that these targeted MB, so called MB_{selectin} could detect the “molecular footprint” of recent cardiac ischemic events. Performance of this newly developed agent was compared to that of MB targeted with antibodies against E- or P-selectin. Finally, we correlated USMI results with the temporal and spatial expression and the accessibility of both E- and P-selectin in the post-ischemic myocardial tissue.

Material and Methods

MB_{selectin} were designed by covalently coupling thiolated versions of the selectin-binding ligand recombinant rPSGL immunoglobulin G (Ig) onto lipid-shelled MBs. MB_{selectin} were lyophilized and stored in septum-sealed vials with a 35:65 volume-to-volume ratio of perfluorobutane to nitrogen. After reconstitution with 1 mL of sterile saline, mean diameter of reconstituted MB_{selectin} was 1.5 µm. Rat model of cardiac ischemia/reperfusion (I/R) was performed by ligating the left anterior descending (LAD) coronary artery during 20 min followed by reperfusion up to 24 h. USMI (Siemens Sequoia, 15L8 transducer, 7 MHz transmit frequency, CPS mode, MI 0.25) was performed 2 h, 5 h or 24 h after reperfusion. Late phase contrast-enhanced ultrasound signals, measured in ischemic and in control

myocardium in the same animal (10 min after MBs injection), were linearized using a prototype software developed in-house. Moreover, post-processing was applied to improve the conspicuity of the bound MB. Localisation of the ischemic area was determined by the absence of contrast enhancement during ischemia using BR38, a non-targeted contrast agent. The derived ischemic to control myocardium ratio obtained with MB_{selectin} was compared to that of MB functionalized with antibodies specific for E- or P-selectin (MB_E and MB_P, respectively) and to that of BR38. Finally, expression and endothelial cell surface accessibility of P- and E-selectin in both control and ischemic myocardium was determined by immunohistochemistry using selectin-targeted liposomes.

Results

In rats subjected to 20 min LAD ligation followed by reperfusion (2 h up to 24 h), left ventricle function (assessed by M-mode echocardiography) was not impaired, which is in agreement with good myocardial viability (as assessed by tetrazolium chloride staining). Following injection of MB_{selectin}, the late phase enhancement was higher in the left myocardial area subjected to ischemia compared to the remote myocardium (Figure 1D). The higher accumulation of MB_{selectin} in rats reperfused for 2 h, 5 h or 24 h matched with the ischemic area as identified by BR38 during ligation of the LAD (Figure 1A).

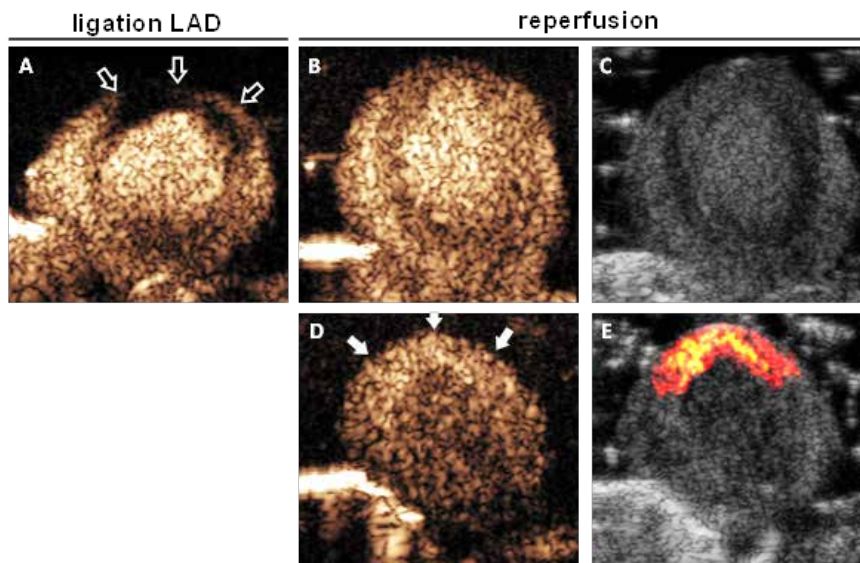


Figure 1: Typical example of USMI of a transient ischemic event in rat subjected to 20 min LAD ligation followed by 2 h reperfusion. (A), during LAD ligation, injection of BR38 allowed imaging of the ischemic territory (opened arrows). (B), late phase enhancement of BR38 revealed uniform enhancement in the left myocardium, suggesting no binding of BR38. (C), image obtained with USMI post-processing method (prototype software) was overlaid on the corresponding B-mode (anatomical) image, and revealed no bound BR38 MB. (D), within the same rat, USMI using MB_{selectin}, revealed higher late phase enhancement whose location matched the previously ischemic area (filled arrows). (E), image obtained with USMI post-processing method (prototype software) revealed bound MB_{selectin}.

Quantitative analyses of USMI signals following MB_{selectin} administration showed that the ratio of late phase enhanced signal in ischemic area vs. that of control myocardium was 3.8 ± 1.0 (n=30), 3.1 ± 0.8 (n=15) and 1.9 ± 0.8 (n=9) after 2 h, 5 h and 24 h reperfusion, respectively ($p < 0.05$, Figure 2).

Within the same hearts, following BR38 administration the ischemic to control myocardium ratio remained constant and close to 1 throughout the duration of reperfusion.

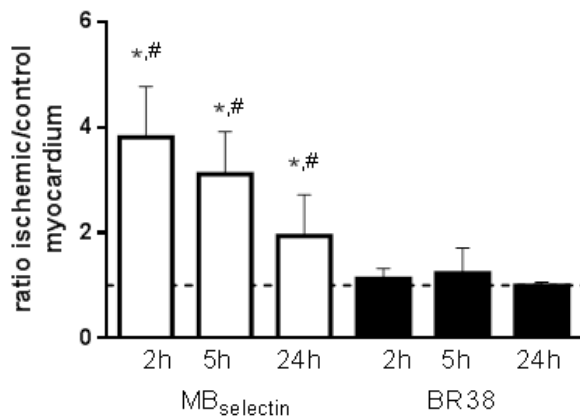


Figure 2: Ratio of late phase enhancement measured in the previously ischemic area to that in the control myocardium in rats after 20 min LAD ligation followed by 2 h, 5 h or 24 h reperfusion, following injection of either MB_{selectin} or BR38. Dotted line indicates ratio of 1. * indicates significant difference when compared to the ratio obtained in response to BR38 after the same duration of reperfusion ($p<0.05$); # indicates significant difference between rats reperfused for 2 h, 5 h and 24 h ($p<0.05$).

Comparison of late phase signals in response to MB_{selectin} to those obtained with MB_E and MB_P, suggested that both E- and P-selectin were expressed after 2 h and 5 h reperfusion. However, MB_P binding was barely detectable after 24 h reperfusion, unlike MB_E. These later results were in agreement with immunohistochemistry data showing concomitant expression of extracellular E- and P-selectin at 2 h and 5 h, whereas after 24 h extracellular P-selectin was barely detectable. Furthermore, we observed that the staining pattern produced by immunostaining of the bound selectin targeted liposomes was consistent with USMI results obtained with MB_{selectin}.

Conclusion

The results of this study suggest that USMI of selectins using MB_{selectin}, a multi-selectins UCA recognizing both P- and E-selectin, provides reliable detection of transient myocardial ischemic events that do not induce ventricular dysfunction or myocardial necrosis. The ability to detect both P- and E-selectin, whose temporal expression differs, offers an extended diagnostic window. USMI of selectins could be an appealing imaging modality to extend and improve the clinical algorithm for the diagnosis and triage of patients with suspected ACS.

References

1. Bettinger T. et al. *Invest Radiol*, 2012; 47(9):516-523
2. Wang H. et al. *Radiology*, 2013; 267(3):818-829

Ultrasound molecular imaging: Overcoming pitfalls in crucial steps

Verya Daeichin^a, Klazina Kooiman^a, Ilya Skachkov*^a, Judith Sluimer^b, Ben Janssen^c,
Mat Daemen^d, Wiggert van Cappellen^e, Ton van der Steen^a, Hans Bosch^a and Nico de Jong^a*

^aDept. of Biomedical Engineering, Erasmus MC, Rotterdam, the Netherlands

^bDept. of Pathology, Maastricht University Medical Center, Maastricht, the Netherlands

^cDept. of Pharmacology, Maastricht University Medical Center, Maastricht, the Netherlands

^dDept. of Pathology, Academic Medical Center, Amsterdam, the Netherlands

^eErasmus Optical Imaging Centre, Dept. of Pathology, Erasmus MC, Rotterdam, the Netherlands

Background

Molecular imaging is defined by the visualization of biological processes at the cellular and molecular level in living systems. Ultrasound molecular imaging makes use of ultrasound contrast agents (microbubbles). For this purpose, microbubbles are designed with specific ligands bound to the coated shell, also referred to as targeted or functionalized microbubbles [1,2]. Recently, the first human phase 0 clinical trial for ultrasound molecular imaging for prostate cancer was presented [3]. However, when looking critically at the steps involved in ultrasound molecular imaging, namely adhering of the microbubbles, imaging, and post-processing, there seems room for improvement. This research aims to investigate the pitfalls in the crucial steps needed in ultrasound molecular imaging. We investigated the ligand distribution within the coating in relation to the binding of targeted microbubbles *in vitro*, optimized the imaging parameters for nonlinear contrast mode, performed ultrasound molecular imaging using two different mouse models, and used post-analysis to distinguish bound from unbound microbubbles.

Methods

For the binding of targeted microbubble study, lipid-coated microbubbles (composition in mol%: DSPC or DPPC 59.1; PEG-40 stearate 35.7; DSPE-PEG(2000) 4.1; DSPE-PEG(2000)-biotin 0.8) with a C₄F₁₀ gas core were made by sonication [4]. Surface contact of targeted microbubbles was studied by adding the lipid dye DiD to the microbubbles before sonication and coating hydrogel-coated quartz glasses (XanTec bioanalytics, Germany) with fluorescent streptavidin Oregon Green 514 (40 µg/ml). Microbubbles adhered to the coated surface by flotation and this was mounted in 87% (v/v) glycerol such that the bound microbubbles were on top of the surface. High-resolution images were recorded with 4Pi microscopy [5]. The overlap of the red and green fluorescence was calculated using Fiji [6] (<http://fiji.sc/wiki/index.php/Fiji>) on basis of intensity threshold.

Ultrasound molecular imaging was performed *in vivo* on tumors (Huh7 liver tumors grown subcutaneously in the hindlimb of NMRI nu/nu mice) and carotid atherosclerotic plaques (ApoE knockout mice) using the Vevo2100. Microbubbles (Target-Ready Vevo MicroMarker) were targeted to VEGFR-2 and $\alpha_v\beta_3$, respectively. Respective control microbubbles were also administered. A high frequency pre-clinical ultrasound scanner was operated at 18 MHz, with a 256-element linear array transducer (Vevo 2100 with MS250 probe, VisualSonics Inc., Toronto, ON, Canada). The transducer was run at 10% transmit power in the contrast mode (amplitude modulation [7]) and wide beam-width setting was chosen in order to have a low uniform transmit pressure over depth in tissue (~400 kPa). Side-by-side Bmode and nonlinear contrast mode images were acquired with a frame rate of 30 to 40 frames per second. DICOM (Digital Imaging and Communications in Medicine) images were exported to MATLAB for further processing. For the 3D mode, the probe was mounted on a linear stepper motor (VisualSonics Inc.) and translated over the tumor area, while acquiring frames every 32 μm . The series of contrast images were then rendered in 3D using the Vevo 2100 3D Mode.

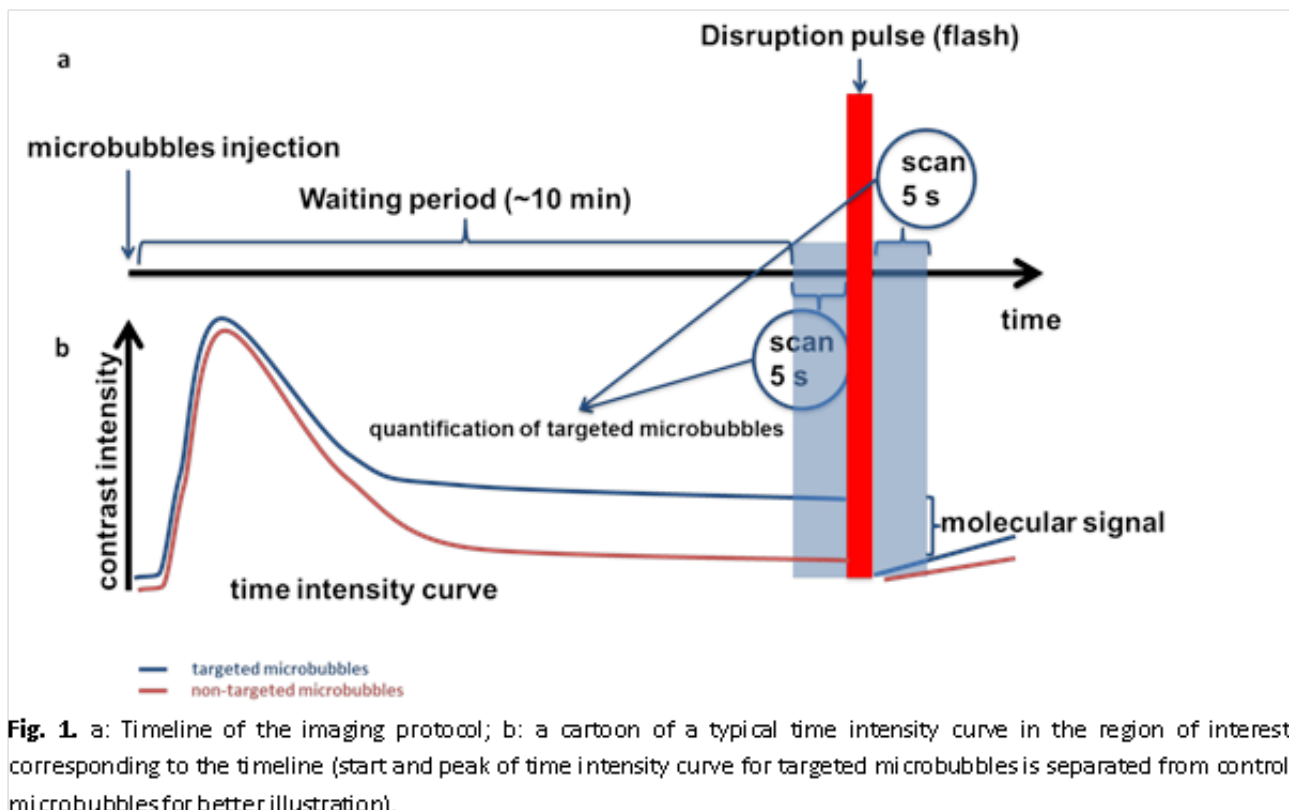


Fig. 1a schematically shows the time sequence of the ultrasound molecular imaging we performed in the mice. After injecting the microbubbles (10E08), a waiting time of about 10 minutes was required for unbound microbubbles to clear from the blood circulation. After this, a series of about 300 frames (~10 seconds) were acquired with flash pulses in the middle to disrupt the microbubbles in the imaging plane. A cartoon of a typical time intensity curve (TIC) in the region of interest (ROI) is shown in Fig.1b for two separate microbubble injections (targeted microbubbles in blue and control microbubbles in red). In the post-processing steps, first tissue motion was compensated using block matching (BM) and multidimensional dynamic programming (MDP) techniques [8]. Then, to preserve only stationary contrast signals a minimum intensity projection (MinIP) or 20th percentile intensity projection (PerIP) was applied on frames before and after the flash pulse. And, after-flash MinIP/ PerIP was subtracted from before-flash MinIP/PerIP. This way, tissue artifacts in contrast images were reduced and signals from stationary MB were enhanced. In the next step, microbubble candidates were detected by matching with artificial bubble templates. Finally templates of 0.1×0.1 mm around detected objects were tracked in subgroups of 20 frames using BM and MDP [9] to classify the candidates as unbound or bound microbubbles based on their displacement

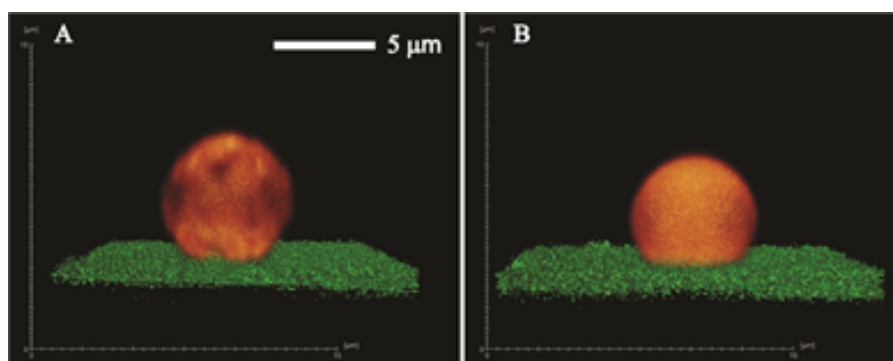


Fig. 2. Targeted lipid-coated microbubbles (red fluorescent) bound to a streptavidin-coated surface (green fluorescent; streptavidin covalently linked to hydrogel on glass coverslip) recorded in high resolution by 4Pi microscopy. A: DSPC as main lipid; B: DPPC as main lipid.

Results/Discussion

An example of a DSPC and a DPPC microbubble targeted to a coated surface is shown in Fig. 2. The DPPC microbubbles had a larger surface contact area than the DSPC microbubbles, as shown in Fig. 3. This can be explained by the distribution of the ligands within the coating, which is homogeneous for the DPPC microbubbles and heterogeneous for the DSPC microbubbles [10,11]. In larger vessels with high blood flow [12], the probability of a successful microbubble binding event is likely to be higher for a

microbubble with a homogeneous ligand distribution. This may favour DPPC microbubbles for molecular imaging.

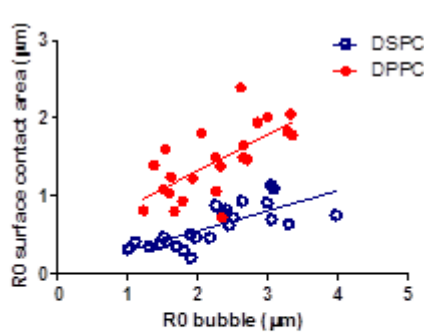


Fig. 3. Surface contact area of targeted lipid-coated microbubbles bound to a streptavidin-coated surface. DSPC: microbubbles with DSPC as main coating component; DPPC: microbubbles with DPPC as main coating component.

For the in vivo molecular imaging, we optimized parameters for the nonlinear contrast mode. This imaging modality and parameters were extracted from a comprehensive systematic in-vitro analysis (108 measurements and 648 analyses in total). Our results show that the nonlinear fundamental imaging is a more suitable approach for deeper and more attenuating media. In most studies, molecular imaging is only performed in 2D [13]. For tumors, it is assumed that such a limited cross section of the tumor is a representative of the entire tumor. However, this assumption may not always hold due to inhomogeneity of the vessel distribution in tumors [14]. Therefore, quantifying the molecular signals in an entire tumor is a much more accurate representative of the vessel structures and therefore molecular signals within the tumor. With our sensitive nonlinear contrast imaging mode, and using mechanical sweeping of the probe, we succeeded in performing 3D molecular imaging of tumors (~8 mm in diameter) with targeted microbubbles (see Fig. 4).

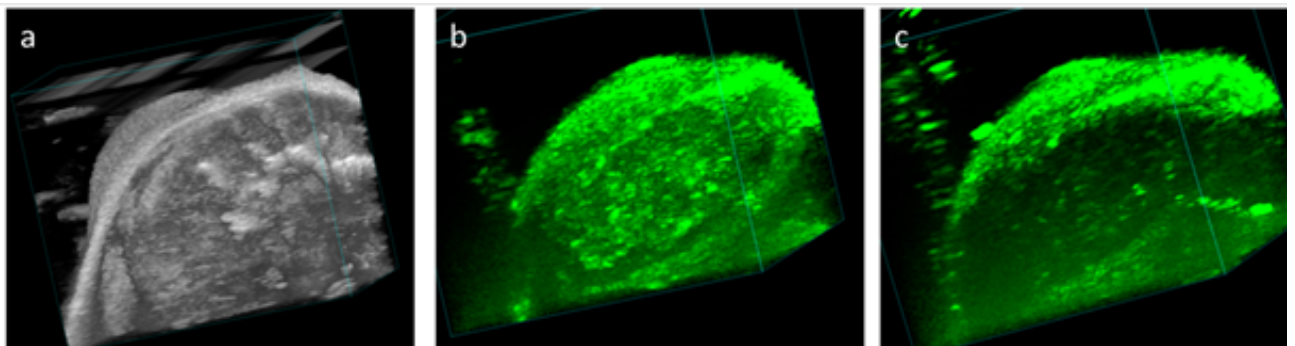


Fig. 4. 3D molecular imaging of a Huh7 liver tumor grown subcutaneously in the hind limb of NMR1 nu/nu mice: a) 3D Brmode image of the tumor (left top) and underlying healthy hind limb tissue; b) 3D contrast imaging of the tumor 10 minutes after injecting targeted microbubbles; c) 3D contrast imaging of the tumor 10 minutes after injecting control microbubbles. For figure b and c, the images are zoomed in to the tumor area.

Shortly after injecting microbubbles, the intensity of contrast in the ROI increases rapidly, then reaches a maximum, which is then followed by a decay of intensity for both targeted and control microbubbles (shown schematically in Fig. 1b). For microbubbles, the level of intensity 10 minutes after injection is expected to be higher for targeted microbubbles than for control ones. For control microbubbles, ideally, 10 minutes after injection, the image intensity in the ROI should reach a baseline level (similar to the level before injection). At the same time, the difference in the intensity levels for bound targeted microbubbles before and after the flash pulse will be a measure of molecular signals in the ROI. Unfortunately, such an ideal situation will not always happen and even 10 minutes after injection there will still be circulating unbound microbubbles for both targeted and control groups. This is what we always observed in our studies. Therefore the true difference in the intensity of the frames after the flash pulse and before that depends on the amount of both bound and unbound microbubbles in the ROI. The increase in the intensity after the flash burst therefore also shows the presence of the remaining unbound microbubbles (Fig 1b). We developed a dedicated targeted ultrasound contrast agent quantification method capable of detecting and classifying the individual contrast spots into bound and unbound microbubbles. This technique is more reliable and robust in different experimental conditions since number of bound microbubbles are quantified compared with classical method relying only on image intensities. Fig. 5 shows that this quantification method allows us to detect and quantify the targeted microbubbles attached to $\alpha_v\beta_3$ receptors in adventitial microvessels underlying the carotid atherosclerotic plaque in mice. Because of the very small size of this ROI and also the very rapid motion due to the carotid pulsation it was not possible to use the classical methods based on only subtracting the frames before the flash pulse from after the flash pulse.

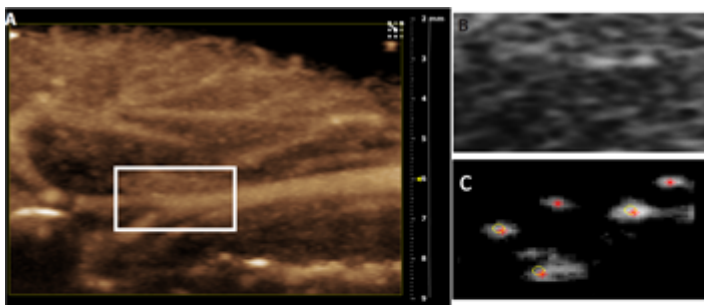


Fig. 5. Carotid ultrasound molecular imaging of adventitial microvessels underlying the plaque in atherosclerotic ApoE^{-/-} mouse using Vevo2100 (18 MHz). A. MIP of carotid bifurcation (indicated by square inset), on top of carotid is salivary gland; B. B-mode of carotid bifurcation; C. $\alpha_v\beta_3$ -targeted microbubble adherence at carotid bifurcation; red stars: total of detected microbubbles, yellow circles: microbubbles classified as targeted.

Conclusion

In conclusion, this study reveals that lipid-coated microbubbles that differ in lipid distribution also differ in surface contact area, solely on the basis of their main lipid component. An optimized nonlinear contrast imaging mode and 3D imaging enabled us to quantify the molecular signals of the entire vasculature at the region of interest. A reliable technique with high sensitivity and specificity facilitated accurate quantification of molecular signals especially in small and moving targets such as carotid atherosclerotic plaques.

Acknowledgments

This research was financially supported by the Center for Translational Molecular Medicine and the Dutch Heart Foundation (PARISK). The authors gratefully thank all colleagues for their help and support who made the experiments possible, especially Tom Kokhuis and Tom van Rooij from the Dept. of Biomedical Engineering, Erasmus MC, and Sandra van Tiel, Gabriela Doeswijk, and Monique Bernsen from the Dept. of Radiology, Erasmus MC, and Agnieszka Strzelecka, Peter Leenders, and Jacques Debets from the Dept. of Pharmacology, MUMC, and Thomas Theelen and Anique Janssen from the Dept. of Pathology, MUMC.

References

1. Lindner et al, *Nat Rev Cardiol* 6:475, 2009
2. Klibanov, *Med Biol Eng Comput* 47:875, 2009
3. Wijkstra et al, *17th European Symposium on Ultrasound Contrast Imaging, Rotterdam, 2012*
4. Klibanov et al, *Invest Radiol* 39:187, 2004
5. Hell et al, *J Microsc-Oxf* 187:1, 1997
6. Schindelin et al, *Nature methods*, 9:676, 2012
7. Needles et al, *UMB* 36:2097, 2010
8. Z. Akkus et al., *Medical Imaging*, 2012
9. A. Hoogi et al., *Ultrasound Med. Biol.*, 2012
10. Kooiman et al, *IEEE Proceedings* 2010
11. Kooiman et al, *IEEE Proceedings* 2012
12. Kornmann et al, *Ultrasound Med Biol* 36: 181, 2010
13. Gessner and Dayton, *Mol Imaging* 9:117, 2010
14. Konerding et al, *Br J Cancer* 80:724, 1999

A simplified translatable targeted microbubble formulation: The use of helper molecules for high-efficiency attachment of peptide ligands to the microbubble shell

S. Unnikrishnan, Z. Du, G.B. Diakova and A.L. Klibanov

Cardiovascular Division, Cardiovascular Research Center, Department of Medicine, Department of Biomedical Engineering, University of Virginia, Charlottesville VA 22908, USA

The problem

In order to prepare targeted microbubbles with a practically useful concentration ($\sim 10^9$ particles/ml or more), we have to use a lipid/surfactant mixture at $\sim 1-2$ mg/ml in the aqueous medium (typically, DSPC:PEG-stearate with several mol% DSPE-PEG-ligand, e.g., biotin [1,2], or a peptide). Thus, when the microbubbles are produced, either by sonication, or via a shaker amalgamation, usually, a relatively small fraction of the lipid material is incorporated into the microbubble shell. So the majority of the ligand-PEG-lipid, as well as the rest of the lipids are not present on the microbubble shell, but in the aqueous micellar form. Not only these lipids are wasted and not used for the microbubble production, but the excess of the free ligand-PEG-lipid conjugate in the aqueous medium will likely saturate the target receptors and inhibit the adhesion of the ligand-decorated microbubbles to the target surface. The excess of ligand molecules needs to be removed from the microbubble dispersant aqueous medium, which implies centrifugal flotation - a procedure difficult to implement e.g., in a hospital environment, so clinical translation will be problematic. Flotation removal of the excess of free ligand from the microbubbles has been in use in the targeted microbubble preparation in the preclinical testing for almost two decades. The procedure improvement is overdue.

The hypothesis

Helper molecules could be added as a supplement to the aqueous media prior to the microbubble preparation, to assist formation of the new gas-liquid interface. Yet these molecules should not be attached to the interface firmly, so that the microbubbles could be finally stabilized with the usual DSPC/PEG-stearate/DSPE-PEG-ligand monolayer shell (we need the ligand to be placed onto a stable microbubble shell, and attach firmly to the shell).

The set of the requirements for the helper molecule is quite challenging.

1. It should be fully biocompatible (preferably on the FDA excipients list).
2. It should aid the formation of gas-liquid interface (as regular surfactants do).
3. It should rapidly depart the gas-liquid interface of the newly formed bubble so the lipid monolayer could take its place.
4. Unlike regular surfactants, it should not destabilize or dissolve the lipid monolayer shell at the concentrations needed for its helper function.

The approach

Glycerol, other polyols (e.g., mannitol) and carbohydrates are too hydrophilic to serve as proper helpers; they do not seem to bind to the newly forming gas-liquid interface and assist the formation of microbubbles of the desired size and concentration, even transiently. These additives may provide significant increase of the media viscosity, which may lead to a drastic increase in the fluid shear stress during microbubble formation. Thus, viscosity and shear are not the likely reasons of the bubble formation efficacy improvement. Alcohols are efficient organic solvents, and their presence in the aqueous dispersant phase may dissolve the microbubble shell lipid monolayer and will make the bubbles unstable. Many biocompatible surfactants which could be considered as helpers would form mixed micelles with the membrane-forming lipids, which results in the instability of the microbubbles, and leads to the extraction of the ligand-PEG-lipid conjugate from the microbubble shell. Propyleneglycol (1,2-propanediol) proved to be the optimal choice as a helper molecule: it aids efficient microbubble formation, yet in its presence in the aqueous medium microbubbles are stable for several hours; most of the DSPE-PEG-ligand along with other shell lipids is transferred to the microbubble shell during the microbubble formation in the presence of the sufficient concentration of propyleneglycol in the aqueous medium.

Methods and Materials

VCAM-1-targeted VHPKQHRGGSK*GC peptide [3] (K*=lysine-FITC) was covalently coupled to maleimide-PEG3400-DSPE via a C-terminal cysteine thiol [4]. Excess free peptide was removed from conjugate micelles by dialysis, and lyophilized. Integrin $\alpha_v\beta_3$ -targeted cyclic peptides c(RGDfK), a matching control c(RADfK), or a linear peptide ATWLPPR (targeted to neuropilin-1, [5]) were modified on the primary aminogroup (respectively, lysine, or N-terminus), with NHS-PEG3400-DSPE. Microbubbles were prepared by Vialmix amalgamator shaking of a sealed vial containing decafluorobutane headspace and aqueous saline media containing 1,2-propanediol and micellar aqueous mixture of DSPC, PEG stearate and peptide-PEG-DSPE conjugate (1:1:0.2 mass ratio), and used on the same day.

For FITC-peptide, coupling to the microbubble shell was confirmed by fluorescence microscopy. Following centrifugal flotation, fluorescence spectroscopy of the infranatant was performed (Molecular Devices Gemini XS instrument) and compared with the fluorescence of the aqueous micellar medium prior to the microbubble preparation, to quantify the transfer of fluorescent peptide to the microbubble shell from the lipid micelles in the aqueous medium.

For comparison of the targeted contrast ultrasound imaging capability of the novel preparation and the traditional earlier microbubble formulations, $\alpha_v\beta_3$ -targeted microbubbles were also prepared, by a standard sonication procedure [2] of an aqueous lipid micellar mixture that contained 2 mg/ml DSPC, 2 mg/ml PEG stearate and 0.4 mg/ml c(RGDfK)-PEG3400-DSPE.

In vitro microbubble targeting was investigated on the receptor protein-coated dishes or on the control albumin surfaces, either in static conditions or in a parallel plate flow chamber (1 dyn/cm² wall shear stress for the latter). For *in vivo* targeted contrast ultrasound imaging studies we used a murine tumor model. A murine colon adenocarcinoma cells ($5 \cdot 10^5$, MC38, generously provided by Dr. J. Schlom, NCI), were injected subcutaneously in the hind leg of C57BL/6 mice. Contrast ultrasound imaging was performed as the tumor size reached 6-8 mm (Siemens Sequoia 512, 15L8 probe, 7 MHz, MI 0.2, CPS mode) 10 min after an intravenous bolus of $2 \cdot 10^7$ microbubbles.

Results

Preparation of peptide-microbubbles by amalgamation in the presence of propyleneglycol was fast and efficient ($>2 \cdot 10^9$ bubbles/ml in 45s). Fluorescent peptide was observed on the microbubble shell by fluorescence microscopy. Over 85% of the added fluorescent peptide conjugate has associated with the microbubbles, as determined by the fluorescence spectroscopy of the infranatant. *In vitro* study confirmed selective adhesion to receptor-coated surfaces and not to albumin ($p < 0.001$ for RGD bubble). Targeted microbubbles accumulated in the tumor but not in contralateral leg ($p < 0.0002$ for VCAM-1 targeted bubble, $p < 0.0005$ for $\alpha_v\beta_3$ -targeted, and $p < 0.0001$ for ATWLPPR-decorated bubble). *In vivo* targeting efficacy of Vialmix-microbubbles prepared with propyleneglycol helper and that of the standard microbubbles prepared by sonication at 2 mg/ml DSPC concentration in the aqueous saline was similar. Control microbubbles did not show preferential tumor accumulation.

Conclusions

We describe a formulation of a targeted ultrasound contrast microbubbles useful for molecular imaging studies, with a simplified and fully translatable preparation procedure. It is based on adding a biocompatible 1,2-propanediol helper molecule to the lipid micellar aqueous phase. It assures an efficient placement of the targeting ligand on the microbubble shell via a PEG-lipid anchor with high

yield, and the removal of excess ligand from the microbubbles is no longer necessary for the targeted ultrasound contrast application.

Peptide-decorated microbubbles prepared by this procedure are excellent contrast agents for ultrasound imaging, and their successful targeting was demonstrated *in vitro* (adhesion to receptor-coated surfaces) and *in vivo*, in a subcutaneous murine tumor model.

References

1. Lindner JR, Song J, Christiansen J, Klibanov AL, Xu F, Ley K. Ultrasound assessment of inflammation and renal tissue injury with microbubbles targeted to P-selectin. *Circulation*. 2001;104(17):2107-2112
2. Klibanov AL, Rychak JJ, Yang WC, Alikhani S, Li B, Acton S, Lindner JR, Ley K, Kaul S. Targeted ultrasound contrast agent for molecular imaging of inflammation in high-shear flow. *Contrast Media Mol Imaging*. 2006;1(6):259-266
3. Nahrendorf M, Jaffer FA, Kelly KA, Sosnovik DE, Aikawa E, Libby P, Weissleder R. Noninvasive vascular cell adhesion molecule-1 imaging identifies inflammatory activation of cells in atherosclerosis. *Circulation*. 2006;114(14):1504-1511
4. Southworth R., Kaneda M., Chen J., Zhang L., Zhang H., Yang X., Razavi R., Lanza G., Wickline S.A. Renal vascular inflammation induced by Western diet in ApoE-null mice quantified by ¹⁹F NMR of VCAM-1 targeted nanobeacons. *Nanomedicine*. 2009;5(3):359-367
5. Starzec A, Ladam P, Vassy R, Badache S, Bouchemal N, Navaza A, du Penhoat CH, Perret GY. Structure-function analysis of the antiangiogenic ATWLPPR peptide inhibiting VEGF(165) binding to neuropilin-1 and molecular dynamics simulations of the ATWLPPR/neuropilin-1 complex. *Neuropilin Peptides*. 2007;28(12):2397-2402

Peptide targeted microbubbles: Potential for targeted imaging

Shah Rukh Abbas, E.A.H. (Lisa) Hall

Department of Chemical Engineering and Biotechnology, University of Cambridge, UK

Targeted Contrast Enhanced Ultrasonography using targeted microbubbles is being widely investigated for their potential to detect specific molecular signal and for targeted drug delivery. This relies on the retention of targeted microbubbles in the specific regions which further depends on targeting microbubbles¹. Targeting of microbubbles have been done using many strategies¹; directly attaching disease specific ligands to shell via covalent binding or via streptavidin-biotin linkage. It is however important for microbubbles to be biocompatible and highly specific for ultimate use for targeted imaging in vivo.

We investigated the potential of using an RF silaffin peptide tag as a coupling agent to tag microbubbles with protein of interests. Our microbubble population comprised of home-made hydrogel based microbubbles with negative charge on the surface and silica microbubbles with hydroxyl groups on the surface.

We made a recombinant construct of R5 silaffin peptide tag and mCherry fluorescence protein (model protein) and investigated its passive binding to microbubbles. R5-silaffin peptide is 19-amino acid long and is synthetic version of a portion of silaffin protein from Diatoms. Silaffins have natural affinity for silica in diatoms and hence responsible for silica deposition. Recently, it was discovered that the synthetic R5 peptide, the repeat unit of silaffin polypeptide, is actually capable of precipitating silica in vitro and at ambient conditions². Since this peptide has got hydroxyl groups on the serines and also have arginine and lysine giving it a net positive charge and so it can bind via hydrogen bonding and electrostatics to our formulated microbubble population.

The affinity of recombinant proteins to different shell materials has been investigated using QCM-D technique which gives the amount of the protein bound to surface under particular conditions and compared it with untagged mcherry Fluorescent Protein for binding efficiency. These findings hence will be useful for further investigations of using R5-tag for targeting microbubbles for both medical and non-medical applications and its affinity constant to different shell material.

References

1. Kaufmann, B. a, & Lindner, J. R. (2007). *Molecular imaging with targeted contrast ultrasound. Current opinion in biotechnology, 18(1), 11–6. doi:10.1016/j.copbio.2007.01.004*
2. Sumper, M., Kro, N., & Regensburg, D.-. (2004). *Silica formation in diatoms : the function of long-chain polyamines and silaffins, 2059–2065*

Ultrasound molecular imaging of tumoral angiogenesis with BR55: Added values for the monitoring of focalised and systemic anti-tumoral therapies

Alexandre Helbert^{1,2}, Jean-Marc Hyvelin², Frederic Padilla¹, Isabelle Tardy², Cyril Lafon¹, Jean-Yves Chapellon¹; Mathew von Wronski², and François Tranquart²

¹LabTau Laboratory - Inserm Unit 1032, Lyon, France

²Bracco Suisse S.A., Geneva Research Center and Manufacturing Site, Plan-les-Ouates / Geneva, Switzerland

Objectives

In cancer patients, “seeing is believing” and imaging plays a daily clinical role in determining whether or not to continue, adjust or change anti-tumoral treatment. This need for objective and reliable assessment of efficacy is also required in the development and validation of new therapies. The efficacy of anti-tumoral therapies is commonly evaluated by measuring direct effects on the tumor by use of the *Response Evaluation Criteria In Solid Tumors* (RECIST) based on anatomical changes. However such criteria suffer from many limitations related to either inter- and intra-observer variability or sensitivity. Delineating tumor edge is subject to observer variability, and might be challenging in case of multifocal and/or small lesions which also can make the use of focal treatment difficult. Conversely, with the advent of anti-angiogenic chemotherapy, vascular changes might occur initially without tumor size reduction. Other methods using functional and molecular criteria are now proposed. In this regard, ultrasound molecular imaging (USMI), combined with quantification software, is a promising non-invasive imaging method that allows tumor detection, but also functional parameters assessment, including tumor perfusion and the quantification of specific molecular markers, such as Vascular Endothelial Growth Factor Receptor-2 (VEGFR2). BR55 (Bracco Suisse SA) is a specific VEGFR2-targeted ultrasound contrast agent that has been recently tested in human prostate.

Aims of the present study were to perform a therapeutic follow-up in two tumor animal models, treated with sunitinib, an anti-angiogenic therapy that acts directly on VEGFR2; or targeted doxorubicin delivery, a potent cytotoxic drug that inhibits cellular division. Functional parameters and molecular markers (VEGFR2) were then assessed by USMI using BR55 and compared to anatomical parameters. Finally we correlated USMI results with immunohistostaining of CD31, a vascular marker, and VEGFR2.

Material and Methods

Two animal tumor models were used. The spontaneous rat mammary tumor, obtained by intraperitoneal injection of N-Nitroso-N-Methyl Urea (50mg/kg *i.p.*) in female rats; and the Copenhagen rats in which adenocarcinoma cells (G Dunning R-3327) were implanted in one lobe of the ventral prostate. Rats bearing mammary tumors received either anti-angiogenic treatment (20 mg/kg/day *p.o.* sunitinib) or vehicle (1mL/kg/day *p.o.*) during 3 days. Rats bearing prostate tumors were randomly assigned to 3 different groups: rats treated with ultrasound only (US); rats treated with [1,2-dierucoyl-sn-glycero-3-phosphocholine]-based liposomal doxorubicin (liposomal-DXR) and rats treated with both US *plus* liposomal-DXR. When US and liposomal-DXR were applied concomitantly, liposomal-DXR (3mg DXR/kg, *i.v.*) was injected 2 days prior US treatment. US treatment was performed with a custom built confocal ultrasound device comprising 2 focused US transducers (1.1 MHz), used to trigger the release of DXR from the liposomes following passive accumulation in the tumors. Coordinates of the tumor were first determined based on USMI of VEGFR2 in response to BR55 injection, and US treatment was then applied (PRF 250 Hz, burst count 44, D.C. 1%, PNP 25MPa) by scanning the tumor with a dedicated 3D stage system. In both models, tumor response was monitored (up to 3 days in rat mammary tumors, and up to 11-12 days in rat prostate tumors) by USMI using BR55 and an ultrasound system (iU22 Philips, L12-5 linear array probe). Contrast enhancement, from the largest section of the tumors, was quantified using a prototype software developed in-house. Peak enhancement (PE) was determined during the early wash-in phase; whereas targeted contrast enhancement (TE) of bound BR55 microbubbles was assessed 10 min after injection of BR55. Finally, expression of endothelial cell marker (CD31) and VEGFR2 in both tumor models, and throughout the treatment duration, was determined by immunohistochemistry.

Results

In the rat mammary tumor model, sunitinib treatment produced a progressive decrease in tumor area (at day 3 post-treatment, tumor area was 60 ± 8 % of the initial value, $p < 0.05$). In vehicle-treated rats, tumor area increased throughout follow up (133 ± 27 % at 3 days post vehicle treatment, $p < 0.05$). Contrast imaging parameters, in response to BR55, showed a greater decrease in both PE and TE compared to anatomical parameters. Furthermore the decrease in TE was faster and more pronounced than that of PE (18 ± 8 % and 40 ± 13 % of the initial values of TE and PE, respectively, $p < 0.05$). Both CD31 and VEGFR2 expression changes correlated with USMI parameters PE and TE (Figure 1).

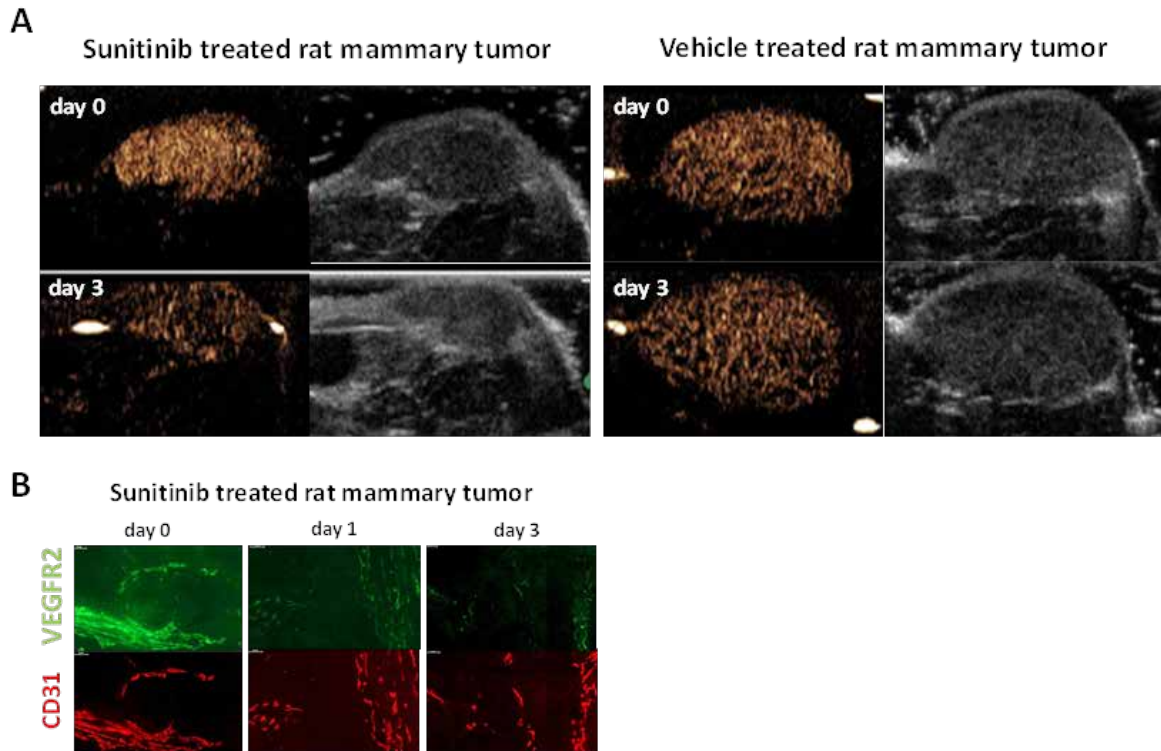


Figure 1: USMI and Immunostaining of VEGFR2 in rat mammary tumor treated with sunitinib. *A*, USMI of VEGFR2 using BR55 in animal treated with sunitinib (left) or vehicle (right). *B*, immunostaining of VEGFR2 (green) and CD31 (red) in rat mammary tumors treated with sunitinib

In the prostate tumor animal model, USMI of VEGFR2 allowed for an adequate delineation of the prostate and consequently the area to be treated with US. In animals treated with US only, tumor area showed gradual increase throughout the follow-up ($209 \pm 46\%$ at day 11 compared to baseline value, $p < 0.05$) suggestive of tumor growth. Conversely, in animals that received only liposomal-DXR, tumor area remained unchanged ($124 \pm 29\%$ at day 11); whereas in rats that received a combined treatment, US activation of liposomal-DXR produced a significant decrease in tumor area as early as 5 days after US activation of liposomal-DXR ($51 \pm 37\%$ of the initial value, $p < 0.05$, Figure 2). With regard to USMI of VEGFR2, data revealed that TE values remained unchanged compared to baseline values. It is noteworthy that area of bound BR55 matched with B-mode tumor area and therefore decreased in rats treated with US + liposomal-DXR (Figure 2). Finally CD31 and VEGFR2 expression remained unchanged throughout follow-up, in agreement with USMI results. (Figure 2). Preliminary results indicated that DXR accumulated mostly at the periphery of the tumor.

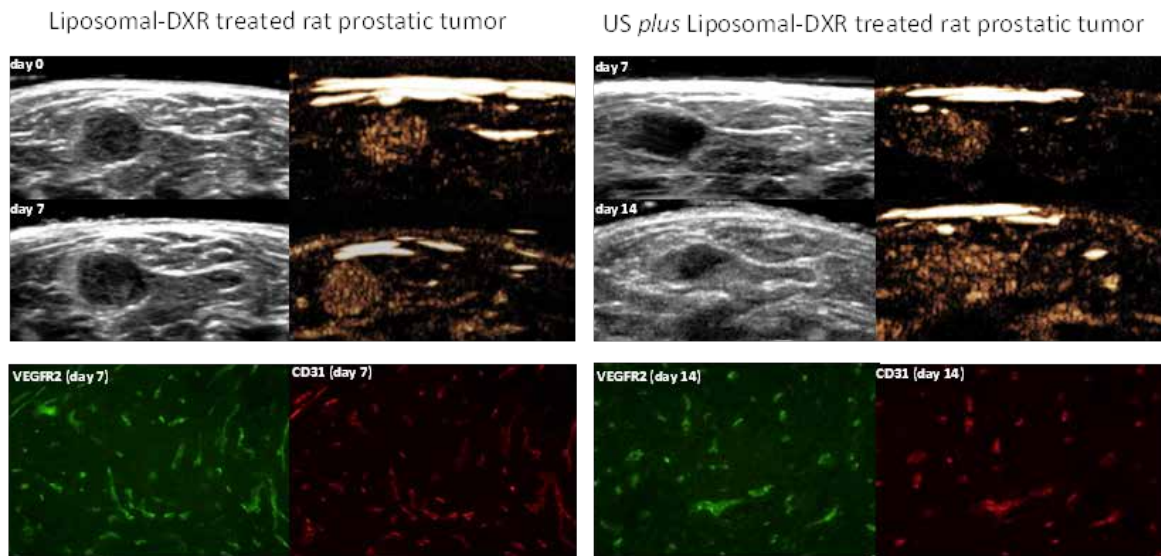


Figure 2: USMI and Immunostaining of VEGFR2 in rat prostate tumor model treated with liposomal-DXR or US-activated liposomal DXR. The upper panel shows B-mode and late phase contrast-enhanced signal in tumor. The lower panel shows immunostaining of both VEGFR2 (green) and CD31 (red).

Conclusion

These results suggest that USMI of VEGFR2 using BR55 provides reliable detection of tumors and also allows the follow-up of various anti-tumoral therapies that act on different cellular targets. USMI parameters, using BR55, show greater and earlier changes in response to anti-angiogenic treatment than anatomical parameters. Conversely, when using cytotoxic drug, USMI parameters remained unchanged. Most importantly we observed that changes in USMI of VEGFR2 correlate well with VEGFR2 expression. Finally we showed that using BR55 improves the delineation of tumor edges, an added value for the use of a focalised activation of drug delivery system in order to spare the surrounding healthy tissue.

Acknowledgment

Authors thank Catherine Botteron, Lucille Vallé, Philippe Bussat and Martine Theraulaz, from Bracco Suisse SA, for their valuable support.

FIRST ANNOUNCEMENT 2015

**20th EUROPEAN SYMPOSIUM ON
ULTRASOUND CONTRAST IMAGING**

22-23 JANUARY 2015

ROTTERDAM, THE NETHERLANDS

**Course Directors: Nico de Jong
Arend Schinkel**

**Scientific Board: Folkert ten Cate, Edward Leen, David Cosgrove,
Mike Averkiou, Eleanor Stride and Paolo Colonna**

The 29th Annual
A d v a n c e s i n
C o n t r a s t U l t r a s o u n d
~ ICUS Bubble Conference
bubbleconference.com



September 18-19, 2014

The Wyndham Grand Chicago Riverfront Hotel

Contact Ms. Gerri Somerville-Kalita for more information – gsomervi@rush.edu

“The 29th Annual Advances in Contrast Ultrasound
~ICUS Bubble Conference”

SAVE the DATE !

September 18-19, 2014

The Wyndham Grand Chicago Riverfront Hotel

Conference Director:

Steven B Feinstein, MD,
Rush University Medical Center, Chicago , IL USA

Co-Directors:

Stephanie Wilson, MD,
University of Calgary, Calgary AB, Canada
Petros Nihoyannopoulos, MD and David Cosgrove, MD
Hammersmith Hospital, Imperial College, London, UK

Conference Manager: Ms. Gerri Kalita, gsomervi@rush.edu, phone 312-942-4601.

THE CONFERENCE:

The annual "bubble conference" plays a unique and critical role in the development of both diagnostic and therapeutic CEUS applications. The conference is the single-most important forum for presenting the latest and best CEUS research across geographical borders and medical specialties. This year the meetings will expand to offer hands on contrast training classes on Friday afternoon.

INDUSTRY FUNDING: To become a recognized supporter of the 2014 meetings, please contact Ms. Gerri Somerville-Kalita by phone, 1-312-942-4601, fax 312-942-6334, or email gsomervi@rush.edu. Supporting the meetings with educational grants, hosting promotional events, renting exhibitor spaces and leading hands on contrast classes to attendees are all available means to show your confidence in the annual Bubble Conference's mission and values.

The Bubble Conference agenda is created through an educational partnership shared by Advances in Contrast Ultrasound (AU) and the International Contrast Ultrasound Society (ICUS)



WWW.BUBBLECONFERENCE.COM

The 19th European Symposium on Ultrasound Contrast Imaging Rotterdam is sponsored by:

Philips Healthcare

J. MacQuarrie
Senior Product Manager
Global Business Innovation Unit
231 Bellevue
DUB 8 Dublin - Ireland

Bracco Suisse SA

M. Graf, Congress Manager
Senior Communication Events Manager
Centro Galleria 2
Via Cantonale
CH-6928 Manno - Switzerland

GE Healthcare - Medical Diagnostics

B. B. Newton
Global Product Leader - Ultrasound
The Grove Centre
White Lion Road
Buckinghamshire, HP7 9LL – UK

ZONARE

L. Steffgen
Manager, International Clinical Marketing
Medical Systems GmbH
Henkestraße 91
91052 Erlangen - Germany

Hitachi Medical Systems

E. Bibby
European Marketing
Sumpfstrasse 24
6300 Zug – Switzerland

Visualsonics

Anil K K Amlani
Acting President and CEO
3080 Yonge Street
Toronto, Ontario
M4N 3N1 – Canada

Oldelft BV

Oldelft Ultrasound
S. Roggeveen
Commercial Manager
Elektronicaweg 10
2628 XG Delft
The Netherlands

Nederlandse Hartstichting

E. Buitenhuis
Manager Research Department
P.O. Box 300
2501 CH Den Haag
The Netherlands

Coeur

H. Boersma
Erasmus MC - Thoraxcenter
Dr. Molewaterplein 50
3015 GE Rotterdam
The Netherlands

The 19th European Symposium of Ultrasound Contrast Imaging, Rotterdam is sponsored by:



PHILIPS

GE Healthcare



**Oldelft
Ultrasound**



ZONARE

HITACHI
Inspire the Next